



HAL
open science

Study of the dielectric properties of HFO gas, and its application to reduce the environmental impact of medium-voltage systems

Simon Soulie

► **To cite this version:**

Simon Soulie. Study of the dielectric properties of HFO gas, and its application to reduce the environmental impact of medium-voltage systems. Electric power. Université Grenoble Alpes [2020-..], 2021. English. NNT: 2021GRALT061 . tel-03524416

HAL Id: tel-03524416

<https://theses.hal.science/tel-03524416>

Submitted on 13 Jan 2022

HAL is a multi-disciplinary open access archive for the deposit and dissemination of scientific research documents, whether they are published or not. The documents may come from teaching and research institutions in France or abroad, or from public or private research centers.

L'archive ouverte pluridisciplinaire **HAL**, est destinée au dépôt et à la diffusion de documents scientifiques de niveau recherche, publiés ou non, émanant des établissements d'enseignement et de recherche français ou étrangers, des laboratoires publics ou privés.

THÈSE

Pour obtenir le grade de

DOCTEUR DE LA COMMUNAUTE UNIVERSITE GRENOBLE ALPES

Spécialité : Génie électrique

Arrêté ministériel : 25 mai 2016

Présentée par

Simon Soulié

Thèse dirigée par **Olivier Lesaint**, Directeur de recherche au CNRS,
et codirigée par **Nelly Bonifaci**, chargée de recherche au CNRS.

préparée au sein du **Laboratoire de génie électrique de Grenoble**
dans l'**École Doctorale Électronique, Électrotechnique,
Automatique & Traitement du Signal**

Étude des propriétés diélectriques du HFO-1234 ze(E) pour le remplacement du SF₆

Thèse soutenue publiquement le **29 septembre 2021**,
devant le jury composé de :

M. Olivier EICHWALD

Professeur des universités à l'Université Toulouse III, Rapporteur

M. Emmanuel ODIC

Professeur à CentraleSupélec, Rapporteur

M. Jean-Hugues PAILLOL

Professeur à l'université de Pau, Président du jury

M. Olivier LESAINT

Directeur de recherche au CNRS, Directeur de thèse

Mme. Nelly BONIFACI

Chargée de recherche au CNRS, Co-directrice de thèse

M. François GENTILS

Ingénieur de recherche à Schneider Electric, invité



Remerciements

Je tiens tout d'abord à remercier le professeur Jean-Hugues Paillol qui m'a fait l'honneur de présider le jury de cette thèse. Mes remerciements vont aussi à Olivier Eichwald et Emmanuel Odic qui ont rapporté sur ce mémoire, pour leur relecture attentive et les discussions que nous avons pu avoir durant la soutenance.

Au terme de ces trois années, je tiens tout particulièrement à remercier mes directeurs de thèse. Je vous remercie pour votre confiance, votre passion, votre gentillesse, votre disponibilité, vos conseils et par-dessus tout, pour votre bienveillance à mon égard.

Olivier, tes qualités scientifiques et ton expertise ont permis de mener à bien cette étude. Ta sympathie et bienveillance ont rendu ce travail agréable mais aussi très enrichissant humainement. Nelly, je te remercie du fond du cœur pour ta bienveillance, ta disponibilité de tous les instants, de m'avoir fait partager ta vision de la recherche et surtout de m'avoir permis d'observer le spectre du soleil !!!

Merci à Schneider Electric de m'avoir accueilli pour cette étude. Tous mes remerciements vont à François Gentils pour avoir suivi l'intégralité de mes travaux et porté un regard critique et scientifique, mais surtout pour challenger ces résultats pour en faire ressortir le meilleur. Merci aux différents personnels de Schneider de m'avoir accueilli au sein de leur laboratoire et de m'avoir fait partager leur vision de la recherche. Merci enfin à tous mes collègues de Schneider que j'ai pu côtoyer durant ces 3 années.

Je voudrais remercier tout particulièrement l'ensemble du personnel du G2elab que j'ai pu côtoyer et avec qui j'ai eu la chance et le plaisir de travailler. Des remerciements tout particuliers vont à Sébastien Flury et Jean-Luc Palenzuela, qui ont tous deux énormément donné pour mettre en place l'ensemble des expériences, les faire évoluer, les améliorer continuellement et sans qui, les dispositifs expérimentaux n'auraient sans doute pas fonctionné. Merci à toutes les personnes qui ont œuvré de près ou de loin à la mise en place de ces dispositifs expérimentaux : Sébastien, Florian, Christophe et Nicolas.

Rachelle je te remercie aussi tout particulièrement pour ta bonne humeur, ta joie de vivre et surtout pour t'être moqué de mon accent Toulousains durant 3 ans.

Ces trois années n'auraient pas été aussi agréables et enrichissantes sans mes collègues et amis doctorants. Mickaël pour les discussions autour d'un merveilleux repas du CROUS et pour les séances de volley, Yoann pour les discussions post-confinement entre 2 séries de mesures, Irena pour le soutien de fin de thèse. Merci à toute la Team MDE, Raphael, Joko, Nathan, François, Chen Cho, Hugo, Gwen.

Merci mes collègues de bureau, Simon et tes merveilleuses chansons que tu passes en boucle, Igor pour ta générosité et ta sympathie. Et je souhaite un bon courage à Gwen pour son installation dans ce bureau.

Merci à toute ma famille et à mes proches pour m'avoir soutenu et encouragé tout au long de cette aventure. En particulier merci à toutes les personnes qui ont fait (ou voulu faire) le long déplacement, merci Jeanne, Ludo et Manon de votre soutien. Un grand merci à ma famille qui m'a toujours soutenu et qui a toujours cru en moi dans cette aventure un peu folle. Et enfin merci à Inès pour tout ce que tu as pu m'apporter durant 3 ans. Sans toi rien de tout cela n'aurait été possible alors encore merci.

Abstract

Replacing SF₆ in electrical devices has been a central concern of the electrical industry for years. Indeed, SF₆ is the gas with the highest known global warming power. For many years alternatives to SF₆ have been studied without success. Hydrofluoroolefins have good aptitudes for substituting SF₆ in medium voltage gas insulated systems.

In this context, preliminary studies have revealed the potential of HFO-1234ze(E) as an insulating gas for medium voltage switchgear. The objective of this work is to gather data and knowledge for the sizing of medium voltage devices with HFO-1234ze(E). Experimental results include measurements of breakdown voltages obtained under various conditions of voltage (DC, impulse shock), pressure (0.1 to 0.3 MPa), inter-electrode distance (10 to 100 mm), and electrodes shape. This wide range of configurations made it possible to highlight two very distinct breakdown modes comparable to those present in SF₆. When the field is strongly inhomogeneous, the most critical geometry for electrical devices, the breakdown is "controlled by the propagation" of pre-discharges. The leaders propagate in the inter-electrode space by steps at velocity of the order of 10⁶ m/s without necessarily leading to breakdown. When the field becomes more homogeneous, the breakdown becomes "controlled by initiation". When a pre-discharge initiates, it systematically leads to breakdown. Pressure plays an important role in initiation voltage as opposed to breakdown voltage. Finally, one of the important results of this work is the highlighting of the complex influence between the degradation of HFO, the presence of solid particles at the surface of the electrode and the loss of dielectric strength in nearly homogeneous field after a single breakdown.

Keywords: Medium voltage GIS, dielectric strength, hydrofluoroolefin (HFO-1234ze(E)), electrical characterization, visualizations

1. REMERCIEMENTS	II
ABSTRACT	IV
LIST OF TABLES	VII
LIST OF FIGURES	IX
LIST OF ABBREVIATIONS	XVII
GENERAL INTRODUCTION	1
1. CHAPTER 1: CONTEXT OF THE STUDY: GASEOUS INSULATION IN MV DEVICES, AND BREAKDOWN PHYSICAL PROCESSES	2
1.I. INTRODUCTION	2
1.II. CONTEXT: USAGE, RESTRICTION, AND SUBSTITUTION OF SULFUR HEXAFLUORIDE SF₆	2
1.II.A. <i>Greenhouse effect and use of SF₆</i>	4
1.II.B. <i>Policy and standards</i>	5
1.III. REDUCTION AND REPLACEMENT STRATEGIES OF SF₆	8
1.III.A. <i>Recovery and recycling of SF₆</i>	8
1.III.B. <i>Use of mixtures</i>	8
1.III.C. <i>Alternatives gases to SF₆</i>	9
1.IV. PROPERTIES OF THE GAS STUDIED IN THIS WORK: HFO-1234 ZE (E)	11
1.IV.A. <i>Physical and environmental properties of HFO-1234ze (E)</i>	13
1.IV.B. <i>Dielectric properties of HFO: preliminary investigations carried out at G2Elab</i>	16
1.V. BREAKDOWN PHYSICAL PROCESSES IN GASES	19
1.V.A. <i>Electronic avalanche</i>	19
1.V.B. <i>Origin of the initial electrons</i>	21
1.V.C. <i>Paschen's law</i>	21
1.VI. STREAMER PHENOMENON	23
1.VI.A. <i>Principle</i>	23
1.VI.B. <i>Propagation velocity of streamers</i>	24
1.VI.C. <i>Propagation length of streamers</i>	25
1.VI.D. <i>Streamer radius</i>	26
1.VI.E. <i>Structure</i>	26
1.VI.F. <i>Transition to breakdown</i>	27
1.VI.G. <i>Modelling of streamers</i>	28
1.VII. LEADER PHENOMENON	28
1.VII.A. <i>Principle</i>	28
1.VII.B. <i>Propagation velocity of leaders</i>	31
1.VIII. ADDITIONAL PARAMETERS INFLUENCING ELECTRIC DISCHARGES AND BREAKDOWN PROPERTIES IN APPLICATIONS	31
1.VIII.A. <i>Electrode geometry and surface roughness</i>	31
1.VIII.B. <i>Applied voltage wave shape</i>	32
1.VIII.C. <i>Impurities in the gas</i>	33
1.IX. CONCLUSIONS AND OUTLINE OF THESIS	33
2. CHAPTER 2: MATERIALS AND METHODS	35
2.I. GASES	35
2.II. DESCRIPTION OF THE TEST CELL	35
2.III. ELECTRODE CONFIGURATIONS	35
2.IV. HIGH VOLTAGE GENERATORS	39
2.IV.A. <i>Direct voltage</i>	39
2.IV.B. <i>Impulse voltage</i>	39
2.IV.C. <i>Breakdown voltage measurement procedures</i>	42
2.V. OPTICAL MEASUREMENTS	44
2.V.A. <i>Measurement of photo-currents</i>	44
2.V.B. <i>Intensified camera</i>	44
2.V.C. <i>Measurements of streamers and leader propagation velocity</i>	44
2.V.D. <i>Spectroscopic measurements</i>	45
3. CHAPTER 3: BREAKDOWN MODES, AND CHARACTERISATION OF PRE-DISRUPTIVE PHENOMENA IN HFO IN DIVERGENT FIELD	47
3.I. DEFINITIONS OF "PROPAGATION" AND "INITIATION"-CONTROLLED BREAKDOWN	47
3.I.A. <i>Introduction</i>	47

3.I.B. Discharge initiation and breakdown initiation frequency.....	49
3.I.C. Summary of tests carried out for propagation-controlled breakdown	51
3.I.D. Degradation of HFO in divergent field	54
3.II. CHARACTERISATION OF PRE-DISRUPTIVE PHENOMENA IN STRONGLY DIVERGENT FIELD IN HFO.....	55
3.II.A. Identification of pre-breakdown phenomena	55
3.II.B. Propagation velocity.....	60
3.II.C. Stopping length of leaders in HFO and SF ₆	67
3.II.D. Temporal development of streamers and leaders	68
3.II.E. Pause time between leader steps	70
3.II.F. Leader step length.....	72
3.II.G. Spectroscopy of emitted light.....	73
3.II.H. Conclusions.....	78
3.III. BREAKDOWN VOLTAGE MEASUREMENTS IN A DIVERGENT FIELD AND CONSEQUENCES FOR INSULATION DESIGN	78
3.III.A. Comparison of HFO with air and SF ₆	78
3.III.B. Consequences for the insulation design in HFO under impulse voltage with inhomogeneous field.....	82
4. CHAPTER 4: CHARACTERIZATION OF HFO IN A WEAKLY DIVERGENT FIELD AND STUDY OF GAS DEGRADATION.....	90
4.I. INTRODUCTION.....	90
4.II. BREAKDOWN VOLTAGE AND DELAY TIME TO BREAKDOWN IN HFO IN QUASI-HOMOGENEOUS FIELD.....	90
4.II.A. Examples of breakdown voltage measurements in HFO.....	90
4.II.B. Breakdown voltage in HFO in comparison with air and SF ₆ in weakly divergent field.....	93
4.II.C. Geometries influencing the loss of dielectric strength of HFO	94
4.II.D. Delay to breakdown	95
4.II.E. Propagation velocity.....	97
4.III. ORIGIN OF THE DROP OF INITIATION FIELD IN HFO AFTER THE 1ST BREAKDOWN.....	99
4.III.A. Influence of test cell cleaning and gas renewal.....	99
4.III.B. Evidence of the influence of solid by-products on discharge initiation	100
4.IV. CHARACTERIZATION OF HFO DEGRADATION BY ENERGY AND FTIR MEASUREMENTS.....	102
4.IV.A. Breakdown energy measurements under uniform field	102
4.IV.B. Correlation of arc energy with breakdown voltage drop in HFO	108
4.IV.C. Correlation of energy with HFO degradation: pressure measurements	110
4.V. PHYSICO-CHEMICAL CHARACTERIZATION OF HFO DEGRADATION	111
4.VI. CONCLUSIONS: DESIGN RULES OF INSULATION WITH HFO.....	114
4.VI.A. Initiation field in HFO in the investigated geometries	115
4.VI.B. Use of the streamer criterion	118
GENERAL CONCLUSION	122
I. PRE-DISRUPTIVE PHENOMENA	122
II. BREAKDOWN VOLTAGE	123
PERSPECTIVES	125
REFERENCES.....	127
ANNEXE 1: SPECTROSCOPY OF EMITTED LIGHT	137
FOR ATOMIC SPECIES.....	137
FOR MOLECULAR SPECIES.....	139
ANNEXE 2: STREAMER CRITERIA.....	142
ANNEXE 3: OBSERVATIONS DURING POST-BREAKDOWN IN HFO	143
ANNEXE 4: PERSPECTIVES	146
GAS CHARACTERIZATION, STUDY OF MIXTURES	146
EFFECTS OF INSULATING SOLIDS ON BREAKDOWN IN HFO	147
RESUME EN FRANÇAIS	149

List of tables

Chapter 1

TABLE 1. 1 : TYPICAL SF ₆ USE CONDITIONS IN MV AND HV ELECTRICAL EQUIPMENT [6]	3
TABLE 1. 2 : RATED INSULATION LEVELS FOR RATED VOLTAGES [17]	7
TABLE 1. 3 : PROPERTIES OF HYDROFLUOROOLEFIN	12
TABLE 1. 4 : CLASSIFICATION OF BREAKDOWN MECHANISM IN TERMS OF PD VALUES IN AIR [47]	29
TABLE 1. 5 : CLASSIFICATION OF BREAKDOWN MECHANISM IN TERMS OF PD VALUES IN SF ₆ [65]	29

Chapter 2

TABLE 2. 1: REPRESENTATION OF THE DIFFERENT GEOMETRIES STUDIED	36
TABLE 2. 2 : CHARACTERISTICS OF THE ARRAYS OF THE ARC SPECTROGRAPH	45

Chapter 3

TABLE 3. 1 : LIST OF CONDITIONS STUDIED IN THIS CHAPTER WHEN BREAKDOWN IS CONTROLLED BY PROPAGATION	53
TABLE 3. 2 : PHOTO AND CURRENT-VOLTAGE CHARACTERISTIC OF PRE-DISCHARGE PHENOMENA IN AIR, HFO, SF ₆ , AT DIFFERENT PRESSURES IN STRONGLY DIVERGENT FIELDS IN POSITIVE POLARITY (R _C = 0.2 MM AND D = 50 MM)	56
TABLE 3. 3 : PHOTO AND CURRENT-VOLTAGE CHARACTERISTIC OF PRE-DISCHARGE PHENOMENA IN AIR, HFO, SF ₆ , AT DIFFERENT PRESSURES IN STRONGLY DIVERGENT FIELDS IN NEGATIVE POLARITY (R _C = 0.2 MM AND D = 50 MM)	58
TABLE 3. 4 : STREAK CAMERA IMAGES IN AIR, HFO, AND SF ₆ AS A FUNCTION OF PRESSURE, AND SYNCHRONIZED RECORDINGS OF CURRENT AND LIGHT EMISSION (R _C = 0.2 MM, AND D = 50MM)	69
TABLE 3. 5 : DIFFERENT SPECIES IDENTIFIED IN HFO, SF ₆ AND AIR WITH CORRESPONDING TEMPERATURES	77
TABLE 3. 6 : VALUE OF THE STABILIZATION FIELD FROM THE LITERATURE AND EXPERIMENTAL.....	82

Chapter 4

TABLE 4. 1 : ELECTRODE CONFIGURATIONS STUDIED IN THIS CHAPTER	90
TABLE 4. 2 : BREAKDOWN VOLTAGE MEASUREMENTS OF HFO IN DIFFERENT ELECTRODE CONFIGURATIONS (IMPULSE VOLTAGE OF POSITIVE POLARITY).....	92
TABLE 4. 3 : ARC CURRENT AND DURATION FOR THE DIFFERENT VALUES OF R ₂ (U _{BD} = 44 KV)	105
TABLE 4. 4 : COMPARISON BETWEEN E/N IN THE LITERATURE AND THE E/N OBTAINED IN THE DC BREAKDOWN MEASUREMENTS WITH UNIFORM FIELD.....	108
TABLE 4. 5 : COMPARISON OF THE BREAKDOWN VOLTAGE IN THE HFO BETWEEN THE DC AND THE IMPULSE (R _C = 5 MM, D = 20 MM, P = 0.1 MPA)	109
TABLE 4. 6 : EXPERIMENTAL AND CALCULATED VIBRATIONAL FREQUENCIES (CM ⁻¹) FOR HFO [101]	112
TABLE 4. 7 : PARAMETER OF EQUATION $E_{max} = exp(a + bRc + c)$ FOR THE CURVES SHOWING IN FIGURE 4. 36	117

TABLE 4. 8 : BREAKDOWN VOLTAGE IN DC AND STI, AND STREAMER CRITERIA IN AIR, HFO DEGRADED AND SF ₆ (RC = 5 MM, D = 10 MM)	119
TABLE 4. 9 : STI BREAKDOWN VOLTAGE COMPARISON FOR HFO AND SF ₆ (RC = 5 MM, D = 10 MM)	120

List of figures

Chapter 1

FIGURE 1. 1 : IMPACT OF THE DISTANCE BETWEEN THE ELECTRODES ON THE BREAKDOWN VOLTAGE IN UNIFORM FIELD [116]	4
FIGURE 1. 2 : QUANTITY OF SF ₆ IN THE EARTH'S ATMOSPHERE BETWEEN 1995 AND 2019 [117]	5
FIGURE 1. 3 : MV GIS	6
FIGURE 1. 4 : REPRESENTATIVE OVERVOLTAGE FORMS AND TESTS DEFINED BY STANDARD IEC 60071 [118]	7
FIGURE 1. 5 : MOLECULAR STRUCTURE OF HFO-1234ZE (E) AND HFO-1234ZE (Z) [35]	12
FIGURE 1. 6 : FLAMMABILITY THRESHOLD OF HFO-1234ZE (E) AS A FUNCTION OF AIR PERCENTAGE AND TEMPERATURE [35].....	13
FIGURE 1. 7 : EVOLUTION OF THE CONCENTRATION OF SOURCE GASES IN THEIR DECOMPOSITION PRODUCTS AFTER 5 HOURS OF DBD TREATMENT AS A FUNCTION OF THE VOLTAGE APPLIED (AS A PERCENTAGE OF THEIR INITIAL CONCENTRATION BEFORE THE DBD TREATMENT). 1, C5K MIXED IN DECOMPOSITION PRODUCTS AT 18.5% C5K: 81.5% DRY AIR; 2, HFO-1234ZE (E) IN THE DECOMPOSITION PRODUCTS OF PURE HFO-1234ZE (E); 3, C5K IN THE DECOMPOSITION PRODUCTS OF PURE C5K; 4, C5K IN THE DECOMPOSITION PRODUCTS OF THE MIXTURE 12% C5K: 88% N ₂ ; 5, TOTAL CONCENTRATION OF C5K, HFO-1234ZE (E) AND CO ₂ IN THE DECOMPOSITION PRODUCTS OF THE MIXTURE AT 9% C5K: 56% HFO-1234ZE (E): 35% CO ₂ ; 6, TOTAL CONCENTRATION OF C5K AND HFO-1234ZE (E) IN THE DECOMPOSITION PRODUCTS OF THE MIXTURE AT 9% C5K: 57.5% HFO-1234ZE (E): 33.5% N ₂ ; 7, HFO-1234ZE (E) IN THE DECOMPOSITION PRODUCTS OF THE MIXTURE AT 75% HFO-1234ZE (E): 25% N ₂ . ALL CONCENTRATIONS ARE GIVEN AS PERCENTAGE BY VOLUME [44]	15
FIGURE 1. 8 : COMPARISON OF BREAKDOWN MEASUREMENTS OBTAINED IN HFO, SF ₆ , AND DRY AIR IN THE SAME CONDITIONS, VERSUS (PRESSURE X DISTANCE) PRODUCT. DC RAMP 1 KV/S, D = 5 MM, PLAN-PLAN. [7]	16
FIGURE 1. 9 : EVOLUTION OF BREAKDOWN VOLTAGE OF HFO SUBJECTED TO REPEATED BREAKDOWN MEASUREMENTS UNDER DC RAMP. P = 0.1 MPA, D = 3 MM [7].....	16
FIGURE 1. 10 : MEASUREMENT OF BREAKDOWN VOLTAGE V _B IN POINT-PLANE GEOMETRY AND CORRESPONDING TIME TO BREAKDOWN T _B IN HFO UNDER IMPULSE VOLTAGE. (R _C = 0.5 MM, D = 5 CM) [7].....	17
FIGURE 1. 11 : TIME TO BREAKDOWN T _B VERSUS BREAKDOWN VOLTAGE V _B IN HFO AT DIFFERENT PRESSURE UNDER IMPULSE VOLTAGE. (R _C = 0.5 MM, D = 5 CM) [7].....	17
FIGURE 1. 12 : BREAKDOWN VOLTAGE VERSUS PRESSURE IN POINT-PLANE GEOMETRY UNDER IMPULSE VOLTAGE, IN HFO, SF ₆ AND DRY AIR. (R _C = 0.5 MM, D = 5 CM) [7]	18
FIGURE 1. 13 : PHOTOGRAPHS OF PRE-BREAKDOWN DISCHARGES IN HFO AT VOLTAGES LOWER THAN THE BREAKDOWN VOLTAGE. (R _C = 0.5 MM, D = 5 CM, P = 0.2 MPA) [7]	18
FIGURE 1. 14 : TOWNSEND AVALANCHE PRINCIPLE [119]	20

FIGURE 1. 15 : PASCHEN CURVE FOR AIR AND SF ₆ AT 20°C IN LOGARITHMIC SCALES FROM [120]	22
FIGURE 1. 16 : POSITIVE STREAMER. A: DEVELOPMENT OF THE STREAMER; B: LINES OF FIELDS AT THE HEAD OF THE STREAMER	24
FIGURE 1. 17 : NEGATIVE STREAMER. A: DEVELOPMENT OF THE STREAMER; B: LINES OF FIELDS AT THE HEAD OF THE STREAMER.....	24
FIGURE 1. 18 : VELOCITY OF POSITIVE AND NEGATIVE STREAMERS IN AIR AT ATMOSPHERIC TEMPERATURE AND PRESSURE AS A FUNCTION OF THE VOLTAGE (GAP = 4 CM, RC = 15 μM) [55].....	25
FIGURE 1. 19 : TIME-INTEGRATED PHOTOGRAPHS OF POSITIVE (LEFT COLUMN) AND NEGATIVE (RIGHT COLUMN) STREAMERS IN AIR IN A SPACE OF 40 MM IN AIR AT 0.1 MPA (RC = 15 μM) [55].....	25
FIGURE 1. 20 : DIAMETERS OF POSITIVE AND NEGATIVE STREAMERS IN AIR ACCORDING TO THE APPLIED VOLTAGE (P = 0.1 MPA, R _c = 15 μM AND D = 40 MM) [55].....	26
FIGURE 1. 21 : PULSE FORM OF A CORONA DISCHARGE IN POSITIVE POLARITY IN DRY AIR UNDER CONDITIONS OF HIGH CONTINUOUS VOLTAGE (U = 7.2 KV, D = 7 MM, TIP-PLANE CONFIGURATION, P = 0.1 MPA) [57]	27
FIGURE 1. 22 : IMAGE OF A STREAK CAMERA OF A POSITIVE CORONA DISCHARGE (U = 7.2 KV, D = 7 MM, TIP-PLANE CONFIGURATION, P = 0.1 MPA) [57].....	27
FIGURE 1. 23 : PROBABILITY OF OCCURRENCE IN AIR WITH A TIP RADIUS R = 0.5 MM AND A GAP D = 10 CM [58].	28
FIGURE 1. 24 : DEVELOPMENT OF A LEADER IN SF ₆ (P = 0.15 MPA, U = 200 KV, RC = 1 MM). SCANNING CAMERA IMAGE (HIGH), APPLIED VOLTAGE AND CURRENT ASSOCIATED WITH LEADER STEPS (LOW) [66].	29
FIGURE 1. 25 : SCHEMATIC DIAGRAM OF LEADER DEVELOPMENT. T _C , TIME OF FORMATION OF THE FIRST CORONA; T _L , LEADER TRAINING TIME; T _{PS} , PROGRESSION TIME OF THE PRECURSOR; T _{LS} , LEADER TRAINING TIME; T _{BD} , BREAKDOWN TIME. ADAPTED FROM [121].	30
FIGURE 1. 26 : CHARGE DISTRIBUTION OF CORONA EFFECT [69].....	31
FIGURE 1. 27 : VOLTAGE VERSUS PRESSURE CHARACTERISTIC OF SF ₆ AND A 75% SF ₆ -25% N ₂ MIXTURE FOR A POINT-PLANE GAP AND LIGHTING IMPULSE (1.2/50 μS) [122].....	32

Chapter 2

FIGURE 2. 1 : TEST CELL FOR MEASUREMENTS UP TO 0.3 MPA AND 200 KV MAXIMUM.....	35
FIGURE 2. 2 : EXAMPLE OF MODELLING OF THE FIELD FOR A NEEDLE WITH A RADIUS OF CURVATURE OF 0.5 MM AND AN INTER-ELECTRODE DISTANCE OF 10 MM FOR AN APPLIED VOLTAGE OF 1 V	37
FIGURE 2. 3 : ELECTRICAL POTENTIAL OBTAINED (R _C = 0.5 MM AND D = 50 MM)	37
FIGURE 2. 4 : EXAMPLE OF MODELLING OF THE MAXIMUM FIELD E _{MAX} (V/MM) (R _C = 0.5 MM AND D = 50 MM)	37
FIGURE 2. 5 : CALCULATION OF THE MAXIMUM FIELD IN THE REAL CONFIGURATION OF THE STUDY (POINT OF RADIUS OF CURVATURE 0.5 MM AND INTER-ELECTRODE DISTANCE OF 10 MM).....	38
FIGURE 2. 6 : FIELD ENHANCEMENT FACTOR η FOR THE DIFFERENT GEOMETRIES STUDIED	38
FIGURE 2. 7 : SCHEMATIC REPRESENTATION OF THE CONFIGURATION USED FOR THE DC BREAKDOWN MEASUREMENTS	39

FIGURE 2. 8 : PHOTOGRAPH OF THE TEST SYSTEM.....	40
FIGURE 2. 9 : SCHEMATIC REPRESENTATION OF THE CONFIGURATION USED FOR THE IMPULSE BREAKDOWN MEASUREMENTS	40
FIGURE 2. 10 : CHARACTERISTIC PARAMETERS OF A PULSE WAVE	41
FIGURE 2. 11 : DISCHARGE CURRENT MEASURING DEVICE ON THE HIGH VOLTAGE SIDE.....	42
FIGURE 2. 12 : EXPERIMENTAL “MULTIPLE STEPS” PROCEDURE TO DETERMINE THE PROBABILITY OF OCCURRENCE OF PD AND BREAKDOWN	43
FIGURE 2. 13 : EXPERIMENTAL PROCEDURE FOR BREAKDOWN MEASUREMENTS.....	43
FIGURE 2. 14 : CHARACTERISTIC MEASUREMENTS OF VOLTAGE, CURRENT, CAMERA SIGNAL AND LIGHT EMISSION	44
FIGURE 2. 15 : IMAGE OF A STREAMER BEING PROPAGATED IN THE AIR ($R_C = 0,5$ MM AND $D = 50$ MM) ALLOWING TO MEASURE THE LENGTH OF PROPAGATION L_P	45
FIGURE 2. 16 : REPRESENTATION OF THE SEGMENTATION OF THE 2D CCD	46

Chapter 3

FIGURE 3. 1 : OSCILLOGRAM OF AN EXPERIMENT LEADING TO BREAKDOWN IN HFO ($R_C = 0.5$ MM, $D = 50$ MM, $P = 0.1$ MPA).....	47
FIGURE 3. 2 : LEADER NOT LEADING TO BREAKDOWN IN HFO ($U_A = 86$ KV, $R_C = 0.2$ MM, $D = 50$ MM, $P = 0.1$ MPA).....	48
FIGURE 3. 3 : LEADER LEADING TO BREAKDOWN IN HFO ($U_A = 94$ KV, $R_C = 0.2$ MM, $D = 50$ MM, $P = 0.1$ MPA) ..	48
FIGURE 3. 4 : BREAKDOWN IN DEGRADED HFO ($U_A = 73$ KV, $R_C = 5$ MM, $D = 10$ MM, $P = 0.1$ MPA).....	49
FIGURE 3. 5 : FREQUENCY OF INITIATION AND BREAKDOWN AS A FUNCTION OF THE PRESSURE OBTAINED ON 15 SHOTS “MULTIPLE STEPS” METHOD.....	50
FIGURE 3. 6 : INITIATION VOLTAGE U_i AS A FUNCTION OF THE APPLIED VOLTAGE U_A IN A VERY INHOMOGENEOUS FIELD IN HFO ($R_C = 0.5$ MM, $D = 50$ MM, $H = 84$).....	51
FIGURE 3. 7 : INITIATION VOLTAGE U_i AS A FUNCTION OF THE APPLIED VOLTAGE U_A IN A WEAKLY INHOMOGENEOUS FIELD IN HFO ($R_C = 5$ MM, $D = 50$ MM, $H = 2.5$).....	51
FIGURE 3. 8 : DIFFERENCE BETWEEN THE INITIATION VOLTAGE AND THE BREAKDOWN VOLTAGE AS A FUNCTION OF THE FIELD STRENGTHENING FACTOR ($\eta = E_{max}E_{moy}$, $P = 0.1$ MPA).....	52
FIGURE 3. 9 : FINE DUST DEPOSITS ON THE ELECTRODES AFTER 15 BREAKDOWNS IN POINT PLANE GEOMETRY IN HFO ($R_C = 0.5$ MM, $D = 10$ MM, $P = 0.1$ MPA).....	54
FIGURE 3. 10 : « UP AND DOWN » METHOD IN HFO FOR 15 BREAKDOWNS (($R_C = 0.5$ MM, $D = 10$ MM, $P = 0.1$ MPA).....	54
FIGURE 3. 11 : CURRENT OF POSITIVE STREAMER IN AIR ($R_C = 0.2$ MM, $D = 50$ MM, $P = 0.1$ MPA, $U_A = 36$ KV) ..	55
FIGURE 3. 12 : VELOCITY OF POSITIVE STREAMERS IN AIR AS A FUNCTION OF VOLTAGE AND PRESSURE ($R_C = 0.2$ MM, $D = 50$ MM, ERROR BAR: STANDARD DEVIATION) WITH THE RESULTS OF [55]	60
FIGURE 3. 13 : VELOCITY OF PROPAGATION OF NEGATIVE STREAMERS IN AIR AS A FUNCTION OF VOLTAGE AND PRESSURE ($R_C = 0.2$ MM, $D = 50$ MM, ERROR BAR: STANDARD DEVIATION).....	61

FIGURE 3. 14 : DIAMETER OF STREAMERS IN AIR AS A FUNCTION OF VOLTAGE FOR DIFFERENT PRESSURES (PROPAGATION VELOCITY OF PRE-DISRUPTIVE PHENOMENA IN AIR AS A FUNCTION OF PRESSURE IN POSITIVE POLARITY ($R_c = 0.2$ MM, $D = 50$ MM, MAX/MIN ERROR BAR) WITH THE RESULTS OF [55]).....	61
FIGURE 3. 15 : PROPAGATION VELOCITY OF STREAMERS AS A FUNCTION OF DIAMETER AND AIR PRESSURE ($R_c = 0.2$ MM, $D = 50$ MM, MAX/MIN ERROR BAR) WITH THE RESULTS OF [55]	62
FIGURE 3. 16 : VELOCITY OF PROPAGATION IN POSITIVE POLARITY IN SF_6 AS A FUNCTION OF VOLTAGE AND PRESSURE ($R_c = 0.2$ MM, $D = 50$ MM, ERROR BAR: STANDARD DEVIATION).....	63
FIGURE 3. 17 : VELOCITY OF PROPAGATION IN NEGATIVE POLARITY IN SF_6 AS A FUNCTION OF VOLTAGE AND PRESSURE ($R_c = 0.2$ MM, $D = 50$ MM, ERROR BAR: STANDARD DEVIATION).....	63
FIGURE 3. 18 : VELOCITY OF PROPAGATION IN POSITIVE POLARITY IN THE HFO AS A FUNCTION OF VOLTAGE AND PRESSURE ($R_c = 0.2$ MM, $D = 50$ MM, ERROR BAR: STANDARD DEVIATION)	64
FIGURE 3. 19 : VELOCITY OF PROPAGATION IN NEGATIVE POLARITY IN HFO AS A FUNCTION OF VOLTAGE AND PRESSURE ($R_c = 0.2$ MM, $D = 50$ MM, ERROR BAR: STANDARD DEVIATION).....	65
FIGURE 3. 20 : PROPAGATION TIME OF PRE-DISCHARGE IN HFO LEADING TO BREAKDOWN IN POSITIVE POLARITY ($P = 0.1$ MPA).....	65
FIGURE 3. 21 : PROPAGATION TIME OF PRE-DISCHARGE IN HFO LEADING TO BREAKDOWN IN POSITIVE POLARITY ($D = 50$ MM)	66
FIGURE 3. 22 : PROPAGATION VELOCITY AS A FUNCTION OF VOLTAGE IN THE DEGRADED HFO FOR DIFFERENT R_c AND PRESSURE ($D = 50$ MM).....	67
FIGURE 3. 23 : STOPPING LENGTH OF LEADER PHENOMENA IN A HIGHLY INHOMOGENEOUS FIELD IN HFO AND SF_6 ($R_c = 0.2$ MM, $D = 50$ MM, MAX/MIN ERROR BAR)	67
FIGURE 3. 24 : STOPPING LENGTH OF LEADER PHENOMENA IN A HIGHLY INHOMOGENEOUS FIELD IN THE HFO ($R_c = 0.2$ MM, $D = 50$ MM, MAX/MIN ERROR BAR)	68
FIGURE 3. 25 : TOTAL NUMBER OF LEADER STEPS AS A FUNCTION OF THE PRESSURE IN THE HFO AND SF_6 IN POSITIVE POLARITY ($R_c = 0.2$ MM, $D = 50$ MM, $P = 0.1$ MPA, MAX/MIN ERROR BAR)	71
FIGURE 3. 26 : TIME BETWEEN 2 RE-ILLUMINATIONS IN HFO AND SF_6 AS A FUNCTION OF THE PRODUCT $U \cdot P$ WITH COMPARISON WITH THE DATA OF QIU ($R_c = 0.2$ MM, $D = 50$ MM AND $A = 1680$) [83].....	71
FIGURE 3. 27 : LEADER STEP LENGTHS IN SF_6 AND HFO AS A FUNCTION OF PRESSURE ($R_c = 0.2$ MM, $D = 50$ MM) IN COMPARISON WITH THE RESULTS OF CHALMERS ET AL. [79] ($R_c = 0.05$ MM, $D = 30$ MM)	72
FIGURE 3. 28 : LEADER STEP LENGTH AS A FUNCTION OF V/P FOR HFO AND SF_6 AND ADAPTED FROM NIEMEYER [79]	73
FIGURE 3. 29 : A TYPICAL EMISSION SPECTRUM FROM STREAMER IN AIR EXHIBITING N_2 ($C_3\Pi-B_3\Pi$) WITH ASSIGNED VIBRATIONAL QUANTUM NUMBERS $V'-V'$ ($R_c = 0.2$ MM, $D = 50$ MM, $P = 0.1$ MPA) SPECTRUM NOT CORRECTED.....	74
FIGURE 3. 30 : EXAMPLE OF COMPARISON BETWEEN SECOND POSITIVE NITROGEN SYSTEM SIMULATED BY SPECAIR (RED) AND MEASURED EXPERIMENTALLY (BLACK) IN AIR DURING THE STREAMER DISCHARGE ($R_c = 0.2$ MM, $D = 50$ MM, $P = 0.1$ MPA) SPECTRUM CORRECTED ($T_v = 5000$ K, $T_R = 500$ K)	75

FIGURE 3. 31 : EXAMPLE OF EXPERIMENTAL SPECTRUM OF LEADER IN SF ₆ (BLACK) WITH A BEST FIT SYNTHETIC SPECTRUM OF FI LINE (RED). THE EXPERIMENTAL SPECTRUM IS CORRECTED FOR THE WAVELENGTH DEPENDING ON SENSITIVITY OF THE SPECTROMETER ($R_C = 0.2$ MM, $D = 50$ MM, $P = 0.1$ MPA).....	75
FIGURE 3. 32 : EXAMPLE OF EXPERIMENTAL SPECTRUM OF BREAKDOWN IN HFO (BLACK) WITH A BEST FIT SYNTHETIC SPECTRUM OF H α LINE (RED). THE EXPERIMENTAL SPECTRUM IS CORRECTED FOR THE WAVELENGTH DEPENDING SENSITIVITY OF THE SPECTROMETER ($R_C = 0.2$ MM, $D = 50$ MM, $P = 0.1$ MPA)	76
FIGURE 3. 33 : EXAMPLE OF COMPARISON BETWEEN THE SPECTRUM OF C ₂ SIMULATED WITH SPECAIR (RED) AND THE ONE OBSERVED EXPERIMENTALLY IN HFO DURING THE BREAKDOWN (BLACK) WITH ($T_V = T_R = 5000$ K, $R_C = 0.2$ MM, $D = 50$ MM, $P = 0.1$ MPA, $U_A = 86$ KV).....	76
FIGURE 3. 34 : EXAMPLE OF COMPARISON BETWEEN THE SPECTRUM OF C ₂ SIMULATED WITH SPECAIR (RED) AND THE ONE OBSERVED EXPERIMENTALLY IN HFO DURING THE BREAKDOWN (BLACK) WITH ($T_E = 10000$ K, $T_V = 5300$ K AND $T_R = 5000$ K, $R_C = 0.2$ MM, $D = 50$ MM, $P = 0.1$ MPA, $U_A = 67$ KV).....	77
FIGURE 3. 35 : « UP AND DOWN » BREAKDOWN MEASUREMENT FOR HFO ($R_C = 0.5$ MM, $D = 50$ MM, $P = 0.1$ MPA, $\eta = 40$)	79
FIGURE 3. 36 : « UP AND DOWN » BREAKDOWN MEASUREMENT FOR HFO ($R_C = 1.2$ MM, $D = 50$ MM, $P = 0.1$ MPA, $\eta = 21$)	79
FIGURE 3. 37 : AVERAGE OF 15 BREAKDOWN VOLTAGE IN AIR, SF ₆ AND HFO AS A FUNCTION OF THE PRESSURE IN POSITIVE POLARITY ($R_C = 0.2$ MM, $D = 50$ MM, MAX/MIN ERROR BAR) “UP AND DOWN” METHOD.	80
FIGURE 3. 38 : AVERAGE OF 15 BREAKDOWN VOLTAGE IN AIR, SF ₆ AND HFO AS A FUNCTION OF THE PRESSURE IN NEGATIVE POLARITY ($R_C = 0.2$ MM, $D = 50$ MM, MAX/MIN ERROR BAR) “UP AND DOWN” METHOD. ..	80
FIGURE 3. 39 : DIFFERENCE BETWEEN INITIATION AND BREAKDOWN VOLTAGE IN POSITIVE POLARITY AS A FUNCTION OF PRESSURE FOR AIR($R_C = 0.2$ MM, $D = 50$ MM, MAX/MIN ERROR BAR).....	81
FIGURE 3. 40 : DIFFERENCE BETWEEN INITIATION AND BREAKDOWN VOLTAGE IN POSITIVE POLARITY AS A FUNCTION OF PRESSURE FOR HFO AND SF ₆ ($R_C = 0.2$ MM, $D = 50$ MM, MAX/MIN ERROR BAR)	81
FIGURE 3. 41 : IDEALISED V/P CHARACTERISTIC FOR A POINT-PLANE GAP IN SF ₆ [79]	83
FIGURE 3. 42 : INITIATION AND BREAKDOWN VOLTAGE IN POSITIVE POLARITY AS A FUNCTION OF PRESSURE FOR HFO ($D = 50$ MM, MAX/MIN ERROR BAR).....	84
FIGURE 3. 43 : LEADER PROPAGATION VOLTAGE U_p IN HFO AS A FUNCTION OF DISTANCE ($P = 0.1$ MPA).	85
FIGURE 3. 44 : VALUE OF THE INITIATION FIELD E_i AS A FUNCTION OF THE DISTANCE WHEN THE BREAKDOWN IS CONTROLLED BY PROPAGATION ($P = 0.1$ AND 0.2 MPA)	86
FIGURE 3. 45 : VALUE OF THE INITIATION FIELD E_i AS A FUNCTION OF R_C WHEN THE BREAKDOWN IS CONTROLLED BY PROPAGATION IN HFO ($D = 50$ MM).....	87
FIGURE 3. 46 : DELAY TIME TO INITIATION WHEN THE BREAKDOWN IS CONTROLLED BY PROPAGATION IN HFO IN POSITIVE POLARITY.....	88
FIGURE 3. 47 : DELAY TIME TO BREAKDOWN WHEN THE BREAKDOWN IS CONTROLLED BY PROPAGATION IN HFO IN POSITIVE POLARITY.....	88

FIGURE 3. 48 : AVERAGE OF 15 BREAKDOWN DELAY TIME AS A FUNCTION OF VOLTAGE FOR AIR, HFO AND SF ₆ (R _c = 0.2 MM, D = 50 MM, MAX/MIN ERROR BAR) IN POSITIVE POLARITY	89
CHAPTER 4	
FIGURE 4. 1 : UP AND DOWN MEASUREMENT SERIES IN HFO INCLUDING 120 SHOTS (R _c = 5 MM, D = 50 MM, P = 0.1 MPA, η = 7)	91
FIGURE 4. 2 : UP AND DOWN MEASUREMENT SERIES IN HFO INCLUDING 80 SHOTS (R _c = 5 MM, D = 10 MM, P = 0.1 MPA, η = 2.5)	91
FIGURE 4. 3 : UP AND DOWN MEASUREMENT SERIES IN HFO FOR DIFFERENT PRESSURE (R _c = 10 MM, D = 20 MM, η =2.5)	92
FIGURE 4. 4 : BREAKDOWN VOLTAGE IN AIR, HFO AND SF ₆ AS A FUNCTION OF PRESSURE. UP AND DOWN METHOD, QUASI-HOMOGENEOUS FIELD (η = 2.5, R _c = 5 MM, D = 10 MM, MAX/MIN ERROR BAR)	93
FIGURE 4. 5 : INFLUENCE OF THE POLARITY ON THE BREAKDOWN VOLTAGE IN A QUASI-HOMOGENEOUS FIELD (UP AND DOWN METHOD, H = 2.5, R _c = 5 MM, D = 10 MM, P = 0.1 MPA, MAX/MIN ERROR BAR).....	94
FIGURE 4. 6 : DIFFERENCE BETWEEN THE 1 ST BREAKDOWN VOLTAGE U _{BD1} AND THE AVERAGE BREAKDOWN VOLTAGE U _{BDMEAN} DEPENDING ON THE AMPLIFICATION FACTOR OF THE FIELD η (P = 0.1 MPA)	94
FIGURE 4. 7 : MAXIMUM INITIATION FIELD AT THE ELECTRODE AS A FUNCTION OF THE DIFFERENCE BETWEEN U _{BD1} AND U _{BDM} (P = 0.1 MPA).....	95
FIGURE 4. 8 : DELAY TIME FOR THE 1 ST BREAKDOWN IN THE HFO AS A FUNCTION OF THE GEOMETRY (P = 0.1 MPA). ORANGE LINE CORRESPONDS TO THE VOLTAGE RISE TIME.....	96
FIGURE 4. 9 : AVERAGE DELAY TIME TO BREAKDOWN IN THE HFO AS A FUNCTION OF THE GEOMETRY (P = 0.1 MPA, MAX/MIN ERROR BAR). ORANGE LINE CORRESPONDS TO THE VOLTAGE RISE TIME.....	97
FIGURE 4. 10 : AVERAGE DELAY TIME TO BREAKDOWN IN THE SF ₆ AS A FUNCTION OF THE GEOMETRY (P = 0.1 MPA, MAX/MIN ERROR BAR). ORANGE LINE CORRESPONDS TO THE VOLTAGE RISE TIME.....	97
FIGURE 4. 11 : PROPAGATION TIME AS A FUNCTION OF VOLTAGE, AND PRESSURE IN THE DEGRADED HFO (R _c = 5 MM, D = 50 MM)	98
FIGURE 4. 12 : PROPAGATION VELOCITY AS A FUNCTION OF PRESSURE IN THE DEGRADED HFO FOR DIFFERENT R _c AND PRESSURE (D = 50 MM).....	98
FIGURE 4. 13 : VARIOUS TESTS TO UNDERSTAND THE ORIGIN OF THE LOSS OF DIELECTRIC STRENGTH AFTER THE 1 ST BREAKDOWN (R _c = 5 MM, D = 10 MM, P = 0.1 MPA)	99
FIGURE 4. 14 : MEASUREMENT SEQUENCE IN HFO AND SF ₆ TO EVALUATE THE EFFECT OF THE POWDER DEPOSIT ON THE DIELECTRIC STRENGTH (η = 2.5, P = 0.1 MPA, UP AND DOWN METHOD)	101
FIGURE 4. 15 : MEASUREMENT SEQUENCE IN HFO AND SF ₆ TO EVALUATE THE EFFECT OF THE DEPOSIT ON THE DIELECTRIC STRENGTH OF THE HFO (η = 9, P = 0.1 MPA, UP AND DOWN METHOD)	101
FIGURE 4. 16 : BLACK DUST DEPOSITS ON THE HV ELECTRODE AFTER 15 BREAKDOWNS IN THE HFO (R _c = 5 MM, D =20 MM, P= 0.1 MPA)	101
FIGURE 4. 17 : DELAY TO BREAKDOWN IN HFO AND SF ₆ BEFORE AND AFTER DEGRADATION (P = 0.1 MPA, η = 2.5).....	102

FIGURE 4. 18 : VOLTAGE MEASURED ACROSS THE POST-BREAKDOWN ARC IN HFO AND NITROGEN FOR DIFFERENT PRESSURE AND DISTANCE (PLANE-PLANE).....	103
FIGURE 4. 19 : EXAMPLE OF MEASUREMENT OF VOLTAGE AND BREAKDOWN CURRENT IN THE HFO (PLANE-PLANE, D = 5 MM, P = 0.1 MPA, U _A = 34 KV, R ₂ = 1000 Ω AND WITHOUT R ₂ C)	104
FIGURE 4. 20 : ARC CURRENT FOR DIFFERENT RESISTANCES R ₂ = 1000 AND 100 Ω (U _{BD} = 44 KV).....	105
FIGURE 4. 21 : TRANSIENT ARC RESISTANCE IN HFO ((PLANE-PLANE, D = 5 MM, P = 0.1 MPA, U _A = 34 KV, R ₂ = 1000 AND 100 Ω).....	105
FIGURE 4. 22 : ARC POWER AND ENERGY IN HFO (PLANE-PLANE, D = 5 MM, P = 0.1 MPA, U _A = 34 KV, R ₂ = 1000Ω)	106
FIGURE 4. 23 : VARIATION OF THE ENERGY DISSIPATED IN THE ARC AS A FUNCTION OF THE SERIES RESISTANCE AND THE GAS (PLAN-PLAN, D = 5 MM)	106
FIGURE 4. 24 : ARC ENERGY AS A PERCENTAGE OF THE MAXIMUM ENERGY STORED IN CAPACITOR (PLAN-PLAN, D = 5 MM)	107
FIGURE 4. 25 : AVERAGE DC BREAKDOWN VOLTAGE IN NITROGEN, AIR, SF ₆ AND HFO IN A HOMOGENEOUS FIELD AS A FUNCTION OF ENERGY (D = 5 MM, PLANE-PLANE, DC)	107
FIGURE 4. 26 : INFLUENCE OF ENERGY ON THE STABILITY OF BREAKDOWNS AND POWDER DEPOSITS ON ELECTRODES WITH NEGATIVE POLARITY (R _C = 5 MM, D = 20 MM, P = 0.1 MPA).....	109
FIGURE 4. 27 : INFLUENCE OF ENERGY ON THE STABILITY OF BREAKDOWNS AND POWDER DEPOSITS ON ELECTRODES WITH POSITIVE POLARITY ELECTRODES (R _C = 5 MM, D = 20 MM, P = 0.1 MPA).....	109
FIGURE 4. 28 : PRESSURE VARIATION IN THE HFO AS A FUNCTION OF THE ENERGY OF ONE BREAKDOWN (R _C = 5 MM, D = 10 MM, P = 0.1 MPA)	111
FIGURE 4. 29 : DEPOSIT WITHIN THE TEST CELL AFTER 75 MINUTES OF DC APPLICATION.....	111
FIGURE 4. 30 : FTIR OF HFO GAS AFTER 20, 30 AND 75 MINUTES	112
FIGURE 4. 31 : FTIR ON HFO POWDER BY-PRODUCT	113
FIGURE 4. 32 : IMAGES OF CLEAN AND POLLUTED ELECTRODE SURFACE OBTAINED BY SEM [102]	113
FIGURE 4. 33 : EDX-SPECTRAL ANALYSIS OF THE DUSTY LAYER ON ELECTRODES AFTER BREAKDOWN TESTS IN HFO-1234ZE(E) [102]	114
FIGURE 4. 34 : VALUE OF THE MAXIMUM FIELD E _i AS A FUNCTION OF THE DISTANCE (P = 0.1 AND 0.2 MPA) FOR DEGRADED HFO	116
FIGURE 4. 35 : VALUE OF INITIATION FIELD E _i AS A FUNCTION OF R _C FOR DEGRADED HFO (D = 50 MM).....	116
FIGURE 4. 36 : INITIATION FIELD AS A FUNCTION OF THE RADIUS OF CURVATURE.....	117
FIGURE 4. 37 : STREAMER CRITERIA FOR AIR AND SF ₆ IN PLANE-PLANE GEOMETRY FOR D = 50 MM	118
FIGURE 4. 38 : CRITERION OF STREAMER IN AIR AND SF ₆ AND COMPARISON WITH MEASUREMENTS IN DC AND STI (R _C = 5 MM, D = 10 MM, K = 20 FOR AIR AND K = 11 FOR SF ₆)	119
FIGURE 4. 39 : STREAMER CRITERIA FOR AIR (R _C = 0.2 MM, D = 50 MM, η = 86, K = 20).....	121
FIGURE 4. 40 : STREAMER CRITERIA FOR SF ₆ (R _C = 0.2 MM, D = 50 MM, η = 86, K = 11)	121

FIGURE 1 : SPECTRUM OF A BREAKDOWN IN THE AIR ($R_c = 0.2$ MM, $D = 50$ MM, $P = 0.1$ MPA) CORRECTED SPECTRUM	138
FIGURE 2 : EXPERIMENTAL SPECTRUM AND SIMULATED SPECTRUM OF N I FOR BREAKDOWN IN AIR ($R_c = 0.2$ MM, $D = 50$ MM, $P = 0.1$ MPA) CORRECTED SPECTRUM.....	139
FIGURE 3 : CURRENT OF ARC AND APPLIED VOLTAGE IN AIR AND HFO (STI, $R_c = 5$ MM, $D = 50$ MM, $P = 0.1$ MPA)	143
FIGURE 4 : LIGHT EMISSION RECORDED BY A PHOTODIODE DURING A BREAKDOWN IN THE AIR AND THE HFO (STI, $R_c = 5$ MM, $D = 50$ MM, $P = 0.1$ MPA).....	143
FIGURE 5 : IMAGE OF EMITTED LIGHT 100 μ S AFTER BREAKDOWN IN HFO ($R_c = 5$ MM, $D = 50$ MM, $P = 0.1$ MPA, $U_A = 90$ KV)	144
FIGURE 6 : ($R_c = 2$ MM, $D = 50$ MM, $P = 0.1$ MPA)	145
FIGURE 7 : ($R_c = 5$ MM, $D = 10$ MM, $P = 0.1$ MPA)	145
FIGURE 8 : REDUCED CRITICAL ELECTRIC FIELD AS A FUNCTION OF HFO1234ZE OR SF ₆ MOLE FRACTION IN N ₂ OR CO ₂ [114]	146
FIGURE 9 : CRITICAL FIELD STRENGTH (E/N) _{CRIT} OF MIXTURES OF SF ₆ WITH HFO1234ZE(E). IN BLUE CIRCLES, A MEASUREMENT SERIES AT PRESSURES OF 360- 480 PA IS SHOWN. IN RED CROSSES, WE USED HIGHER, VARIABLE PRESSURES FROM 4-12 KPA. IN BLACK SQUARES, BREAKDOWN RESULTS (E/N) _{BD} FOR THE MIXTURE OF SF ₆ WITH C ₃ F ₆ IS GIVEN AT PRESSURE OF 67 KPA [115].	147
FIGURE 10 : BREAKDOWN VOLTAGES SOLID/GAS INSULATION WITH PPA AND EPOXY WITH SF ₆ , DRY AIR AND HFO1234ZEE [7]	147
FIGURE 11 : EPOXY SAMPLES AFTER 20 BREAKDOWN DEGRADATION IN DIFFERENT GASES AT 0.2 MPA [7]....	148

List of abbreviations

AC : Alternative Current

AIHA : American Industrial Hygiene Association

BIL : Basic Insulation Level

DBD : Dielectric Barrier Discharge

DC : Direct Courant

EDX : Energy Dispersive X-Ray

E_{\max} : Maximum field applied to the high voltage electrode

FTIR : Fourier Transform InfraRed spectroscopy

GWP : Global Warming Potential

GIS : Gas Insulated Systems

GIL : Gas Insulated Lines

HFO : HFO-1234 ze(E), 1,3,3,3-tétrafluoroprop-1-ène

HV : High Voltage

HSE : Health Safety Environment

IPCC : Intergovernmental Panel on Climate Change

STI : StepLighting Impulse (0.8/1400 μ s)

MV : Medium voltage

N_e : Electron density

ODP : Ozone Depletion Potential

PD : Partial Discharge

PM : Photomultiplier

LI : Standard Lighting Impulse (1.2/50 μ s)

t_{BD} : Delay to breakdown (μ s)

t_{BD1} : Delay to 1st breakdown (μ s)

t_d : Wave fall time

T_{exc} : Excitation temperature (K)

t_i : Delay to initiation (μs)

t_m : Wave rise time

t_p : Time to propagation (μs)

U_a : Applied voltage (kV)

U_{BD1} : 1st breakdown voltage (kV)

U_{BDm} : Average of breakdown voltage (kV)

U_i : Initiation voltage (kV)

UV : Ultraviolet

General Introduction

This PhD work is part of a wider research program aiming at replacing SF₆ in medium voltage devices. SF₆ is a gas with excellent dielectric properties (its breakdown voltage is about three times that of air), very widely used in high voltage systems, either for dielectric insulation or for current interruption in circuit breakers. Unfortunately, it is the most powerful greenhouse gas [1]. The use of SF₆ has been severely restricted in recent years [2], [3]. In the last decades, manufacturers of gas-insulated switchgear (GIS) have reduced the size of compartments and improved their devices to reduce SF₆ leakage [4]. However, measurements of atmospheric SF₆ content show an ever-increasing trend with an even increasing growth rate in recent years. Therefore, substituents should be found.

Hydrofluoroolefin HFO-1234 ze(E) was selected as a potential candidate for replacement of SF₆ in MV GIS. This gas is part of the so-called "4th generation" refrigerant gas. It is notably used as a refrigerating fluid in air conditioning, as a propellant gas (in aerosols) or as a blowing agent (foams) [5]. So, this gas is widely available and very well documented (non-toxic, low Global Warming Potential, and zero Ozone Depletion Potential) [6]. The first studies show the insulating potential of HFO [7], namely a high dielectric strength (in a uniform field) of the order of 80% that of SF₆. The objective of this thesis is to provide an exhaustive study of the dielectric properties of HFO in a wide range of configurations (pressure, distance, enhancement factor), and of its stability in real MV switchgear. The product design rules must be adapted and redefined accordingly.

The first chapter focuses on the context of electrical insulation at medium voltage, and on breakdown phenomena in gases. The experimental techniques are discussed in Chapter 2. Chapter 3 focuses on the study of the behaviour of the HFO in divergent field. Experiments concerning the characterization of the leaders (propagation velocity, stopping lengths, ...) for various gas pressure are carried out. Spectroscopy measurements are also performed, a study of the breakdown voltage as a function of the pressure and the distance is presented. Chapter 4 deals on breakdown measurements in the HFO under a quasi-homogeneous field, i.e. configurations representative of medium voltage devices. The problems related to the degradation of the breakdown properties of HFO after breakdown will be investigated, and design rules will be extracted from these measurements.

Chapter 1: Context of the study: gaseous insulation in MV devices, and breakdown physical processes

1.I. *Introduction*

The question of alternatives to SF₆ is already quite old. In the 1970s and 1980s, intense research aimed to identify gases with insulating properties “superior” to those of SF₆ [8]. In 1997, SF₆ was listed in the Kyoto protocol. Today's research is focused on alternatives which are not necessarily better than SF₆, but which show at least similar insulating capacity and significantly less impact on the environment. SF₆ in high voltage gas-insulated switchgear (GIS) has two quite distinct functions [8]:

1. High voltage insulation,
2. Arc extinction and current interruption in circuit breakers.

In modern medium voltage GIS, SF₆ acts often only as a gaseous insulator, since breaking can be performed with vacuum interrupters.

1.II. *Context: Usage, restriction, and substitution of sulfur hexafluoride SF₆*

Besides atmospheric air, sulfur hexafluoride (SF₆) is the most widely used gas in the electrical industry. Among the 8,000 tons of SF₆ produced annually, around 80% of this is consumed by the energy industry for switchgear.

Switchgear is a broad term that covers a range of equipment that can carry, switch and interrupt currents in a power supply system under normal and abnormal (fault) conditions, for the protection and control of the power supply system [9]. The application of SF₆ to the switchgear can have two distinct roles; to isolate live components at different voltage (eg. Phase-to-phase and phase-to-earth), and to interrupt the arc when opening the circuit breaker contacts.

The main types of HV systems using SF₆ either as insulator or as breaking fluid are (see Table 1. 1):

Table 1. 1 : Typical SF₆ use conditions in MV and HV electrical equipment [6]

	Type	Voltage range	Typical operating pressure of SF ₆ (relative)	temperature range	Mass of SF ₆ (order of magnitude)
MV	Ring main unit (RMU) / GIS	3.6-52 kV	Mainly 30 kPa, up to 250 kPa for the highest voltage range	-25 to 40 °C (indoor)	~1 kg
	Load break switches	3.6-52 kV	30 kPa	-25 to 40 °C (indoor)	~0.1 kg
	Circuit breaker	3.6-52 kV	250 - 500 kPa	-25 to 40 °C	~0.2 kg
	Auto-recloser	3.6-52 kV	30 kPa	-40 to 50 °C (outdoor)	~0.4 kg
HV	Gas-insulated switchgear	72.5 - 1200 kV	400 - 650 kPa	-30 (-50 °C with heating) to 40°C	30 - >1200 kg
	Circuit breakers (Live tank and Dead tank)	72.5 - 1200 kV	400 - 650 kPa	-30 to 40 °C	2 - >400 kg, various designs
	Gas-insulated lines	115 - 1200 kV	350 - 900 kPa at 20 °C (depending on voltage level and gas mixture)	-25 to 40 °C	5 - 30 kg/m, depending on voltage level
Mixtures with SF ₆ :					
SF ₆ /N ₂	Circuit Breakers	72.5 - 735 kV	325 - 890 kPa	-50 to 40 °C	36-80 Vol% SF ₆ 3 kg to 73 kg
	Gas-insulated lines	230 - 550 kV	340 - 930 kPa	-30 to 40 °C	20-60 Vol% SF ₆ 3 - 6 kg/m
SF ₆ /CF ₄	Circuit breakers	72.5 - 735 kV	600 - 900 kPa	-60 to 40 °C	25-52 Vol% SF ₆ 1 - 83 kg

SF₆ density at 20°C and 0.1 MPa is 6.139 kg/m³, nearly five times that of air. Its molecular weight is 146.06. It is colorless and odorless. The volumetric specific heat of SF₆ is 3.7 times greater than that of air. This has important consequences for reducing the heating effects in electrical equipment.

SF₆ has a very high dielectric strength (Figure 1. 1) thanks to fluorine's highly electronegative properties, yielding in a very short lifetime of free electrons, because they combine with SF₆ molecules to form heavy ions with low mobility. Thus, the probability of dielectric breakdown by avalanche is reduced. The deionization time constant is extremely low, in the order of 0.25 ms. The dielectric strength of SF₆ is about 2.5 times higher than that of air under the same conditions.

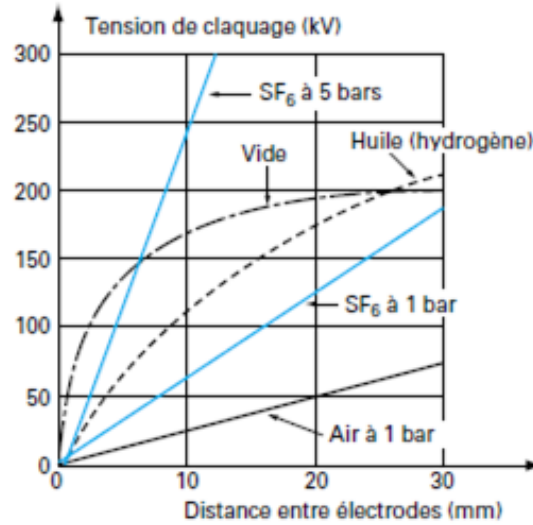


Figure 1. 1 : Impact of the distance between the electrodes on the breakdown voltage in uniform field [116]

Our study focuses only on MV GIS used in medium voltage, for which the gas plays a role of insulating gas only (current interruption and arc quenching properties are not considered).

1.II.A. Greenhouse effect and use of SF₆

Extremely potent and long-lived greenhouse gas emissions could irreversibly alter the climate on a millennium scale [10]. SF₆ has a very pronounced absorption band at an infrared frequency where the earth's atmosphere is relatively transparent and therefore absorbs radiation 42,000 times more efficiently than CO₂. The Intergovernmental Panel on Climate Change (IPCC) currently reports a lifetime in the atmosphere of 3,200 years and a global warming potential (GWP) value of 23,500 (100-year time horizon) [11], assuming that photolysis of SF₆ by ultraviolet (UV) radiation is the main removal process. Due to its very long lifetime, SF₆ accumulates in the atmosphere.

Global Warming Potential is the ratio of the warming effect caused by a substance to the warming caused by a similar mass of carbon dioxide. Thus, the GWP of CO₂ is set to 1 [12]. This means that one kilogram of SF₆ released into the atmosphere is equivalent to 23.5 tons of CO₂.

The annual emission of SF₆ into the atmosphere has increased sharply since the 1960s (approximately 2 kt (kilotons) in 1978 to reach a peak of 6.4 kt in 1995). Data collected in 2018 indicate that the emission of SF₆ continues to increase (7.2 kt in 2008) [13], despite all the regulatory actions.

Due to its very long lifetime, SF₆ released into the atmosphere accumulates and contributes to global warming. SF₆ was listed by the Kyoto Protocol in 1997 as a remarkable greenhouse gas whose emissions must be reduced. Since 1995, two different sampling programs have measured the level of sulfur hexafluoride in the atmosphere. Measurements with weather balloons began in 1995 with eight stations and continue today at 15 locations [14]. In addition to these probe balloons, a four-channel gas

chromatograph was developed in 1998 (called CATS) to measure the level of SF₆ in the atmosphere [15]. CATS gas chromatographs are currently deployed at six sites and take measurements hourly. The red line shows an increase of 0.24 ppt per year of SF₆.

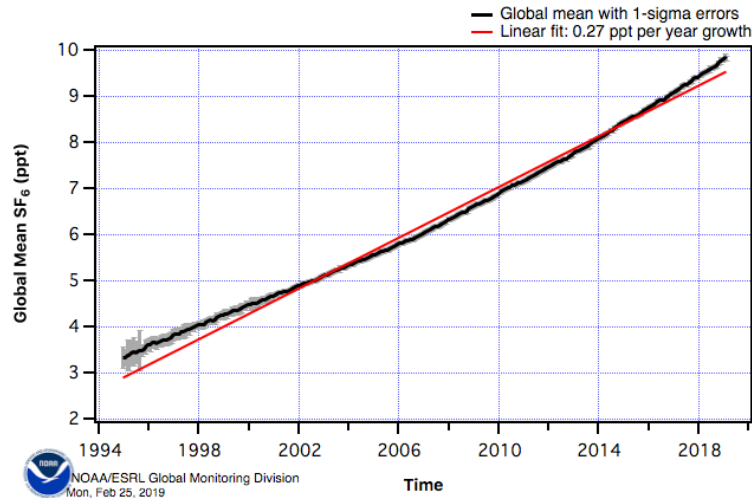


Figure 1.2 : Quantity of SF₆ in the Earth's atmosphere between 1995 and 2019 [117]

Among the 8,000 tons of SF₆ produced annually, around 80% of this is consumed by the energy industry for switchgear [9]. Typical examples of switchgear include circuit breakers, fuses, and insulators. The application of SF₆ to the switchgear can have two distinct roles; to isolate live components from the earth and to interrupt the arc when opening the circuit breaker contacts. The main types of HV systems using SF₆ either as insulator or as breaking fluid are:

- GIS (gas insulated switchgear for high voltage in indoor and outdoor applications);
- Assemblies of HV and GIL devices (gas insulated lines).

Our study focuses only on GIS used in medium voltage, where SF₆ plays a role of insulating gas.

1.II.B. Policy and standards

1.II.B.i. Environmental policy

Regulation CE n°517/2014 [16], which entered into force in January 2015, aims to reduce fluorinated greenhouse gases, including SF₆. The applied policy hopes to see an 80% reduction in fluorinated gas emissions by 2035. This long-term goal indicates that there may be a stricter policy or amendments in the future that will induce more restrictions on the use and emissions of SF₆.

The United States announced the US CLEAN Future Act for Climate Leadership to reduce greenhouse gas pollution by 50% from 2005 levels by 2030, and net zero greenhouse gas pollution

greenhouse by 2050. The European Commission has announced the Green Deal, with an objective of climate neutrality and without net greenhouse gas emissions by 2050 [6].

1.II.B.ii. Switchgear testing policy

A number of alternative media to SF₆ are still in their development phase, there are no standardized methods to test and validate these technologies. An attempt is given in [6]. One can also refer to the available SF₆ standards, for gas handling, but an attention should be paid to specific risks (inflammability, toxicity, ...) of these new molecules and mixtures. In the end, the new SF₆-free switchgear has to respect the product standard, independently of the insulation medium, as IEC 62271 “High-voltage switchgear and control-gear” (especially part 1: Common specifications, and part 200: AC metal-enclosed switchgear and control-gear for rated voltages above 1 kV and up to and including 52 kV).

1.II.B.iii. Considerations for testing and validating SF₆ alternatives

For MV GIS (as for example an RMU “Ring Main Unit” in Figure 1. 3), the breaking of current can be performed using vacuum interrupters. This PhD thesis will not discuss the interruption performance of new gases. Insulating gas (SF₆ or new gas) is used around this vacuum interrupter to prevent any breakdown outside the vacuum interrupter, and also in other parts of the system. Since SF₆ has very good insulation properties, operation at rather low pressure (< 0.15 MPa) is possible, keeping a reduced size of the devices, which constitutes a practical and economical advantage.



Figure 1. 3 : MV GIS

All equipment must undergo various tests to ensure reliable operation for long duration (30 years), and the safety of consumer, that are defined by standardization committees: IEC for international products, but also IEEE for the USA, GB/DL for China, just to name a few.

Concerning insulation and dielectric:

- The IEC 60071 defines standardized overvoltage ratings for the medium and high voltage equipment (see Figure 1. 4). A real lightning stroke can induce a stress of several millions of volts overvoltage. However, considering all the voltage surge protections, the IEC 60071 defines standardized voltage ratings and impulses shape that are representative of real overvoltage that could appear on the network. The so called “Basic Insulation Level (BIL) is a standardized voltage wave with a fast-rising edge of 1.2 μ s and a halfway fall time of 50 μ s.
- The IEC 60060 describe the test facility from a laboratory point of view: procedure, equipment, and the applied statistics to treat the results.
- The IEC 62271-1 and -200 define the application of the procedure on a real switchgear.

overvoltage class	low frequency		transient		
	permanent	temporary	slow front	fast front	very fast front
shape					
shape range (frequency, rising front, term)	$f = 50$ or 60 Hz $T_1 \geq 3,600$ s	$10 < f < 500$ Hz $3,600 \geq T_1 \geq 0.03$ s	$5,000 > T_p > 20$ μ s 20 ms $\geq T_2$	$20 > T_1 > 0.1$ μ s 300 μ s $\geq T_2$	$100 > T_f > 3$ ns $0.3 > f_1 > 100$ MHz $30 > f_2 > 300$ kHz 3 ms $\geq T_t$
standardised shape	$f = 50$ or 60 Hz T_1 (*)	$48 \leq f \leq 62$ Hz $T_1 = 60$ s	$T_p = 250$ μ s $T_2 = 2,500$ μ s	$T_1 = 1.2$ μ s $T_2 = 50$ μ s	(*)
standardised withstand test	(*)	short duration power frequency test	switching impulse test	lightning impulse test	(*)

(*) to be specified by the relevant product Committee

Figure 1. 4 : Representative overvoltage forms and tests defined by standard IEC 60071 [118]

Table 1. 2 : Rated insulation levels for rated voltages [17]

Rated AC voltage (kV) (RMS value)	Lightning impulse withstand voltage (kV) (peak value)	Power-frequency withstand voltage (kV) (RMS value during 60 seconds)
7.2	60	20
12	75	28
17.5	95	38
24	125	50
36	170	70

The insulation of the device must be designed to withstand, without damage, a fixed minimum impulse voltage defined by the BIL level. The operating voltage level of surge protection devices should

be less than the minimum withstands of the equipment. For example, for a device operating under AC at 24 kV or less, its resistance to a lightning impulse must be greater than 125 kV (Table 1. 2).

1.III. *Reduction and replacement strategies of SF₆*

The environmental impact of SF₆ can be minimized:

- By the reduction of its emission (less leakage in products, more recycling, control of life cycle). This started in the '90 after the Kyoto protocol.
- By its replacement with alternative insulation technologies, with a lower GWP.

1.III.A. Recovery and recycling of SF₆

To supervise the recovery and recycling of SF₆, international procedures such as the IEC 60373 standards [18] or the Cigré guide [19] have been put in place. These practical guides share know-how concerning the recovery and recycling SF₆ used. These procedures also standardize the purity of reusable SF₆. After the life of the device, SF₆ may contain impurities (air, humidity and by-products generated during electric shocks). After its life cycle, SF₆ is treated to eliminate these by-products and thus be able to be reused if the quantity of by-products after treatment remains below an authorized threshold. With increasingly efficient SF₆ recovery and purification technologies, this method can significantly reduce SF₆ emissions into the atmosphere.

1.III.B. Use of mixtures

Another strategy is to reduce the amount of SF₆ by using mixtures coupling a small amount of SF₆ with environmentally friendly gases (air, nitrogen (N₂), CO₂). For electrical insulation, only SF₆-N₂, CO₂ or air mixtures are useful. Indeed, a synergy is observed with these three mixtures for low concentrations of SF₆ [20].

The increase in dielectric performance is significant at low levels of SF₆. This synergy makes it possible to obtain a higher dielectric strength than pure N₂, air or CO₂ by considerably reducing the quantities of SF₆ used. These mixtures are also economically interesting (abundant in the atmosphere).

These blends have been used successfully in the electrical industry, for example, in circuit breakers where very low temperature operation is required [21]. More recently, it has been used for second generation gas-insulated transmission lines (GIL) [22], which have been on the market since 2001 (e.g. GIL 220 kV at Palexpo in Geneva, Switzerland) [23].

1.III.C. Alternatives gases to SF₆

1.III.C.i. Requirements

The search for alternative gas to SF₆ that can be used in electrical equipment has been going on for several years given the large ecological challenges. Potential candidates for the replacement of SF₆ must meet several criteria [8].

First, the intrinsic properties of the gas, depending on its chemical structure, must be taken into account. These properties are independent of the application and the environment in which a gas is placed. Indeed, to be a good substitute, the dielectric strength of the gas is fundamental and must be high. The properties providing high dielectric strength are those leading to reduce the number of electrons present in an electrically stressed gas. The gas must then:

- Be an electronegative gas to capture free electrons and prevent avalanche phenomena which are at the origin of discharge initiation and propagation;
- Having a small ionization cross section and high ionization energy to prevent ionization phenomena by collision of electrons;
- Have a high collision cross section which allows to slow down the free electrons remaining in the gas. This will prevent them from being accelerated by the action of the electric field and thus delay the formation of the seed electrons of the discharge.

Another basic parameter is the liquefaction temperature which must be high (high vapor pressure). This liquefaction temperature must be lower than the minimum operating temperature of the equipment at the selected operating pressure. Thermal stability over long periods of time at temperatures above 400 K is also required. Thermal stability is expressed by two criteria:

- The decomposition temperature of the gas must be higher than the maximum temperature that could occur in the equipment under operation;
- The gas must not ignite in a decomposition reaction caused by partial discharges.

In addition, the gas must be chemically inert relative to other parts of electrical equipment to prevent wear, non-toxic (for maintenance and technical personnel), and non-explosive [6].

Next, the gas must exhibit suitable “extrinsic” properties. These properties describe the behavior of the gas in interaction with its environment and its behavior under external influences such as discharges and electrical breakdown. To be used in MV equipment, a dielectric gas should:

- Not undergo any extensive decomposition;
- Lead to no polymerization;

- Do not form any conductive deposit (carbon layers or other deposits);
- Be non-corrosive and non-reactive to metals, insulators, and seals;
- Do not give any toxic and reactive by-product upon discharge;
- Show a high breakdown voltage under various field configurations: uniform and non-uniform electric fields;
- Be insensitive to the surface roughness of metal and to moving metal particles;
- Do not give rise to any adverse reaction with humidity and impurities.

Finally, the gas must be environmentally friendly. It should not contribute to global warming, deplete the ozone layer or persist in the environment for long periods. The critical parameters that have the most impact on the environment are the ozone depletion potential (ODP) and the global warming potential (GWP).

1.III.C.ii. Proposed solutions

The first research about the general behaviour of gas insulations began in the mid-20th century. Subsequent studies of potential SF₆ replacements were particularly intense in the 1980s, mainly focused on pure gases. Several gases are today widely studied, such as fluoroketone or fluoronitrile, both for insulation and current breaking at very high voltage. This thesis concerns the replacement of SF₆ for medium voltage applications only (up to 52 kV). In modern MV GIS, the breaking of current is made in vacuum interrupters. The SF₆ replacement gas for MV GIS does therefore not need to have the same breaking properties (thermal conductivity and self-healing) as SF₆, but only a good insulating property at medium voltage levels.

Pure gases naturally present in the Earth's atmosphere (O₂, CO₂, N₂) are commonly used at high pressure as insulating materials and as a means of extinguishing the electric arc in high voltage switches. They are the most suitable candidates for the environment given their low ozone depletion potential (ODP). Dry air and gas mixtures exhibit better dielectric strength than that of N₂ or CO₂ alone [24]. The dielectric strength of CO₂ is greater than that of N₂ under pulse voltage [25]. The pressure of CO₂ must be three times that of SF₆ to achieve the same level of insulation performance. Air is present in large quantities and costs nothing, presents no toxicity and no risk to humans or the environment. However, air has a low dielectric strength (30% that of SF₆ in homogeneous field) [26]. The insulation distances must therefore be greater leading to larger devices. This problem can be overcome by increasing the operating pressure of air-insulated devices.

Trifluoroiodomethane (CF₃I) has excellent dielectric properties equivalent to SF₆. Its GWP is equivalent to CO₂, its ozone depletion potential is less than 0.08 [27] and its lifetimes in the atmosphere is very short. Its boiling point is 25°C at 0.5 MPa (SF₆ filling pressure in GIS). To prevent it from

boiling, it is used with a gas buffer such as CO₂. A 60% mixture of CF₃I and CO₂ has insulating characteristics similar to pure SF₆ [28]. However, CF₃I is a moderately toxic gas [29]; it is classified as a type 3 mutagen [30]. It should therefore be handled with care.

Fluoroketone has a boiling point of 24°C. Due to this high boiling point, the gaseous state of this chemical element is maintained at a pressure lower than atmospheric pressure. Fluoroketones can only be used as an additive at a pressure below the saturated vapor pressure. Fluoroketones do not exhibit, after ionization in the plasma state, a recombination capacity similar to that of SF₆. Therefore the quantity of fluoroketone, present in the gaseous state in an apparatus, decreases as the number of arc extinctions obtained in this apparatus increases. Fluoroketones C₅F₁₀O (C₅Fk) and C₆F₁₂O (C₆FK) have very low toxicity in their pure state and exhibit high dielectric strength, and show an extremely low global warming potential (GWP) [31]. Hyrenbach et al. [32] have shown that the dielectric performance of the C₅FK gas mixture is superior to that of the C₆FK mixture (but only 12% that of SF₆). C₄FK mixtures gave even better results but these mixtures must be excluded because of their toxicity.

Heptafluoro-iso-butyronitrile or gaseous fluoronitrile belongs to the family of fluorinated nitriles. Fluoronitrile has been synthesized and marketed under the name NOVECTM4710. Fluoronitrile has a high liquefaction temperature (-4.7°C). Therefore, fluoronitriles must be mixed with other buffer gases such as CO₂, dry air or N₂. The global warming potential (GWP) of fluoronitrile gas is less than 2400 and its ozone depletion potential (ODP) is zero. Recent tests and analyses performed on the NOVEC 4710 conclude that this gas is not CMR (Carcinogens Mutagenic Reprotoxic) and that the TLV TWA (Threshold Limit Values-Time Weighted Average) is equal to 65 ppm [33], [34].

Hydrofluoroolefins (HFO) have a low GWP but also a zero ODP. These fluids are widely used in the refrigeration industry. Their low toxicity is widely documented. It would be possible to use the HFO only for medium voltage GIS where the current breaking does not take place in the gas. Indeed, without an electric arc, HFO does not degrade and has a dielectric strength close to SF₆. This gas will be described in detail in the next section.

1.IV. *Properties of the gas studied in this work: HFO-1234 ze (E)*

Hydrofluoroolefins are synthetic gases manufactured and patented by Honeywell, they are part of the fourth generation of refrigerants marketed under the name SOLSTICE®. Several gases can be found in the hydrofluoroolefin family, HFO-1234yf (2,3,3,3-Tetrafluoropropene) and HFO-1234ze (1,3,3,3-tetrafluoroprop-1-ene) are the most known [35], to which the ASHARE standard has assigned the nomenclature R-1234ze. For HFO-1234ze, there are two isomers. The two molecules have the same chemical formula C₃H₂F₄, but are differentiated by the geometric structure (Figure 1. 5).

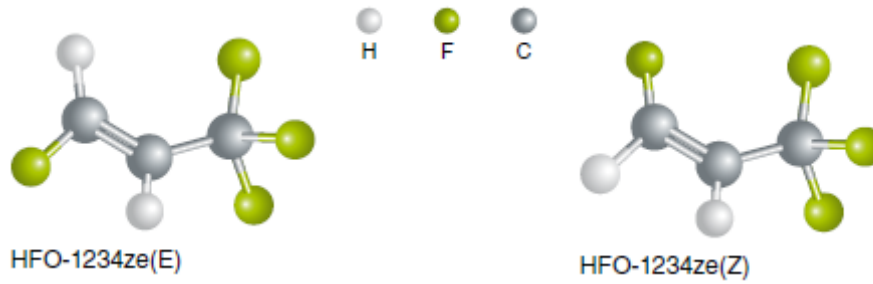


Figure 1. 5 : Molecular structure of HFO-1234ze (E) and HFO-1234ze (Z) [35]

This isomerism confers different physical properties as shown in Table 1. 3. Unlike HFO1234ze, HFO1234yf is slightly flammable under near normal conditions, which disqualifies it from the list of potential substitutes for SF₆.

Table 1. 3 : Properties of hydrofluoroolefin

Gas	R1234ze(E)	R1234ze(Z)	R1234yf	SF ₆	Reference	
Chemical formula	CHF=CHCF3	CHF=CHCF3	CH2=CF3		[36], [37]	
Molecular weight (kg/mol)	114,04			146.045		
Critical temperature (°C)	109,40	153,60	94,70	45,55		
Critical pressure (MPa)	3,64	3,97	3,38	3.78		
Boiling temperature (at 0.101 MPa)	-18,95	9,00	-29,50	-64		
Global warming potential (GWP CO ₂ = 1)	1	6	6	22800		
Ozone Depletion Potential (ODP)	0	0	0	0		
Lifetimes (years)	0,045	-	0,029	850		
Inflammability	21°C	No	Slightly flammable	No		[35]
	100°C	7-12%	-	No		

Even though they have the same global warming potential, their thermodynamic properties are quite different [36], notably the boiling point. HFO-1234ze(E) seems to be the most interesting for electrical applications (low boiling temperatures and low flammability).

1.IV.A. Physical and environmental properties of HFO-1234ze (E)

Hereinafter, HFO-1234ze (E) is abbreviated as HFO for ease of reading.

1.IV.A.i. GWP and ODP

With a GWP of 1, HFO-1234ze(E) has a very short lifetime in the atmosphere of about 15 days [38]. Ozone Depletion Potential (ODP) is the ratio of the impact of a chemical on ozone to the impact of a similar mass of CFC-11. Thus, the ODP of CFC-11 is set to 1 [12]. With an ODP of 0, HFO does not contribute to the depletion of the ozone layer.

1.IV.A.ii. Boiling point

The boiling point (T_b) is, by definition, the temperature at which and below which the gas is liquefied at a pressure of 0.1 MPa [12]. For example, SF_6 has a boiling point of $T_b = -64^\circ C$ [39] and can therefore be used at very low operating temperatures (generally between $-5^\circ C$ and $-25^\circ C$) without risk of condensation. The boiling point of HFO is $-19^\circ C$ (see Table 1. 3), which is suitable for MV applications where the minimum operating temperature most commonly requested by customers is $-15^\circ C$ [39].

1.IV.A.iii. Flammability

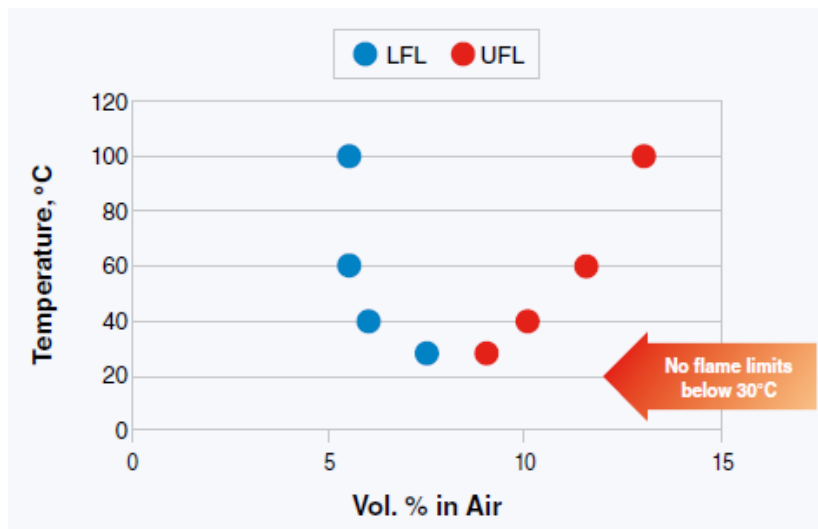


Figure 1. 6 : Flammability threshold of HFO-1234ze (E) as a function of air percentage and temperature [35]

Flammability is a very important criterion in any gas application. HFO is completely non-flammable at temperatures below $30^\circ C$ (Figure 1. 6) [40], [36]. When used in a system, HFO can become mildly-flammable in air if leaked [35]. However, the risk is limited, as HFO requires 10 times more

concentration and 250,000 times more energy than hydrocarbons to become flammable, but only at temperatures above 30°C.

If a flame would appear, the effect of that flame would be extremely mild. Indeed, its very low heat of combustion (5 times less than propane) associated with an ultra-low combustion rate would not be sufficient to propagate a fire.

1.IV.A.iv. Toxicity

HFO has been shown to be non-toxic, non-carcinogenic, non-toxic for reproduction and non-mutagen [40] neither on man nor on flora and fauna [41]. The American Industrial Hygiene Association (AIHA) Workplace Environmental Exposure Level Committee recommended 800 ppm as the 8-hour time-weighted average exposure limit for HFO [42].

1.IV.A.v. Compatibility with materials

In an MV device, the insulation gas is often in direct contact with different types of materials (grease, polymers, metals, etc.). Honeywell has performed a two-week compatibility test with several polymers, elastomers and some metals (stainless steel, copper, brass and aluminium) immersed in HFO-1234ze (E) and has shown good compatibility with most of these materials [35]. In addition, Préve et al [43] performed accelerated compatibility tests, in which the gas was contacted with many materials found in the MV tank for a period of 30 days at elevated temperature and pressure in order to accelerate the phenomena of aging. The results showed very good compatibility with these materials. Jarahnejad [40] states, however, that it is best to keep HFO1234ze (E) separate from alkali metals (e.g. potassium) to avoid a likely reaction.

1.IV.A.vi. Degradation by electrical discharges

Previous studies have reported that the degradation of HFO (E) generates solid by products in the form of very fine black dust [7].

Piccoz et al. [44] studied the decomposition products of HFO (E) and different mixtures by dielectric barrier discharge (DBD). Figure 2.5 shows the change in the concentration of gases after 5 hours of DBD treatment as a function of the voltage applied (as a percentage of their initial concentration before DBD treatment). For HFO-1234ze (E) (curve 2 Figure 1. 7), after 5 hours of treatment at 10 kV, only 10% of HFO-1234ze (E) was broken down into by-products. Moreover, the addition of 25% N₂ to HFO-1234ze (E) decreases this degradation percentage (curve 7 Figure 1. 7).

The formation of toxic decomposition products in HFO1234ze (E) was studied in [44]. Measurement of the amount of toxic products (CF₄, C₂F₄, C₃F₆ and CF₃=CH) produced during the decomposition of HFO (E) reveals that pure HFO (E) has a relatively low resistance to the discharge. Therefore, it appears that HFO cannot be used in breakers, and only for pure dielectric insulation.

Dilution of HFO-1234ze (E) with nitrogen significantly reduces the degree of gas conversion by discharges. However, the results of these studies have been obtained for much more intense discharge regimes than those occurring in real systems, if HFO is used only for insulation. Therefore, the proposed use for dielectric insulation in high voltage electrical equipment requires preliminary long-term experiments at high voltage in real devices, to quantify the degradation rate in more realistic conditions.

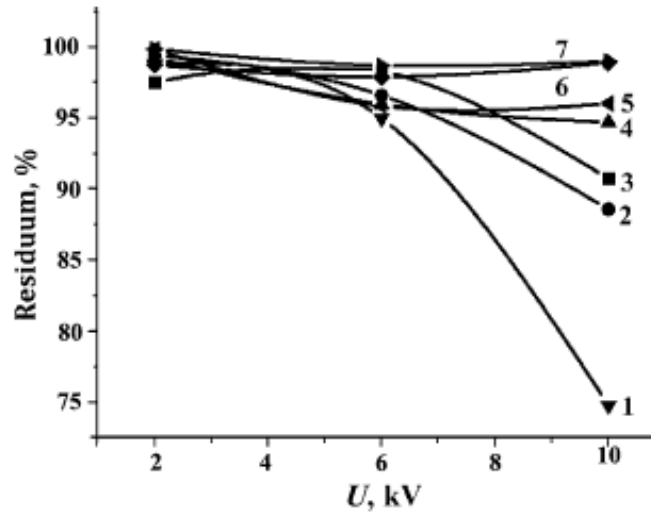


Figure 1. 7 : Evolution of the concentration of source gases in their decomposition products after 5 hours of DBD treatment as a function of the voltage applied (as a percentage of their initial concentration before the DBD treatment). 1, C5K mixed in decomposition products at 18.5% C5K: 81.5% dry air; 2, HFO-1234ze (E) in the decomposition products of pure HFO-1234ze (E); 3, C5K in the decomposition products of pure C5K; 4, C5K in the decomposition products of the mixture 12% C5K: 88% N₂; 5, total concentration of C5K, HFO-1234ze (E) and CO₂ in the decomposition products of the mixture at 9% C5K: 56% HFO-1234ze (E): 35% CO₂; 6, total concentration of C5K and HFO-1234ze (E) in the decomposition products of the mixture at 9% C5K: 57.5% HFO-1234ze (E): 33.5% N₂; 7, HFO-1234ze (E) in the decomposition products of the mixture at 75% HFO-1234ze (E): 25% N₂. All concentrations are given as percentage by volume [44]

Zhai et al. [45] established a mechanism map for the combustion reaction of R1234ze (E) into stable products (ignition by electric spark, 298.15 K, 0.1 MPa). In addition, chemical reaction equations have been proposed to describe the stoichiometric combustion of R1234ze (E) under different conditions.

1.IV.B. Dielectric properties of HFO: preliminary investigations carried out at G2Elab

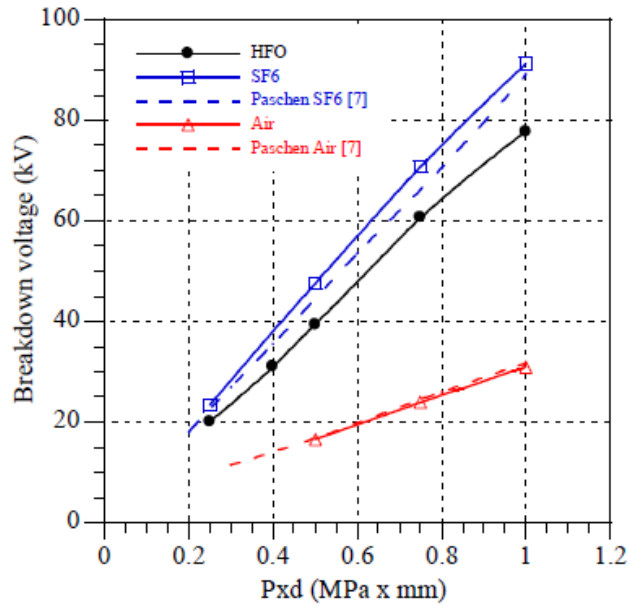


Figure 1. 8 : Comparison of breakdown measurements obtained in HFO, SF₆, and dry Air in the same conditions, versus (Pressure x distance) product. DC ramp 1 kV/s, d = 5 mm, plan-plan. [7]

Figure 1. 8 from [7] represents the Paschen plot obtained in a uniform field curve with HFO in comparison with air and SF₆ with an inter-electrode space of 5 mm. The critical field of SF₆ is 90 kV/cm and that of HFO is 79 kV/cm. As previously reported [43], breakdown measurements in HFO are slightly below those in SF₆. On average, breakdown voltages in HFO represent 83% of those measured in SF₆ with the same conditions, and 250% of those measured in air.

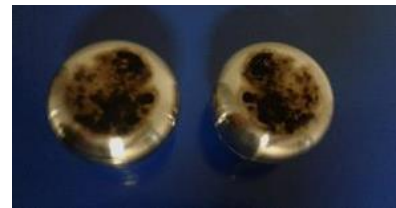
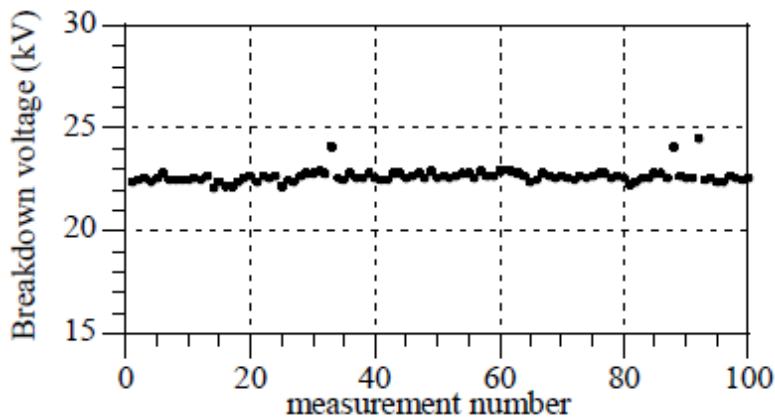


Figure 1. 9 : Evolution of breakdown voltage of HFO subjected to repeated breakdown measurements under DC ramp. P = 0.1 MPa, d = 3 mm [7]

During these experiments requiring numerous breakdown tests, solid back deposits were observed on the electrodes following a hundred breakdowns [7] but the dielectric strength of the HFO

was not affected even after a hundred flashovers (Figure 1. 9). This effect was probably due to a low discharge energy, due to the presence of a high limiting resistor in the circuit.

Figure 1. 10 to Figure 1. 12 shows the measurements of impulse breakdown voltages U_b obtained in point-plane geometry at different pressure, together with the corresponding time to breakdown t_b . U_b show a moderate increase with pressure (Figure 1. 12). Shorter times to breakdown are observed at higher pressure and voltage. Plotting t_b versus breakdown voltage (Figure 1. 11) shows a clear correlation, with a uniform decrease whatever the pressure.

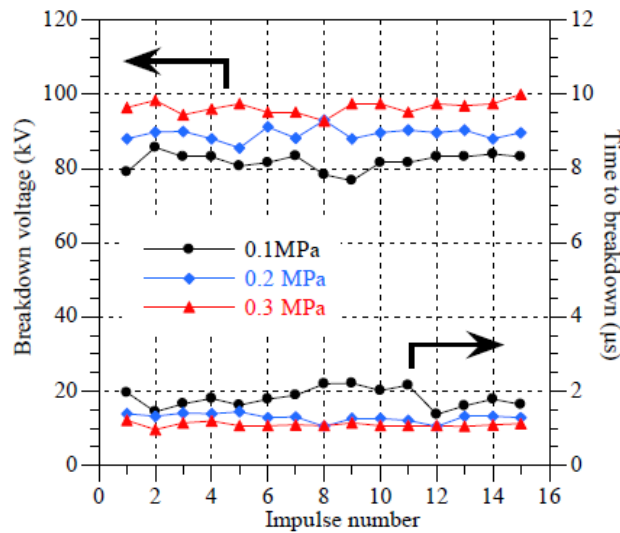


Figure 1. 10 : Measurement of breakdown voltage V_b in point-plane geometry and corresponding time to breakdown t_b in HFO under impulse voltage. ($R_c = 0.5$ mm, $d = 5$ cm) [7]

Once again, no obvious decrease of the breakdown voltage was recorded in this study, when repetitive impulse breakdown tests were done without changing the gas (Figure 1. 10).

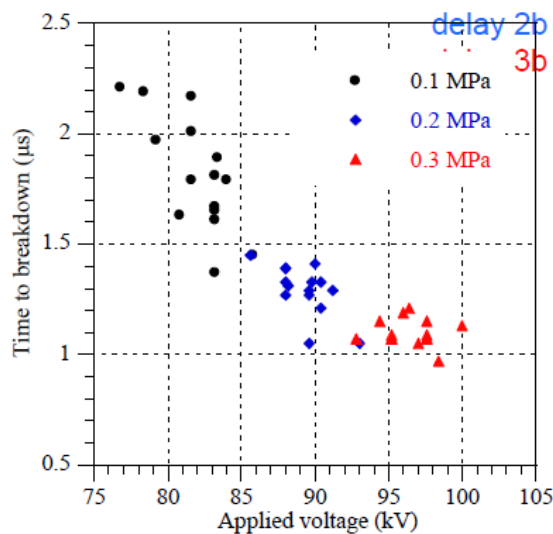


Figure 1. 11 : Time to breakdown t_b versus breakdown voltage V_b in HFO at different pressure under impulse voltage. ($R_c = 0.5$ mm, $d = 5$ cm) [7]

In HFO (Figure 1. 12) as in SF₆ a moderate increase of breakdown voltage in divergent field versus pressure was observed, and the difference between HFO and SF₆ reduces when pressure is increased. At atmospheric pressure, the breakdown voltage of HFO in point-plan gap is 74% that of SF₆, and 94% at 0.3 MPa.

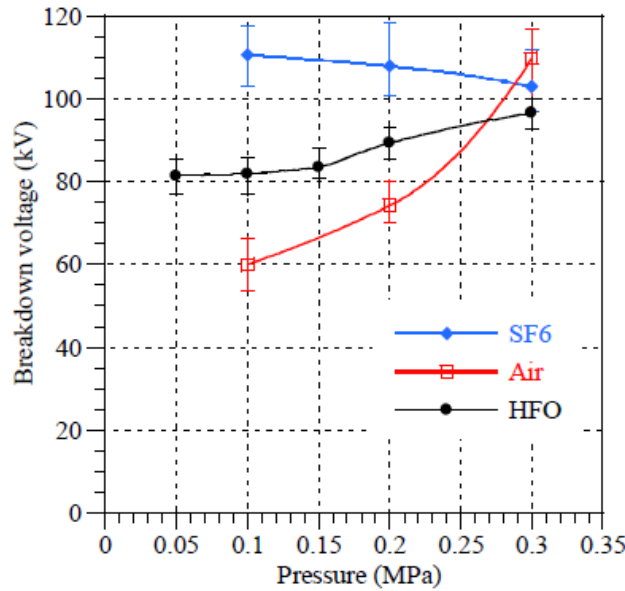


Figure 1. 12 : Breakdown voltage versus pressure in point-plane geometry under impulse voltage, in HFO, SF₆ and dry Air. ($R_c = 0.5$ mm, $d = 5$ cm) [7]

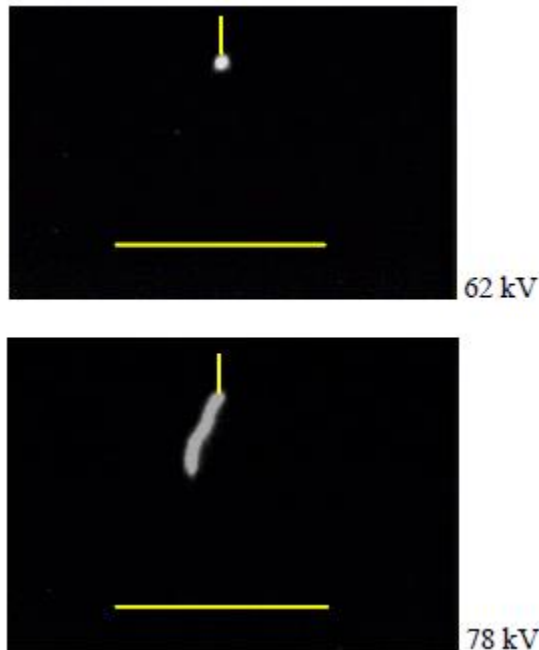


Figure 1. 13 : Photographs of pre-breakdown discharges in HFO at voltages lower than the breakdown voltage. ($R_c = 0.5$ mm, $d = 5$ cm, $P = 0.2$ MPa) [7]

In [7], photographs of pre-breakdown discharges were taken in HFO (Figure 1. 13) at a voltage lower than the breakdown voltage (i.e., no breakdown occurred after these discharges). In HFO, the pre-breakdown discharges consist of a propagating luminous channel which stops at a certain distance from the plane when the voltage is lower than the breakdown voltage. In most experiments, only one propagating channel was observed. Its length increases rapidly with voltage and breakdown occurs when the channels reach the flat electrode. Its shape, as well as the associated transient currents formed by series of fast pulses, are reminiscent of the propagation of stepped leaders, typical of electronegative gases. Similar phenomena have been previously described in SF₆.

Since the discharge initiation voltages are slightly lower than the breakdown voltages U_b , the values of U_b measured here in the divergent field in HFO and SF₆ represent the minimum voltage required to induce the propagation of the leader up to the plane. Figure 1. 12 shows that this "propagation voltage" is slightly lower in HFO compared to SF₆, and does not much depend much on pressure. The propagation velocity is estimated from $5 \cdot 10^4$ to 10^5 m/s, almost identical to those already reported for SF₆.

1.V. *Breakdown physical processes in gases*

Gases are almost perfect insulators since they include a very small proportion of charged particles. When subjected to an electric field, the gases allow a very weak current to flow (a few femto-amperes for a few centimeters of air under a few tens of volts). However, when they are subjected to a sufficient electric field, they can allow a much greater current to flow when pre-breakdown and breakdown phenomenon occur. Depending on the experimental conditions (pressure, configuration of the electric field, type of voltage applied, etc.), pre-breakdown phenomena can be of different types [46].

1.V.A. Electronic avalanche

When a seed electron (free electron) in a gas is subjected to an electric field E , it is accelerated and acquires energy. If the energy is sufficient, the electron can ionize a gas molecule by collision, which creates new free electrons. The phenomenon of ionization is opposed to the phenomenon of attachment by gas molecules. When E exceeds a critical value (E_{crit}), ionization becomes preponderant over attachment. Then, new electrons can be accelerated and in turn ionize gas molecules (Figure 1. 14). This constitutes the electronic avalanche mechanism. It can lead, under certain conditions, to gas breakdown.

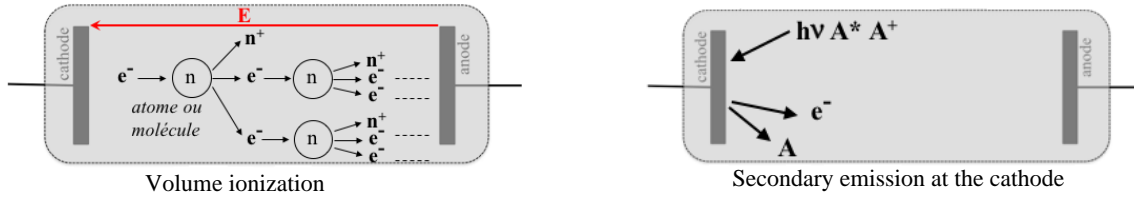


Figure 1.14 : Townsend avalanche principle [119]

With plane and parallel electrodes separated by a distance d , n being the number of electrons in a plane of abscissa x , n_0 the number of initial electrons (at the cathode at $x = 0$) and $\bar{\alpha}$ the net ionization coefficient ($\bar{\alpha} = \alpha - \eta$, with α the ionization coefficient and η the attachment coefficient), we obtain:

$$dn(x) = \bar{\alpha} n(x) dx, \text{ which gives by integration } n(x) = n_0 \exp(\bar{\alpha} d).$$

The current is then given by:

$$I = e n(d) = I_0 \exp(\bar{\alpha} d) \quad (1)$$

With $I_0 = e \cdot n_0$.

Experimentally, equation (1) is only valid for $d < d_s$ where d_s is the critical distance for which the current increases faster than expected, and leads to breakdown. In such conditions, new phenomena appear, not only defined by the coefficients α and η . For example, the emission of secondary electrons at the cathode produces new avalanches. Depending on the conditions (pressure, nature and state of the gas and the electrodes, etc.), secondary electrons are produced by various secondary processes such as the collision of positive ions or photons at the cathode. Townsend improved the previous equations by introducing the "generalized secondary ionization coefficient γ ", which represents all possible secondary processes.

$$n(d) = n_0 \frac{e^{\bar{\alpha} d}}{1 - \gamma(e^{\bar{\alpha} d} - 1)} \quad (2)$$

$$I = I_0 \frac{e^{\bar{\alpha} d}}{1 - \gamma(e^{\bar{\alpha} d} - 1)} \quad (3)$$

Equation (3) describes the variation, observed experimentally, of the current with the distance d . The current has an infinite value when its denominator vanishes, this is called the Townsend breakdown criterion:

$$1 - \gamma(e^{\bar{\alpha} d} - 1) = 0 \quad (4)$$

This current divergence however has no physical significance because in practice the current is limited by the resistance of the electrical circuit.

This first breakdown criterion (Townsend breakdown mechanism) is based on a series of successive avalanches. In SF₆, the corresponding critical electric field is about three times higher than for air (90 kV/cm.bar versus 30 kV/cm.bar for air).

1.V.B. Origin of the initial electrons

The electronic avalanche can exist only if an initial electron starts the series of ionizing shocks. There exist natural radioactive sources capable of ionizing gas, mainly by α and β radiation. However, in systems with a metallic enclosure (test cells, shielded stations), this radiation is attenuated. The contribution of terrestrial radioactivity is normally around 10^{-4} electrons.s⁻¹.cm⁻³.Pa⁻¹ [47] but in shielded systems this value is reduced to around 2.10^{-5} electrons.s⁻¹.cm⁻³.Pa⁻¹. The contribution of cosmic radiation is then comparable and amounts to about 2.10^{-5} electrons.s⁻¹.cm⁻³.Pa⁻¹ [48].

Under positive voltage polarity, collisional detachment appears to be the main source of seed electrons. Niemeyer et al. [49] states that ions are created by cosmic rays, and lost by ion-ion recombination or by collisions with metallic components. Ions, accelerated by the field, collide with atoms and release their free electron. The creation rate is approximately 10 ion pairs/cm³.s.bar. The mobility of ions in air is approximately 2 cm²/V.s. Under negative polarity, the field emission from the electrode is considered.

1.V.C. Paschen's law

At the beginning of the century, Paschen showed experimentally that the breakdown voltage of a gas in homogeneous electric field is a function of the product (pressure * distance between electrodes): $U_{cl} = f(Pd_s)$ (Figure 1. 15). Townsend's theory makes it possible to account for this variation satisfactorily. However, to eliminate the influence of temperature, it is however preferable to replace the pressure P , at a given temperature, by the density N (at $T = 300K$, $0.1 \text{ MPa} = 10^5 \text{ Pa}$), which provides: $U_{cl} = f(Nd_s)$

If we assume an energy balance of electrons in the gas, the coefficients $\alpha\gamma$ and $\bar{\alpha}$ are functions only of the reduced electric field E/N . The breakdown criterion can therefore be written by setting:

$$\frac{\bar{\alpha}}{N} = g\left(\frac{E}{N}\right) \text{ and } \frac{\alpha\gamma}{\bar{\alpha}} = h\left(\frac{E}{N}\right)$$

Moreover, with $\frac{E_{cl}}{N} = \frac{U_{cl}}{Nd_s}$:

$$h\left(\frac{U_{cl}}{Nd_s}\right) \left[\exp\left(g\left(\frac{U_{cl}}{Nd_s}\right) Nd_s\right) - 1 \right] = 1 \quad (5)$$

The functions h and g are determined from measurements of the ionization and secondary emission coefficients. Equation (5) shows that the breakdown voltage U_{cl} is only a function of the product Nd_s .

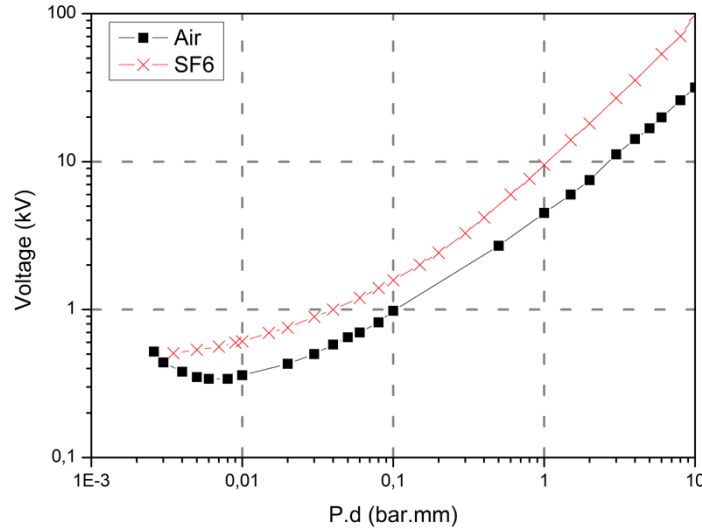


Figure 1.15 : Paschen curve for air and SF₆ at 20°C in logarithmic scales from [120]

In the Paschen plot, three types of breakdown can be identified (Figure 1.15):

- Townsend breakdown, around the Paschen minimum, due to electronic avalanches;
- Streamer type breakdown, for high $P.d$ products;
- Pseudo-spark type breakdown, for weak $P.d$ products.

At very low values of the product Pd , the breakdown voltage increases even when Pd decreases. Indeed, for low pressures the mean free path of the electron becomes larger than the inter-electrode gap, and electrons are able to pass through it without encountering a single gas molecule. The proposed mechanisms involve the release of gas or vapour from electrodes, thus breakdown takes place in this gas or vapour [50].

For high values of Pd , the measured breakdown value U_{cl} becomes less than the value provided for by Paschen's law. The breakdown voltage then depends on the pressure and the distance separately. These deviations are attributed to the nature of electrodes and to the "magnification" of the electrode roughness as the pressure increases [50], [51].

Pedersen demonstrated that the electric field must be very close to a perfectly uniform field for the Townsend avalanche mechanism to occur, and for Paschen's law to be valid. Such field can only be reached between electrodes of almost infinite dimensions. In a real configuration, the condition for Paschen's law application is [52] :

$$\frac{E_{average} - E_{min}}{E_{average}} < \frac{M}{Nd} \quad (6)$$

With $E_{average}$ and E_{min} the average and minimum electric field in the gap. M depends on constants of the gas considered, and indicates the sensitivity of the gas to field reinforcements on electrodes: the weaker M , the more sensitive the gas, and the largest deviations from Paschen's law for low Nd values.

1.VI. *Streamer phenomenon*

1.VI.A. Principle

Townsend's breakdown theory is characterized by the continuous development of electronic avalanches by secondary emission processes. It has been very successful in explaining breakdown phenomena under various discharge conditions over the past century. In the years 1930-1940, Raether was able to observe, at high pd values ($> 10^3$ Pa.m), breakdown characteristics too fast to be explained by a Townsend mechanism. Raether on the one hand, Meek et. Loeb [53] on the other hand, proposed the basis of a new breakdown theory, known as streamer breakdown, taking into account the effects of the space charge of the electronic avalanche.

In this theory, the breakdown process still begins with an electronic avalanche. However, the multiplication of charges in this first avalanche is so great that the space charge at its head creates a field of the same order of magnitude as the applied field. Thus an avalanche-streamer transition occurs. According to the criterion established by Meek [54], this transition occurs when the number of electrons exceeds a critical threshold of $N_{cr} = 10^8$ [47].

Raether formulated another criterion close to that of Meek, described by the integral equation (7):

$$\ln N_{cr} = \int_0^x (\alpha - h) dx = K_{str} \quad (7)$$

with x is the distance from the origin of the avalanche, N_{cr} the number of electrons in the critical avalanche and $(\alpha - h) = \bar{\alpha}$ the effective ionization coefficient. The streamer criterion is met for a certain value K_{str} . The value originally obtained by Raether was $K_{str} = 18$ and it shows a good agreement with Meek's theory.

We thus observe the propagation of a weakly ionized channel (called "streamer" or "ionization wave") between electrodes. The space charge in the streamer head creates a high local field which allows the formation of secondary electronic avalanches Figure 1. 16. This channel develops extremely rapidly and can propagate in regions where the applied field is too weak for an effective ionization reaction to

take place. Typical velocity are around 10^6 m/s, much faster than Townsend breakdown phenomena ($\sim 10^3$ m/s). Many aspects of the streamer mechanism, such as propagation and branching processes, remain a very active field of research.

In non-uniform field there exists a marked difference between a positive streamer (when the electrode under high field is positive) and negative. In a positive streamer, photons at the head of the avalanche create secondary avalanches by photoionization, and possibly by photo-detachment from negative ions (Figure 1. 16).

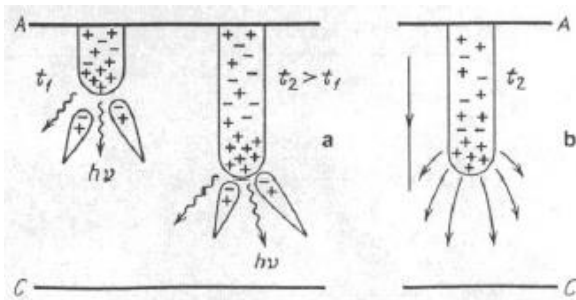


Figure 1. 16 : Positive streamer. a: development of the streamer; b: lines of fields at the head of the streamer

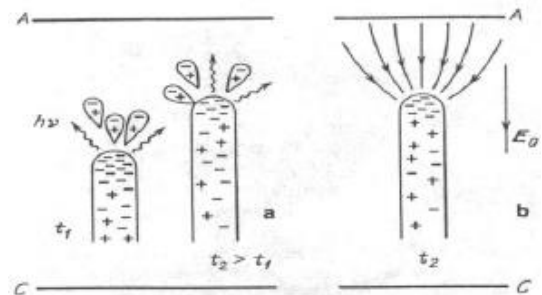


Figure 1. 17 : Negative streamer. a: development of the streamer; b: lines of fields at the head of the streamer

Due to the differences between the mobility of ions and electrons, the streamer head has a high charge concentration. As the streamer propagates, the head leaves behind it a more or less neutral imprint that looks like a weakly ionized plasma, usually called a filament.

The main propagation mechanism of a positive streamer is based on photoionization. Some species excited during the avalanche are able to emit a photon energetic enough to ionize a neutral molecule. The new electrons trigger a second electronic avalanche. Once it reaches the streamer head, the latter is neutralized, and ions left in the front form the new streamer head.

For negative streamers, the electrons drift upstream, so “seed” electrons created by photoionization are not necessary.

1.VI.B. Propagation velocity of streamers

Many researchers have studied the formation and propagation of streamers in air. Briels et al. [55] characterized the streamers by their length, radius, charge, and field. They observed that for the same voltage, positive streamers propagate faster and their diameter is approximately 10 % larger than negative streamers. They proposed an empirical law for the velocity and diameter of positive and negative streamers:

$$v = 0.5d^2 [mm^{-1}ns^{-1}] \quad (8)$$

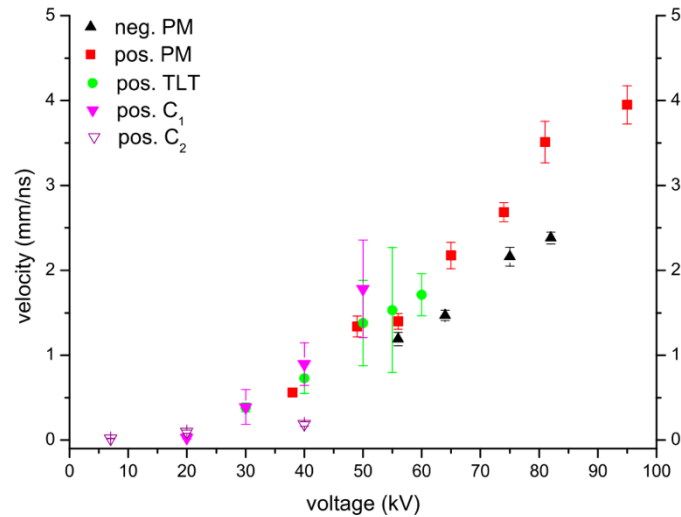


Figure 1. 18 : Velocity of positive and negative streamers in air at atmospheric temperature and pressure as a function of the voltage (gap = 4 cm, $R_c = 15 \mu\text{m}$) [55]

Luque et al [56] modelled streamers of both polarities in plane to plane and point-to-plane geometries. Their results are in agreement with the work of Briels. The velocity of positive streamers was described by the same empirical equation (Equation (8)), without any adjustment parameter. The slower velocity of the negative streamers is believed to be due to the broadening of the streamer head, as a result of the drifting of electrons, which causes a decrease of field at the streamer head.

The average velocity of streamers in air is around 10^6 m/s (Figure 1. 18). With such a velocity, the crossing time in an interval of 5 cm is 50 ns, i.e. small compared to the typical timescale of a lightning pulse of $1.2/50 \mu\text{s}$.

1.VI.C. Propagation length of streamers

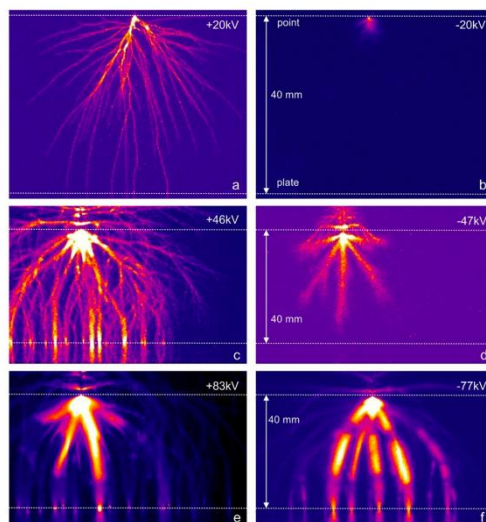


Figure 1. 19 : Time-integrated photographs of positive (left column) and negative (right column) streamers in air in a space of 40 mm in air at 0.1 MPa ($R_c = 15 \mu\text{m}$) [55]

At low voltages, positive and negative discharges in air are remarkably different (Figure 1. 19). Positive discharges initiate at lower voltages than negative discharges.

As the voltage increases, positive streamers in air fill the inter-electrode space, whereas negatives only form a cloud of light around the tip (see Figure 1. 19). In addition, positive discharges are much more branched than the negative one.

1.VI.D. Streamer radius

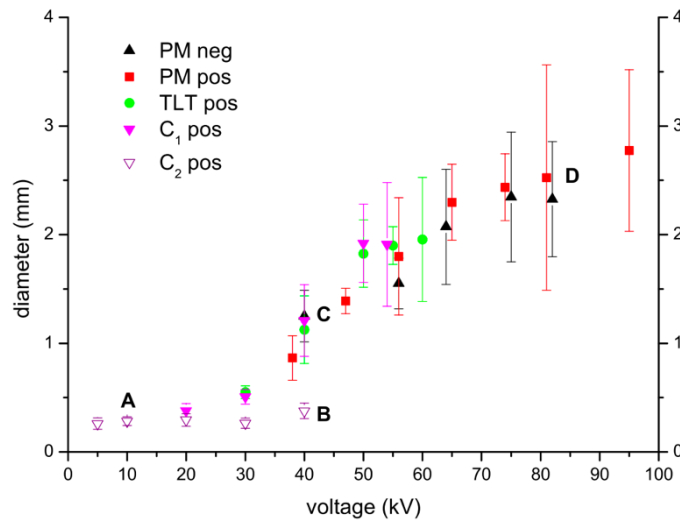


Figure 1. 20 : Diameters of positive and negative streamers in air according to the applied voltage ($P = 0.1 \text{ MPa}$, $R_c = 15 \text{ }\mu\text{m}$ and $d = 40 \text{ mm}$) [55]

Briels et al. [55] measured the variation of the streamer diameter as a function of the voltage. As shown in Figure 1. 20, an increase in voltage causes an increase in the radius of the positive and negative streamers.

1.VI.E. Structure

Two main phases can be distinguished within streamers. The first corresponds to the propagation of the primary streamer from the anode towards the cathode. It propagates as a light spot which gives the light trail shown in streak image of Figure 1. 22. The time scale t , giving a correspondence between the discharge current (Figure 1. 21) and the streak image (Figure 1. 22), is shown by broken lines. The sudden increase in the current pulse corresponds to the arrival of the primary streamer at the cathode with a velocity estimated to about 10^5 m/s . The development of a secondary streamer is observed from the time where the primary streamer arrives at the cathode [57].

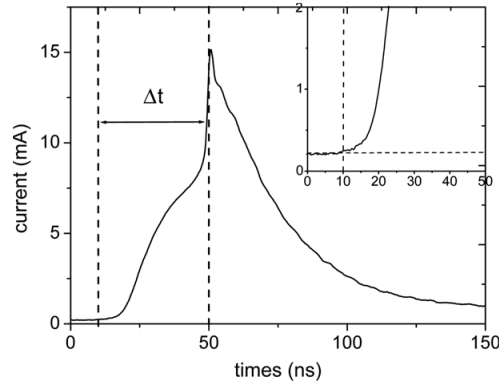


Figure 1. 21 : Pulse form of a corona discharge in positive polarity in dry air under conditions of high continuous voltage ($U = 7.2$ kV, $d = 7$ mm, tip-plane configuration, $P = 0.1$ MPa) [57]

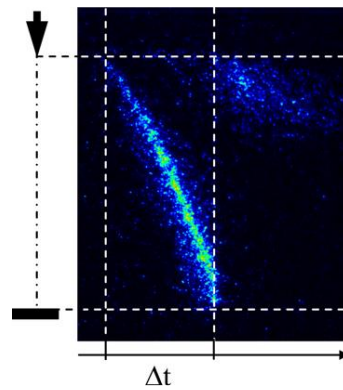


Figure 1. 22 : Image of a streak camera of a positive corona discharge ($U = 7.2$ kV, $d = 7$ mm, tip-plane configuration, $P = 0.1$ MPa) [57]

The development of the secondary streamer limits the current drop just after the current peak. The propagation of primary and secondary streamers create thin ionized channels.

1.VI.F. Transition to breakdown

Streamers, in strongly divergent fields, can propagate to the plane without leading to breakdowns. The process of transition to breakdown is complex, and not well understood [58]. Several authors [59] [60] discuss a gradual increase in temperature, inducing a decrease in density in the channel, and consequently an increase of the reduced E/N field. If E/N exceeds the critical field, a new phase of massive ionization can occur, leading to the transition to the arc.

Two cases are to be distinguished for the streamer:

- In a divergent field (Figure 1. 23), the initiation and propagation of the streamer does not constitute a breakdown criterion. Indeed, the streamer propagates to the plane without leading to breakdown;

- In a homogeneous field, the appearance of a streamer systematically leads to breakdown. In the latter case, the streamer criterion constitutes a valid breakdown criterion.

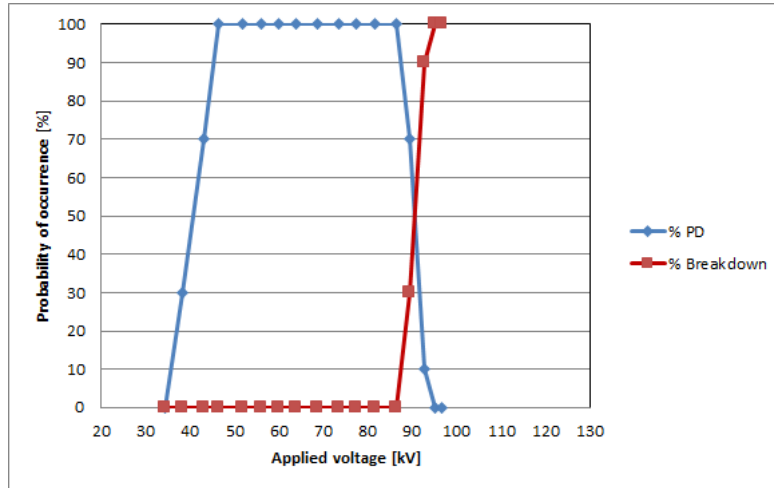


Figure 1.23 : Probability of occurrence in air with a tip radius $r = 0.5$ mm and a gap $d = 10$ cm [58].

1.VI.G. Modelling of streamers

For many years, many research groups have been working on the modelling of streamers, but the tree structure of streamers ("branching") remains complex to simulate.

Several strategies have been adopted, leading to various more or less sophisticated discharge models in the literature:

- behaviour models [56], [61],
- particles models [62]: the gas is studied under its microscopic particulate aspect. The microscopic approach is based on the resolution either direct or by Monte Carlo-type methods of the Boltzmann equation;
- fluids models [63]: the behaviour of gas is studied as a whole as a continuous medium thanks to hydrodynamic equations.

The exhaustive description of these models will not be presented here.

1.VII. *Leader phenomenon*

1.VII.A. Principle

The leader is a "secondary" discharge process that follows the formation of streamers. This occurs due to heating of the streamer channel by electrons. Unlike the case of Townsend and streamer mechanisms, the leader mechanism leads to the formation of a high temperature channel ($T > 1500$ K),

and therefore very conductive. The mean E_{ld} field along the leader channel can reach values of the order of 1 kV/cm ($E_{ld} \ll E_{cr}$). Its formation strongly depends on the gas nature. In air, leaders appear for high values of the product pressure*distance ($Pd > 100$ cm.bar), while in SF₆ the threshold is $Pd > 1$ cm.bar [64].

Table 1. 4 : Classification of breakdown mechanism in terms of pd values in air [47]

$10^{-4} < pd < 0.3$ bar.cm	Townsend's breakdown with a predominant secondary cathode emission. Typical discharge regime of glow discharges.
$0.3 < pd < 5$ bar.cm	Townsend and streamer breakdown can be observed depending on conditions (electrode geometry, applied voltage, etc.).
$5 < pd < 100$ bar.cm	The Townsend theory fails, streamer breakdown dominates. Faster breakdown process, at much lower fields than ones predicted by the Paschen's curve. Secondary cathode emission can be ignored
$pd > 100$ bar.cm	Leader breakdown mechanism. At atmospheric pressure, the leader mechanism becomes predominant in gaps ≥ 1 m.

Table 1. 5 : Classification of breakdown mechanism in terms of pd values in SF₆ [65]

$pd \leq 0.3$ bar.cm	Streamer
$pd \geq 1$ bar.cm	Leader channel

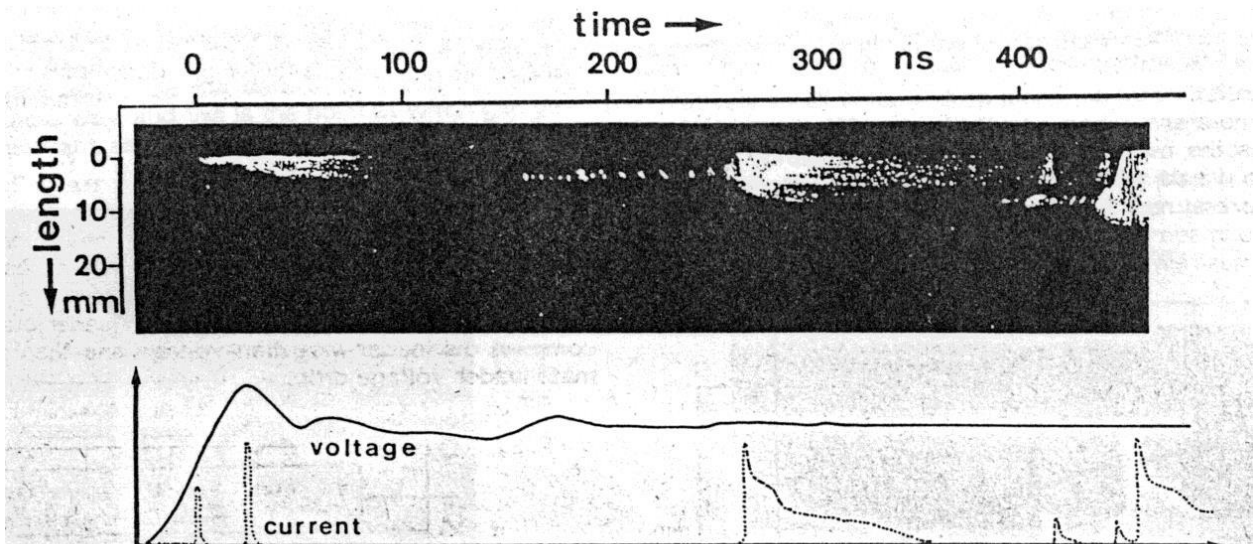


Figure 1. 24 : Development of a leader in SF₆ ($P = 0.15$ MPa, $U = 200$ kV, $R_c = 1$ mm). Scanning camera image (high), applied voltage and current associated with leader steps (low) [66].

In non-uniform electrode geometry, the local maximum field may be greater than the critical field. This allows the development of an electronic avalanche confined to the strong field area (corona).

Under certain conditions (high pressure, electronegative gas), a discharge can however propagate further, while the minimum field is much lower than the critical field. In this case, the discharge propagates in successive steps, according to the following sequence [64], [66] Figure 1. 24:

- Development of a corona of streamers in the strong field area. By concentration of the current in a small area of the corona, heating of the gas leading to the formation of a first leader channel;
- Rapid development of an ionization zone at the head of this leader channel, accompanied by a brief re-illumination of the channel and a current peak;
- Pause time τ at the end of which the ionization zone turns into a new section of the leader channel, and creates a new ionization zone in front of the discharge.

Studies show that the leader channel is strongly heated, its temperature being higher than the dissociation temperature of the gas. In SF₆ this implies $T \approx 3000$ K. This strongly conductive channel behaves like a “virtual electrode” at the end of which a corona is formed at every step. Compared to the streamer, the leader presents a single channel, much warmer and conductive. The average breakdown field can then be much smaller than the critical field of the gas.

The time interval between two leader steps (that is, the time between the formation of a corona and the completion of the transition from streamer to leader) can be divided into a "delay time t_l ", after which the leader becomes observable, and a " t_{ls} leader propagation time". The “leader propagation time” is the total formation of the leader which can be subdivided into “time steps t_{ps} ”, characteristics of the extensions of the leaders (Figure 1. 25). When the leader propagates to the ground plane, breakdown occurs systematically.

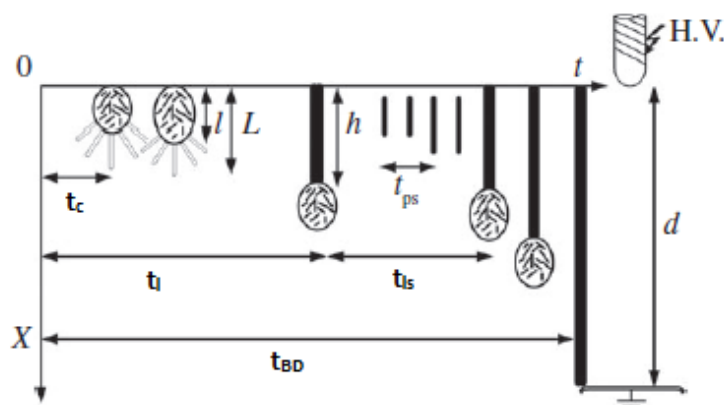


Figure 1. 25 : Schematic diagram of leader development. t_c , time of formation of the first corona; t_l , leader training time; t_{ps} , progression time of the precursor; t_{ls} , leader training time; t_{BD} , breakdown time. Adapted from [121].

1.VII.B. Propagation velocity of leaders

Seeger et al. [67] measured leader propagation velocity in SF₆ at around 10⁴ m/s. These results are confirmed by the studies of Chatterton et al. [68] who measured leader propagation velocity in various electronegative gases, between 10⁴ and 10⁵ m/s.

1.VIII. *Additional parameters influencing electric discharges and breakdown properties in applications*

1.VIII.A. Electrode geometry and surface roughness

1.VIII.A.i. Corona stabilisation process in divergent fields

The influence of geometry will be explained by distinguishing two typical cases: quasi-homogeneous and divergent field. One way to measure the distortion of the electric field is to express the “field utilization” factor $z = \frac{E_{average}}{E_{maximum}}$ or “enhancement factor” $\eta = \frac{1}{z}$.

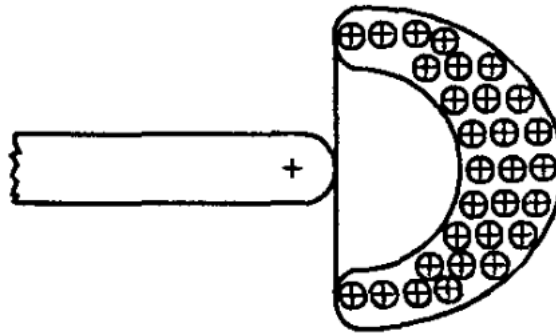


Figure 1. 26 : Charge distribution of corona effect [69]

In divergent field (tip-plane, η large), the strengthening of the electric field leads to a corona discharge near the tip. The space-charge (Figure 1. 26) reduces the maximum field near the electrode, and thus an increased voltage is required to initiate the leader process, and the breakdown voltage is raised [69]. This effect called “corona stabilization” only exists in strongly divergent geometries.

In strongly divergent electric field, the corona threshold voltage is significantly lower than the breakdown voltage. The corona threshold voltage always increases linearly with pressure (Figure 1. 27), but the breakdown voltage follows another variation. It increases with pressure before decreasing until reaching the threshold voltage corona effect for a pressure value called critical pressure. The breakdown voltage then merges with the corona threshold voltage and increases again with the pressure.

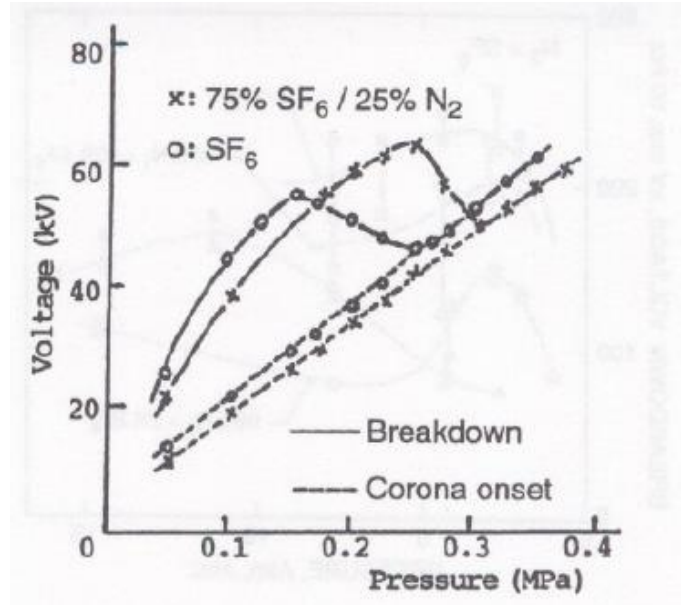


Figure 1. 27 : Voltage versus pressure characteristic of SF_6 and a 75% SF_6 -25% N_2 mixture for a point-plane gap and lighting impulse (1.2/50 μs) [122]

1.VIII.A.ii. Surface condition of the electrodes

The surface condition of electrodes especially that of the cathode, can locally modify the electric field and therefore the breakdown voltage of the gas. Many studies have been carried out on this subject in different gases.

In air, at atmospheric pressure, Feet et al [70] demonstrated that for quasi-uniform and non-uniform fields, the microscopic field enhancement due to surface roughness has a very limited effect on the breakdown voltage, even at high degrees of surface roughness ($> 200 \mu m$). In SF_6 , in a uniform field, with electrodes of maximum roughness R_{max} , the breakdown voltage will follow the Paschen curve as long as the product $P.R_{max}$ is less than 40 bar. μm [71].

1.VIII.B. Applied voltage wave shape

Under uniform field, the presence of seed electrons is necessary for the discharge to start. The probability that a seed electron is present in the high field region is equal to 1 for long duration DC or AC voltages, but lower during an impulse voltage of small duration. The time between the application of voltage and the moment a seed electron appears is called the “statistical delay time”. The application of a field greater than the critical field will not systematically lead to breakdown [72]. Thus, under a short duration impulse the breakdown voltage gets a statistical character, and we can determine the voltage level corresponding to some breakdown probability (usually 5%, 10% or 50%).

In an inhomogeneous field, the phenomenon is more complex and two cases must be distinguished:

- For low pressures when corona stabilization is effective, a pulsed voltage allows less time for the space charge to form. The stabilization effect is lower, which leads to a reduced breakdown voltage compared to the alternating or DC wave.
- Beyond a critical pressure, breakdown occurs systematically if the voltage is sufficient and if a seed electron is present: the breakdown voltage is then a statistical quantity and is larger under a pulse wave [65].

1.VIII.C. Impurities in the gas

The influence of impurities (mainly humidity) on the breakdown voltage strongly depends on the geometry of the electrodes, on the nature and on the pressure of the gases [73].

In air, the influence of humidity on dielectric strength is small. For relative humidity values below 80 %, the breakdown voltage increases slightly with increasing humidity [74]. The presence of water molecules, which are denser than gas, slows down the avalanche phenomenon. For SF₆, humidity favors the leader mechanism, and above all it plays an important role on the nature of the decomposition by-products of SF₆. Under alternating voltage, it favours the appearance of a stabilized corona [75].

1.IX. *Conclusions and outline of thesis*

The development of alternative gases to SF₆ is a major challenge for reducing the impact of high voltage electrical installations on the environment. Hydrofluoroolefin constitutes a promising replacement solution for medium voltage systems, due to its low environmental impact, its non-toxicity, and its availability.

As discussed in this chapter, a few studies already described the dielectric strength and the basic characteristics of the discharges in the HFO in strongly divergent fields. The degradation of HFO due to discharges was observed, but a negligible influence on breakdown values in divergent fields was reported. To design and optimize the use of HFO in practical insulations, it is necessary to much better characterize and understand the behaviour of discharges. In the context of an application to medium voltage gas-insulated switchgear, several very specific characteristics of this application are scarcely (or not at all) represented in the literature, and therefore require significant additional experimental studies:

- The behavior of the HFO when subjected to a strong quasi-uniform electric field;
- The influence of electrode geometry and pressure on the behavior of the HFO;

Chapter 1: Context of the study: gaseous insulation in MV devices, and breakdown physical processes

- The effect of degradation due to discharges on the dielectric strength of the HFO, and the main parameters relevant for the gas degradation.

Chapter 2 describes the experimental approach implemented, via the presentation of the experimental device and the physical diagnostics deployed to characterize the discharges generated. The methods used to evaluate the breakdown voltage in the application context are also presented.

Chapter 3 corresponds to the experimental characterization of the physical properties of pre-discharges in a strongly divergent field.

- The fundamental characteristics of the pre-discharges generated in the HFO by a pulse wave are compared to that of air and SF₆ as a function of pressure, applied voltage and electrode geometry. The different breakdown processes in the HFO (streamer and leaders) will be evoked to understand its behavior. The properties of leaders will be evaluated by high speed images, streak recording, and optical emission spectroscopy. Electrical properties will be determined by time-resolved current and voltage measurements, to describe leaders as they propagate.
- The study of “breakdown modes”, either controlled by initiation or propagation depending on geometry, and leading to rather different influence of pressure;
- The proposition of first design rules under strongly divergent field for the application in MV devices.

Chapter 4 is devoted to the dielectric properties of the HFO under conditions closer to those of the application, namely a quasi-homogeneous field.

- A significant degradation of the HFO properties with breakdown will be demonstrated in a quasi-homogeneous field. The evolution of the breakdown voltage and the delay time in a homogeneous field will be studied under different pressure and waveform conditions, and gap geometry.
- The parameters of the HFO degradation will be studied according to the energy injected into the discharge, highlighting the influence of the dust deposit formed on the electrodes. Physico-chemical measurements of the degraded gas and dust will provide information on the degradation of HFO.
- A conclusion, taking up the results of chapters 3 and 4, will allow us to discuss the design rules applicable in MV with the HFO.

The conclusion will include a summary of the main results obtained, discuss the capacity of HFO to replace SF₆, and present perspectives associated with this work.

CHAPTER 2: Materials and methods

2.I. Gases

HFO-1234ze(E) or trans-1,3,3,3-tetrafluoropropene comes from the company Inventec performance chemicals with a purity greater than 99.5% and a water content of less than 50 ppm. Sulfur hexafluoride, SF₆, comes from the same company with a purity greater than 99.9%. The air used comes from Air Liquide with a purity greater than 99.999%.

2.II. Description of the test cell

The test cell has been designed to perform measurements up to 0.3 MPa absolute pressure and 200 kV maximum voltage. The cell (Figure 2. 1) consists of a cylindrical PVC structure, with two quartz windows to allow visualization of the discharges. For filling the cell, the filling circuit is different from the pumping circuit to avoid polluting the cell with discharge by-products during filling.

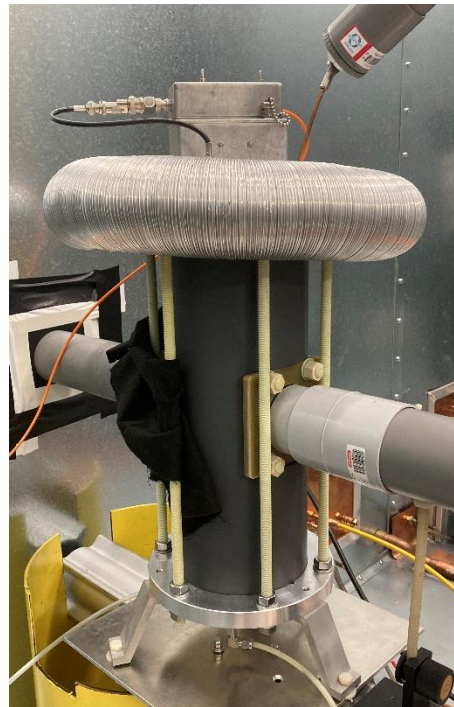
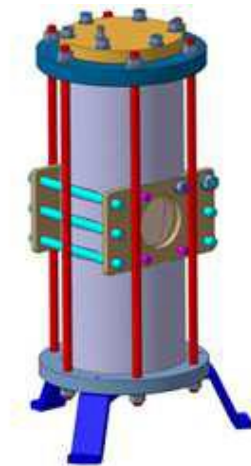


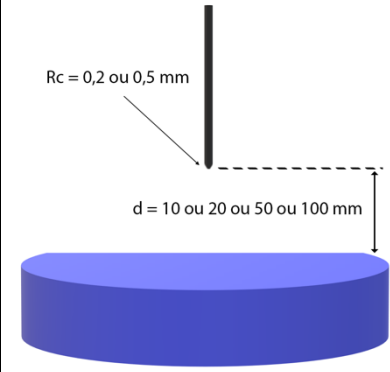
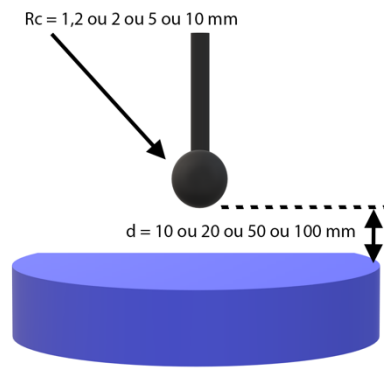
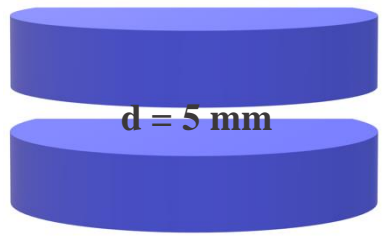
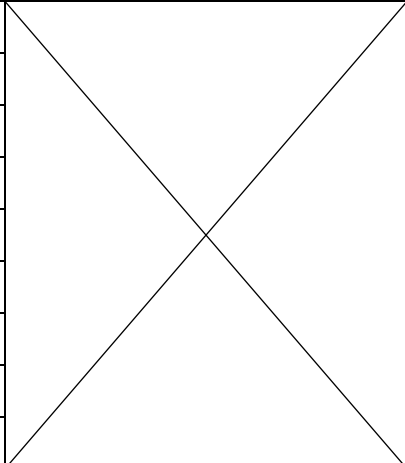
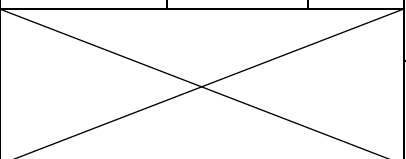
Figure 2. 1 : Test cell for measurements up to 0.3 MPa and 200 kV maximum

2.III. Electrode configurations

The inhomogeneous fields ($\eta > 10$) are chosen for a more convenient study of pre-discharge phenomena with low statistical delays, and for studying the worst breakdown conditions in MV devices (occurring e.g. at triple point). Weakly heterogeneous fields ($\eta < 10$) are chosen to study the behaviour

of the gas under conditions close to those present in MV devices. The electrode configurations (Table 2. 1) consist of an upper electrode connected to high voltage. This electrode shape was changed depending on the experiments carried out. It can be a point electrode (radius of curvature: $R_c = 0.2$ or 0.5 mm) or a sphere ($R_c = 1.2$ mm, 2 mm, 5 mm or 10 mm). The material of these electrodes is stainless steel. The lower electrode is a 15 cm diameter aluminium disc connected to ground.

Table 2. 1: Representation of the different geometries studied

Strongly inhomogeneous			Weakly inhomogeneous			Homogeneous
						
R_c (mm)	d (mm)	η	R_c (mm)	d (mm)	η	Rogowski profile, $\eta = 1,1$
0,2	10	28	1,2	10	7	
	50	90		50	21	
0,5	10	13	2	50	14	
	20	22	3,5	10	3,5	
	50	40	5	10	2,5	
	100	64		20	4	
			10	50	7	
				10	1,7	
				20	2,5	

A characteristic parameter of the studied geometry is the enhancement factor of the field $\eta = \frac{E_{max}}{E_{moy}}$. The closer η is to 1, the more homogeneous the field. In order to characterize this parameter, simulations with the ComsolTM software are carried out for the various geometries studied in order to calculate the maximum field E_{max} at the tip electrode. Simulations were also carried out with another electromagnetism software (GetDP) [76], [77]

Figure 2. 2 is an example of simulation of the maximum electric field for a geometry with a radius of curvature (rod-plane with $R_c = 0.5$ mm), an applied voltage of 1 V and an inter-electrode distance ($d = 10$ mm). In these simulations, the maximum values of the electric field are concentrated

around the electrode brought to the high voltage, i.e. the upper electrode. It is important to consider a mesh domain at least three times greater than the inter-electrode distance to obtain a correct result.

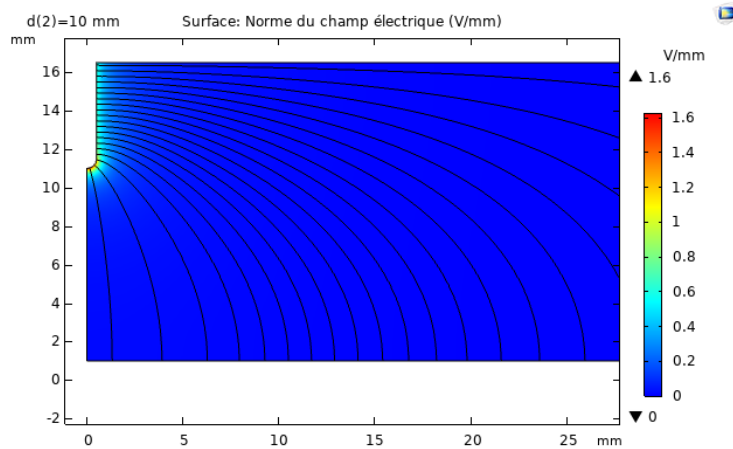


Figure 2. 2 : Example of modelling of the field for a needle with a radius of curvature of 0.5 mm and an inter-electrode distance of 10 mm for an applied voltage of 1 V

Figure 2. 3 shows the distribution of the voltage and Figure 2. 4 shows the distribution of the electric field with a maximum of 1.6 V/mm. To obtain a value of the maximum field closest to reality, the whole electrode support (Figure 2. 5) was also modelled. In this case, the value of the maximum field at 1 V is 1.32 V/mm instead of 1.6 V/mm with a simplified configuration (rod-plane in Figure 2. 2, variation of 18%). Therefore, all calculations of the maximum field were obtained while respecting the real electrode configuration of the experiment.

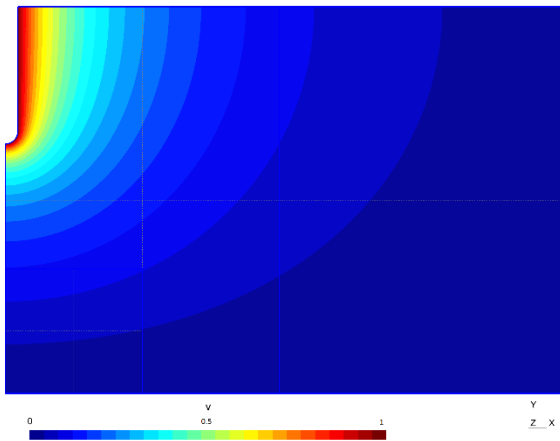


Figure 2. 3 : Electrical potentiel obtained ($R_c = 0.5 \text{ mm}$ and $d = 50 \text{ mm}$)

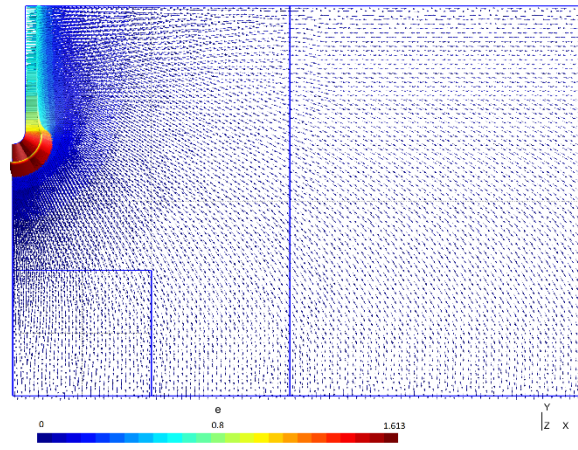


Figure 2. 4 : Example of modelling of the maximum field E_{max} (V/mm) ($R_c = 0.5 \text{ mm}$ and $d = 50 \text{ mm}$)

Figure 2. 6 represents the field enhancement factor η for the different geometries studied. The field reinforcement factor η varies from 90 for the most inhomogeneous geometries to 1.5 for the most homogeneous geometries.

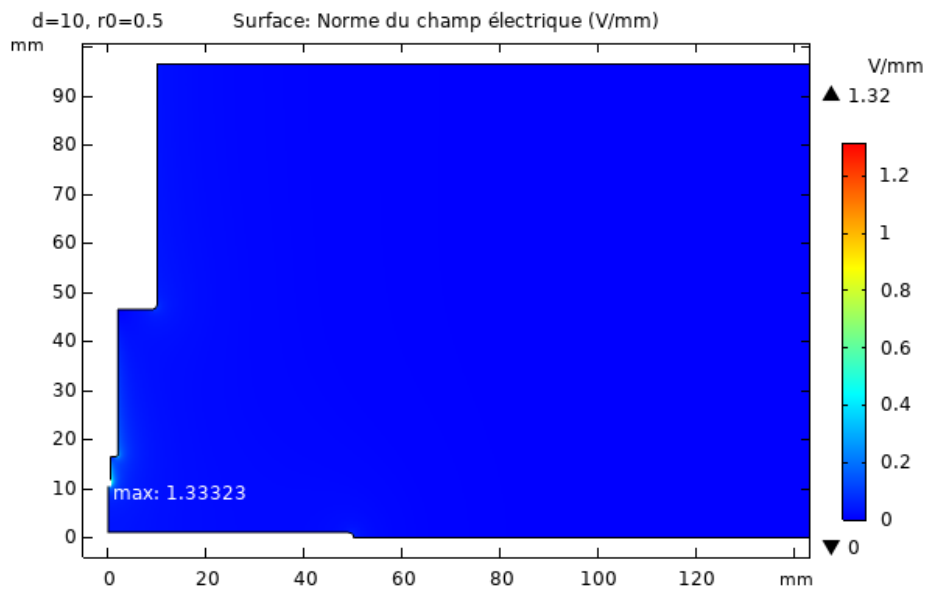


Figure 2. 5 : Calculation of the maximum field in the real configuration of the study (point of radius of curvature 0.5 mm and inter-electrode distance of 10 mm)

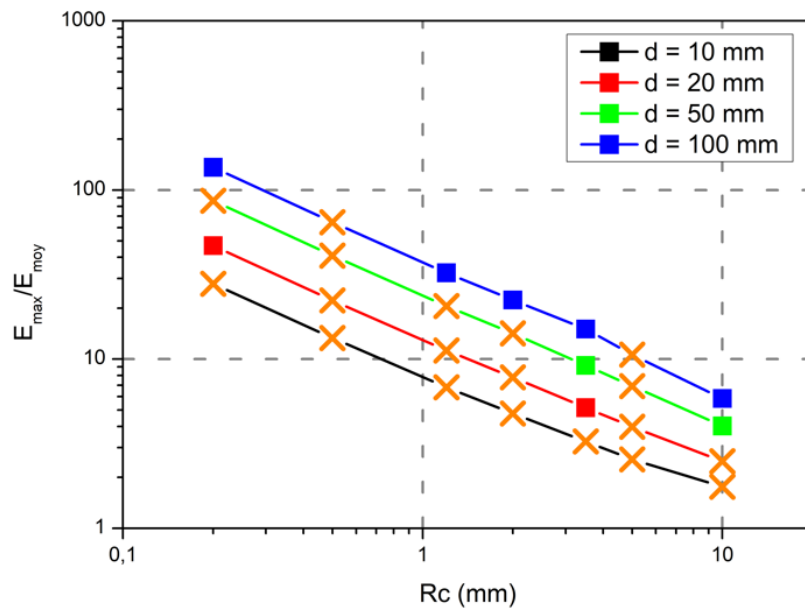


Figure 2. 6 : Field enhancement factor η for the different geometries studied

2.IV. High voltage generators

The voltages used during the tests are DC or pulse, each type requiring a specific generator.

2.IV.A. Direct voltage

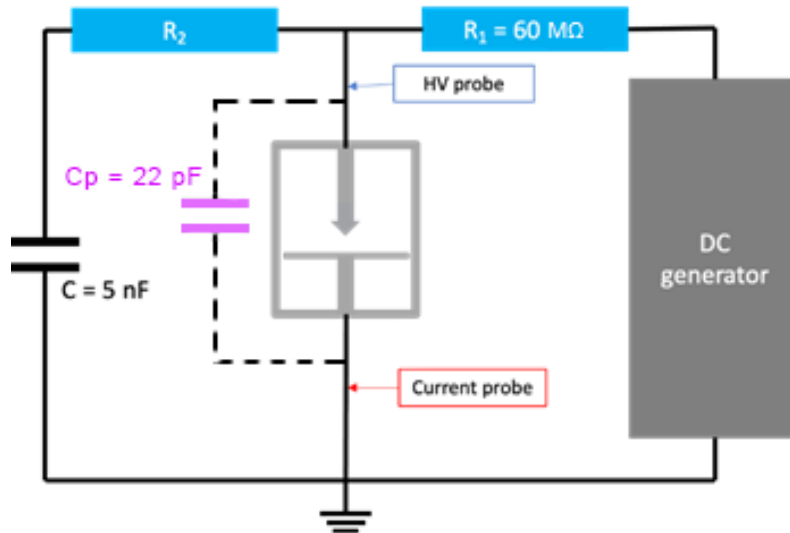


Figure 2. 7 : Schematic representation of the configuration used for the DC breakdown measurements

DC voltage experiments were carried out to characterize the degradation of the gas as a function of the energy injected (chapter 4). Time-resolved arc voltage is measured with a NorthStar PVM-5 high voltage probe (60 kV, 120 MHz). The breakdown current is measured at ground level with a current probe (Stangenes model N°0.5-0.01, risetime = 20 ns). In order to modify the energy injected into the discharge, the non-inductive carbon resistor R_2 (10 Ω to 1 k Ω) was modified to obtain the different energies. Voltage is applied with a ramp of 500V/s. When measurements are performed without R_2 and C , the energy dissipated into the arc is limited by the charge of the parasitic capacitance C_p of the test cell and connections. The measured value of this capacitance C_p is 22 pF.

2.IV.B. Impulse voltage

The setup (see Figure 2. 9) includes a Marx pulse generator, voltage divider, series resistor, test cell, oscilloscope, intensified camera, photomultiplier, and computer. These test devices are placed in a Faraday cage and controlled by a control desk outside the cage.



Figure 2. 8 : Photograph of the test system

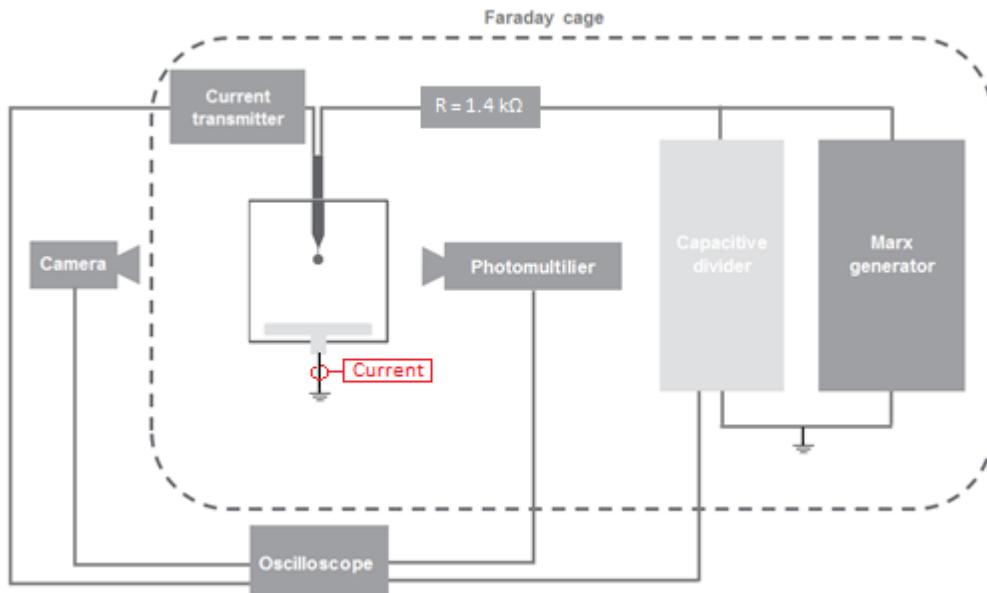


Figure 2. 9 : Schematic representation of the configuration used for the impulse breakdown measurements

A pulse voltage is characterized by its amplitude, its rise time t_m (time taken for the signal to go from 10% to 90% of its maximum value) and its fall time t_d (time taken for the signal to decrease from its maximum value down to 50% of this, see Figure 2. 10).

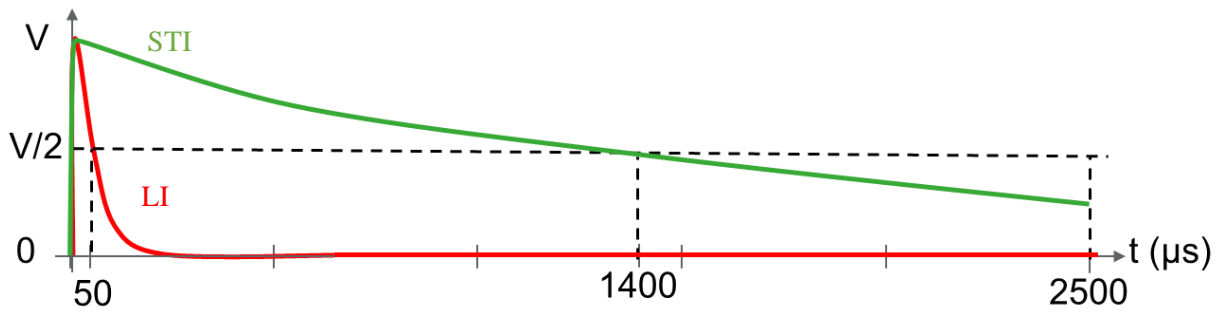


Figure 2.10 : Characteristic parameters of a pulse wave

A Marx generator is used to obtain this type of voltage; it is a set of resistors, spark gaps and capacitors arranged in 5 stages such that the capacitors are charged in parallel under a maximum voltage of 100 kV, and are connected in series at the desired instant thanks to spark gaps: the available maximum voltage is then 500 kV, neglecting the losses.

The series and parallel resistors respectively determine the rise time and the fall time of the voltage wave. Their values were chosen in order to obtain two types of impulse waves during the experiments. In the first case, we used a standard lightning shock wave LI ($t_m = 1.2 \mu\text{s}$, $t_d = 50 \mu\text{s}$) in accordance with the standards for testing electrical equipment. The second wave used has a shorter rise time and a longer fall time, to get a more constant voltage during the initiation and propagation of the discharge STI ($t_m = 0.8 \mu\text{s}$; $t_d = 1400 \mu\text{s}$).

The voltage is measured via a very high voltage capacitive divider. For impulse waves, this is a capacitive divider ($C_{\text{measure}} = 150 \text{ pF}$) in parallel with the cell. The electrical signals are recorded with a Tektronix MDO 3054 digital oscilloscope with a bandwidth of 500 MHz and a high-velocity sampling rate of 2.5 G/s. The current associated with the generation and propagation of gas discharge phenomena is measured on the tip electrode side using an optical fiber coupling system made in the laboratory. Its bandwidth is 100 Mhz. The transient currents are measured across a 5Ω resistance in series with the electrode and the system is protected against over-currents due to breakdowns by spark gaps connected in parallel.

Current measurements on the high voltage side offer many advantages over measurements made at ground level. In particular, during the rising edge of the voltage, only the charging current of the point extremity is measured (a few mA). Provided this current is smaller than discharge current, discharges (e.g. streamers) can be detected even during the voltage rise.

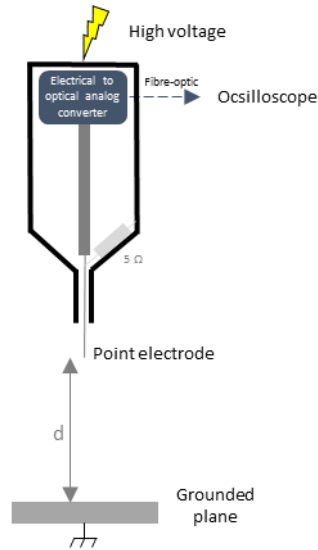


Figure 2. 11 : Discharge current measuring device on the high voltage side

2.IV.C. Breakdown voltage measurement procedures

The purpose of these measurements is to obtain comparative breakdown voltage values for a large range of configurations. Breakdown voltage varies as a function of several parameters such as voltage polarity, geometry of electrodes, distance between electrode, etc. The measurements usually show some scatter, and it is necessary to perform several measurements for each configuration, in order to appreciate the statistical scatter.

2.IV.C.i. Method 1: Experimental procedure to determine the probability of occurrence of PD and breakdown: “multiple steps method”.

In addition to the breakdown voltage measurements, the initiation voltage of pre-disruptive phenomena is characteristic of gases. To obtain this information, the following method has been applied. At a fixed voltage 15 voltage shots are taken and the number of pre-discharges and/or breakdowns are counted. Thus, the probability of pre-discharges and breakdowns occurrence is obtained. Then the voltage is increased by 5 kV steps, the procedure stops when the breakdown probability is 100%. According to the standard CEI-60060, this procedure corresponds to the “class 1” test method. With this method any probability of breakdown can be determined (1% to 99%).

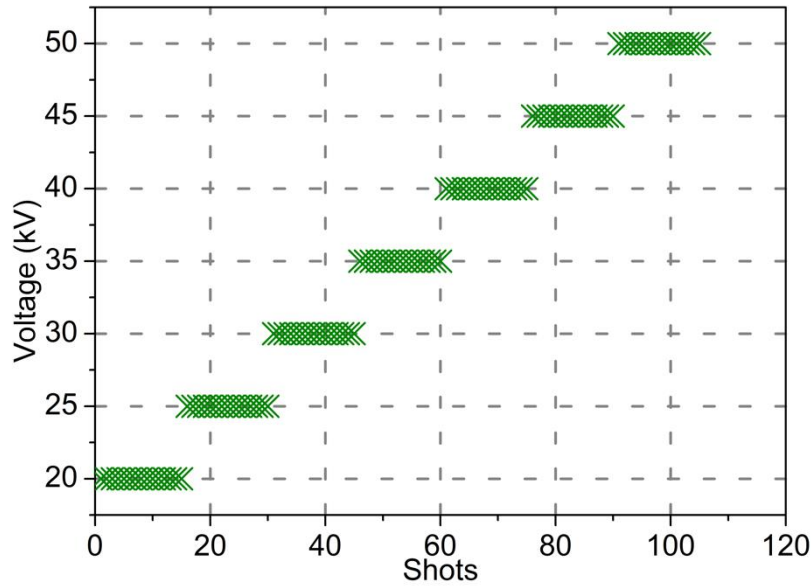


Figure 2.12 : Experimental “multiple steps” procedure to determine the probability of occurrence of PD and breakdown

2.IV.C.ii. Method 2: Experimental procedure for breakdown measurements: “up and down” method

Several different procedures can be used to measure breakdown voltages. In our investigations, the procedure described below is used. It provides a good repeatability of measurements, and it’s close to the industrial procedure used for validation of apparatus.

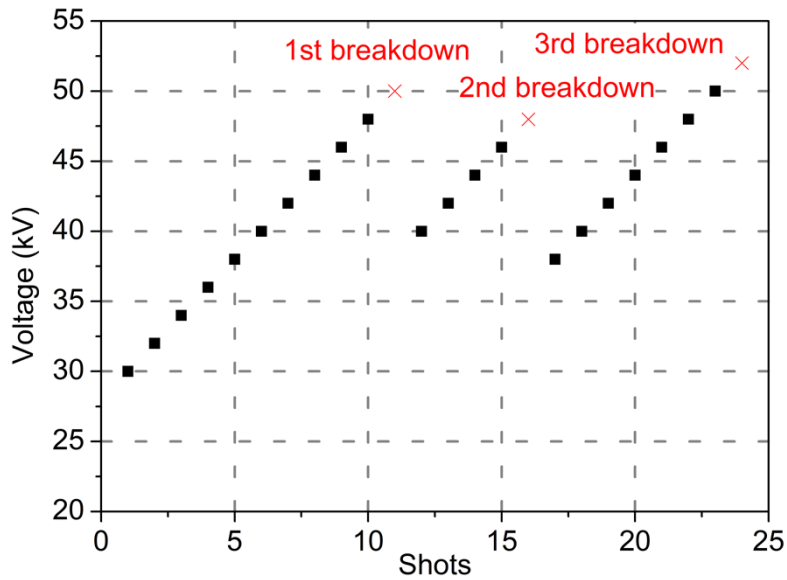


Figure 2.13 : Experimental procedure for breakdown measurements

The measurement starts from 15 kV (i.e. the minimum value which can be applied with our Marx generator). The applied voltage is raised by 2 kV steps until breakdown (Figure 2.13). The time between each shot is fixed to 30 s. After breakdown, the voltage is lowered by 10 kV and raised again up to breakdown. This process was repeated 15 times for each sample. According to CEi-60060, this

procedure corresponds to “class 2” methods. With this method the probability of breakdown is estimated at around 25%.

2.V. *Optical measurements*

2.V.A. Measurement of photo-currents

The light emitted during the propagation of the discharge is measured by a photomultiplier (RTC 56AVP) placed in front of a window of the test cell and connected to a $50\ \Omega$ input of the oscilloscope. This photomultiplier detects light with a wavelength between 300 nm and 600 nm. An adjustable diaphragm makes it possible to limit the quantity of light received below the saturation threshold of the photomultiplier.

2.V.B. Intensified camera

To visualize the discharges, a high-speed gated image intensifier (Hamamatsu C9546-03) was used to capture a "snapshot" of the high velocity phenomena occurring in extremely short time frames, by means of a gate operation (down to 3 ns). The spectral response of the intensifier is between 200 and 800 nm. The intensifier is coupled to a Hamamatsu C11440 digital camera in order to obtain an image. The lens used has a focal length of 50 mm.

2.V.C. Measurements of streamers and leader propagation velocity

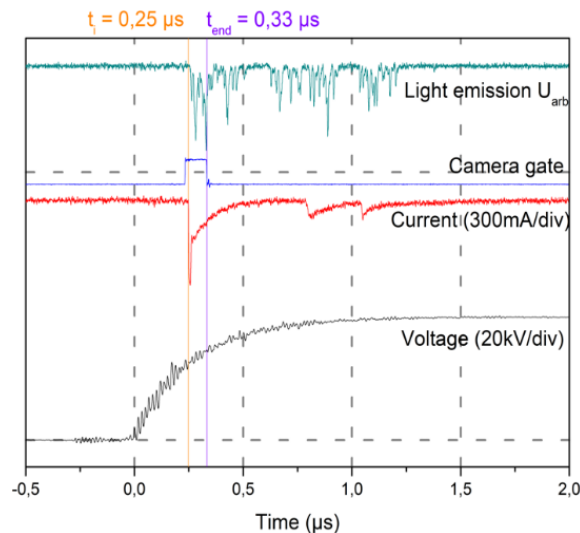


Figure 2. 14 : Characteristic measurements of voltage, current, camera signal and light emission

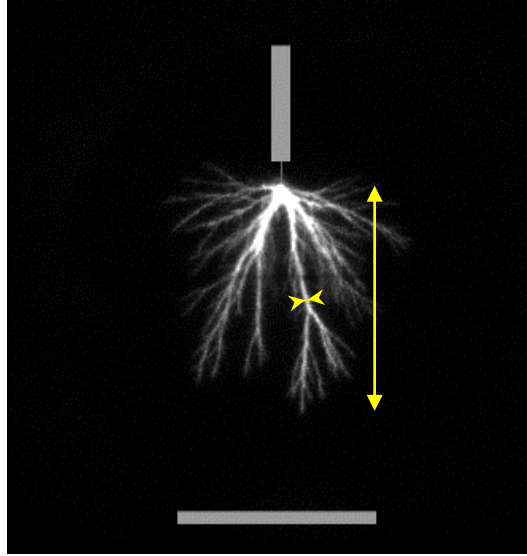


Figure 2. 15 : Image of a streamer being propagated in the air ($Rc = 0,5 \text{ mm}$ and $d = 50 \text{ mm}$) allowing to measure the length of propagation l_p

From the measurements of photo-currents and currents coupled to imaging, a propagation velocity of the pre-discharges is obtained. For this, the voltage, current, camera and photo-current signals are synchronized with a resolution less than 1 ns in order to correct measurements from experimental delays in cables, photomultiplier, and current probe. Thus in Figure 2. 14, the propagation time of the phenomenon is obtained ($t_i - t_{end}$). With the camera, the corresponding propagation length l_p of the phenomenon is extracted (Figure 2. 15). Then the velocity is simply calculated: $v = \frac{l_p}{t_i - t_{end}}$. From these images, the diameter D of the streamers or leaders is also measurable.

2.V.D. Spectroscopic measurements

The light emitted by the discharge is recorded by a 2D CCD detector. This light is analyzed by an Acton Research Corporation spectrograph of the Spectra-Pro 300i model with a focal length of 300 mm and an $f/4$ aperture. This spectrograph is equipped with three gratings: one of 150 lines/mm and two of 1200 lines/mm.

Table 2. 2 : Characteristics of the arrays of the ARC spectrograph

Network (lines/mm)	Spectral window (mm)	Blaze (nm)	Dispersion (nm/pixels)
150	260	500	0.507
1200	33	300	0.065
1200	33	750	0.065

The photo-detector is cooled with liquid nitrogen, and background noise is minimal when the temperature is around -130°C . Geographical segmentation of the discharge channel is carried out using the CCD control software, which allows several areas of the visualized space to be recorded. It is thus

possible, for example, to define 7 lines of five pixels in width. These lines are adjacent and cover an area centered on the fault. 2D CCD has a definition of 512*512 pixels. The device function (spectrograph + CCD) can be described by a Gaussian of width at half height equal to 0.12 nm for gratings at 1200 lines/mm.

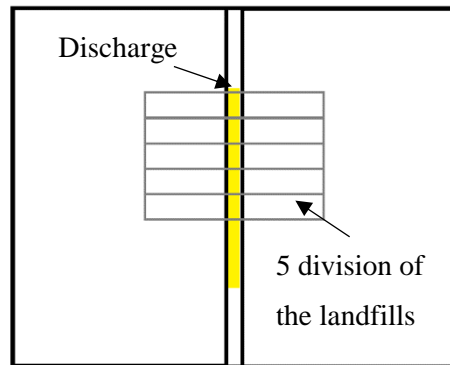


Figure 2. 16 : Representation of the segmentation of the 2D CCD

In order to obtain usable electric discharge spectra, it is necessary to accumulate light on a high number of breakdowns. In practice, the CCD is opened for 300 seconds during which about fifty voltage pulses are applied. The conditions are chosen to systematically trigger either a leader discharge or a streamer. For the breakdown, an acquisition of 20 seconds on a single breakdown is carried out.

Chapter 3: Breakdown modes, and characterisation of pre-disruptive phenomena in HFO in divergent field

This chapter presents the different discharge regimes and breakdown modes recorded in HFO in a highly inhomogeneous field. Their phenomenology will be described and discussed (pre-breakdown mechanism, propagation velocity, stopping length, etc...). In identical conditions, experiments will be also carried out in SF₆ to highlight the main differences between these electronegative gases. Although this work is mainly focused on HFO, some results will be also obtained in air, since this gas may also constitute an alternative to SF₆ for medium voltage insulation. Lastly, the results obtained in a strongly divergent field will be analysed in order to derive practical consequences for the design of MV switchgear insulation with HFO.

3.I. Definitions of “propagation” and “initiation”-controlled breakdown

3.I.A. Introduction

Figure 3. 1 shows an example of an oscillogram obtained during a breakdown experiment, in a strongly divergent field. The three curves represent the applied voltage (black), the discharge current (blue) and the light emitted by the discharge (dark cyan). Current and light appear as negative signals due to measurement systems (photomultiplier, and current probe).

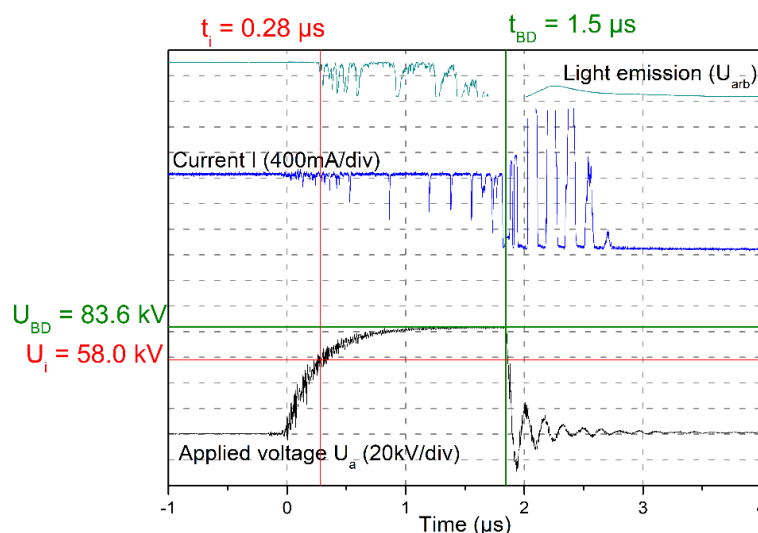


Figure 3. 1 : Oscillogram of an experiment leading to breakdown in HFO ($R_c = 0.5 \text{ mm}$, $d = 50 \text{ mm}$, $P = 0.1 \text{ MPa}$)

From this recording, four types of information are extracted:

- The instantaneous initiation voltage U_i : it corresponds to the first peak of light (and current) emitted by the pre-discharge;
- The breakdown voltage U_{BD} : it is obtained just before the applied voltage drops suddenly at the moment of breakdown;
- The initiation delay t_i : this is the delay for the appearance of a first discharge. It is measured at the time of the first current or light peak. The origin of time is arbitrarily taken at the onset of voltage rise;
- The breakdown delay t_{BD} : it is taken at the moment when the voltage drops suddenly.

Two breakdown modes have been identified in HFO depending on the geometry. For very divergent fields, light emission as well as current peaks are observed without systematically leading to breakdown (Figure 3. 2). These phenomena constitute partial discharges (PDs). When the applied voltage is increased, the amount of light and current pulses is larger, and the discharge propagation lengths increases until the plane electrode at the breakdown instant (Figure 3. 3).

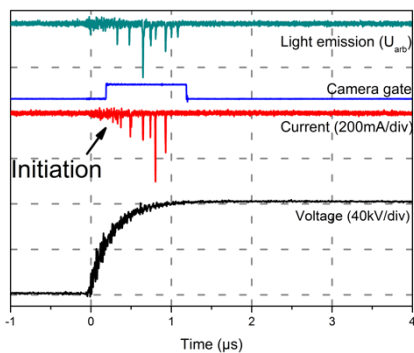
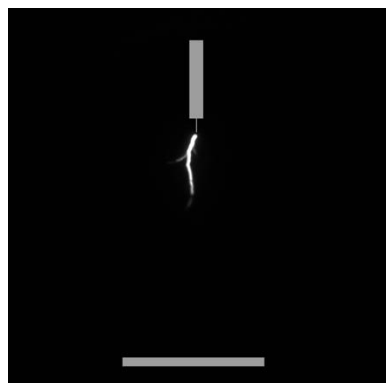


Figure 3. 2 : Leader not leading to breakdown in HFO ($U_a = 86 \text{ kV}$, $R_c = 0.2 \text{ mm}$, $d = 50 \text{ mm}$, $P = 0.1 \text{ MPa}$)

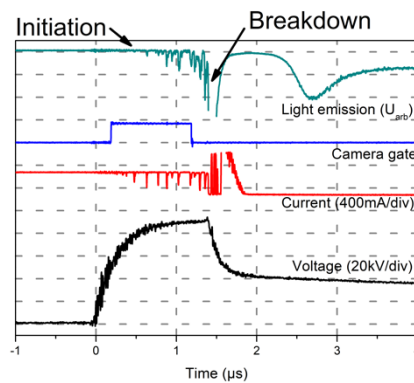
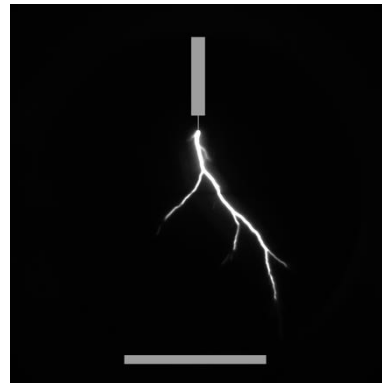


Figure 3. 3 : Leader leading to breakdown in HFO ($U_a = 94 \text{ kV}$, $R_c = 0.2 \text{ mm}$, $d = 50 \text{ mm}$, $P = 0.1 \text{ MPa}$)

On the other hand, when the field distribution is more homogeneous, no phenomenon of pre-discharges preliminary to the breakdown is visible at voltage lower than U_{BD} . Every pre-breakdown phenomenon initiated propagate very quickly to breakdown. It is very difficult to obtain an image of pre-breakdown phenomenon due to the very short time between initiation and breakdown (≈ 200 ns).

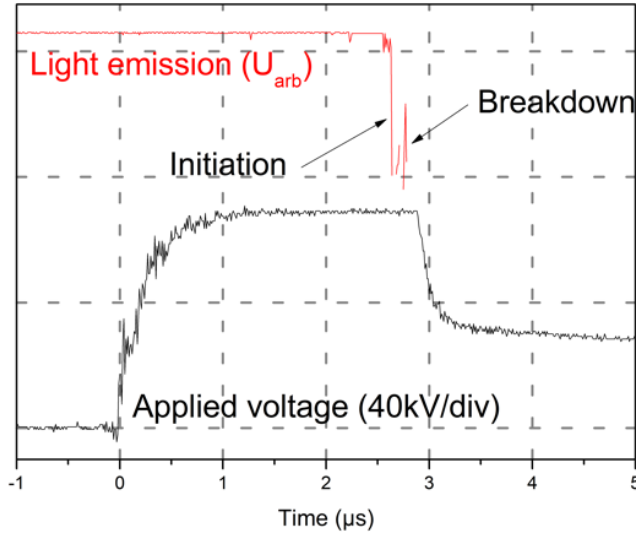


Figure 3. 4 : Breakdown in degraded HFO ($U_a = 73$ kV, $R_c = 5$ mm, $d = 10$ mm, $P = 0.1$ MPa)

These two different breakdown modes have been observed in HFO in a variety of conditions (electrode geometry and pressure), and will be discussed more thoroughly in chapters 3 and 4. Since these modes will be frequently used in the following text to classify experiments into two categories, we will summarize their main features in the next section.

3.I.B. Discharge initiation and breakdown initiation frequency

Depending on the enhancement field factor (which depends on R_c and d), a statistical frequency of occurrence of pre-discharges and breakdowns can be determined. From the current and voltage measurements (Figure 3. 1), the initiation voltage U_i and the breakdown voltage U_{BD} are measured in order to plot the occurrence probability frequency graphs, using the “multiple steps” method (see 2.IV.C.i p.42)

In a very inhomogeneous field (Figure 3. 5 for $\eta = 40$ and $\eta = 21$), the initiation voltage is lower than the breakdown voltage and increases with pressure, whereas the breakdown voltage remains almost unchanged when the pressure increases. In a more homogeneous field ($\eta = 7$) the breakdown voltage is equal to the pre-discharge initiation voltage, and increases with pressure.

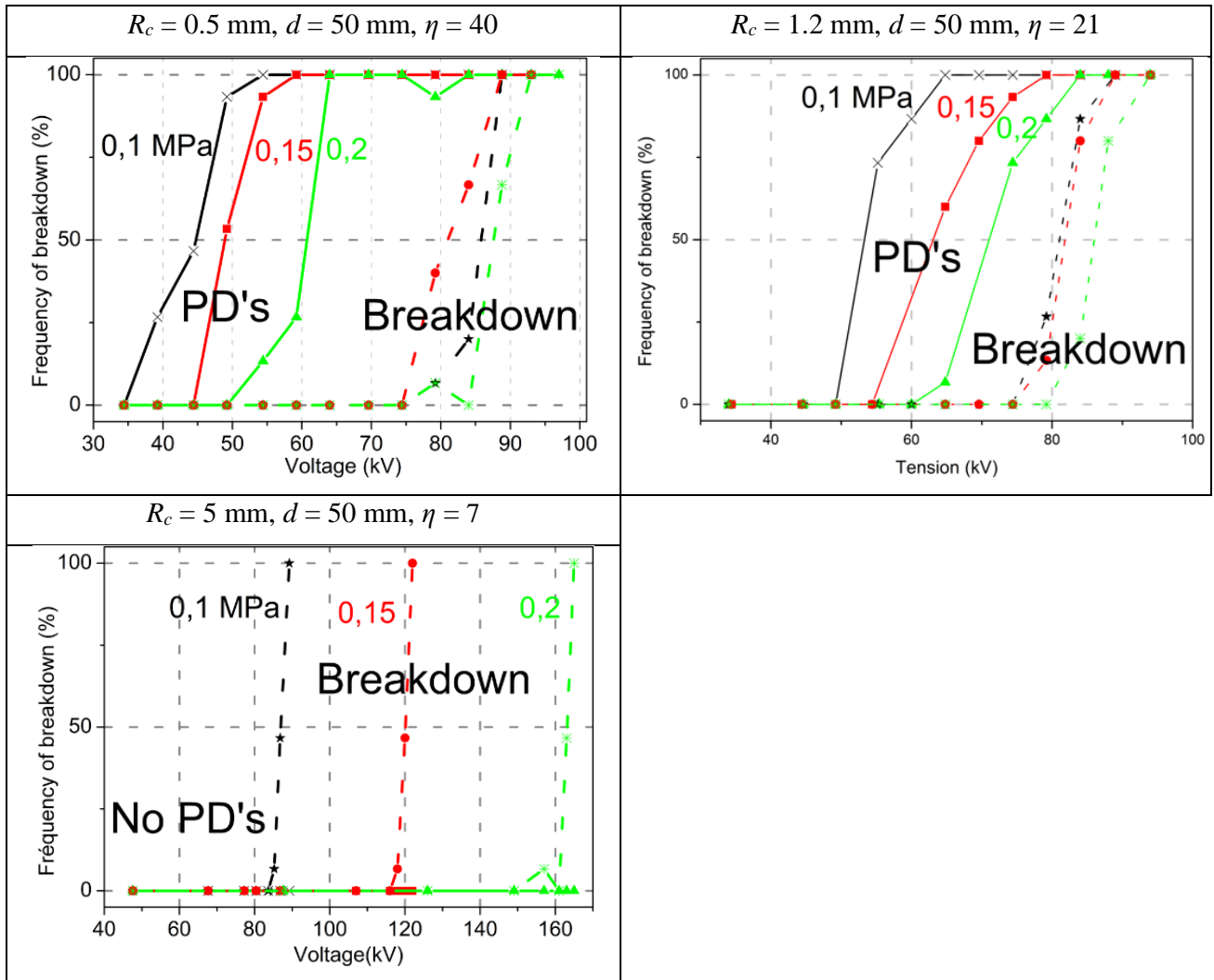


Figure 3.5 : Frequency of initiation and breakdown as a function of the pressure obtained on 15 shots “multiple steps” method.

To further illustrate the difference between the strongly and weakly inhomogeneous cases, Figure 3.6 and Figure 3.7 represent the instantaneous initiation voltage U_i as a function of the maximum applied voltage U_a . With a strongly divergent field (Figure 3.6), the initiation voltage remains almost constant as the applied voltage U_a increases. In this case, the initiation of the discharge occurs during voltage rise at a nearly constant voltage for fixed pressure. The breakdown is not determined by the onset of initiation, but occurs at higher voltage, when discharges are able to propagate up to the opposite electrode (see next sections). In a strongly divergent field, we will then speak of breakdown “controlled by propagation”. The measured breakdown voltage U_{BD} represents the voltage required to induce propagation up to the plane ($U_i < U_{BD}$).

When the field is more homogeneous (Figure 3.7), the initiation voltage is equal to the maximum applied voltage (i.e. discharge appear after the voltage rise), and also to the breakdown voltage. Indeed, when a pre-discharge is initiated, it systematically leads to breakdown. We will then

speak of breakdown “controlled by initiation”: the measured breakdown voltage U_{BD} represent the voltage required to initiate a discharge ($U_i \approx U_{BD}$).

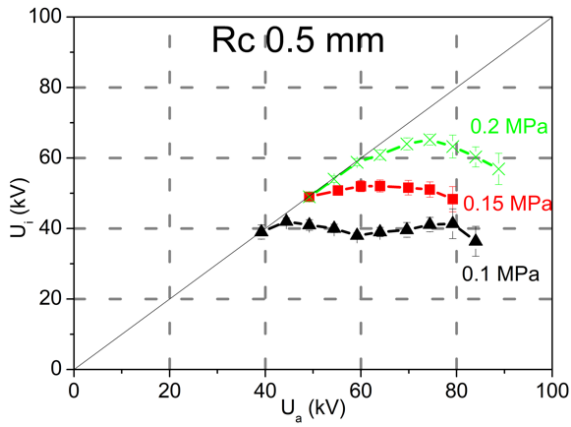


Figure 3. 6 : Initiation voltage U_i as a function of the applied voltage U_a in a very inhomogeneous field in HFO ($R_c = 0.5 \text{ mm}$, $d = 50 \text{ mm}$, $\eta = 84$)

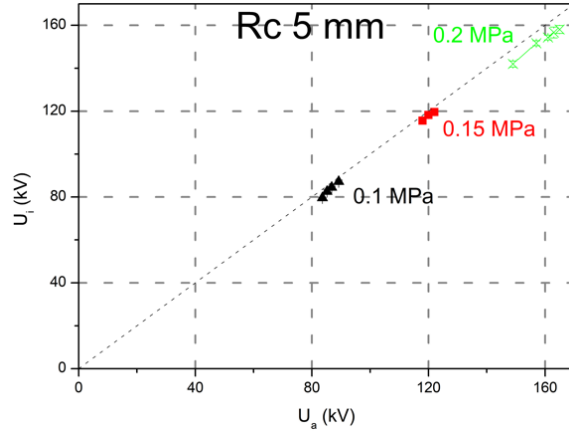


Figure 3. 7 : Initiation voltage U_i as a function of the applied voltage U_a in a weakly inhomogeneous field in HFO ($R_c = 5 \text{ mm}$, $d = 50 \text{ mm}$, $\eta = 2.5$)

When the breakdown is controlled by propagation (Figure 3. 6), the increase in pressure slightly increases the initiation voltage U_i of discharges (+ 50% between 0.1 and 0.2 MPa). When breakdown is controlled by initiation, the increase in pressure also increases the initiation voltage (+ 100% between 0.1 and 0.2 MPa). In the latter case, since $U_{BD} = U_i$ in inhomogeneous field (Figure 3. 7), increasing the pressure will significantly increase the breakdown voltage of HFO.

3.I.C. Summary of tests carried out for propagation-controlled breakdown

Since two breakdown modes have been identified, it is interesting to know at which field enhancement factor η the breakdown mode transition occurs (Figure 3. 8). The figure includes numerous experiments (in divergent and quasi-homogeneous field) carried out in a wide range of electrode radii R_c (from 0.2 to 10 mm), and gap distances d (from 10 to 100 mm). It appears that $\eta \approx 10$ constitutes a reasonable criterion able to distinguish between breakdown modes.

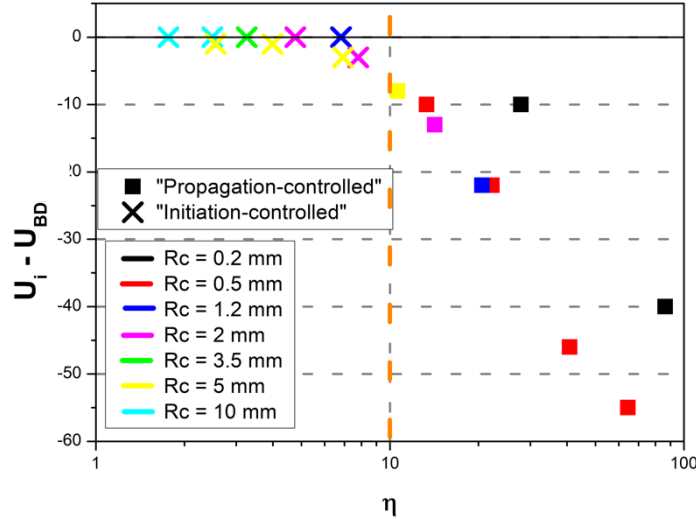


Figure 3. 8 : Difference between the initiation voltage and the breakdown voltage as a function of the field strengthening factor ($\eta = \frac{E_{max}}{E_{moy}}$, $P = 0.1$ MPa).

When $U_i < U_{BD}$ ($\eta > 10$), breakdown is controlled by propagation of the discharges. If $U_i \approx U_a = U_{BD}$ ($\eta > 10$), the breakdown is controlled by initiation. In a real medium voltage system, the design will be optimized to achieve a low η (usually $\eta < 10$), and breakdown should be controlled by initiation. However, under exceptional circumstances, local high field ($\eta > 10$) may occur (for instance around triple points, or with moving metallic particles). The problem of discharges occurring along solid surfaces constitutes another issue that will not be considered in this work. Either initiation and/or propagation of discharges can be influenced by surfaces, and the criteria for initiation or propagation-controlled breakdown may hence be modified.

The measurements presented in Figure 3. 8 were obtained using repetitive breakdown tests, i.e. in slightly degraded gas. The measurements obtained when $\eta < 10$ will be detailed in chapter 4. Table 3. 1 presents a summary of the experimental conditions used for the tests detailed in this chapter when $\eta > 10$.

Chapter 3: Breakdown modes, and characterisation of pre-disruptive phenomena in HFO in divergent field

Table 3. 1 : List of conditions studied in this chapter when breakdown is controlled by propagation

Gas	Rc (mm)	Gap (mm)	η	Pressure (MPa)	Polarity	Ui (kV)	ti (μ s)	UBDm (kV)	tBD (μ s)	
HFO	0,2	10	28	0.13	+	X		42 ± 2	1 ± 0,1	
				0.13	-			69 ± 4	2 ± 1	
SF6				0.13	+			48 ± 6	1,3 ± 0,2	
				0.13	-			60 ± 2	2 ± 1,4	
HFO	0,2	50	86	0.01	+	15 ± 3	0,4 ± 0,3	23 ± 1	6	
				0.02		21 ± 2	0,3 ± 0,1	49	1,5	
				0.03		32 ± 13	0,3 ± 0,1	64	1,4	
				0.03		43 ± 13	0,6 ± 0,2	75	1,4	
				0.05		34 ± 6	0,2 ± 0,2	82	1,2	
				0.1		50 ± 4	0,8 ± 0,1	90 ± 7	1,7 ± 0,4	
				0.2		60 ± 7	0,5 ± 0,1	93 ± 5	1,4 ± 0,2	
				0.3	76 ± 6	0,6 ± 0,1	102 ± 2	1,1 ± 0,1		
				0.01	-	18	0,3	32	3	
				0.05		58 ± 15	0,3 ± 0,2	115 ± 12	16	
0.1	105 ± 25	0,5 ± 0,2	157 ± 7	2,5 ± 0,5						
SF6	0,2	50	86	0.01	+	24 ± 4	3 ± 2	45 ± 4	3 ± 2	
				0.02		59 ± 13	1 ± 0,4	65 ± 3	1,3 ± 0,4	
				0.05		33 ± 3	0,2 ± 0,1	95 ± 0,5	1,3 ± 0,2	
				0.07		59 ± 15	0,7 ± 0,5	103 ± 4	1,4 ± 0,2	
				0.1		70 ± 12	0,4 ± 0,1	120 ± 7	1,2 ± 0,3	
				0.2		85 ± 14	0,4 ± 0,1	124 ± 6	1,2 ± 0,2	
				0.3		81 ± 17	0,5 ± 0,1	115 ± 5	1,3 ± 0,4	
				0.01	-	40 ± 2	1,5 ± 0,1	45 ± 1	16 ± 5	
				0.05		68 ± 11	0,2 ± 0,1	144 ± 7	1,7 ± 0,2	
				0.1				201 ± 6	2 ± 0,2	
Air	0,2	50	86	0.1	+	37 ± 6	0,5 ± 0,2	55 ± 1	3 ± 1	
				0.2		33 ± 8	0,2 ± 0,1	84 ± 1	15 ± 6	
				0.3		51 ± 7	0,4 ± 0,2	97 ± 1	10 ± 2	
				0.1	-	44 ± 6	0,4 ± 0,2	89 ± 5	15 ± 5	
				0.2		30 ± 10	0,3 ± 0,2	160 ± 10	30 ± 20	
HFO	0,5	10	13	0.1	+	26 ± 2	0,6 ± 0,4	36 ± 2	0,8 ± 0,1	
				0.1	+	34 ± 4	0,3 ± 0,1	56 ± 1	1 ± 0,1	
		50	40	0.1	+	39 ± 3	1,8 ± 0,3	85 ± 3	1,6 ± 0,5	
				0.15	+	50 ± 1	1,6 ± 0,1	80 ± 2	0,8 ± 0,2	
			100	64	0.2	+	61 ± 3	1,3 ± 0,1	88 ± 3	0,8 ± 0,6
					0.1	+	60 ± 7	0,3 ± 0,1	115 ± 2	2,6 ± 0,3
	1,2	50	21	0.1	+	57 ± 2	1,8 ± 0,2	79 ± 2	2 ± 0,5	
				0.15	+	63 ± 4	0,6 ± 0,3	86 ± 4	1 ± 0,2	
				0.2	+	71 ± 3	1 ± 0,6	87 ± 3	1 ± 0,2	
	2	50	14	0.1	+	68 ± 3	2,4 ± 0,8	81 ± 4	2 ± 0,5	
				0.15	+	71 ± 2	1 ± 0,8	82 ± 4	1 ± 0,2	
				0.2	+	82 ± 2	0,8 ± 0,3	86 ± 1	0,8 ± 0,1	
				0.1	+	X		99 ± 5	5 ± 30	
				0.1	+			71 ± 5	21 ± 30	
Air				0.1	+					
SF6				0.1	+					
HFO	5	100	11	0.1	+	113 ± 3	1,3 ± 0,5	121 ± 4	3,3 ± 0,4	

3.I.D. Degradation of HFO in divergent field

All the measurements presented in this chapter 3 were carried out in HFO having undergone many breakdowns with a low energy (< 1 J, see chapter 4, p.90). An irregular layer constituted by very fine black dust is visible on electrodes (Figure 3. 9), but does not affect the dielectric strength of HFO (Figure 3. 10). When repetitive breakdown are produced, no marked decrease of U_{BD} is recorded, as previously reported in [7] with similar divergent field conditions. The results of chapter 3 were obtained mainly with degraded HFO, but no difference with undegraded HFO was observed in such divergent field. Chapter 4 will provide a quantitative study of HFO degradation, as a function of the energy dissipated in the discharge.

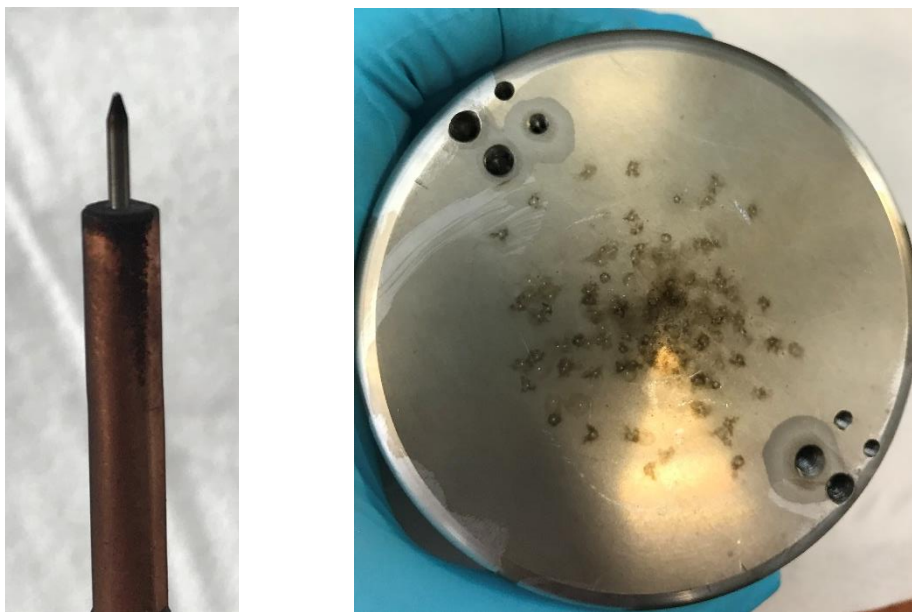


Figure 3. 9 : Fine dust deposits on the electrodes after 15 breakdowns in point plane geometry in HFO ($R_c = 0.5$ mm, $d = 10$ mm, $P = 0.1$ MPa)

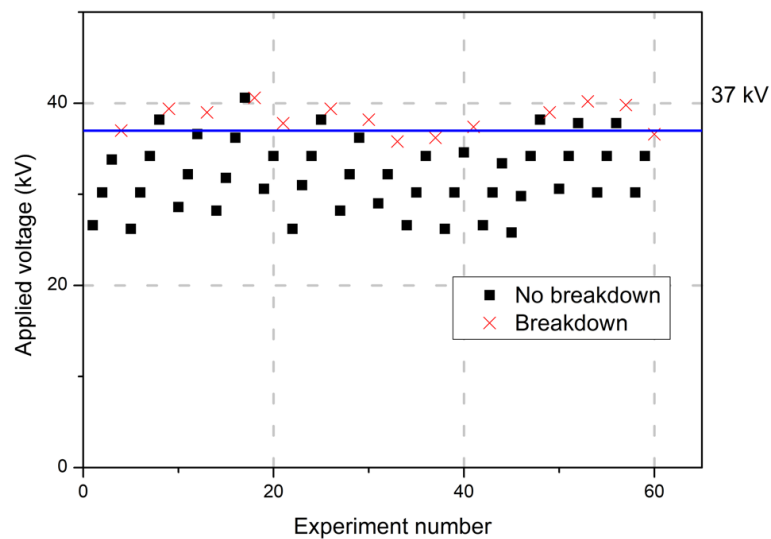


Figure 3. 10 : « Up and down » method in HFO for 15 breakdowns ($R_c = 0.5$ mm, $d = 10$ mm, $P = 0.1$ MPa)

3.II. *Characterisation of pre-disruptive phenomena in strongly divergent field in HFO*

As discussed in Chapter 1, there exists two main pre-discharge processes in conditions relevant to MV insulation: streamers and leaders. The occurrence of these phenomena will be studied in HFO, and compared with air and SF₆.

3.II.A. Identification of pre-breakdown phenomena

In air, at pressure close to 0.1 MPa, for centimeter distances, it is well known that the pre-disruptive phenomena are streamers (Table 3. 2). These streamers propagate in the inter-electrode space to the plane without systematically leading to breakdown [55]. As the pressure increases, streamers propagate less easily, and their propagation lengths decrease significantly. Another characteristic of streamers is visible on the current signals obtained (Figure 3. 11). The streamer propagates as a single “jump” from the tip to the plane. It is associated with a fast current pulse with a short rise time (10-50 ns) and a longer almost exponential tail (200-500 ns). When streamers propagate, a sharp drop in the electric field at the point electrode occurs due to the formation of a positive space charge [78]. The streamer is constituted of multiples branches propagating simultaneously (Table 3. 2).

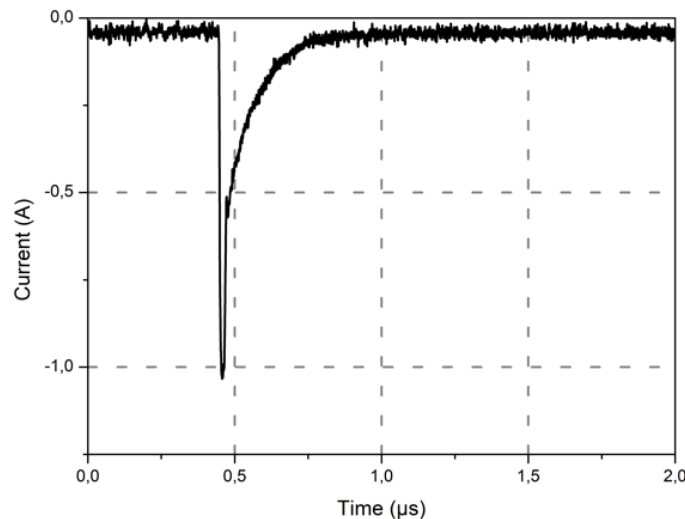
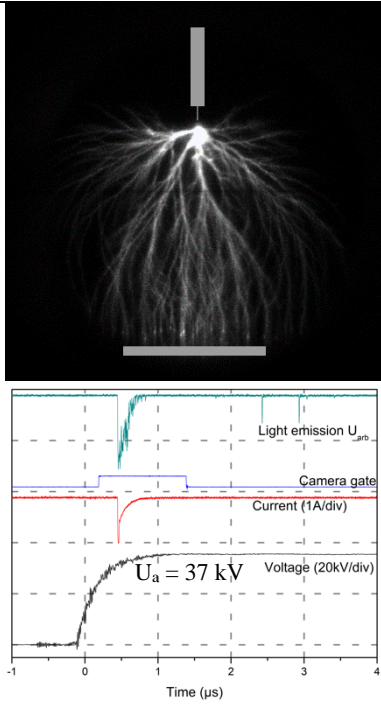
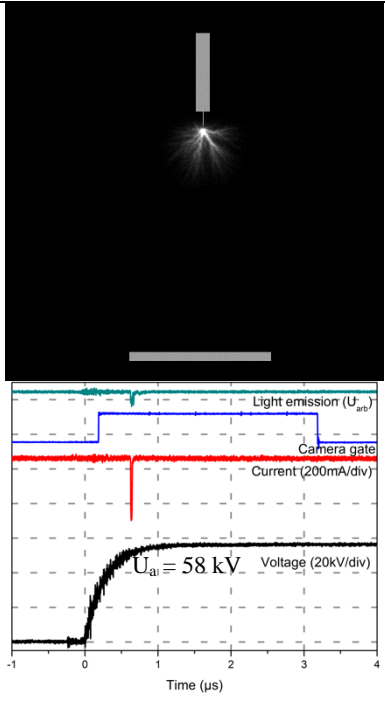


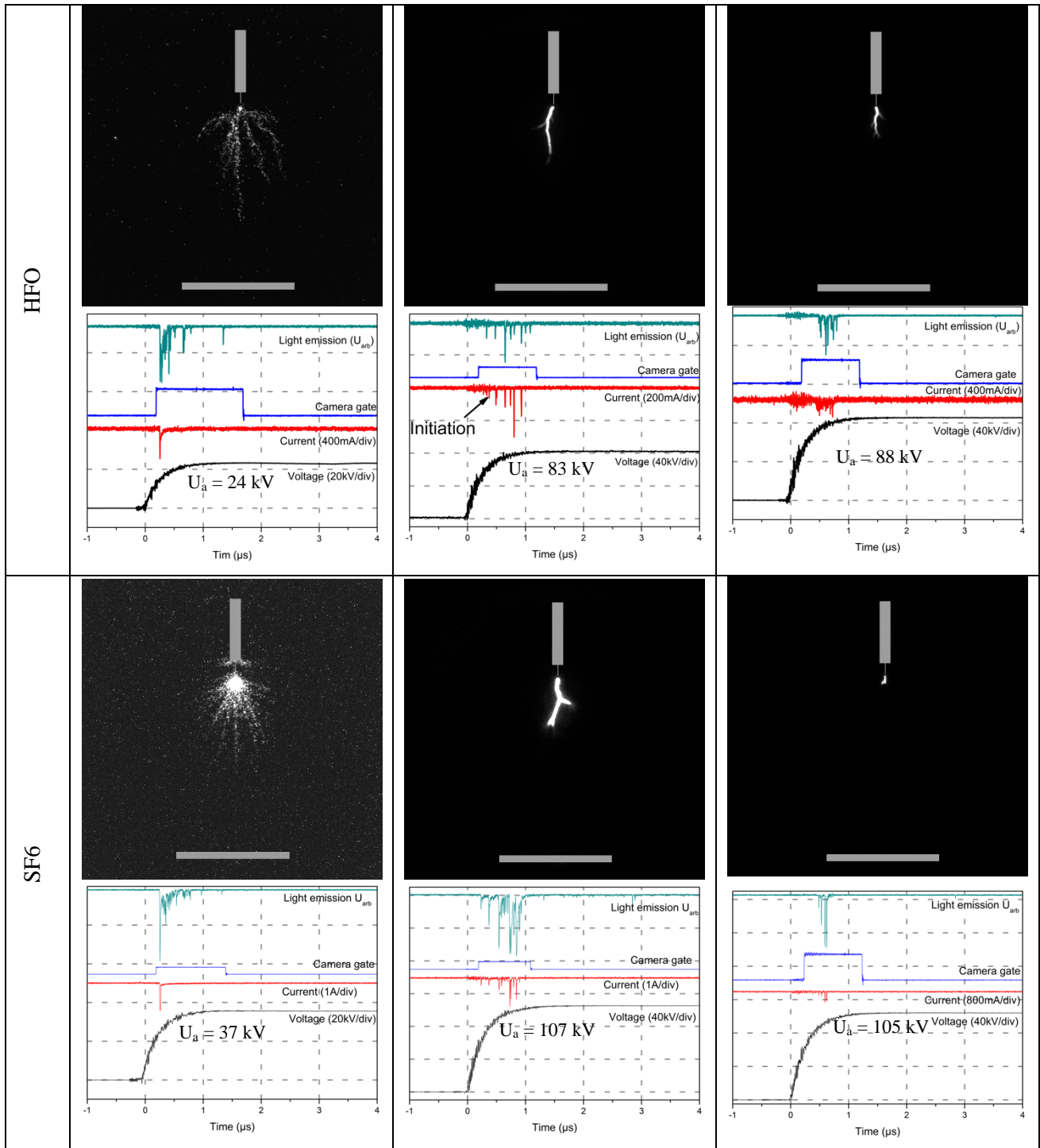
Figure 3. 11 : Current of positive streamer in air ($R_c = 0.2$ mm, $d = 50$ mm, $P = 0.1$ MPa, $U_a = 36$ kV)

For SF₆, at atmospheric pressure, a single very luminous channel is visible in the image in Table 3. 2. On light and current signals, several successive peaks during propagation are visible. These recordings are characteristic of stepped leader propagation [65]. As the pressure increases, the length of the leaders decreases only slightly [79]. At low pressure (0.01 MPa), a clear change is observable. Several luminous channels are present as well as a single current peak. These features correspond to the same phenomena as in air, i.e. transition to streamers in SF₆.

In HFO, the phenomena are almost identical to those observed in SF₆. Namely, leader phenomena at 0.1 and 0.3 MPa, with several successive current peaks and a single bright channel during propagation, and streamers at low pressure (0.1 MPa) with numerous weakly luminous channels, and a single current pulse. From these observations, in highly inhomogeneous geometry, the HFO behaves as SF₆ in terms of pre-discharge process. This conclusion is not very surprising, since HFO includes electronegative fluorine atoms.

Table 3. 2 : Photo and current-voltage characteristic of pre-discharge phenomena in air, HFO, SF₆, at different pressures in strongly divergent fields in positive polarity ($R_c = 0.2 \text{ mm}$ and $d = 50 \text{ mm}$)

P	0.01 MPa	0.1 MPa	0.3 MPa
Air	Too fast phenomena for recording		

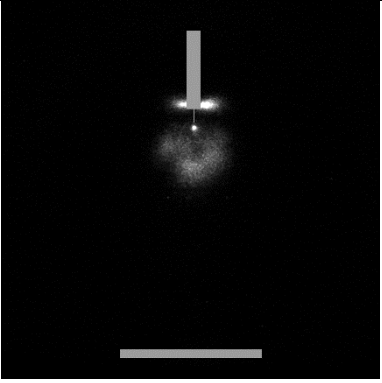
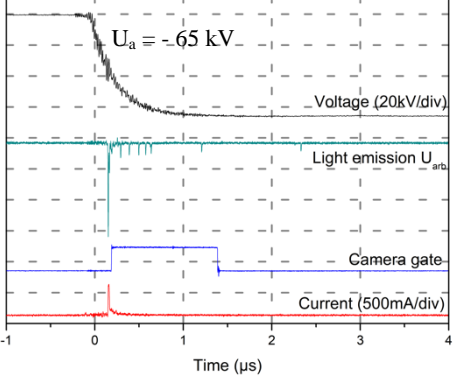


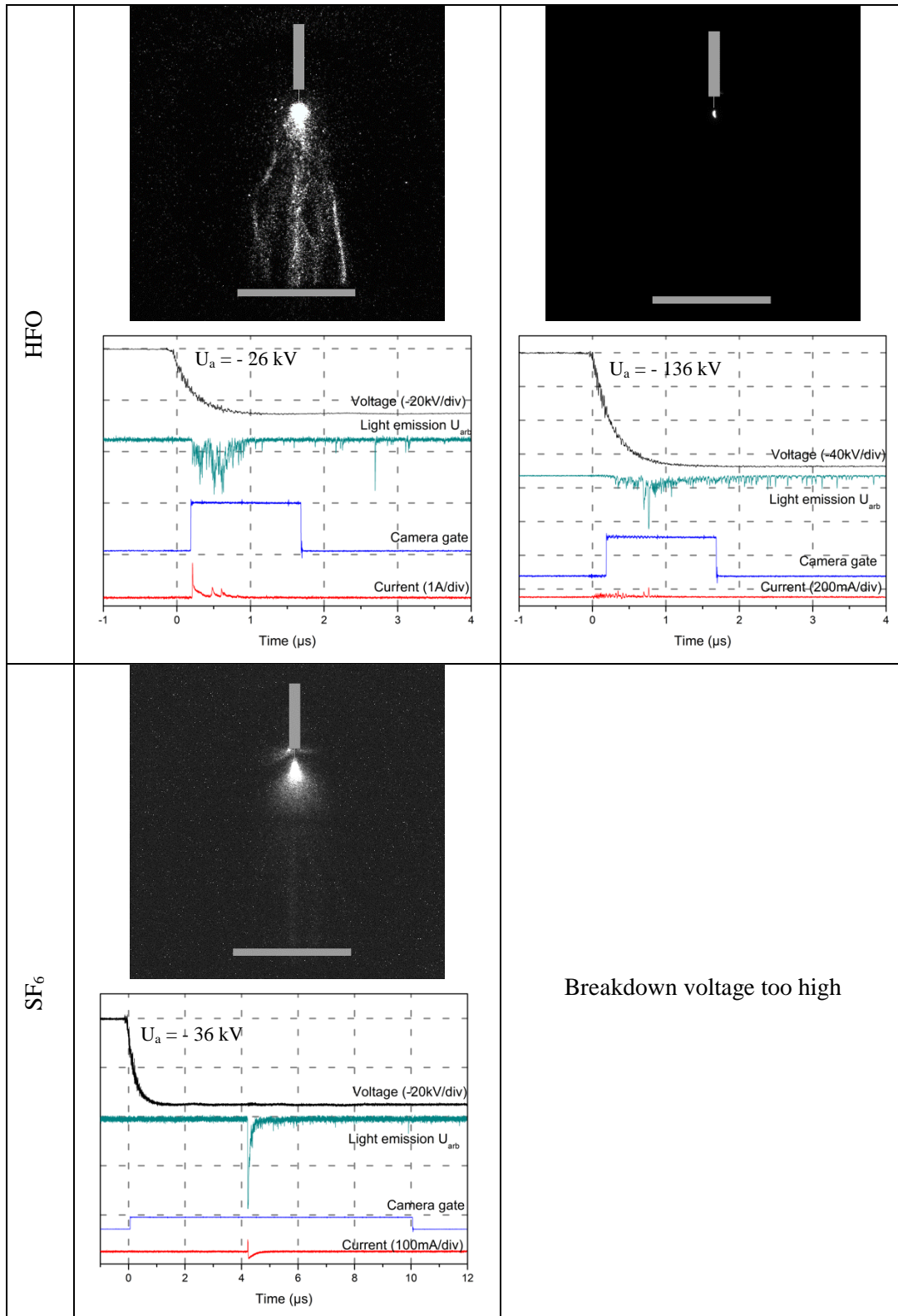
The less numerous measurements obtained in negative polarity present a different aspect from the positive polarity. For air, at 0.1 MPa, the negative discharges form very prominent cloud. This is related to the fact that lateral electron drift suppresses field enhancement in negative streamers. The streamer is more diffuse, it is difficult to observe branches. Our measurements indicate that the inception and propagation processes of positive and negative streamers in ambient air are quite different. In our measurements, the minimum delay for the opening of the camera (blue curve Table 3. 3) was 200 ns.

The initiation delay of streamers is of the same order of magnitude, or below. Our images correspond therefore to the end of the propagation of streamers, and do not show the entire propagation.

In HFO at 0.1 MPa, the leaders still propagate, but the propagation lengths are shorter than in positive polarity. At low pressure (0.01 MPa), the discharge regime is of the streamer type in HFO and SF₆, as in positive polarity.

Table 3. 3 : Photo and current-voltage characteristic of pre-discharge phenomena in air, HFO, SF₆, at different pressures in strongly divergent fields in negative polarity ($R_c = 0.2 \text{ mm}$ and $d = 50 \text{ mm}$)

P	0.01 MPa	0.1 MPa
Air		 



3.II.B. Propagation velocity

The behavior of the pre-discharge in the HFO is compared to that of air and SF₆ in a divergent field. From the images and oscillograms in Table 3. 2 and Table 3. 3, the length and the propagation time of the streamers or leaders is obtained for air, SF₆, and HFO. From these measurements, the propagation velocity can be calculated.

3.II.B.i. Propagation velocity and streamer shape in air

In air, from 0.1 to 0.3 MPa, only streamers are observed in positive polarity (Figure 3. 12). At 0.1 MPa, the streamers in air propagate always up to the plane. For 0.2 and 0.3 MPa, the propagation length of the streamers depends on the applied voltage. Two important facts are noted:

- For a fixed pressure, the streamer propagation velocity increases with the voltage.
- For a fixed voltage, the propagation velocity of propagation decreases with the pressure.

The calculated velocity is between 10⁵ and 10⁶ m/s in agreement with previous measurements (perform at 0.1 MPa [55]). The increase in pressure decreases the propagation velocity in air (Figure 3. 12) [80]. When the pressure increases, the density of the gas increases, the collision number of particles also increases and the streamers propagation is impeded.

In air, the transition from streamers to leaders could not be studied. Indeed, this transition occurs at products pressure x distance much higher (approximately 0.1 MPa/m).

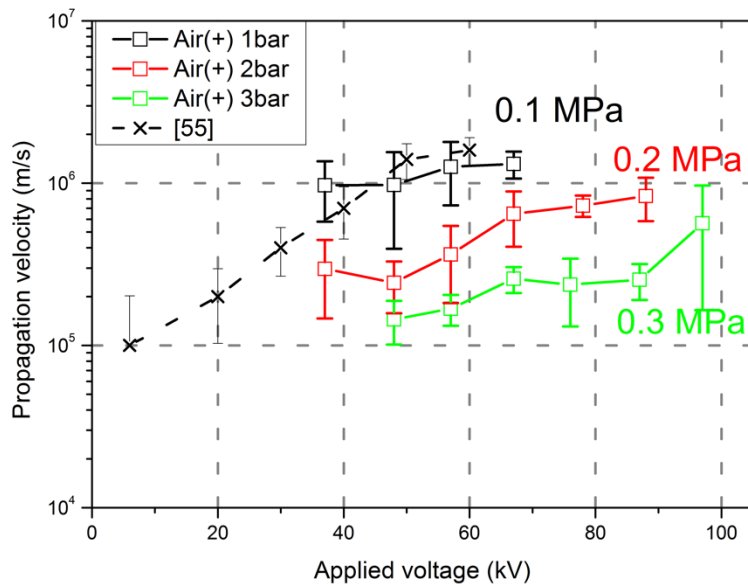


Figure 3. 12 : Velocity of positive streamers in air as a function of voltage and pressure ($R_c = 0.2$ mm, $d = 50$ mm, error bar: standard deviation) with the results of [55]

In negative polarity, fewer measurements could be carried out (due to the voltage limit of the test cell: 200 kV) but the observation is the same: the pressure decreases the propagation velocity of streamers.

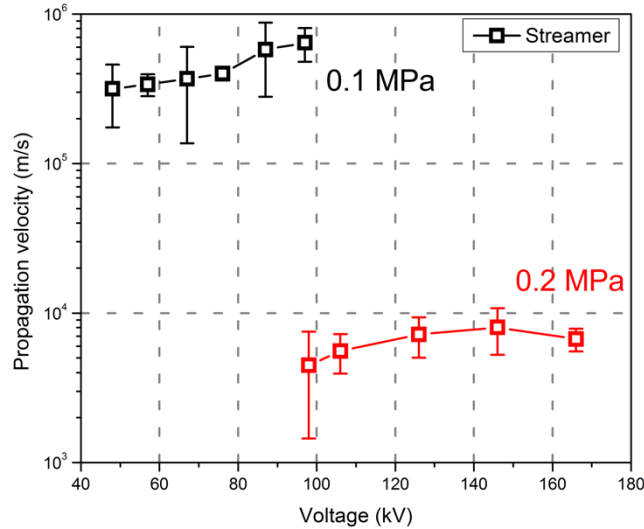


Figure 3.13 : Velocity of propagation of negative streamers in air as a function of voltage and pressure ($R_c = 0.2$ mm, $d = 50$ mm, error bar: standard deviation)

From measurements made in air, the observed diameters of the streamers as a function of the pressure are shown in Figure 3.14. The diameter of the streamers increases with voltage and decreases with pressure.

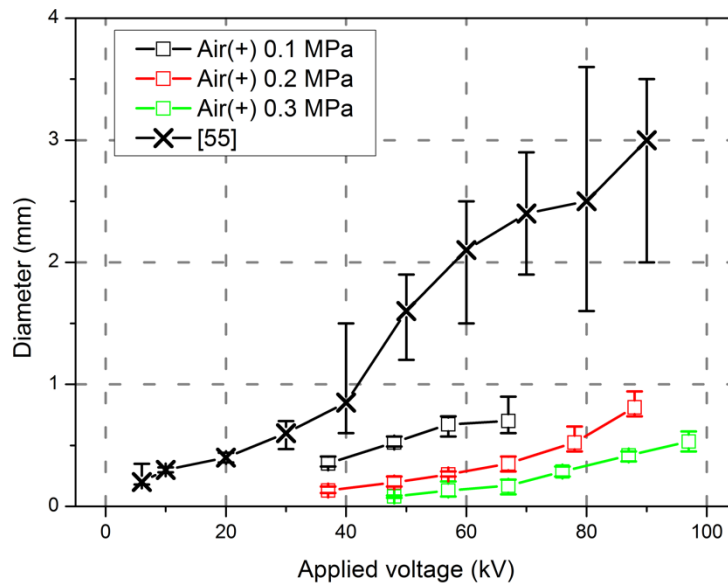


Figure 3.14 : Diameter of streamers in air as a function of voltage for different pressures (Propagation velocity of pre-disruptive phenomena in air as a function of pressure in positive polarity ($R_c = 0.2$ mm, $d = 50$ mm, max/min error bar) with the results of [55])

These measurements present a large difference compared to the results published by Briels et al [55], and various factors may explain this difference. First, the applied voltage wave is different. Briels made his study with an impulse with a very fast rising front (< 150 ns), and a duration of more than

50 ns. The diameter of the streamers is strongly impacted by the rise time of the wave [81]. In addition, measuring the diameter of the streamers may show variations according to the method used. Depending on where the diameter is measured (close to the tip or the plane), the result is not the same. Also, depending on the gain of the camera and on the light intensity, the width of the streamer observed is different.

Conversely, the velocity of streamers as a function of the diameter shows a good match between the results of Briels et al [55] and our measurements. At 0.1 MPa, for a diameter of 0.5 mm, the propagation velocity is close to 10^6 m/s. As the diameter of the streamer increases at higher voltage, the propagation velocity also increases. As the pressure increases, the velocity and diameter of the streamers decrease.

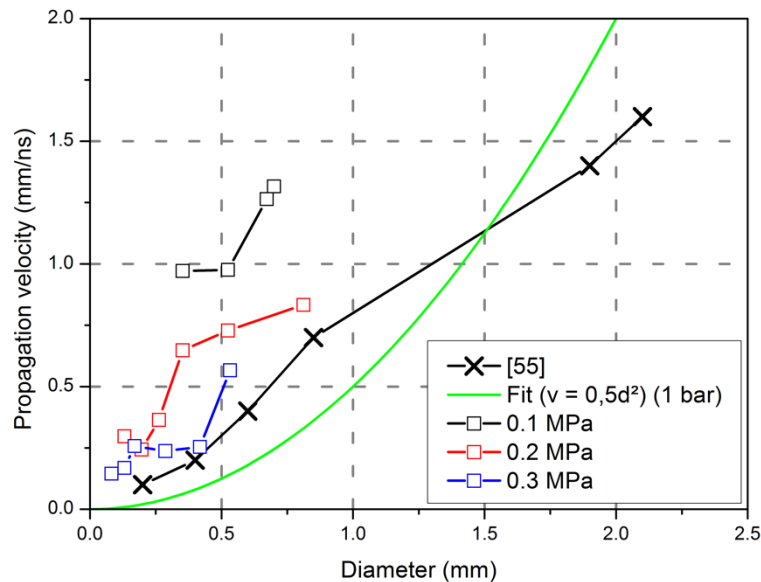


Figure 3. 15 : Propagation velocity of streamers as a function of diameter and air pressure ($R_c = 0.2$ mm, $d = 50$ mm, max/min error bar) with the results of [55]

3.II.B.ii. Propagation velocity for SF₆

In SF₆ a large range of pressure has been investigated to observe the transition from streamer to leader. Three areas on Figure 3. 19 can be distinguished:

- At low pressure (0.01 MPa), the breakdown is of the streamer type, and the velocity is of the order of 10^6 m/s as for streamers in air.
- At intermediate pressure (0.02 to 0.05 MPa), it is difficult to define exactly the type of discharges: this constitutes a transition zone between the streamer and the leader. The average velocity is around 10^5 m/s
- For pressures greater than 0.07 MPa, the breakdown is of leader type. Considering the scatter of measurements, the influence of pressure on the velocity of leaders is not

obvious. On the other hand, whatever the pressure, the increase of the voltage increases the leader propagation velocity.

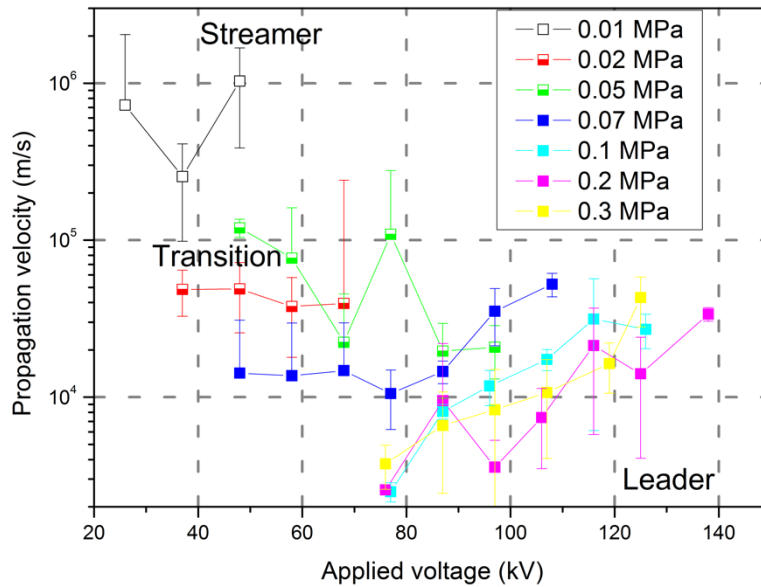


Figure 3. 16 : Velocity of propagation in positive polarity in SF₆ as a function of voltage and pressure ($R_c = 0.2$ mm, $d = 50$ mm, error bar: standard deviation)

In negative polarity (Figure 3. 17), the conclusions are similar as in positive polarity, despite the few measurements that could be carried out.

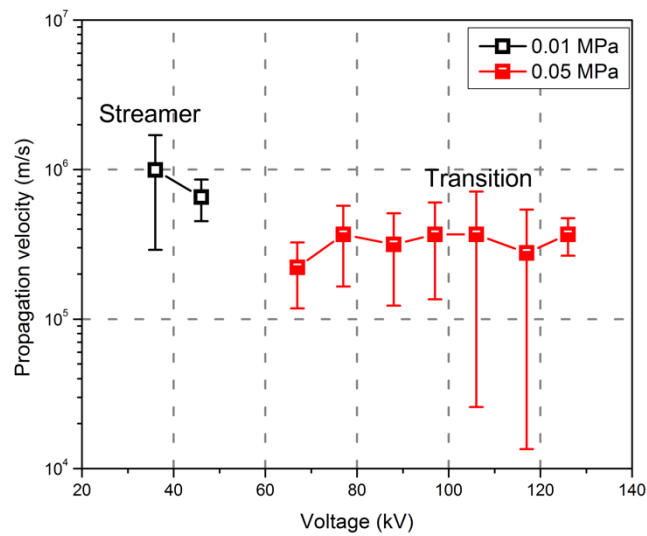


Figure 3. 17 : Velocity of propagation in negative polarity in SF₆ as a function of voltage and pressure ($R_c = 0.2$ mm, $d = 50$ mm, error bar: standard deviation)

3.II.B.iii. Propagation velocity for HFO

In HFO, the same 3 zones defined in SF₆ are observed.

- At low pressure (0.01 MPa), the breakdown is also of the streamer type, and its velocity is of the order of 10⁶ m/s, like with streamers in air and SF₆.

- At intermediate pressure (0.02 MPa), this is a transition zone between the streamer and the leader.
- For pressures greater than 0.05 MPa, the breakdown is of leader type. In this case the pressure has no effect on the leader velocity. Whatever the pressure, the increase of the voltage increases the propagation velocity of leaders.

When the pressure increases, the streamer propagation velocity (around 10^6 m/s) decreases whatever the gas nature. In HFO and SF₆, the streamer-to-leader transitions are visible between 0.02 and 0.05 MPa, and the propagation velocity drops from 10^6 to 10^4 m/s. In this transition area, the large error bars reflect a random number of streamers and/or leaders occurring. Above 0.05 MPa, the propagation velocity of leaders remains constant in the HFO and SF₆ whatever the pressure, evidencing the large physical difference between streamer and leader processes. In contrast with streamers, leaders are constituted by a hot and therefore very conductive ionized channel ($\approx 2000^\circ\text{C}$).

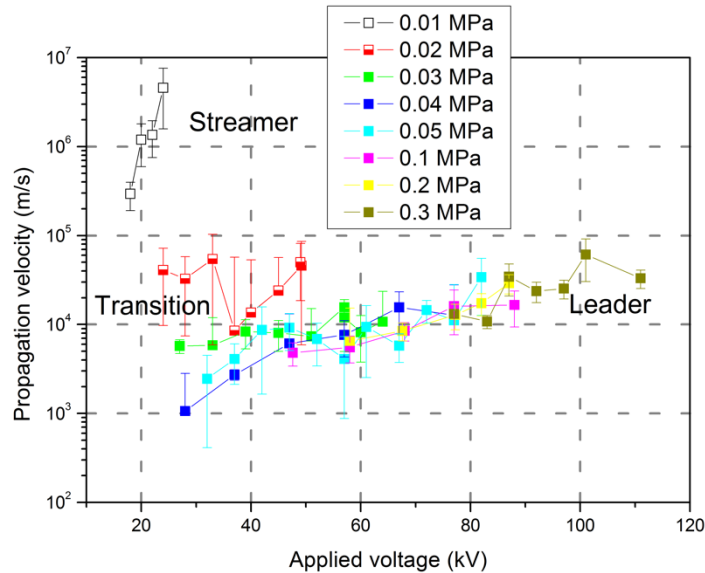


Figure 3. 18 : Velocity of propagation in positive polarity in the HFO as a function of voltage and pressure ($R_c = 0.2$ mm, $d = 50$ mm, error bar: standard deviation)

In negative polarity, few measurements were carried out due to a breakdown voltage greater than 200 kV in the HFO and SF₆. From the available data, the conclusions are similar to positive polarity:

- The velocity of the streamers is around 10^6 m/s and decreases with pressure (Figure 3. 13).
- In HFO and SF₆, the increase in pressure causes a change in the propagation mode from streamer to leader. Consequently, the velocity of propagation is closer to that of the leaders, namely 10^4 m/s (Figure 3. 19 and Figure 3. 17).

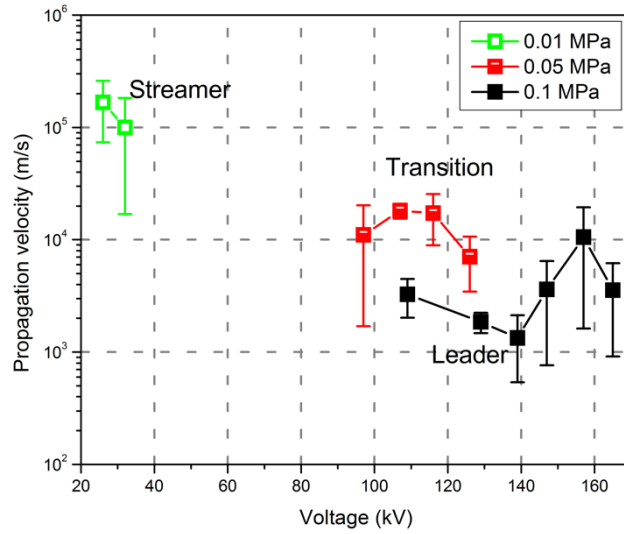


Figure 3.19 : Velocity of propagation in negative polarity in HFO as a function of voltage and pressure ($R_c = 0.2$ mm, $d = 50$ mm, error bar: standard deviation)

The previous measurements were obtained from images and oscilloscope recordings with a fixed radius of curvature (0.2 mm) and distance (50 mm) for different pressure. Provided leaders induce immediately breakdown when they touch the plane, another method to estimate velocities can be obtained from the gap distance and the propagation time, calculated as $t_p = t_{BD} - t_i$. From the large panel of measurements carried out (Table 3.1), the propagation times and therefore the average propagation velocity of the leaders propagating to breakdown in different geometries can be extracted. Figure 3.20 presents the set of measurements obtained for $\eta > 10$. The color of the symbols represents the different distances, and their shape the different radius of curvatures.

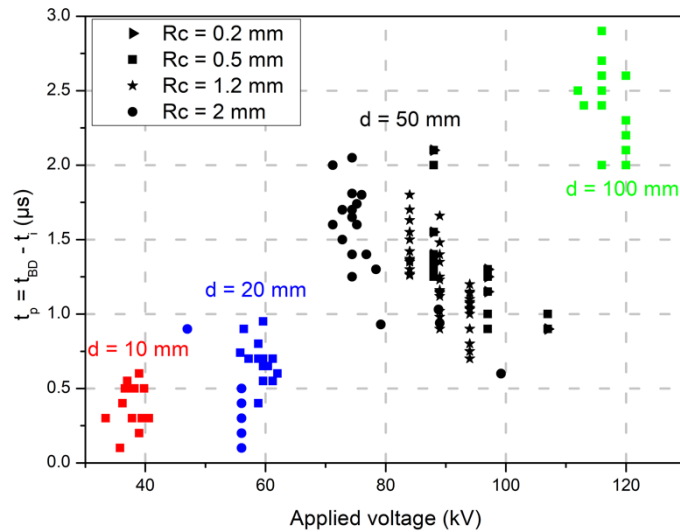


Figure 3.20 : Propagation time of pre-discharge in HFO leading to breakdown in positive polarity ($P = 0.1$ MPa)

Propagation times in the HFO deduced from breakdown measurements at $P = 0.1$ MPa are between 0.1 and 3 μs (Figure 3. 20). When the gap distance increases, the propagation time logically also increases.

Figure 3. 21 shows the propagation time plotted versus voltage at different pressures with a fixed distance of 50 mm. The shape of the symbols represents the different R_c and the pressure is represented by the color. Considering the scatter of measurements, it is almost impossible to clearly observe an influence of pressure and electrode radius. For a fixed voltage, the pressure and the radius of curvature hardly modify the propagation time of the leaders. On the other hand, when the applied voltage increases, whatever the pressure and the radius of curvature, the propagation time decreases on average.

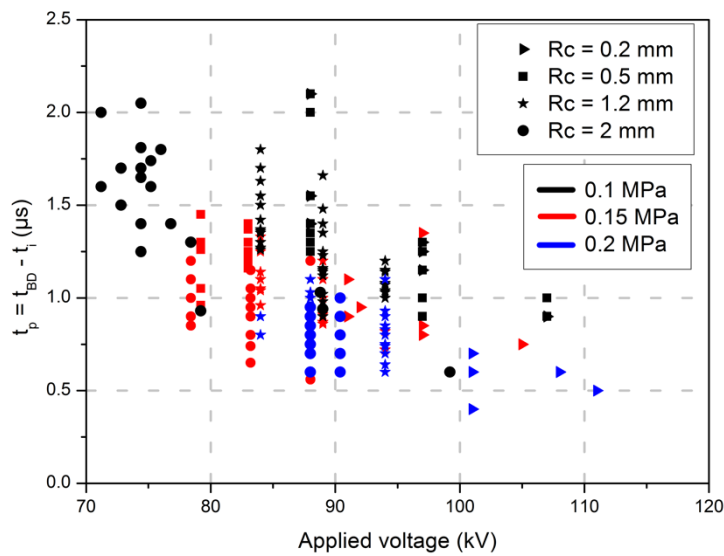


Figure 3. 21 : Propagation time of pre-discharge in HFO leading to breakdown in positive polarity ($d = 50$ mm)

From the data in Figure 3. 21, the average leader propagation velocity (Figure 3. 22) is calculated by dividing the distance (50 mm) by the propagation time. The propagation velocity of leader in the HFO, although scattered, increases from about 2 to $9 \cdot 10^4$ m/s versus voltage, whatever the pressure and electrode radius. This result is in good agreement with the velocity measurements obtained from the camera (Figure 3. 18 for voltages greater than 70 kV). At other distances, similar velocities can be deduced (Figure 3. 20), but not enough data were collected to check the influence of voltage such as in Figure 3. 22.

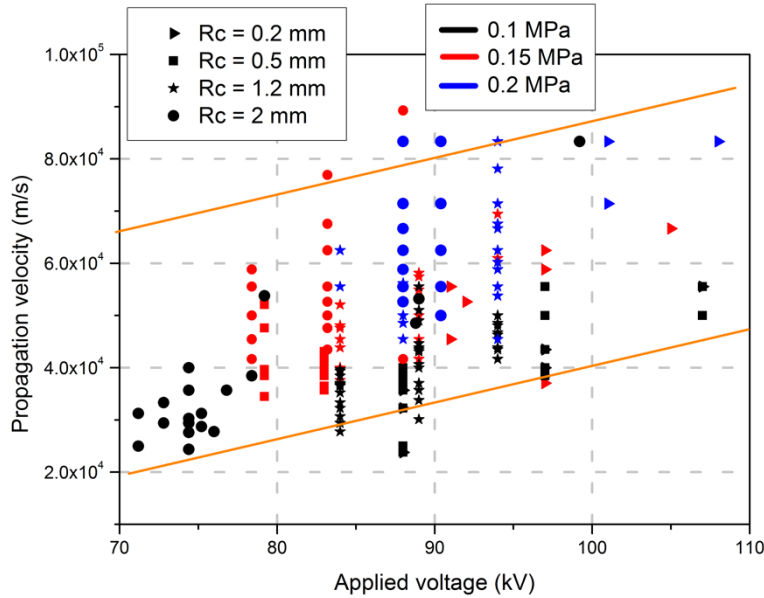


Figure 3. 22 : Propagation velocity as a function of voltage in the degraded HFO for different R_c and pressure ($d = 50$ mm)

3.II.C. Stopping length of leaders in HFO and SF₆

An important characteristic of leaders is the length to which they are able to propagate without leading to breakdown. Figure 3. 23 illustrates the “stopping length” l_s of leaders in HFO and SF₆ as a function of pressure and voltage. The stopping length increases versus voltage, and when leaders reach the counter electrode ($d = 50$ mm), breakdown occurs. The figure shows marked differences between the two gases.

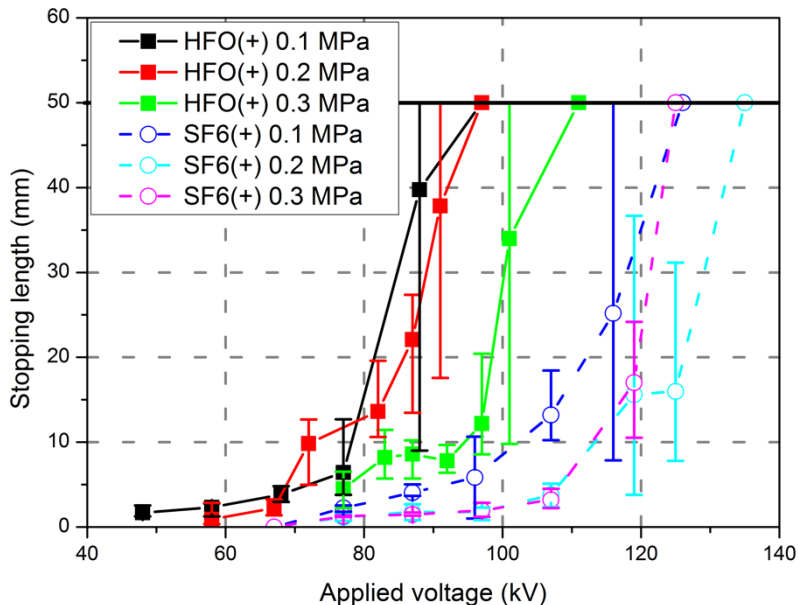


Figure 3. 23 : Stopping length of leader phenomena in a highly inhomogeneous field in HFO and SF₆ ($R_c = 0.2$ mm, $d = 50$ mm, max/min error bar)

First, the development of leaders in HFO starts at voltages lower than in SF₆ (- 30 kV on average) regardless of the pressure. Second, leader stopping length grows more slowly in SF₆ compared

to HFO: the applied voltage must be increased by 50 kV between initiation of the first leaders to breakdown in SF₆, and only by 30 kV in HFO. These two observations allow us to conclude that leaders are initiated and propagate more easily in the HFO compared to SF₆. These properties are consistent with the slightly lower breakdown voltages recorded in HFO in divergent field compared to SF₆.

In HFO, increasing the pressure to 0.2 MPa, induces no change in stopping length. At 0.3 MPa, slightly lower lengths are recorded, inducing a moderate increase of breakdown voltage. Similar conclusions are obtained in SF₆. In both cases, the pressure has a small impact on propagation.

In negative polarity (Figure 3. 24), the very few available data shows that the behaviour is similar to positive polarity, but for much higher voltages.

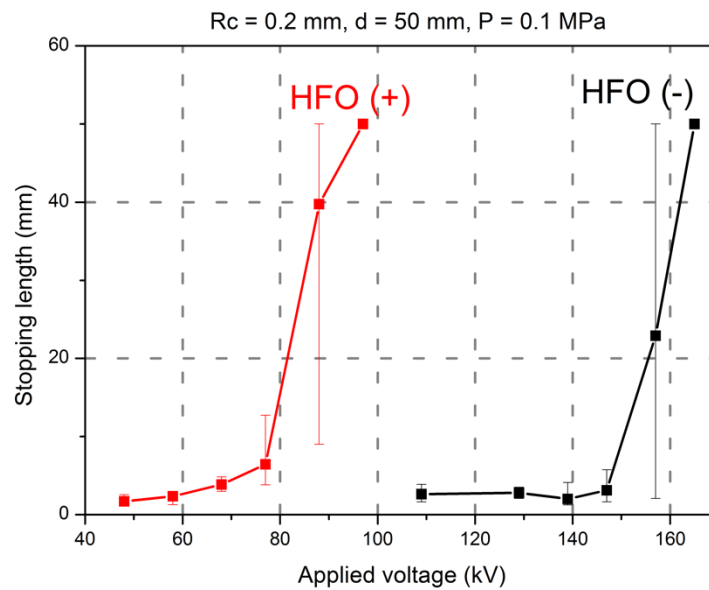


Figure 3. 24 : Stopping length of leader phenomena in a highly inhomogeneous field in the HFO ($R_c = 0.2$ mm, $d = 50$ mm, max/min error bar)

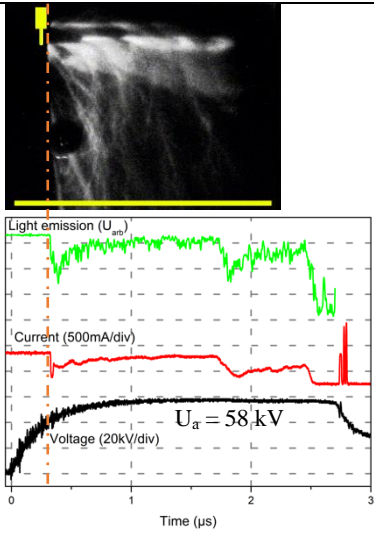
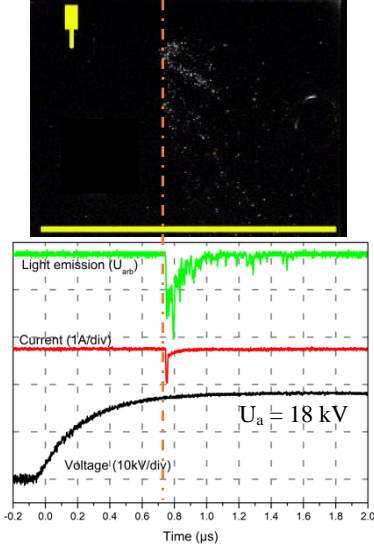
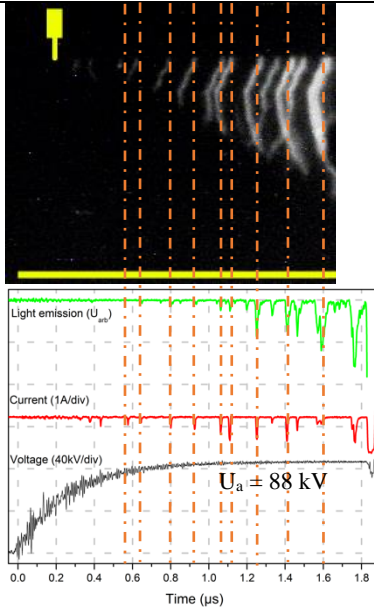
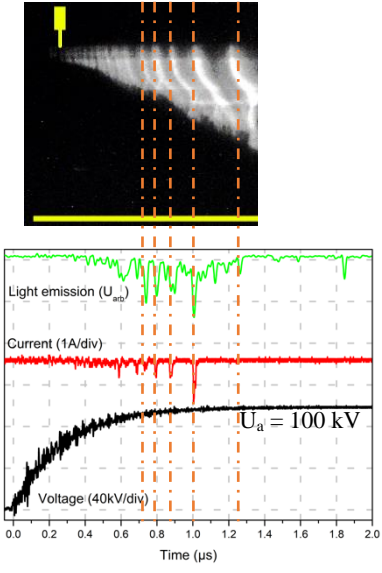
3.II.D. Temporal development of streamers and leaders

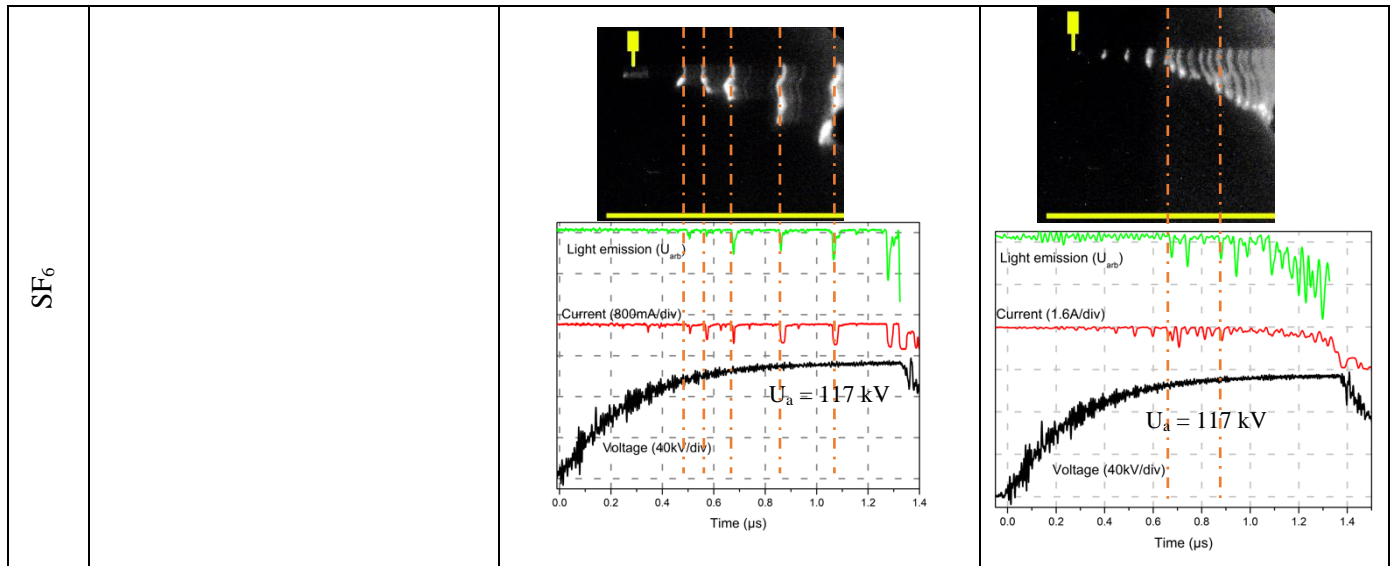
The aim of this section is to describe the sequence of phenomena leading to breakdown in a strongly divergent field. Our objective is to determine if the behaviour of HFO is fully comparable to that of SF₆, and obtain a more precise description of pre-discharge propagation.

On Table 3. 4, the scale and position of images obtained with the streak camera were adjusted to fit the time base of current and light measurements with the oscilloscope.

Chapter 3: Breakdown modes, and characterisation of pre-disruptive phenomena in HFO in divergent field

Table 3. 4 : Streak camera images in air, HFO, and SF₆ as a function of pressure, and synchronized recordings of current and light emission ($R_c = 0.2 \text{ mm}$, and $d = 50\text{mm}$)

P	0.01 MPa	0.1 MPa	0.3 MPa
Air			
HFO			



In SF_6 and HFO for pressures of 0.1 and 0.3 MPa, the phenomenon of stepped leaders [65] characterizing electronegative gases is clearly identified. The current peaks correspond to the propagation of the leader steps, followed by a pause time before the next reillumination. As the pressures is increased, the leader steps become progressively smaller and the time interval between steps becomes shorter. The number of re-illumination and the pause time between 2 successive steps depends on the pressure and the nature of the gas.

In air, at 0.1 MPa, phenomena leading to breakdown decompose in 2 main stages. First, the streamer propagates to the plane (1st current peak); we will speak of “primary streamer”. The second process is called “secondary streamer”. In the HFO at low pressure (0.01 MPa), there is a single streamer current peak, due to a single streamer propagating to the plane without systematically leading to breakdown.

3.II.E. Pause time between leader steps

Niemeyer [64] showed that an increase in pressure decreases the time between 2 re-illumination in SF_6 . It is difficult to give an exact time value between these 2 re-illuminations, but the figures in Table 3. 4 in SF_6 and in Figure 3. 25 show obviously a greater number of re-illuminations during the same time when the pressure increases, for SF_6 and HFO.

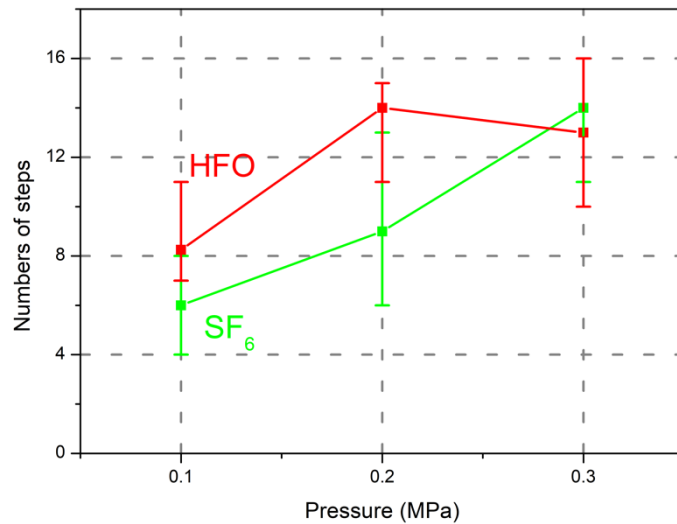


Figure 3. 25 : Total number of leader steps as a function of the pressure in the HFO and SF₆ in positive polarity ($R_c = 0.2$ mm, $d = 50$ mm, $P = 0.1$ MPa, max/min error bar)

Qiu et al. [80], [81] have shown that the time between 2 re-illuminations varies according to $1/U_a P$ (Figure 3. 26), and also that the initiation time varies as $1/P^2$. This delay could not be measured due to the high speed of the phenomena.

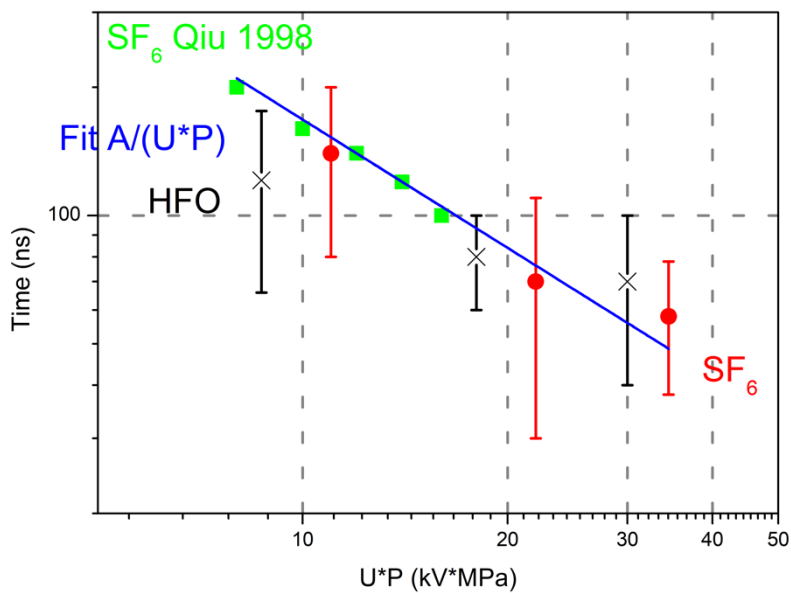


Figure 3. 26 : Time between 2 re-illuminations in HFO and SF₆ as a function of the product $U*P$ with comparison with the data of Qiu ($R_c = 0.2$ mm, $d = 50$ mm and $A = 1680$) [83]

This delay could not be measured because of the excessively high velocity of the phenomena. Our measurements in HFO and SF₆ show a good match with the results published in [83].

3.II.F. Leader step length

Average leader step lengths were measured and are shown as a function of pressure in Figure 3. 27. While there is clearly some uncertainty in the measured values, an inverse dependence of pressure is shown.

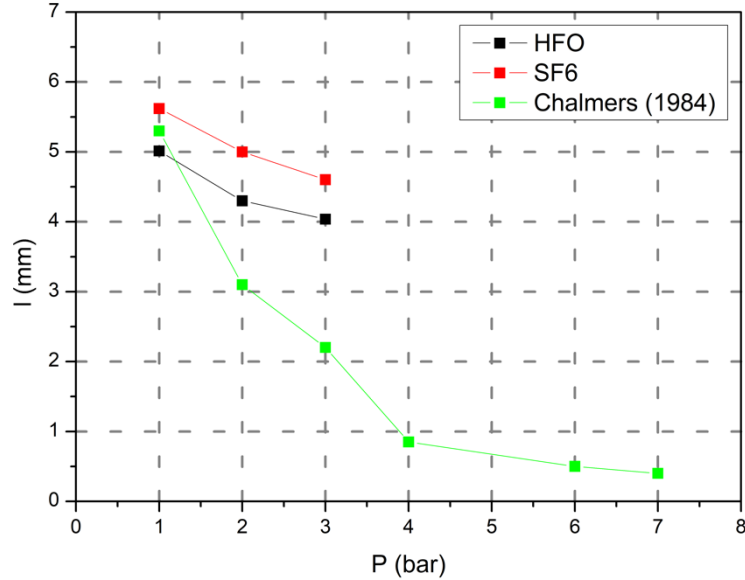


Figure 3. 27 : Leader step lengths in SF₆ and HFO as a function of pressure ($R_c = 0.2$ mm, $d = 50$ mm) in comparison with the results of Chalmers et al. [79] ($R_c = 0.05$ mm, $d = 30$ mm)

Niemeyer and Pinnekamp [64] developed a simplified model for leader propagation, assuming that leader step progression is controlled by the range over which streamers can develop from the previous leader tip. By making a number of hypotheses, they show that the length of the step l can be expressed by the equation:

$$l = \frac{\gamma}{\left(\frac{E}{P}\right)_{st}} \times \frac{U}{P} \quad (9)$$

where U is the applied potential, P the gas pressure, $(E/P)_{st}$ is the reduced field (around $4 \text{ kV/mm}^{-1} \cdot \text{bar}^{-1}$) and γ is a constant. Based on comparisons with step length measurements, Niemeyer and Pinnekamp concluded that equation 9 was valid in the range $1 \text{ mm} < l < 30 \text{ mm}$ with the constant $\gamma = 0.3$.

By taking again the results published in [79], and by adding the measurements carried out in the HFO and the SF₆ (Figure 3. 28), the variation of lengths of leaders steps roughly agrees with data of [79], but the limited pressure range investigated (0.1 to 0.3 MPa) prevents further conclusion.

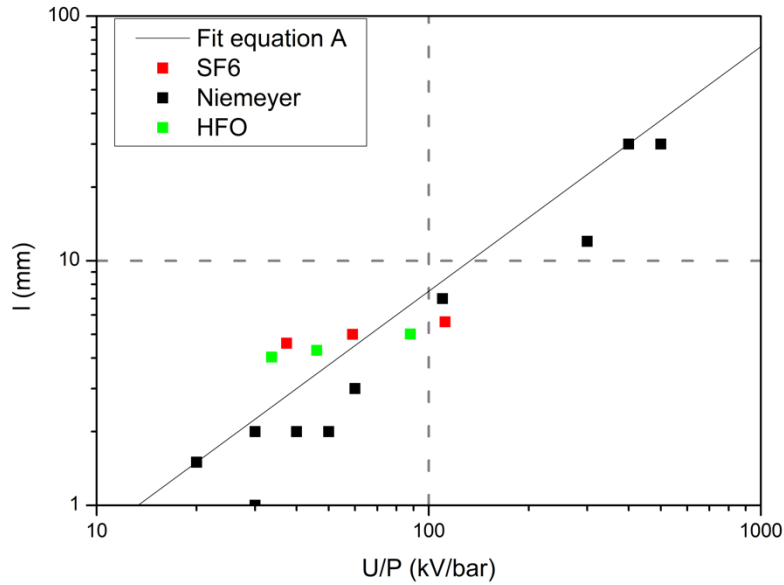


Figure 3. 28 : Leader step length as a function of V/p for HFO and SF₆ and adapted from Niemeyer [79]

3.II.G. Spectroscopy of emitted light

A diagnostic technique commonly used for the investigation of gas discharges is the optical emission spectroscopy. This method can give information about a number of plasma properties, such as rotational and vibrational temperatures (T_{rot} , T_{vib}), electron density and temperature (N_e , T_e), etc.

Spectroscopy measurements were performed in air, HFO and SF₆ either at the time of breakdown, or for non-breakdown pre-disruptive phenomena in strongly divergent field ($\eta = 86$). These discharge phenomena do not propagate exactly along the gap axis. This complicates the acquisitions, by reducing the amount of light collected by the spectrometer entrance slit. To reduce this problem, the acquisitions were carried out for 8 minutes for series of 30 leaders.

Figure 3. 29 shows the typical emission spectra of the streamer in air in the range 200–500 nm and the identification of the respective bands of the second positive system of molecular nitrogen N₂ ($C^3\Pi_u^+ - B^3\Pi_g^+$). To obtain the rotational temperature of N₂ the simulated spectral profiles of N₂ obtained from two simulation programs (SpecairTM and a simulated code) are compared with the measured ones, as shown in Figure 3. 30. We get the values of the rotational temperature T_r when a best fit between the two profile is achieved. Rotational temperature measurements are very important for gases discharges because the translational temperature inside a plasma (i.e. gas temperature) can be obtained by measuring T_r . Indeed, the nitrogen molecule has a nearly Maxwellian distribution among the rotational sublevels of a nitrogen emission spectrum, and rotational-translational relaxation mechanisms are nonadiabatic, which implies a fast equilibrium between rotational and translational degrees of freedom. Figure 3. 30 shows an example of an experimental spectrum compared with a calculated spectrum with

$T_{rot} = 400$ K. The vibrational temperature typically has values that lie between the gas temperature and the electron temperature [84].

During the breakdown phase, line emissions of neutral nitrogen and oxygen atoms can occur due to electron impact excitation of ground state atomic species, by direct dissociative excitation of N_2/O_2 molecules or by dissociative electronic recombination. The most important N I atomic emissions are NIR multiplets ($3s^4P-3p^4S_0$), ($3s^4P-3p^4P_0$), ($3s^4P-3p^4D_0$) and ($3s^2P-3p^2D_0$) at 746, 820, 868 and 939. In the case of atomic oxygen, three multiplets, ($3s^5S_0-3p^5P$), ($3s^3S_0-3p^3P$) and ($3d^5D_0-3p^5P$), occurring at 777, 845 and 927 nm seem to be prominent.

Iron I and II were also observed near the tip, linked to erosion of the tip during breakdowns. The excitation temperature was determined using relative line intensity method by using the iron and nitrogen spectral line, which was found to be in the range 9000 – 10000 K.

In order to measure the Stark broadening precisely, the Ha half width was corrected to account for Van der Waals broadening (see Annex), the electron density was estimated to $N_e = 10^{23} \text{ m}^{-3}$.

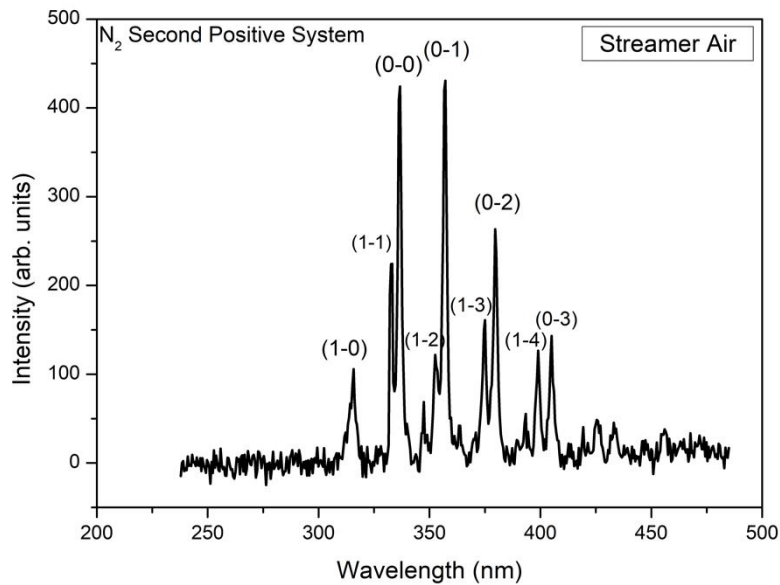


Figure 3. 29 : A typical emission spectrum from streamer in air exhibiting N_2 (C_3II-B_3II) with assigned vibrational quantum numbers $v'-v'$ ($R_c = 0.2$ mm, $d = 50$ mm, $P = 0.1$ MPa) spectrum not corrected

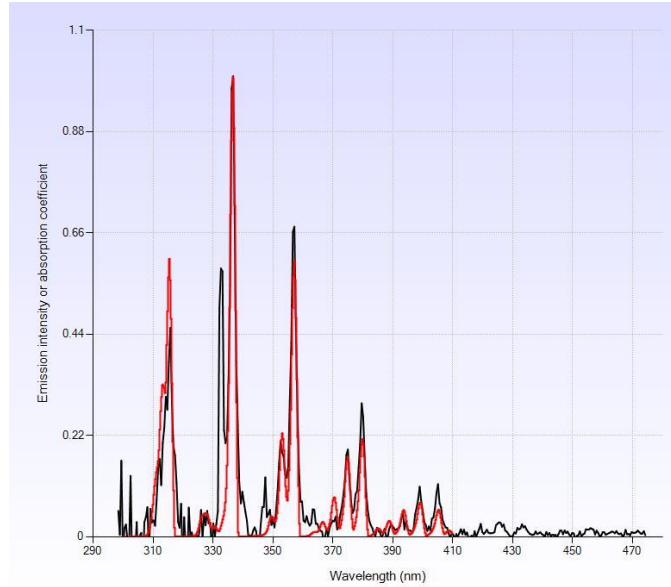


Figure 3. 30 : Example of comparison between second positive nitrogen system simulated by Specair (red) and measured experimentally (black) in air during the streamer discharge ($R_c = 0.2$ mm, $d = 50$ mm, $P = 0.1$ MPa) spectrum corrected ($T_v = 5000$ K, $T_r = 500$ K)

In SF₆, in both cases (leaders and breakdowns), F I was visualized (Figure 3. 31) at an excitation temperature of 7000 K. This is the excitation temperature, and not the gas temperature.

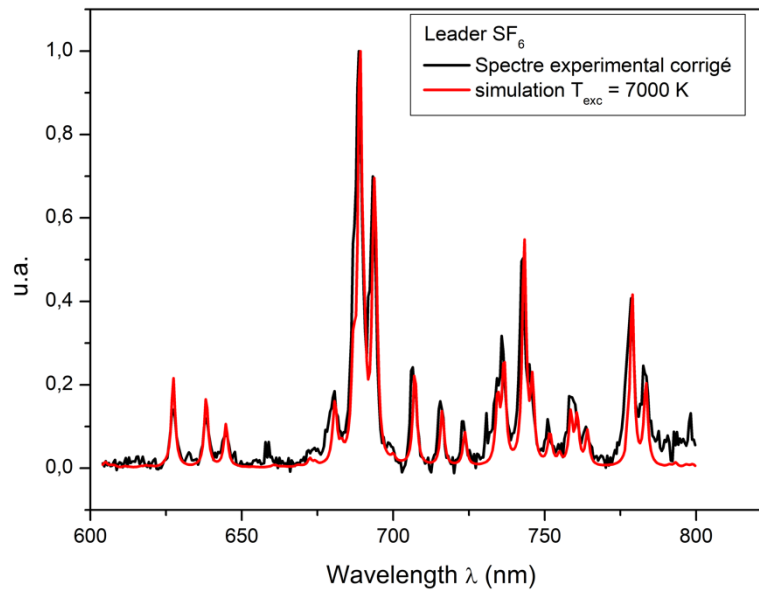


Figure 3. 31 : Example of experimental spectrum of leader in SF₆ (black) with a best fit synthetic spectrum of F I line (red). The experimental spectrum is corrected for the wavelength depending on sensitivity of the spectrometer ($R_c = 0.2$ mm, $d = 50$ mm, $P = 0.1$ MPa)

HFO is a complex gas, and many excited species are present. We find Fe I and II linked to the erosion of the electrode. There are also F I and II, C2, and C I naturally present in the HFO molecule. The electron densities obtained with Stark broadening of the H β and H α lines are in the range $(6.5 - 10) \times 10^{22} \text{ m}^{-3}$ (Figure 3. 32). Spectroscopic measurements of the C2 transition are illustrated in Figure 3. 33 and Figure 3. 34 which show spectra obtained in the breakdown phase and in the leader

phase respectively. The rotational temperature was determined by fitting the spectrum with SPECAIR. The best-fit SPECAIR spectrum yields a rotational temperature of 5000 K in the breakdown phase and in the leader phase. However, the spectrum in Figure 3. 33, seems to show non-Boltzmann behaviour in the C2 rotational population distribution.

The results of the analysis are presented in Table 3. 5. In the case of streamer in air, the gas temperature remains low (400 K) while the temperature in the case of leader in HFO reaches 5000 K.

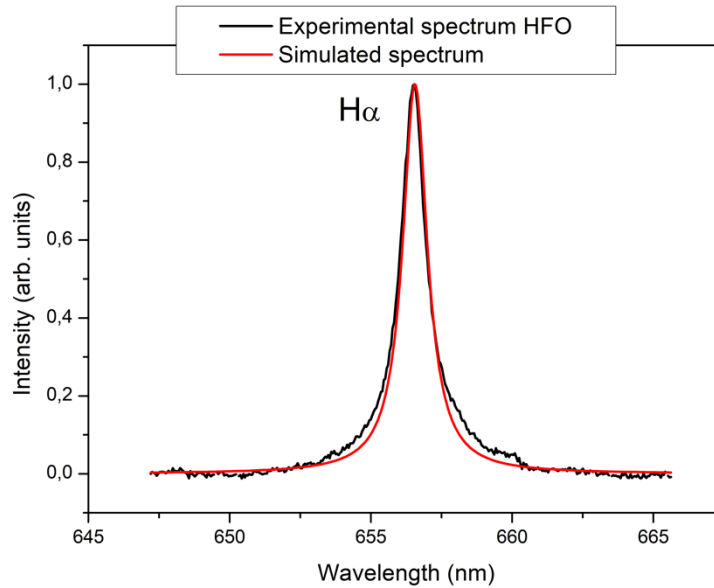


Figure 3. 32 : Example of experimental spectrum of breakdown in HFO (black) with a best fit synthetic spectrum of H α line (red). The experimental spectrum is corrected for the wavelength depending sensitivity of the spectrometer ($R_c = 0.2$ mm, $d = 50$ mm, $P = 0.1$ MPa)

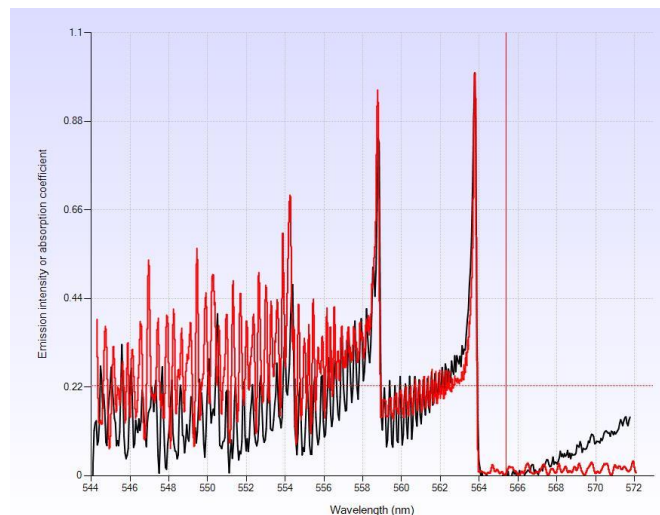


Figure 3. 33 : Example of comparison between the spectrum of C₂ simulated with Specair (red) and the one observed experimentally in HFO during the breakdown (black) with ($T_v = T_r = 5000$ K, $R_c = 0.2$ mm, $d = 50$ mm, $P = 0.1$ MPa, $U_a = 86$ kV)

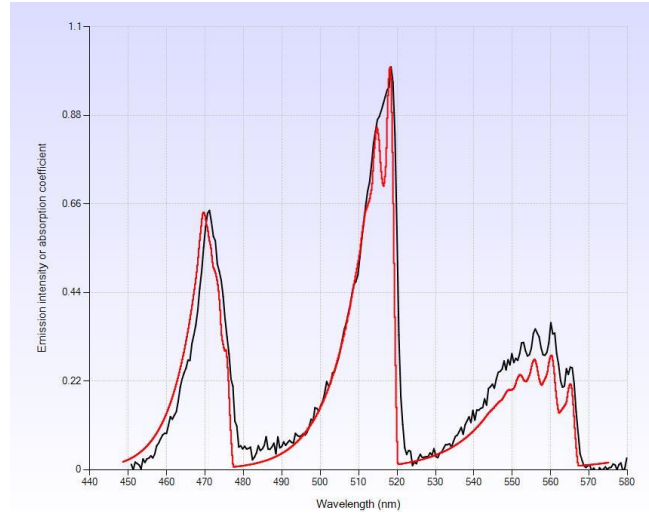


Figure 3. 34 : Example of comparison between the spectrum of C_2 simulated with Specair (red) and the one observed experimentally in HFO during the breakdown (black) with ($T_e = 10000$ k, $T_v = 5300$ K and $T_r = 5000$ K, $R_c = 0.2$ mm, $d = 50$ mm, $P = 0.1$ MPa, $U_a = 67$ kV)

Table 3. 5 highlights the species identified by spectroscopy as well as the corresponding temperature in air, HFO and SF_6 .

Table 3. 5 : Different species identified in HFO, SF_6 and air with corresponding temperatures

Gas	Pre-disruptive phenomenon		Breakdown		
	Species	Temperature (K)	Species	Temperature (K)	N_e (m^{-3})
Air (streamers)	N_2	$T_r = 400 \pm 50$	N I	$T_{exc} = 9000 \pm 500$	
			O I		
		$T_v = 3000 \pm 500$	Fe I and II	$T_{exc} = 10000 \pm 500$	
			$H \alpha$		$N_e = 10^{23} m^{-3}$
HFO (leaders)	C_2	$T_r = 5000 \pm 500$ $T_v = 5300 \pm 500$	$H \beta$		$N_e = 6.5-8.10^{22} m^{-3}$
			$H \alpha$		$N_e = 10^{23} m^{-3}$
			Fe I and II	$T_{exc} = 10000 \pm 500$	
	$H \alpha$	Weak	F I and II	$T_{exc} = 12000 \pm 500$	
			C_2	$T_r = 5000 \pm 500$	
SF_6	F I	$T_{exc} = 7000 \pm 500$	F I	$T_{exc} = 10000 \pm 500$	
			S II	$T_{exc} = 9000 \pm 500$	

3.II.H. Conclusions

The phenomenological behaviour of the HFO discharges in divergent field is very similar to that of SF₆. Stepped leaders propagating at a velocity of 10⁴ m/s are seen, which velocity is independent of the pressure. The time between re-illuminations is proportional to 1/UP and the step propagation length is dependent on the inverse of the pressure.

A clear difference between SF₆ and HFO is however illustrated by the stopping length of the leaders. The leader initiation voltage is lower in HFO than in SF₆. The difference between initiation and breakdown voltage is also smaller in HFO than in SF₆. Negative polarity is less critical than positive polarity, showing much higher initiation and breakdown voltage.

In air, the propagation regime is of the streamer type (between 0.5 and 0.15 MPa/cm) with a velocity of 10⁶ m/s. This propagation regime is also found in HFO and SF₆ for product pressure x distance less than 0.1 MPa/cm, i.e. in conditions not relevant of applications.

3.III. *Breakdown voltage measurements in a divergent field and consequences for insulation design*

3.III.A. Comparison of HFO with air and SF₆

Dielectric design rules for MV switchgear are derived from the electric strength of the gas, determined in realistic field distributions, and with standardized voltage impulses. Generally, the positive lightning impulse wave is the most critical, and is thus used for the design.

Breakdown voltages were measured using the “up and down” statistical method, relevant to characterize self-restoring dielectric materials (such as gases), and/or insulation with a very limited impact of the degradation due to repetitive breakdown experiments (Figure 3. 35 and Figure 3. 36).

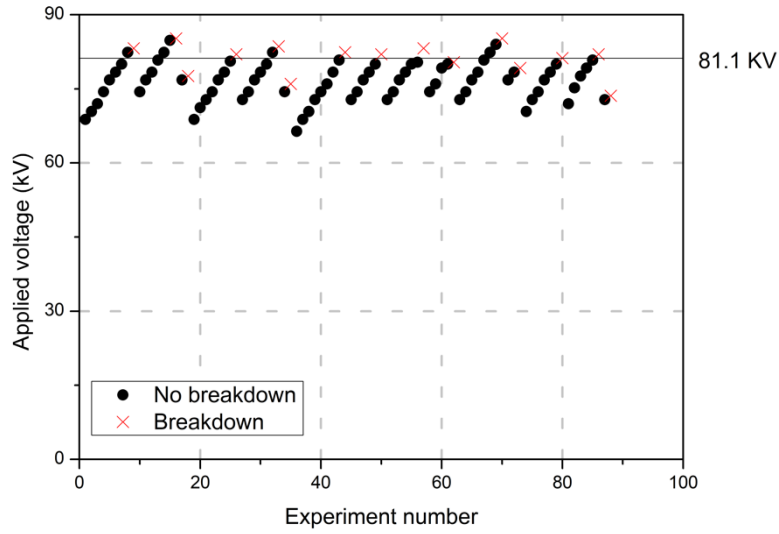


Figure 3. 35 : « Up and down » breakdown measurement for HFO ($R_c = 0.5 \text{ mm}$, $d = 50 \text{ mm}$, $P = 0.1 \text{ MPa}$, $\eta = 40$)

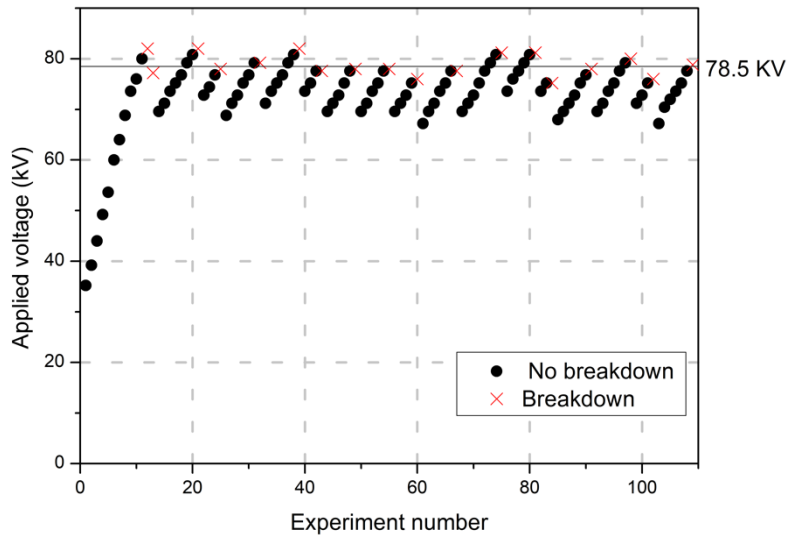


Figure 3. 36 : « Up and down » breakdown measurement for HFO ($R_c = 1.2 \text{ mm}$, $d = 50 \text{ mm}$, $P = 0.1 \text{ MPa}$, $\eta = 21$)

If we consider the breakdown voltage obtained with the "up and down" method for $\eta = 40$, $U_{BD} = 81 \text{ kV}$ (Figure 3. 35). This voltage corresponds to a breakdown probability of 23 % determined with multiple steps method in Figure 3. 5 for $\eta = 40$. For $\eta = 21$, with the "up and down" method, the breakdown voltage is 78.5 kV (Figure 3. 36), this voltage corresponds to a breakdown probability of 16 % in Figure 3. 5 for $\eta = 21$. The "up and down" method used to obtain the breakdown voltage of the different gases gives an estimate of the breakdown probability at $\approx 20 \%$.

Figure 3. 37 and Figure 3. 38 compare the inhomogeneous field impulse breakdown voltage ($R_c = 0.2 \text{ mm}$ and $d = 50 \text{ mm}$) of air, SF_6 and HFO. Very inhomogeneous fields distributions constitute a critical configuration, normally absent in a GIS.

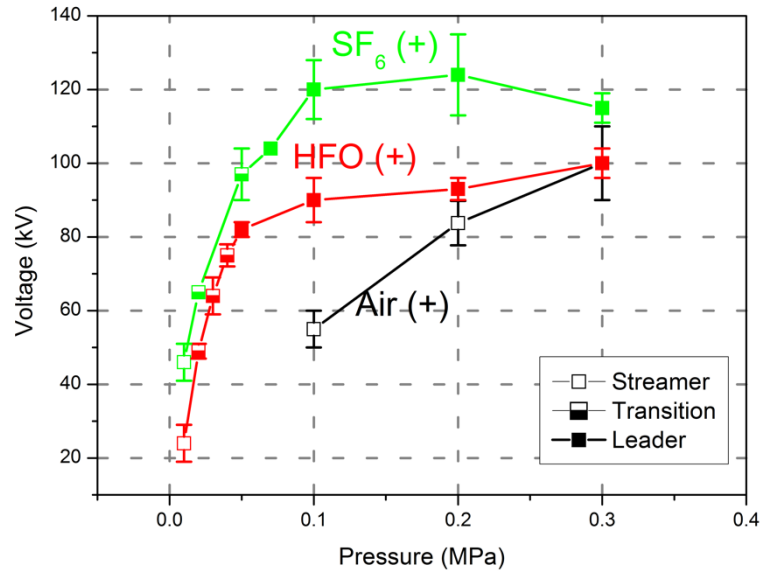


Figure 3. 37 : Average of 15 breakdown voltage in air, SF₆ and HFO as a function of the pressure in positive polarity ($R_c = 0.2$ mm, $d = 50$ mm, max/min error bar) “up and down” method.

In positive polarity (Figure 3. 37), at 0.1 MPa, the breakdown voltage of the HFO is 80 % that of SF₆ and 150 % that of air. At 0.3 MPa, the breakdown voltage for the 3 gases is approximately the same (about 110 kV). When the breakdown regime is of the leader type, the increase in pressure does not influence very much the breakdown voltage (HFO and SF₆ for pressures greater than 0.1 MPa). Conversely, when the breakdown regime is of the streamer type, the increase of pressure induces a large increase of the breakdown voltage (for HFO and, SF₆ at $P < 0.05$ MPa and for air at all pressures).

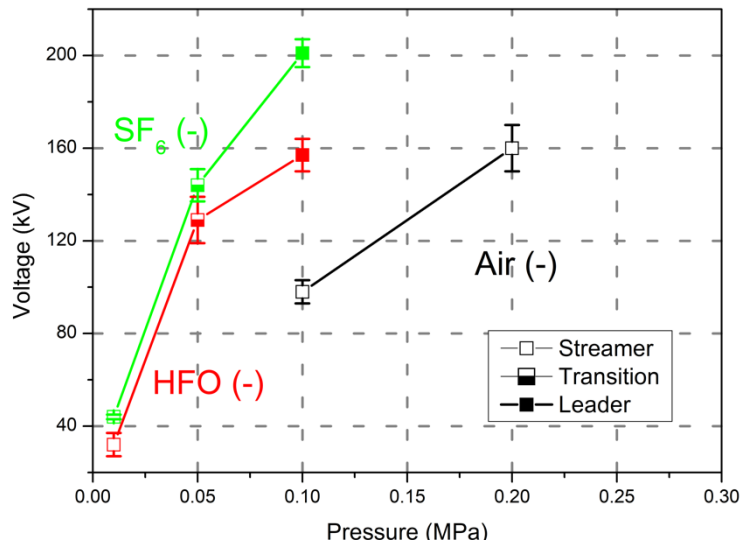


Figure 3. 38 : Average of 15 breakdown voltage in air, SF₆ and HFO as a function of the pressure in negative polarity ($R_c = 0.2$ mm, $d = 50$ mm, max/min error bar) “up and down” method.

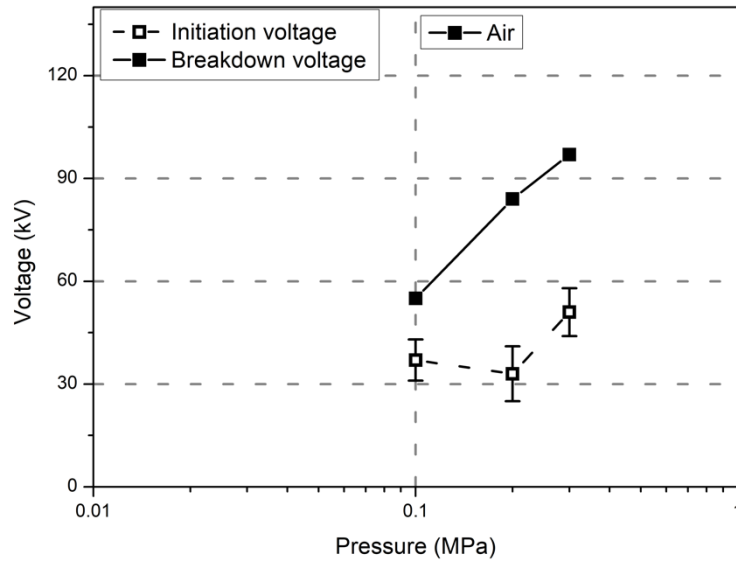


Figure 3.39 : Difference between initiation and breakdown voltage in positive polarity as a function of pressure for air ($R_c = 0.2$ mm, $d = 50$ mm, max/min error bar)

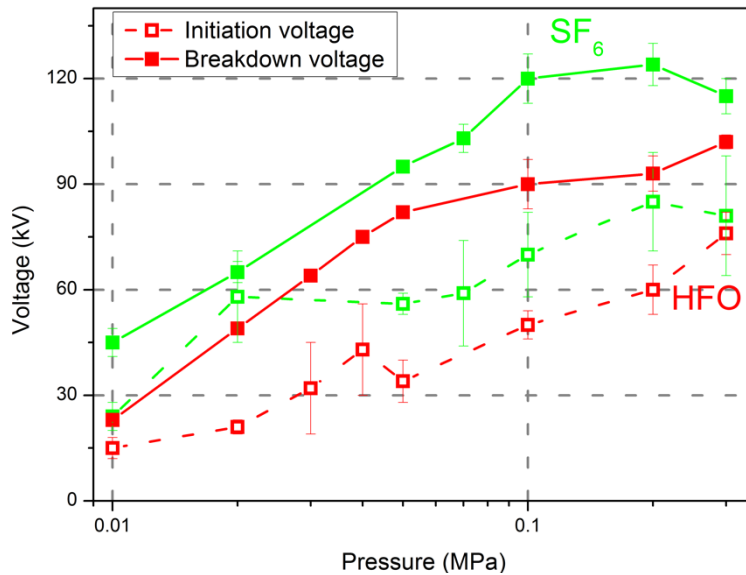


Figure 3.40 : Difference between initiation and breakdown voltage in positive polarity as a function of pressure for HFO and SF₆ ($R_c = 0.2$ mm, $d = 50$ mm, max/min error bar)

An interesting characteristic is the difference between the initiation voltage and the breakdown voltage. In air (streamer mode), the initiation and breakdown voltage increases with pressure (+ 60% between 0.1 and 0.3 MPa, Figure 3.39). This means that streamers already propagate at a voltage 2-3 times lower than the breakdown voltage. In this case the breakdown criteria is not the initiation of the streamer, nor its propagation to the plane [58]. The measured breakdown voltage U_{BD} represents the voltage required to induce a transition from streamer to breakdown, involving secondary streamers. In the same streamer regime in HFO and SF₆ at 0.01 MPa, this difference between U_{BD} and U_i is smaller (about 15 kV in both cases at 0.01 MPa Figure 3.40). This means that the transition from a streamer to a breakdown arc occurs more easily in HFO and SF₆ compared to air.

Concerning streamers, a common hypothesis is that there exists a “stability field”, i.e. a minimal field allowing streamers to propagate. This field would also be the characteristic field present inside the streamer. This hypothesis is guided by the empirical observation that the ratio of applied voltage over maximal streamer length is approximately constant for a fixed gas and polarity, in point–plane and plane-plane geometry. This ratio has the dimension of an electric field. From Figure 3. 37, stability fields ($E_{mean} = U_a/d$) for streamers can be determined in air at 0.1 MPa, SF₆ at and HFO at 0.01 MPa. Table 3. 6 shows the stability field obtained, and the comparison with values from the literature.

Table 3. 6 : Value of the stabilization field from the literature and experimental

Gas	E _{stabilisation} (kV/cm/bar)	References	E _{stabilisation} experimental (kV/cm/bar)
Air	4.4-5	[85], [86]	6.2 – 7.4
SF ₆	40 – 50	[87]	48 – 46
HFO	No data		30

In air, the stabilization field must be greater than 5 kV/cm/bar for streamers to propagate up to the plane. In our measurements, the average field is greater than 6 kV/cm/bar, and streamers logically propagated up to the plane.

In SF₆ at 0.01 MPa, the experimental stabilization field is greater than the theoretical one, and streamers also propagated to the plane.

In HFO at 0.01 MPa the stabilization field is not known. From our measurements, the stabilization field of streamers is approximately 30 kV/cm/bar, i.e. slightly lower than in SF₆.

Concerning leaders in HFO and SF₆ ($P > 0.05$ MPa), U_i increases when the pressure increases but the breakdown voltage is much less affected. The values of leader initiation voltages in SF₆ are higher than in HFO (+ 30% at 0.01 and 0.1 MPa) in agreement with those derived the stopping length plot (Figure 3. 23).

3.III.B. Consequences for the insulation design in HFO under impulse voltage with inhomogeneous field

Several practical first conclusions can be derived from the data obtained under inhomogeneous field, regarding the insulation design under impulse voltage

3.III.B.i. Leader minimum propagation voltage versus distance.

In point-plane gap, Chalmers et al [79] show that when the pressure is lower than P_I (Figure 3. 41), the breakdown in SF₆ is of the streamer type and increases with pressure (a). Above P_I , when the applied voltage wave is of pulsed type, breakdown results from leader propagation, and the breakdown

voltage shows a plateau (b). Under AC or DC, it goes through a maximum value due to corona stabilisation, and then decreases. The streamer onset voltage increases linearly with the pressure, and becomes equal to the breakdown voltage at a pressure noted P_c that depends on the geometry. This critical pressure decreases when the field becomes more homogeneous.

The increase at low pressure (a) and the plateau (b) are also observed in our measurements with HFO under impulse (Figure 3. 42), with P_I about 0.05 MPa. In our measurements, the critical pressure P_c is equal to 0.2 MPa for $R_c = 2$ mm. For other R_c , it would be necessary to take measurements at higher pressures.

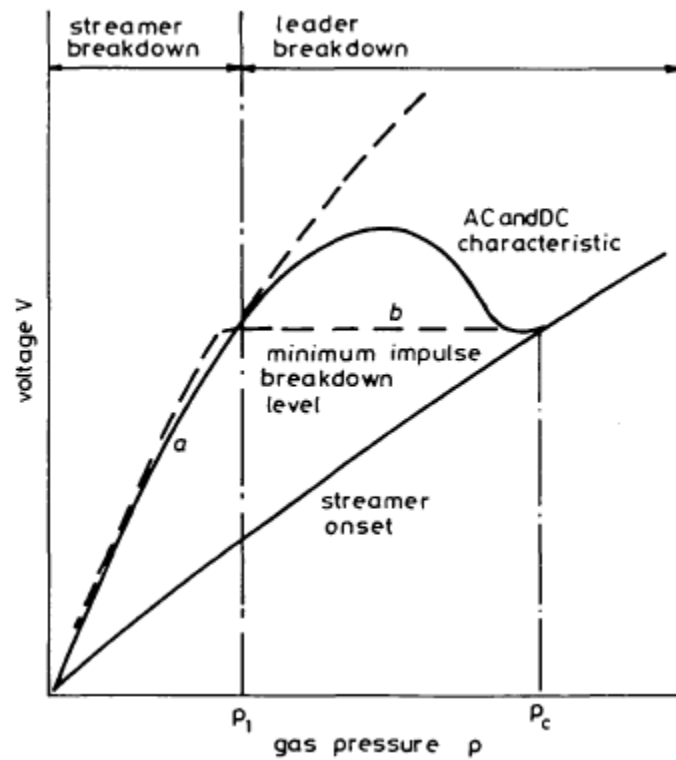


Figure 3. 41 : Idealised V/P characteristic for a point-plane gap in SF_6 [79]

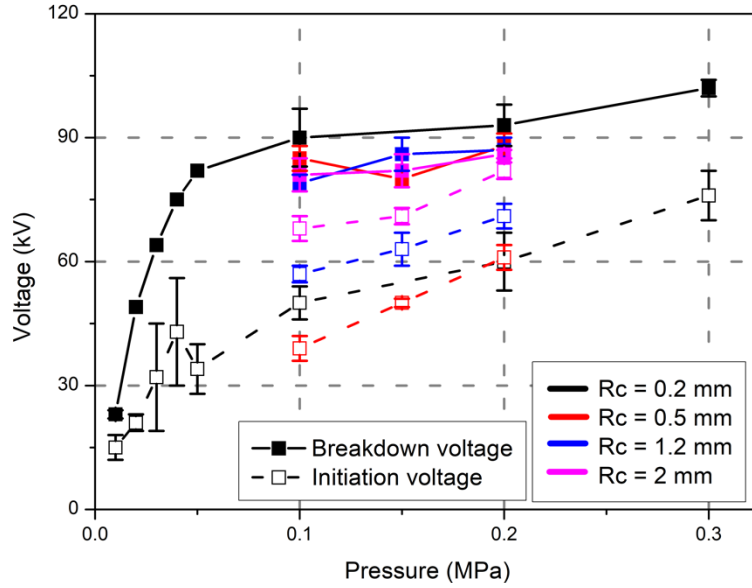


Figure 3.42 : Initiation and breakdown voltage in positive polarity as a function of pressure for HFO ($d = 50$ mm, max/min error bar)

On Figure 3.42 it is interesting to observe that the initiation voltage increases with electrode radius R_c and pressure. Conversely, above 0.05 MPa the breakdown voltage U_{BD} (i.e. the voltage required for leader propagation up to the plane) remains almost unchanged when R_c and pressure are changed. When distance is increased (Figure 3.43), the breakdown voltage (i.e. leader propagation voltage U_p) increases, since leaders must cross a longer distance to induce breakdown (their stopping length increases with voltage, see Figure 3.23).

With the available data, it is possible to show the influence of the distance on the leader propagation voltage (see Figure 3.23). This plot can be fitted according to:

$$U_p = 14.1341 \times d^{0.45291} \quad (9)$$

with U_p the voltage in kV, and d the distance in mm.

This equation provides the breakdown voltage (with a probability of about 20 %) that may occur in slightly degraded HFO, whatever the pressure and electrode radius, provided breakdown is in propagation-controlled mode (i.e. $\eta > 10$). A similar variation is observed in SF₆, with breakdown voltage about 30 % higher.

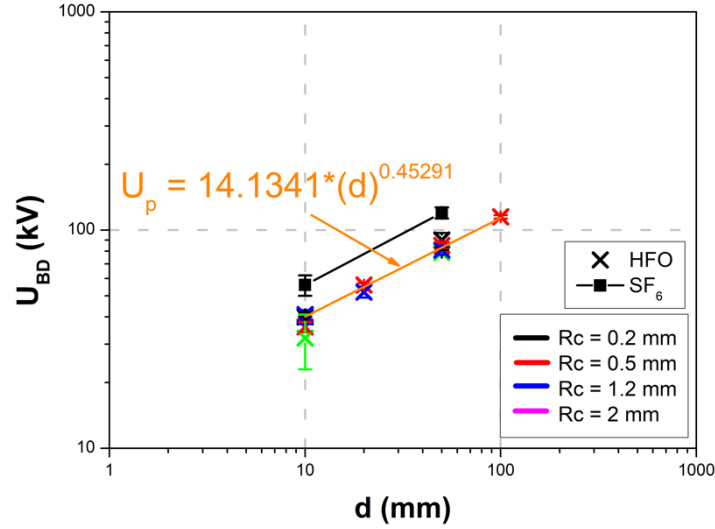


Figure 3. 43 : Leader propagation voltage U_p in HFO as a function of distance ($P = 0.1$ MPa).

The slope of the $U_p(d)$ plot in Figure 3. 43 corresponds to the average longitudinal field existing along the leader channel [88]. In HFO, the slope at 0.1 MPa is 0.9 kV/mm, compared to 1.6 kV/mm in SF₆. This confirms that leader propagation in HFO is easier (more conducting channel), as previously concluded from stopping length measurements. Figure 3. 43 also confirms that leader propagation does not depends on R_c .

3.III.B.ii. Criterion for leader initiation

In the general case, breakdown in HFO can then be described with two typical parameters:

- An initiation voltage U_i that depends on pressure and electrode radius R_c ;
- A “total propagation voltage” U_p almost independent on pressure and radius R_c , that changes with distance d . U_p is provided by equation 9.

Depending on parameters (R_c , d , P), two typical cases can occur:

- when $U_i < U_p$, breakdown is propagation-controlled, and $U_{BD} \approx U_p$;
- when $U_i > U_p$, breakdown is initiation-controlled, and $U_{BD} \approx U_i$.

In propagation-controlled conditions ($\eta > 10$), the Figure 3. 43 shows the variation of the propagation voltage U_p versus distance, directly providing the value of breakdown voltage whatever the electrode radius and pressure. Below this curve, no breakdown can occur in HFO. It should be noted that U_p in HFO is 70 % that of SF₆, whatever the distance.

In initiation-controlled mode, since initiation is primarily related to the maximum field in the gap, it is interesting to calculate the maximum field E_i occurring at the initiation voltage U_i with different electrode geometries (R_c , d). As the distance increases with fixed R_c (Figure 3. 43), the breakdown

voltage increases, but E_i remains constant for HFO and SF₆ (Figure 3. 44). When the radius of curvature R_c , is increased, E_i decreases. This shows that the maximum field in the gap does not constitutes a sufficient criterion to predict the initiation voltage. This has been observed in gases since a long time.

A much better criterion is provided by the “streamer criterion” ($\int_0^x \bar{a} dx = K_{str}$), considering that the initial avalanche must reach a minimum size to initiate a discharge (see chapter 1). Unfortunately data required to calculate this criterion in HFO (multiplication and attachment parameters) are not available today in the literature. Comparisons between the streamer criterion and measurements in air and SF₆ will be carried out in next chapter 4, with less divergent field.

Figure 3. 44 also shows that E_i with HFO and SF₆ with $R_c = 0.2$ mm and 1.2 mm are close. Notice that this conclusion is valid for HFO slightly degraded by repetitive low energy discharges in our experiments. This suggests that methods already used to predict initiation in SF₆ would provide a reasonable estimation for HFO. This assumption will be discussed in chapter 4.

Figure 3. 45 shows E_i in HFO for the different radius of curvature at different pressure for a distance of 50 mm. At 0.2 MPa, the initiation field is higher than at 0.1 MPa. The pressure has indeed an effect on the initiation but not on the propagation nor on the breakdown in divergent field. A more elaborated analysis of initiation, integrating results obtained with initiation–controlled breakdown conditions will be presented in next chapter.

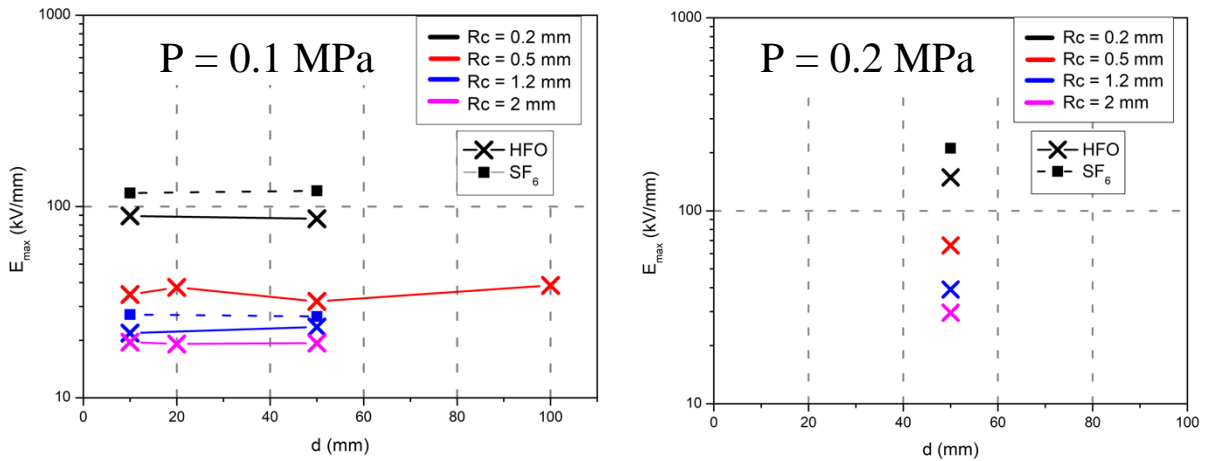


Figure 3. 44 : Value of the initiation field E_i as a function of the distance when the breakdown is controlled by propagation ($P = 0.1$ and 0.2 MPa)

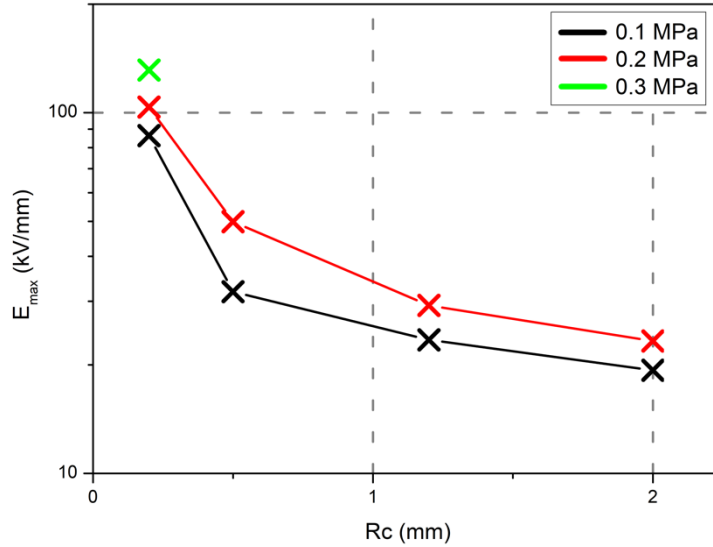


Figure 3. 45 : Value of the initiation field E_i as a function of R_c when the breakdown is controlled by propagation in HFO ($d = 50$ mm)

3.III.B.iii. Influence of high voltage impulse shape.

In addition to breakdown voltage measurements, the initiation and breakdown delay times provide additional information relevant for the practical properties of the gas.

Figure 3. 46 and Figure 3. 47 showing t_i and t_{BD} versus calculated maximum field E_i at the tip are complicated to understand because they represent all measurements made when the breakdown is controlled by the propagation. Let's focus only on the position of the points, and not on the electrode configuration, nor on the pressure used.

- Zone A corresponds to a time lower than the rise time of the pulse wave used ($0.8 \mu\text{s}$). Pre-discharges phenomena in HFO (Figure 3. 46) appear nearly always during this rise time with propagation-controlled conditions. Therefore, t_i does not represents a purely statistical delay time, but it is strongly affected by the rise time of the wave;
- Zone B in Figure 3. 46 shows that longer initiation times up to $2 \mu\text{s}$ can be observed only at low E_i values, i.e. with large $R_c > 1$ mm. This tendency will be confirmed in chapter 4 with larger R_c .

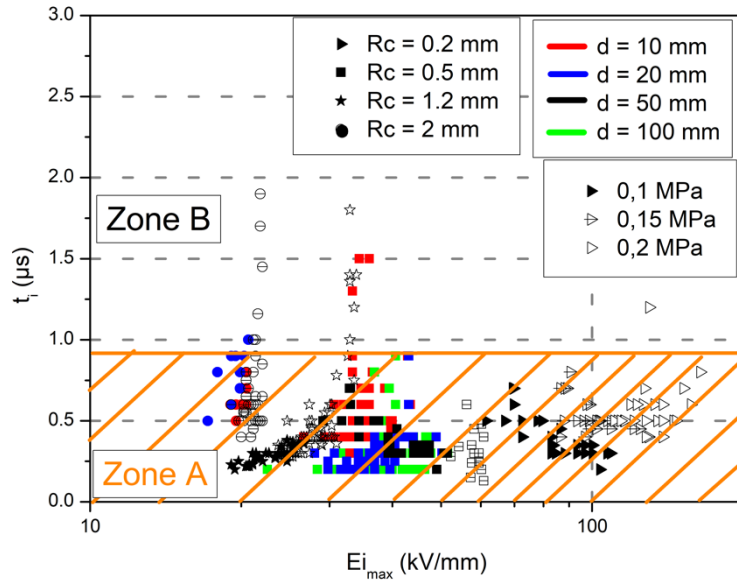


Figure 3.46 : Delay time to initiation when the breakdown is controlled by propagation in HFO in positive polarity

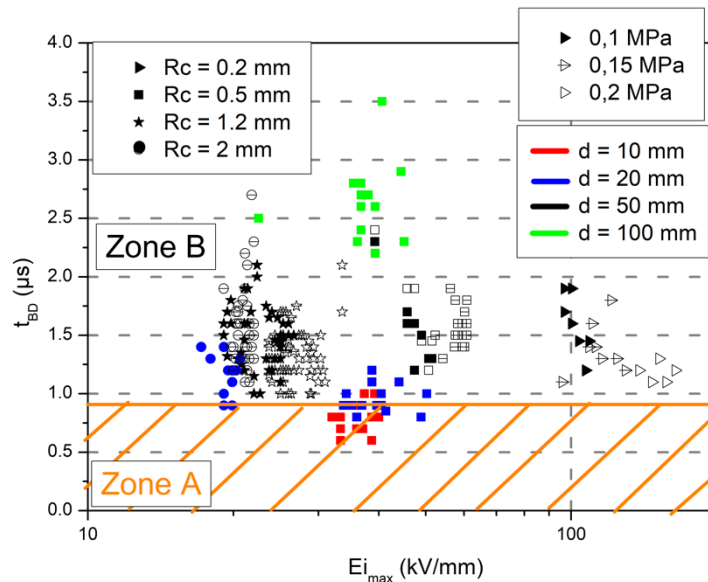


Figure 3.47 : Delay time to breakdown when the breakdown is controlled by propagation in HFO in positive polarity

Figure 3.47 illustrates the breakdown delay time t_{BD} in HFO (i.e. the sum of t_i + leader propagation time). The majority of breakdowns occurs around the maximum voltage (between 1 and 4 μs in zone B). In our measurements the fall time of the voltage wave is long (1400 μs). However, since $t_{BD} < 4 \mu\text{s}$, one may conclude that with the shorter 1.2/50 μs standard wave (fall time at half value: 50 μs), no large impact on measured breakdown voltage should occur. One again, this conclusion is valid only for slightly degraded HFO. We will see in the next chapter that large deviations from this conclusion will occur with less divergent fields and non-degraded HFO.

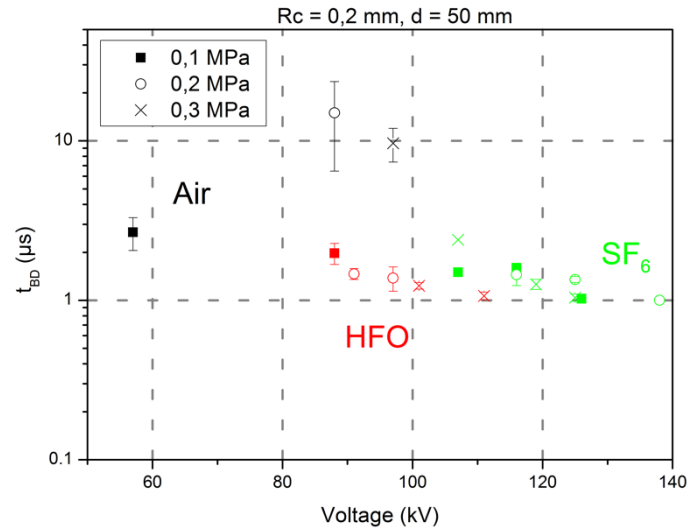


Figure 3. 48 : Average of 15 breakdown delay time as a function of voltage for air, HFO and SF₆ (R_c = 0.2 mm, d = 50 mm, max/min error bar) in positive polarity

Comparable short breakdown delays (a few μs) are seen both in degraded HFO and SF₆ (Figure 3. 48). In air, the breakdown delay time in identical conditions is much greater. This phenomenon is related to the long statistical delay for initiation of discharges in the air (up to more than 20 μs in Figure 3. 20.) One may conclude than in air, the high voltage impulse shape should get a larger influence compared to SF₆ and HFO. A slight increase of breakdown voltage should occur in air with shorter impulse such as the standard lighting pulse.

Chapter 4: Characterization of HFO in a weakly divergent field and study of gas degradation

4.I. Introduction

As detailed in the previous chapter, depending on the geometry two breakdown modes have been identified. In inhomogeneous field, the breakdown is controlled by the propagation of the pre-discharges (Chapter 3) and in a quasi-homogeneous field, the breakdown is controlled by the initiation of these pre-discharges (Figure 3. 8, $\eta < 10$).

In this chapter, only breakdown controlled by initiation will be studied, in the electrode configurations of Table 4. 1 with $\eta < 10$.

Table 4. 1 : Electrode configurations studied in this chapter

R_c (mm)	d (mm)	η	Gas	Pressure (MPa)	Polarity	Wave
2	10	5	HFO	0.1	+	STI
	20	8		0.1	+	STI
3.5	10	3.2	HFO	0.13	+/-	LI
5	10	2.5	HFO, SF ₆ , air	0.1 to 0.3	+/-	STI, DC
	20	4	HFO	0.1	+	STI
	50	7	HFO	0.1, 0.15, 0.2	+/-	STI
10	10	1.8	HFO	0.1	+	STI
	20	2.5	HFO	0.1	+	STI

4.II. Breakdown voltage and delay time to breakdown in HFO in quasi-homogeneous field

4.II.A. Examples of breakdown voltage measurements in HFO

When the field is quasi-homogeneous, a large difference is observed between the breakdown voltage of the 1st experiment within a series and the following ones. A significant drop of dielectric strength is observed between the first breakdown and the following. Figure 4. 1, Figure 4. 2, and Figure 4. 3 illustrate this phenomenon. These measurements are obtained when the electrodes and the test cell are initially well cleaned (with ethanol), and when the HFO is new at the beginning of series.

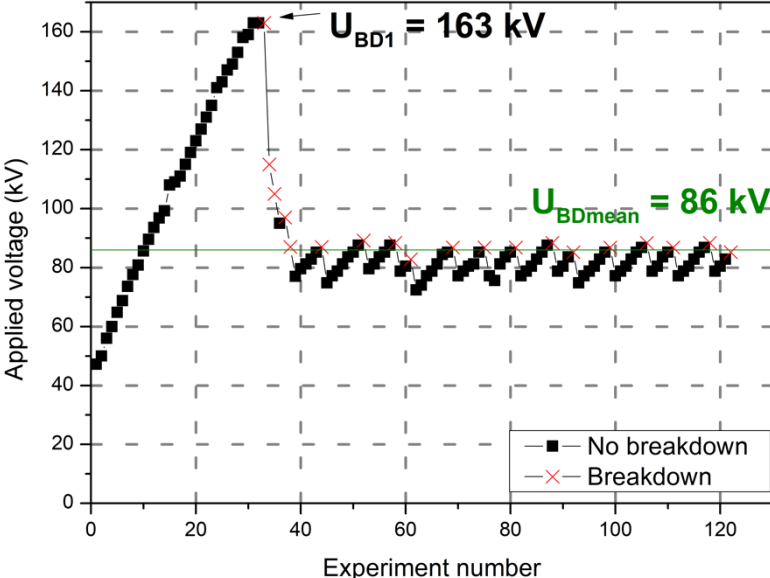


Figure 4. 1 : Up and down measurement series in HFO including 120 shots ($R_c = 5 \text{ mm}$, $d = 50 \text{ mm}$, $P = 0.1 \text{ MPa}$, $\eta = 7$)

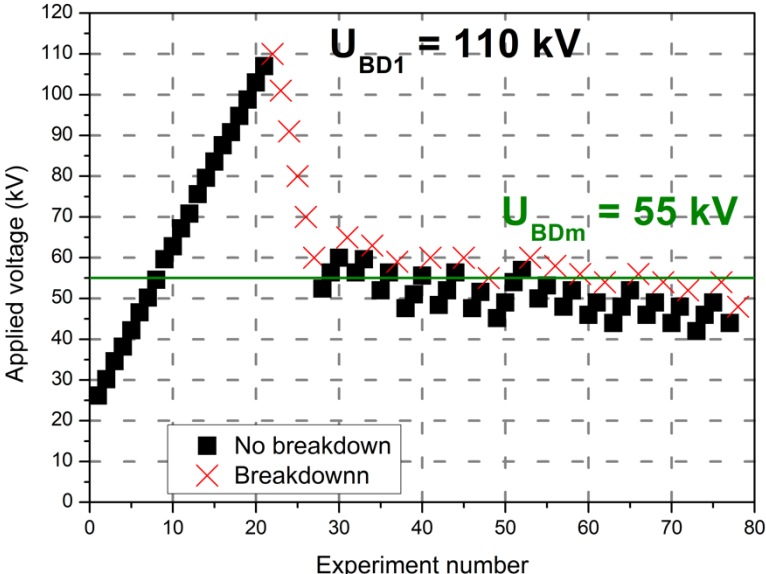
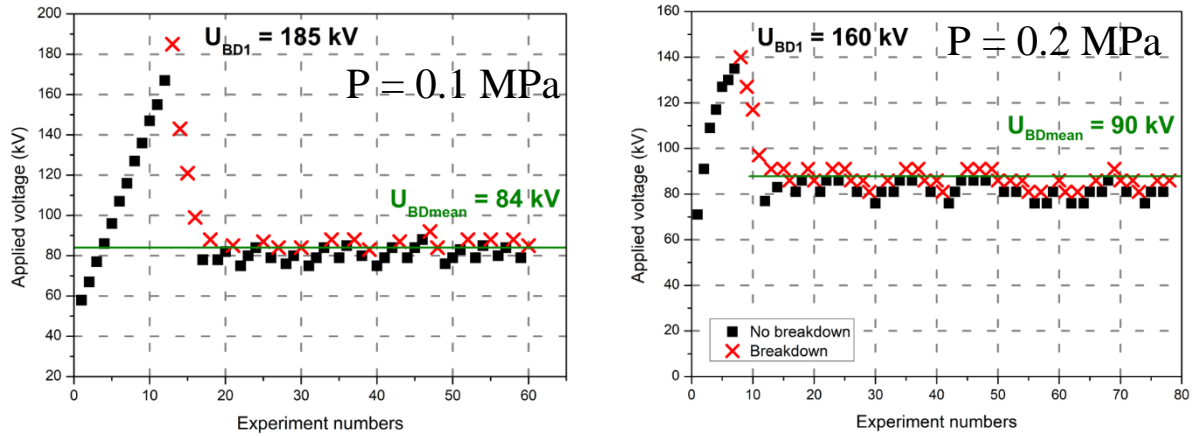


Figure 4. 2 : Up and down measurement series in HFO including 80 shots ($R_c = 5 \text{ mm}$, $d = 10 \text{ mm}$, $P = 0.1 \text{ MPa}$, $\eta = 2.5$)


 Figure 4. 3 : Up and down measurement series in HFO for different pressure ($R_c = 10$ mm, $d = 20$ mm, $\eta = 2.5$)

Whatever the distance or the pressure, the observation is the same: a large drop of the dielectric strength immediately occurs after the first breakdown, and U_{BD} becomes stable afterwards. For the rest of the discussion, the 1st breakdown U_{BD1} and the average of subsequent breakdown voltage U_{BDm} are to be distinguished.

Table 4. 2 shows all the breakdown voltages measured for the different geometries where the breakdown is controlled by the initiation. The initiation of subsequent discharges is strongly facilitated by the gas degradation occurring during the first shot. The relative drop of U_{BD} is larger when the field factor η is lower.

Table 4. 2 : Breakdown voltage measurements of HFO in different electrode configurations (impulse voltage of positive polarity)

R_c (mm)	d (mm)	η	P (MPa)	U_{BD1} (kV)	U_{BDmean} (kV)	U_{BD1}/U_{BDmean}
2	10	5	0.1	65	41 ± 1	1.58
	20	8	0.1	75	52 ± 3	1.45
3.5	10	3.2	0.1	94	78 ± 3	1.20
5	10	2.5	0.1	120 ± 11	55 ± 5	2.18
			0.2	141	94 ± 2	1.50
			0.3	236	121 ± 3	1.95
	20	4	0.1	125	64 ± 2	1.95
	50	7	0.1	163	93 ± 3	1.75
10	10	1.8	0.1	112	68 ± 6	1.65
	20	2.5	0.1	171	84 ± 2	2.03

4.II.B. Breakdown voltage in HFO in comparison with air and SF₆ in weakly divergent field

In this part, the values quoted as “new HFO” corresponds to the values of the first breakdown. New HFO corresponds to a well cleaned test cell, electrodes, and HFO having undergone no previous discharges. No statistical treatment was carried out on these values provided the small number of data obtained, due to the difficulty of repeating these experiments many times. The values quoted as “degraded HFO” corresponds to the average of the breakdown voltage U_{BDm} consecutive to the 1st.

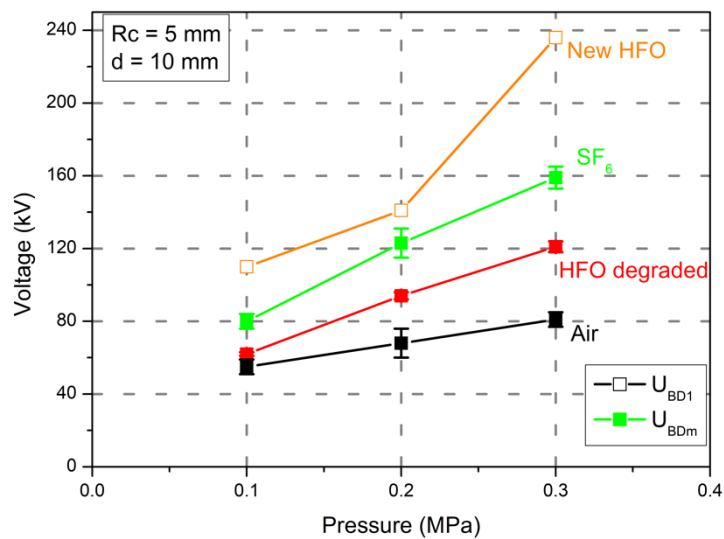


Figure 4. 4 : Breakdown voltage in air, HFO and SF₆ as a function of pressure. Up and down method, quasi-homogeneous field ($\eta = 2.5$, $R_c = 5$ mm, $d = 10$ mm, max/min error bar)

When the HFO is new, its dielectric strength is clearly higher to that of SF₆ (130 % of SF₆ at 0.1 MPa and 160 % at 0.3 MPa, Figure 4. 4). Since the breakdown is controlled by the initiation, the pressure has a large positive influence on the dielectric strength in the three gases.

After the 1st breakdown, the breakdown voltage of the HFO drops to 80 % that of the SF₆, and remains higher than that of the air. No similar drop is recorded in air and SF₆, and no comparable effect was previously reported in other gases in the literature. At 0.1 MPa, the degraded HFO unfortunately shows properties similar to air, and 50 % better at 0.3 MPa.

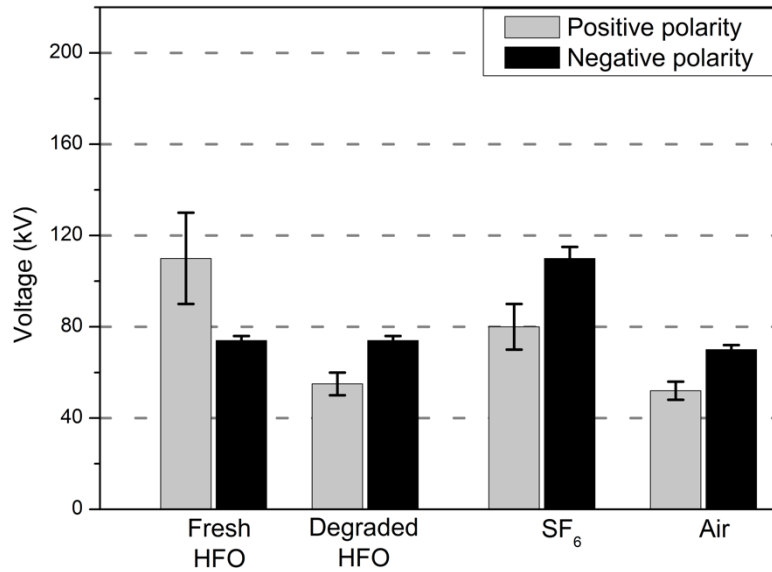


Figure 4.5 : Influence of the polarity on the breakdown voltage in a quasi-homogeneous field (Up and down method, $\eta = 2.5$, $R_c = 5$ mm, $d = 10$ mm, $P = 0.1$ Mpa, max/min error bar)

Another information concerns the polarity. In negative polarity, the first breakdown value in HFO is lower than in positive, contrary to other gases. However, no difference is observed between the 1st negative breakdown and the following ones (Figure 4.5). In degraded HFO, the situation becomes comparable with other gases (i.e. lower breakdown voltage in positive polarity). The dielectric strength of HFO in negative polarity is 60 % that of SF₆ and comparable to air. The very specific behaviour of HFO can be summarized by its unexpectedly high breakdown strength in positive polarity, in “clean” conditions.

4.II.C. Geometries influencing the loss of dielectric strength of HFO

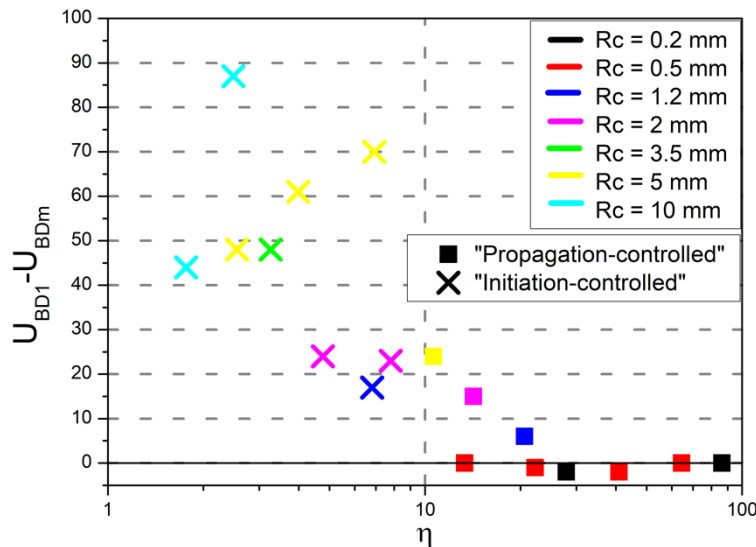


Figure 4.6 : Difference between the 1st breakdown voltage U_{BD1} and the average breakdown voltage U_{BDmean} depending on the amplification factor of the field η ($P = 0.1$ MPa)

In all cases, when initiation controls breakdown, immediately after the first breakdown the breakdown voltage becomes stable (standard deviation less than 5 kV). Figure 4. 6 shows that the loss of dielectric strength is observed when the field amplification factor η is less than 10, i.e. when breakdown is controlled by initiation. It is obvious that gas degradation during 1st breakdown has a large influence on initiation in positive polarity, and negligible on leader propagation.

As this loss of dielectric strength is related to initiation, it is relevant discuss it in terms of maximum field E_{max} at the high voltage electrode, i.e. where initiation occurs. To assess the influence of geometry, the difference (in percentage) between the first breakdown (U_{BD1}) and the average breakdown voltage (U_{BDmean}) is plotted versus the maximum field (E_i) calculated at the breakdown voltage (i.e. at the initiation voltage) in Figure 4. 7.

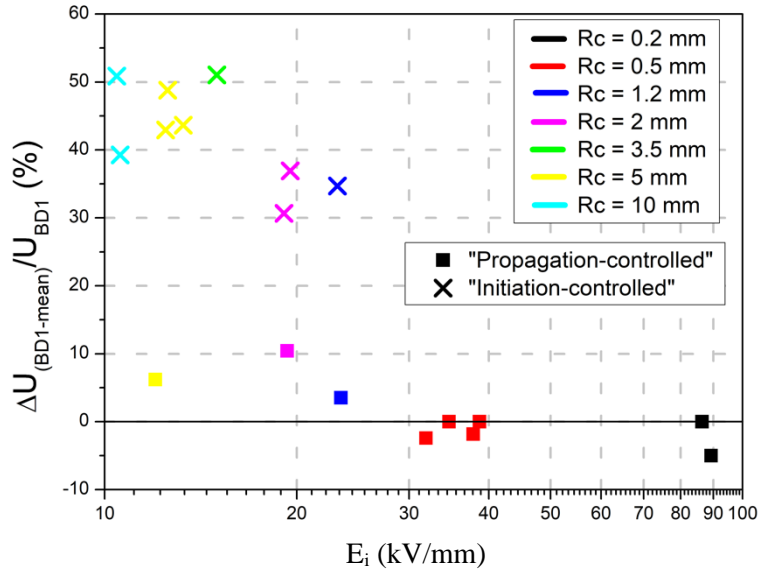


Figure 4. 7 : Maximum initiation field at the electrode as a function of the difference between U_{BD1} and U_{BDm} ($P = 0.1$ MPa)

For values of E_i greater than 30 kV/mm, the 1st breakdown has no deleterious effect. When the values of E_i are less than 30 kV/mm (at 0.1 MPa), the 1st breakdown occur at a value clearly greater than the following.

4.II.D. Delay to breakdown

In order to better understand the consequences of degradation, the study of the breakdown delay time provides additional information (Figure 4. 8 and Figure 4. 9). The breakdown time with either new or degraded HFO is close to 2 μ s when $E_i > 30$ kV/mm. When the maximum field is lower ($E_i < 30$ kV/mm), a large difference appears between the delay time of the 1st breakdown t_{BD1} and the subsequent ones. t_{BD1} shows a large scatter, and may rise to 100 μ s (Figure 4. 8). The lower the field, the higher the maximum delay. Following the 1st breakdown, the breakdown delay times return to a

“normal” value of less than 10 μs , even at low field. In the degraded HFO (Figure 4. 9) delays become comparable to SF_6 in identical conditions (Figure 4. 10), i.e. less than 10 μs .

In a weakly inhomogeneous field ($\eta < 10$, $E_i < 30$ kV/mm at 0.1 MPa), the gas degradation by the 1st breakdown strongly facilitates the initiation of subsequent discharges. If a standard lighting wave was used (voltage drop of 50 % at 50 μs), breakdown would not occur with delay times greater than 50 μs . This indicates that the breakdown voltage with new HFO would be even higher with a standardized lightning impulse than with our long duration impulse. Conversely, this phenomenon should not occur in degraded HFO when $t_{BD} < 10$ μs .

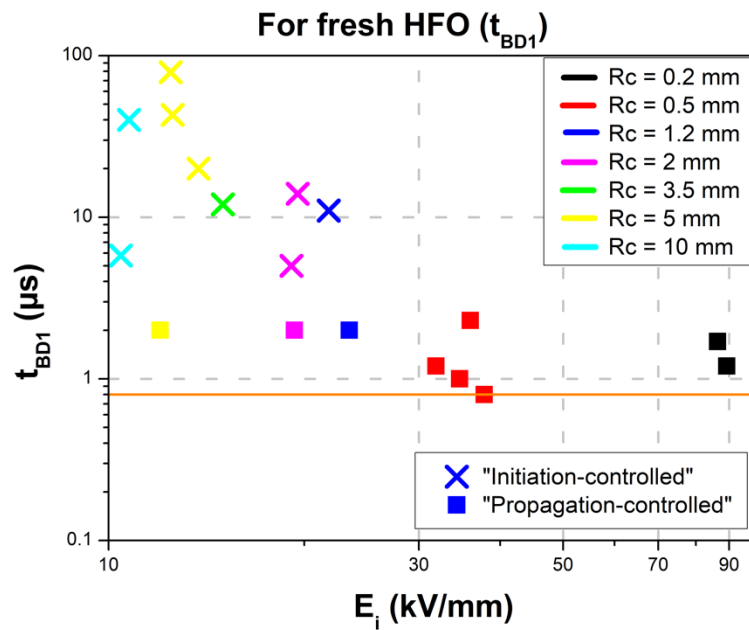


Figure 4. 8 : Delay time for the 1st breakdown in the HFO as a function of the geometry ($P = 0.1$ MPa). Orange line corresponds to the voltage rise time

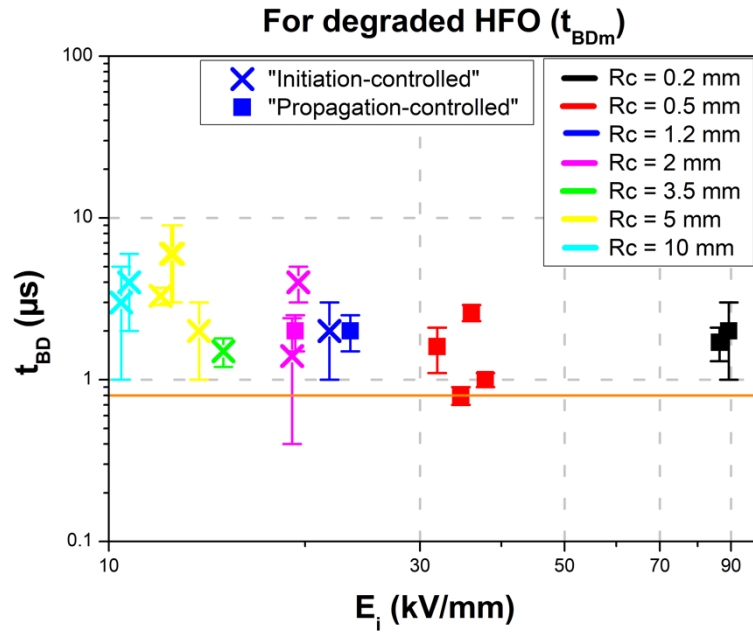


Figure 4. 9 : Average delay time to breakdown in the HFO as a function of the geometry ($P = 0.1$ Mpa, max/min error bar). Orange line corresponds to the voltage rise time

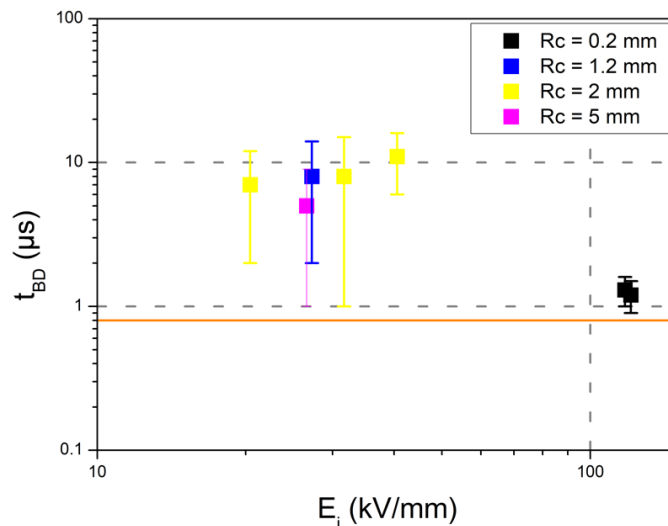


Figure 4. 10 : Average delay time to breakdown in the SF_6 as a function of the geometry ($P = 0.1$ Mpa, max/min error bar). Orange line corresponds to the voltage rise time

4.II.E. Propagation velocity

The propagation time deduced from breakdown measurements ($t_{BD} - t_i$) mainly depends on the applied voltage. Figure 4. 11 shows that when the voltage increases, the propagation time decrease. Shorter propagation times are also logically recorded at shorter distances (10 and 20 mm), but quite few data were obtained in such conditions.

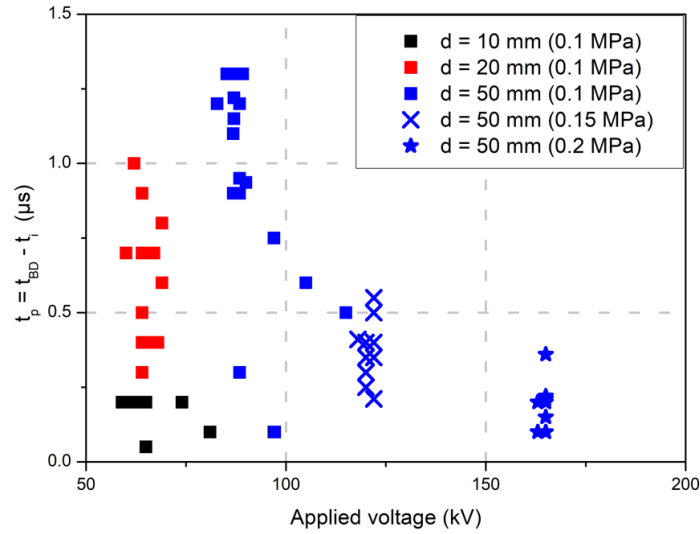


Figure 4. 11 : Propagation time as a function of voltage, and pressure in the degraded HFO ($R_c = 5 \text{ mm}$, $d = 50 \text{ mm}$)

From the propagation time (Figure 4. 11), the propagation velocity is calculated (Figure 4. 12). In this figure, the data obtained in divergent field and propagation-controlled conditions (chapter 3) are plotted with those obtained here in initiation-controlled conditions. The increase of propagation velocity when the applied voltage is raised at fixed distance is observed over a wider voltage range, whatever the pressure and electrode radius. The propagation velocity increases by nearly one decade (3×10^4 to $3 \times 10^5 \text{ m/s}$) when the voltage is doubled.

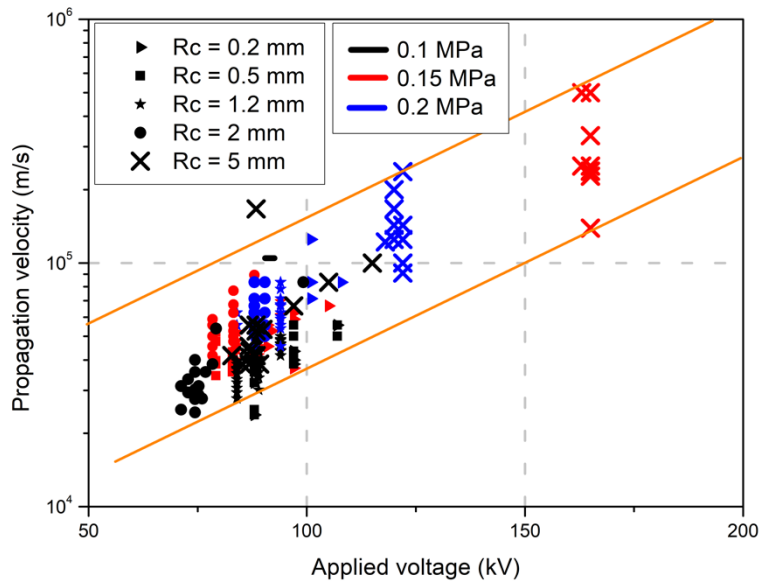


Figure 4. 12 : Propagation velocity as a function of pressure in the degraded HFO for different R_c and pressure ($d = 50 \text{ mm}$)

4.III. *Origin of the drop of initiation field in HFO after the 1st breakdown*

4.III.A. Influence of test cell cleaning and gas renewal

Different experiments were performed (in a single configuration $R_c = 5$ mm, $d = 10$ mm, and $\eta = 2.5$) in order to better understand this effect. In this configuration Figure 4. 13, the 1st breakdown is at $U_{BD1} = 120$ kV and the average of the following breakdowns at $U_{BDm} = 55$ kV.

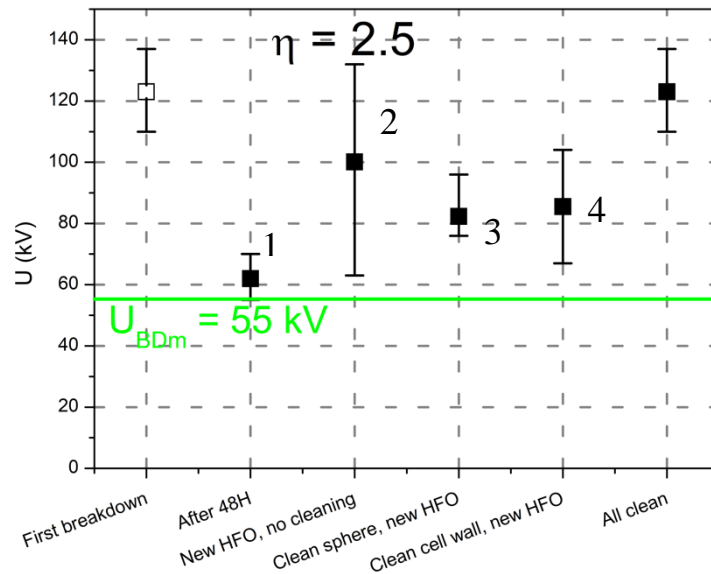


Figure 4. 13 : Various tests to understand the origin of the loss of dielectric strength after the 1st breakdown ($R_c = 5$ mm, $d = 10$ mm, $P = 0.1$ MPa)

To understand the origin of the loss of dielectric strength of the HFO, the following experiments are carried out:

1. After 20 breakdowns in the HFO, the gas remained in the cell for 48 hours. After this time, a new series of measurements was carried out. Figure 4. 13 shows that despite waiting, the breakdown voltage remains around 60 kV;
2. Several series of measurements were carried out by changing the gas after a breakdown (without opening or cleaning the cell). In the Figure 4. 13, the renewal of gas does not make it possible to restore the initial dielectric properties of the HFO, and the scatter is very important, from 120 to 60 kV;
3. Only the HV electrode is cleaned and the HFO is replaced. In this case, the breakdown voltage remains quite low (66% of the 1st breakdown);
4. Only the plane electrode and the cell walls are cleaned, and the HFO is replaced. In this case, the voltage is 72% that of the 1st breakdown.

These measurements suggest that the presence of fine powder by-product (on the electrodes, on the cell walls, and possibly in the gas volume) has a major influence on breakdown: only the complete cleaning allows restoring the initial breakdown value.

4.III.B. Evidence of the influence of solid by-products on discharge initiation

To further evaluate the effect of the pollution by powder on the dielectric strength, another procedure was followed with two different geometries. The first geometry for a $\eta = 9$ ($R_c = 1.2$ mm and $d = 10$ mm, Figure 4. 15) and the second with a $\eta = 2.5$ ($R_c = 5$ mm and $d = 10$ mm, Figure 4. 14).

- A first series of 30 shots was carried out in SF₆ with the test cell initially cleaned. This series corresponds to the fresh SF₆ of Figure 4. 14 for $\eta = 2.5$, and Figure 4. 15 for $\eta = 9$. This gives us the initial breakdown voltage of SF₆ in the 2 configurations;
- SF₆ was replaced by HFO, without opening the test cell. With 30 shots, we obtain the U_{BDl} and the U_{BDm} of HFO. After the first shot, a deposit of thin black powder formed on electrodes and the breakdown dropped. This series corresponds to the column “Replace SF₆ with HFO” in Figure 4. 14, and Figure 4. 15;
- HFO was replaced by SF₆ without opening or cleaning anything. In Figure 4. 14, and Figure 4. 15, the SF₆ breakdown voltage is now equivalent to that of degraded HFO after the 1st breakdown. The powder deposit on the electrodes therefore has a large effect on the dielectric strength of both HFO and SF₆, by facilitating discharge initiation in both gases;
- Finally, we put HFO back in place of SF₆. This showed a slight increase in dielectric strength of the HFO, but without restoring its initial properties.

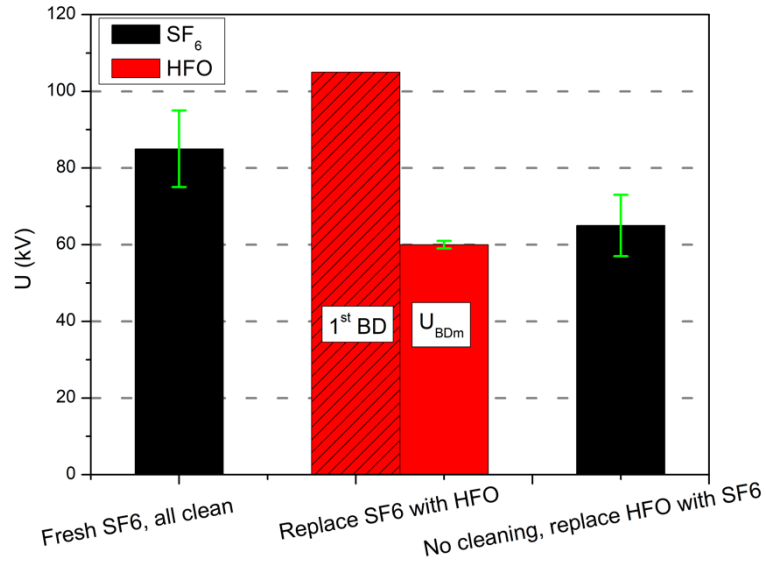


Figure 4. 14 : Measurement sequence in HFO and SF₆ to evaluate the effect of the powder deposit on the dielectric strength ($\eta = 2.5$, $P = 0.1$ MPa, up and down method)

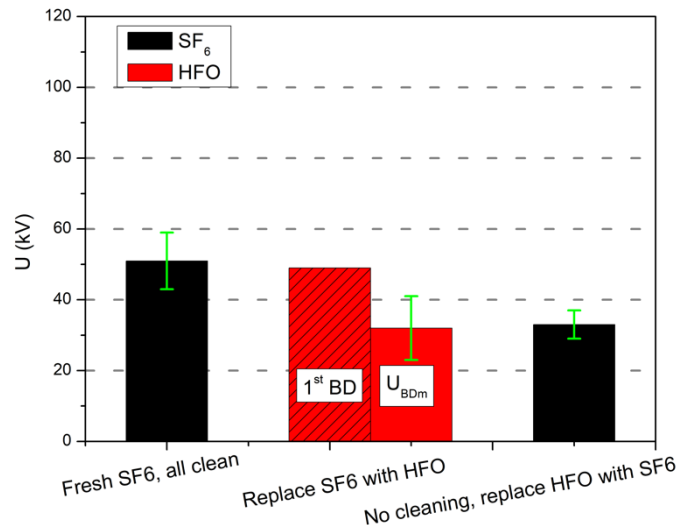


Figure 4. 15 : Measurement sequence in HFO and SF₆ to evaluate the effect of the deposit on the dielectric strength of the HFO ($\eta = 9$, $P = 0.1$ MPa, up and down method)

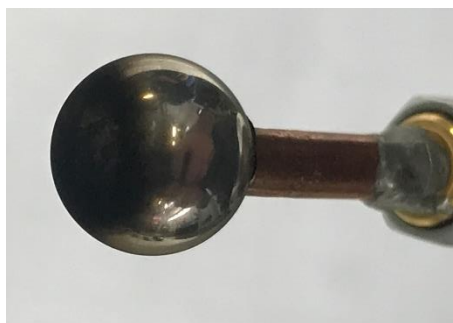


Figure 4. 16 : Black dust deposits on the HV electrode after 15 breakdowns in the HFO ($R_c = 5$ mm, $d = 20$ mm, $P = 0.1$ MPa)

In addition to the effect on breakdown voltage, surface pollution of electrodes with dust by-product has an effect on delay time, as previously described in HFO. In Figure 4. 17, the breakdown delay time of the new HFO is greater than 100 μs at a higher voltage than that of SF_6 with clean electrodes. When measurements are carried out in SF_6 with a deposit on the electrodes, the breakdown voltage of SF_6 is lower, and the breakdown delay times considerably reduced ($< 10 \mu\text{s}$) and less scattered. This effect is even more marked in HFO with polluted electrodes.

Thanks to this series of measurements, it is possible to conclude that the deposit of powder by-product on the electrodes is mainly responsible for the loss of dielectric strength after the 1st breakdown. This fine black powder facilitates considerably the initiation of discharges in positive polarity, which initiation voltage is divided by 2, and initiation delay divided by ~ 30 . Since the statistical initiation delay time is usually attributed to the random appearance of an initial electron able to trigger the discharge process, one may suppose that the appearance of such electron is facilitated by the presence of powder. No similar effect was previously reported in the literature, and no simple mechanism can be postulated.

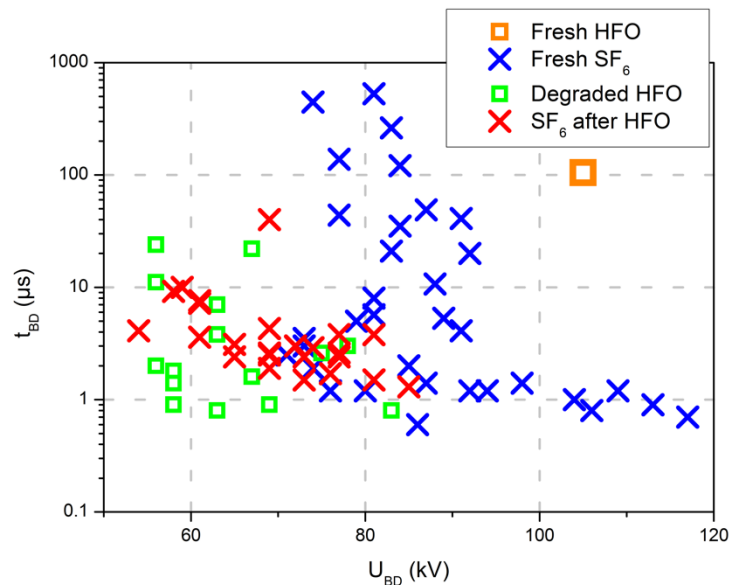


Figure 4. 17 : Delay to breakdown in HFO and SF_6 before and after degradation ($P = 0.1 \text{ MPa}$, $\eta = 2.5$)

4.IV. *Characterization of HFO degradation by energy and FTIR measurements*

4.IV.A. Breakdown energy measurements under uniform field

The impact of the energy injected during breakdown was studied in order to characterize the degradation of the HFO.

DC breakdown measurements under uniform field were carried out to record the energy actually dissipated in the discharge. To measure the arc energy, it is necessary to measure accurately the voltage across the arc and the current. The measurement of the energy of a transient arc is a difficult task that requires a careful validation, since many experimental artefacts may induce measurements errors, or even make measurements impossible:

- During breakdown, very large $\frac{dV}{dt}$ and $\frac{di}{dt}$ occur, inducing strong electromagnetic perturbations, oscillations due the circuit inductance, and energy dissipation in the external circuit when large current flow;
- Measuring the transient arc voltage requires careful attention. The voltage probe is first submitted to a fast transient step from the applied voltage (~ 30 kV) down to the arc voltage (100 to 1000 V, i.e. about 1 % of applied voltage) after some 10 ns. The probe response to such large and fast step must be precisely checked, in order to provide trustable arc voltage measurements. Even small errors on probe equilibrium (i.e. overshoot, undershoot, ringing) can lead to large errors.

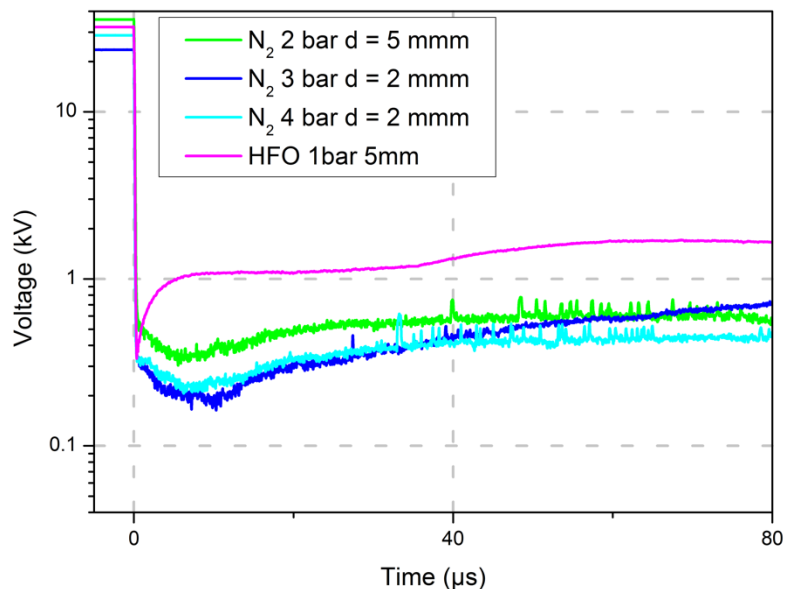


Figure 4. 18 : Voltage measured across the post-breakdown arc in HFO and nitrogen for different pressure and distance (plane-plane)

The circuit used was described on Figure 2. 7. The HV probe measures the applied voltage before breakdown (approximately 30 kV), and the arc voltage after breakdown. In order to verify the validity of this measurement, measurements under different conditions were carried out. Figure 4. 18 shows different measurements of arc voltage following breakdown, as a function of distance, pressure, and gas nature. Distance and pressure were chosen to provide a similar breakdown voltage (about 30 kV), and thus an identical initial transient step applied to the probe. By changing the distance, gas, and pressure conditions, the arc voltage should be changed. Figure 4. 18 indeed shows a different

response of the probe depending on the conditions, whereas the initial voltage step remained unchanged. We can thus confirm that the measurement of the arc voltage via the probe is correct, and not due to an experimental artefact (inadequate response of the probe, overshoot, undershoot or ringing should not depend on the gas nature).

Figure 4. 19 is an example of a current and voltage measurement obtained in HFO at 0.1 MPa with and without the external circuit composed by R_2 and C . With R_2 and C , the recording mainly shows the post-breakdown arc voltage and current flowing for about 20 μs . At the initial instant of breakdown, high frequency oscillations are observed for some 10 ns, due to the large $\frac{dV}{dt}$ and $\frac{di}{dt}$.

Without R_2 and C , only the initial oscillations are seen, and almost no post-breakdown arc current. In this case, the available energy is limited by the initial charge of the parasitic cell capacitance $C_p = 22$ pF (Figure 2. 7). This energy ($W_p = C_p \cdot U^2 / 2 = 10$ mJ @ 30 kV) is dissipated during the pre-breakdown phase (leader), and possibly during a very short arc phase (not measurable). The measured voltage does not drop to zero after breakdown, probably because the limited energy does not allow establishing a high current conducting arc.

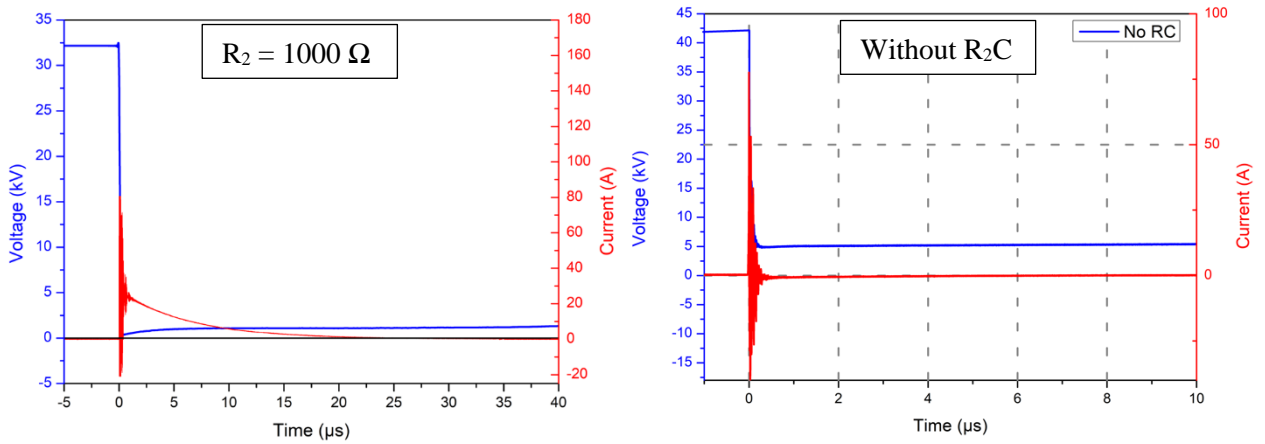


Figure 4. 19 : Example of measurement of voltage and breakdown current in the HFO (plane-plane, $d = 5$ mm, $P = 0.1$ MPa, $U_a = 34$ kV, $R_2 = 1000$ Ω and without R_2C)

With an external circuit (R_2 , C), the current injected in the arc is limited by the resistance R_2 . When R_2 decreases (Figure 4. 21), the current flowing in the arc is larger, but for a shorter duration. Table 4. 3 shows typical values of the post-breakdown arc current and duration versus R_2 . These measurements are achievable due to the presence of the series resistor R_2 that limits the arc current and prevents oscillations. With $R_2 = 0$ Ω , large oscillations due to the circuit inductance prevents such measurements.

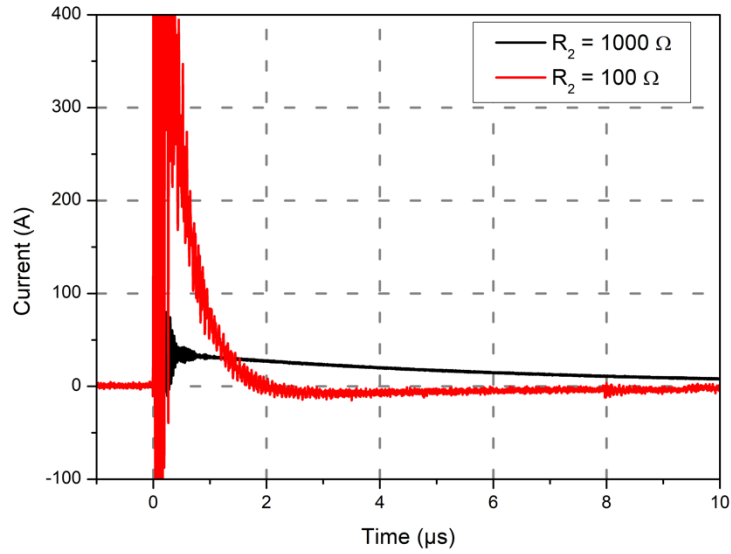


Figure 4. 20 : Arc current for different resistances $R_2 = 1000$ and 100Ω ($U_{BD} = 44$ kV)

Table 4. 3 : Arc current and duration for the different values of R_2 ($U_{BD} = 44$ kV)

R_2 (Ω)	I_{arc} (A)	t_{arc} 50% (μs)
1000	30	4
100	250	0.8
10	1500	0.4

From voltage and current, it is possible to calculate the post-breakdown arc resistance ($R_{arc} = U_{arc} / I_{arc}$ Figure 4. 21). Immediately after breakdown, the arc resistance is very low (a few ohms). As the current decreases, the arc cools down and its resistance increases. The arc energy is obtained by integrating the power ($E_{arc} = \int_0^t U_{arc} \times I_{arc} dt$ Figure 4. 22).

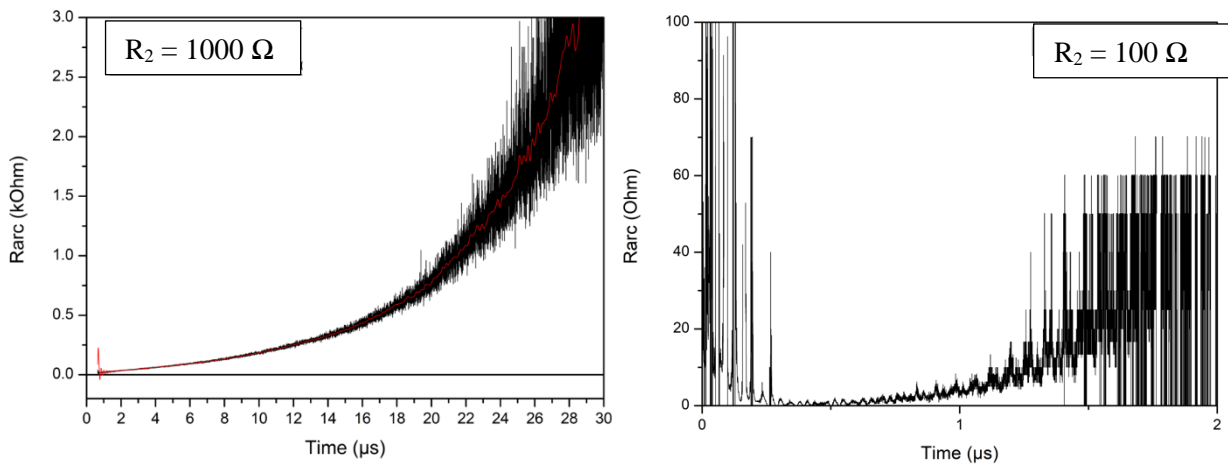


Figure 4. 21 : Transient arc resistance in HFO ((plane-plane, $d = 5$ mm, $P = 0.1$ MPa, $U_a = 34$ kV, $R_2 = 1000$ and 100Ω)

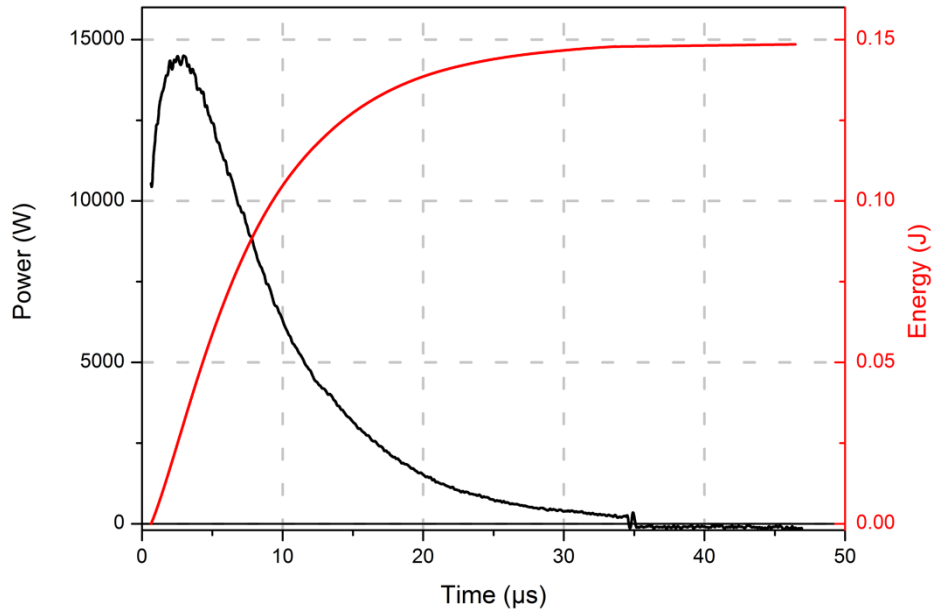


Figure 4. 22 : Arc power and energy in HFO (plane-plane, $d = 5 \text{ mm}$, $P = 0.1 \text{ MPa}$, $U_a = 34 \text{ kV}$, $R_2 = 1000\Omega$)

Figure 4. 23 shows the evolution of the arc energy as a function of resistance R_2 and gas nature. This graph represents the arc energy at slightly different voltages. By plotting the percentage of the arc energy compared to the initial capacitor energy ($W_c = C \cdot U^2/2$), the 3 curves are superimposed (Figure 4. 24). Depending on R_2 the arc energy varies from 4 to 45 % of the capacitor energy. The remaining of energy is dissipated in the external circuit. Breakdown experiments carried out with the Marx generators involved a series resistor of $1 \text{ k}\Omega$, and an equivalent capacitor (from 5 to 10 nF depending on the number of stages used). Therefore, a small arc energy $< 1 \text{ J}$ was involved in these tests.

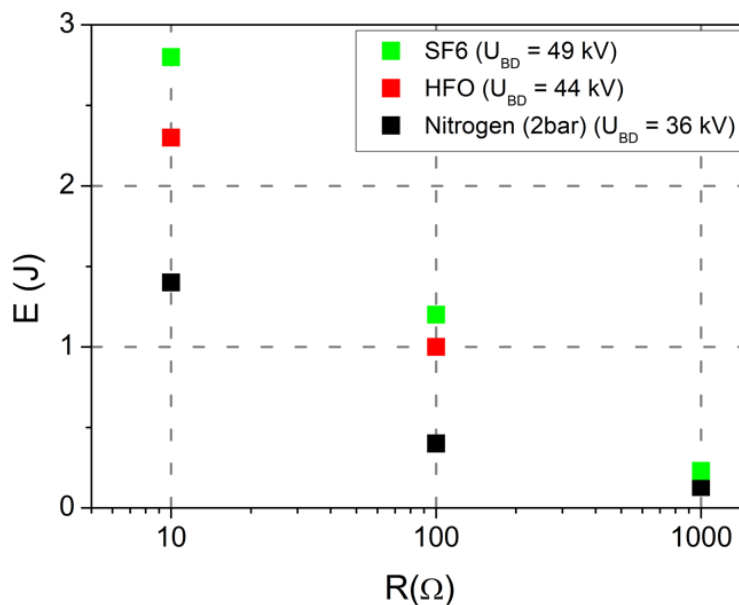


Figure 4. 23 : Variation of the energy dissipated in the arc as a function of the series resistance and the gas (plan-plan, $d = 5 \text{ mm}$)

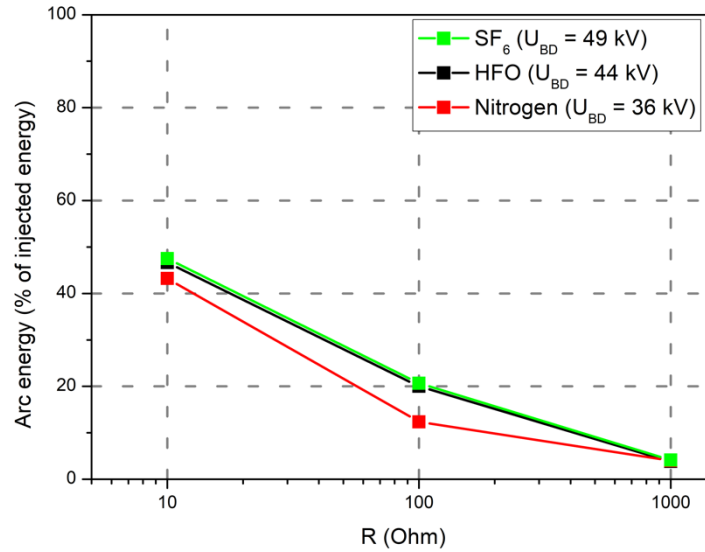


Figure 4. 24 : Arc energy as a percentage of the maximum energy stored in capacitor (plan-plan, $d = 5 \text{ mm}$)

Regardless of the energy injected into the arc (Figure 4. 25), the breakdown voltage of the 3 gases remains logically unchanged. From DC breakdown measurements under uniform field (Figure 4. 25), the reduced field (E/N) is obtained for the different gases in Table 4. 4. For SF₆ and HFO, the estimation of E/N (from our measurements) is close to the theoretical value in the literature (1.2 times higher see Table 4. 4). For air, the calculation is fairly good, but for nitrogen, the difference is very important. The theoretical field E/N represents the minimum value for the formation of a discharge. The measured E/N field is always higher than the theoretical one, thus allowing the formation of a discharge.

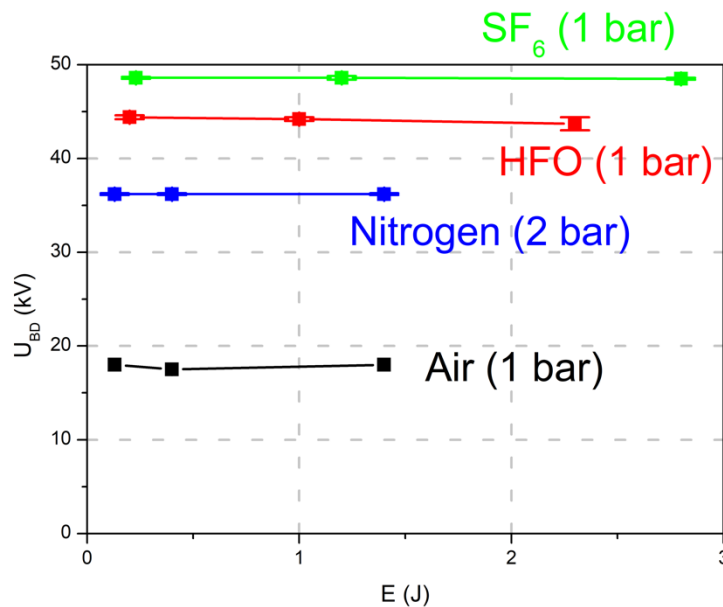


Figure 4. 25 : Average DC breakdown voltage in nitrogen, air, SF₆ and HFO in a homogeneous field as a function of energy ($d = 5 \text{ mm}$, plane-plane, DC)

From Figure 4. 25, the reduced field (E/N) is deduced for the different gases in Table 4. 4.

Table 4. 4 : Comparison between E/N in the literature and the E/N obtained in the DC breakdown measurements with uniform field

	(E/N) _{cr} (Td)	References	(E/N) _{breakdown plan-plan} (Td) Measurements (Figure 4. 25)	(E/N) _{breakdown plan-plan} /(E/N) _{cr}
Air	94.7	[89]	158	1.67
	99.4	[90]		1.59
	98.5	[91]		1.60
Nitrogen	60	[92]	150	2.50
HFO	305	[93]	366	1.20
	302	Figure 1. 8 [7]		1.21
SF ₆	359	[94]	408	1.14
	360	[95]–[97]		1.13
	361	[98]		1.13
	362	[99], [100]		1.12

4.IV.B. Correlation of arc energy with breakdown voltage drop in HFO

Breakdown energy measurements were also made in a quasi-homogeneous field ($R_c = 5$ mm, $d = 20$ mm) more representative of MV GIS design. Depending on the arc energy, the powder deposit visible on electrodes after 10 breakdowns is more or less important, regardless of the polarity. When the energy is low (0.3 J with $R_2 = 1000 \Omega$), a uniform black layer is visible on the sphere electrode brought to the HV, and a large difference is noted between the 1st breakdown and the following ones (87 % in negative polarity Figure 4. 26 and 63 % in positive polarity of U_{BD1} Figure 4. 27).

When the energy increases (2.3 J with $R_2 = 10 \Omega$), almost no (or very few) deposits are still visible on the electrodes, and a small difference is observed between the 1st breakdown and the following ones (100 % in negative polarity Figure 4. 26 and 80 % in positive polarity Figure 4. 27 of U_{BD1}). Surprisingly, the higher the discharge energy, the lower the powder deposition and the loss of dielectric strength. In addition, the degradation is lower in negative polarity. Increasing the energy per shot slightly increases the average breakdown voltage of repetitive shots. This result was quite unexpected and counter intuitive. We may make the hypothesis that with a larger arc energy, the more intense shock wave produced contributes to detach and sweep the fine black dust from electrodes.

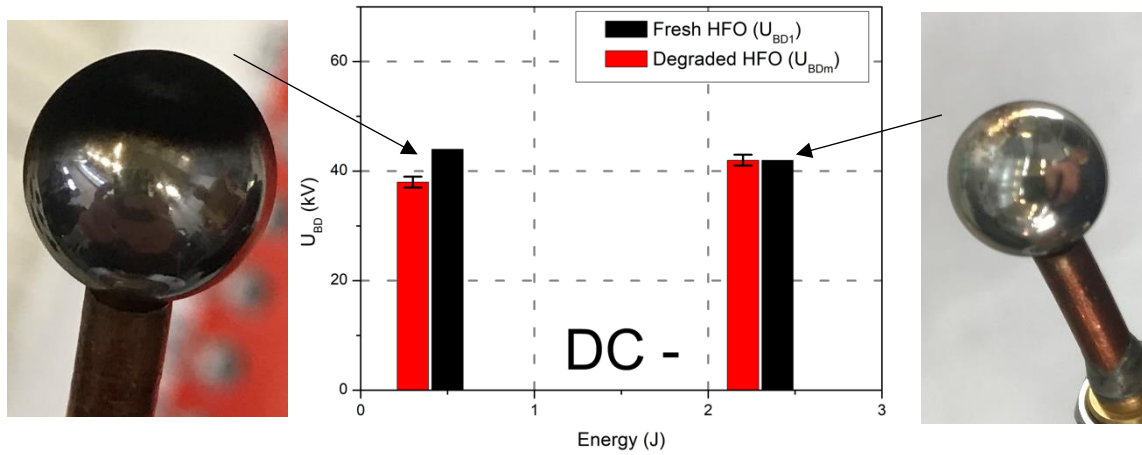


Figure 4. 26 : Influence of energy on the stability of breakdowns and powder deposits on electrodes with negative polarity ($R_c = 5 \text{ mm}$, $d = 20 \text{ mm}$, $P = 0.1 \text{ MPa}$)

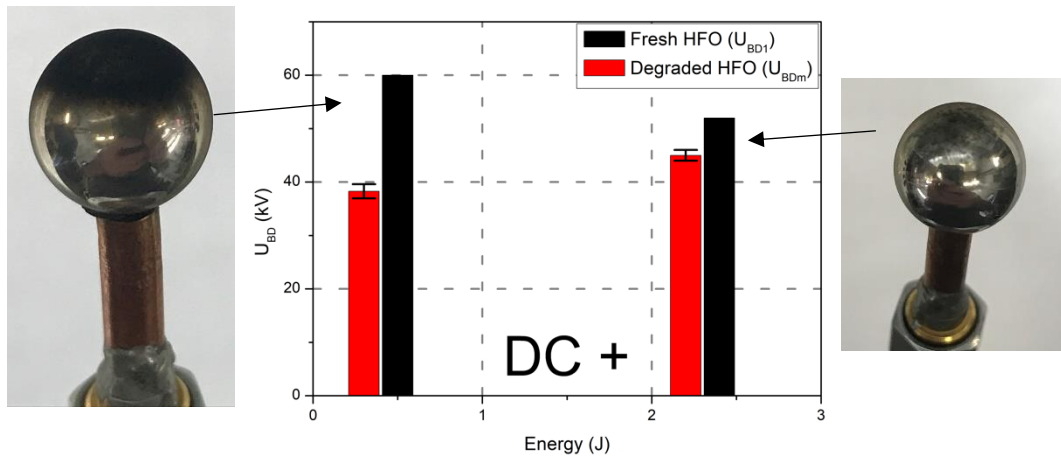


Figure 4. 27 : Influence of energy on the stability of breakdowns and powder deposits on electrodes with positive polarity electrodes ($R_c = 5 \text{ mm}$, $d = 20 \text{ mm}$, $P = 0.1 \text{ MPa}$)

As with impulse voltage, the same unexpected observation is made here in DC, namely that the negative polarity is more critical for fresh HFO. When the HFO is degraded, the breakdown voltage becomes the same between the 2 polarities ($\approx 40 \text{ kV}$)

Table 4. 5 : Comparison of the breakdown voltage in the HFO between the DC and the impulse ($R_c = 5 \text{ mm}$, $d = 20 \text{ mm}$, $P = 0.1 \text{ MPa}$)

	Fresh HFO U_{BD1} (kV)	Degraded HFO U_{BD} (kV)
STI	125	64
DC	60	39
STI/DC	2.1	1.6

Table 4. 5 shows that the breakdown voltage is lower in DC compared to the impulse voltage. This difference observed in nearly all dielectric materials is explained by the influence of the statistical delay time with impulse voltage, linked to the occurrence of a seed electron leading to breakdown. Under

DC (or even AC), this delay has no influence, since voltage is applied for a long duration, and the breakdown voltage is minimum.

4.IV.C. Correlation of energy with HFO degradation: pressure measurements

To study the degradation of HFO as a function of energy, measurements were made with repetitive DC breakdown of controlled energy, together with a precise measurement of the pressure and temperature to monitor the gas decomposition. The following hypothesis is formulated: as solid by-products are produced, the gas pressure may decrease due to gas consumption. To see this pressure drop, the total energy dissipated within a fixed gas volume by repetitive discharges was fixed to 1 kJ. The energy of breakdown depends on the series resistance R_2 . 4 situations were studied, with the total number of breakdowns adapted to keep a constant total energy ≈ 1 kJ:

- Without resistance R_2 and capacitance C , the maximum possible arc energy comes from the parasitic capacitance of the test cell (20 mJ at 42 kV). To obtain a total energy $E_t = 1000$ J, the number of breakdowns is $n_{BD} = 49470$;
- with 1400 Ω resistance and 5 nF capacitance, the arc energy is $E_{BD} = 200$ mJ, the number of breakdowns $n_{BD} = 5000$ (total energy $E_t = 1000$ J);
- with 100 Ω resistance and 5 nF capacitance, $E_{BD} = 1.5$ J, the number of breakdowns $n_{BD} = 668$ (total energy $E_t = 1002$ J);
- with 10 Ω resistance and 5 nF capacitance, $E_{BD} = 2.5$ J, the number of breakdowns $n_{BD} = 401$ (total energy $E_t = 1002$ J).

The gas pressure was measured before and after the application of 1 kJ discharges. Figure 4. 28 shows the results obtained. Preliminary experiments carried out with N_2 , showed no pressure drop after 1 kJ arc dissipation, which is logical since discharges in N_2 produce no by-products (either solid or gaseous).

In HFO, pressure drops from 0.2 to 5 % of the initial pressure (0.1 MPa) were recorded. For an identical total energy (1 kJ), the pressure drop is much larger when a large number of breakdowns of low energy occurs (i.e. without R_2 and C). The pressure drop is clearly linked to the nature of the discharge, and not only to the total energy. Without R_2 and C , almost no post-breakdown arc exists, but a large number of low-energy breakdown (leaders and presumably very short arcs) was applied. We can therefore conclude that the majority of the degradation occurs during the initial breakdown phase of low energy (leaders), and that the degradation induced by the post-breakdown arc is considerably smaller.

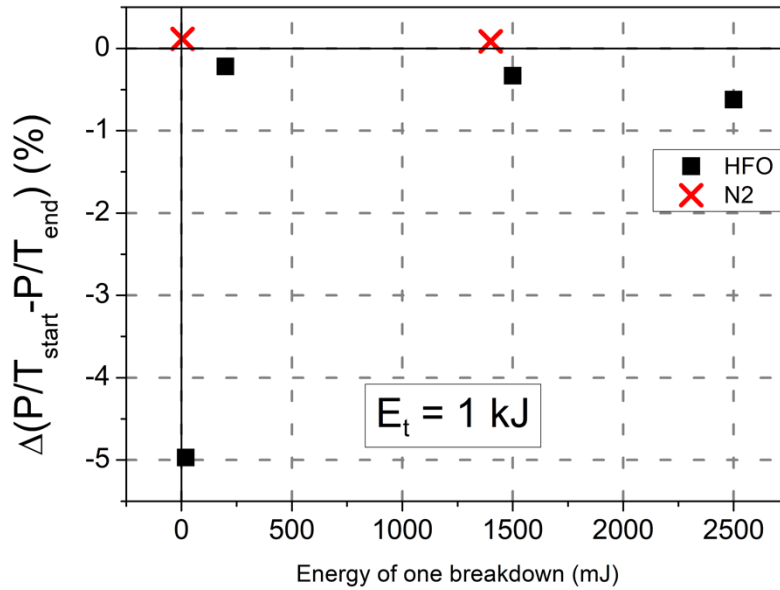


Figure 4. 28 : Pressure variation in the HFO as a function of the energy of one breakdown ($R_c = 5 \text{ mm}$, $d = 10 \text{ mm}$, $P = 0.1 \text{ MPa}$)

4.V. Physico-chemical characterization of HFO degradation

A physico-chemical investigation was also undertaken to try to characterize the degradation of the gas, and the solid by-product powder.

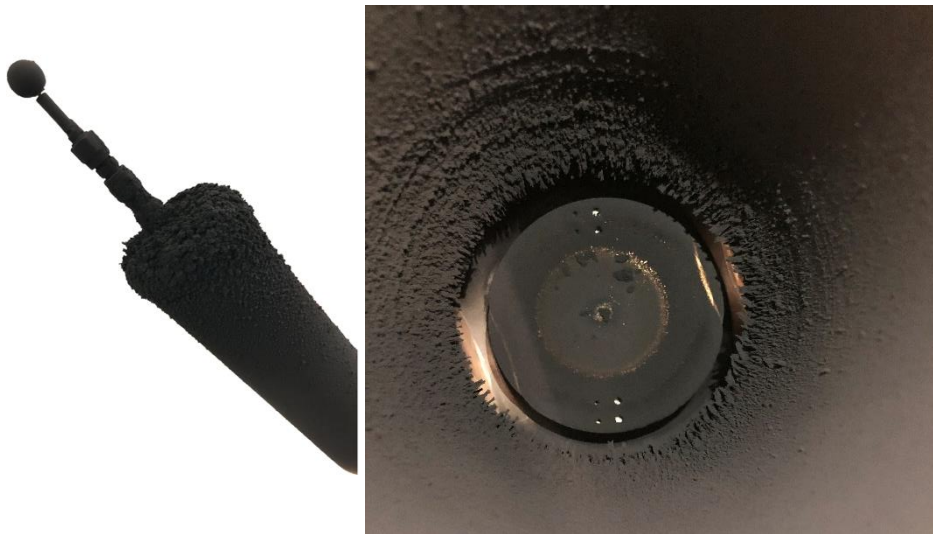


Figure 4. 29 : Deposit within the test cell after 75 minutes of DC application

As shown in the previous section, the fastest and easiest way to degrade a large amount of HFO is to apply a continuous voltage (45 kV) to the plane-sphere electrode system ($R_c = 5 \text{ mm}$, $d = 10 \text{ mm}$, $\eta = 2.5$) without R_2 and C . The same circuit, the same electrodes as in the previous part were used, i.e. an injected energy of $\approx 40 \text{ kJ}$ was dissipated after 75 minutes ($\approx 500 \text{ J/min}$). A considerable amount of powder was produced (Figure 4. 29) leading to accumulations of thickness up to 1 mm on the cell walls.

The amount was lower on electrodes, confirming that the powder is swept by discharges. Despite this deposit, the breakdown voltage remained unchanged (≈ 45 kV).

To see the evolution of the gas composition over time, HFO samples were taken at different times. These samples were analysed by gaseous FTIR (Figure 4. 30). The FTIR identifies the chemical bonds of gas. For fresh HFO, the characteristic bonds of HFO are present. Namely the C=C double bond at 1698 cm^{-1} , the vibrations of the C-F₃ bonds at 1336 and 1106 cm^{-1} , the vibration of the CF₃ bond at 1336 cm^{-1} and the vibration of the C-C bond at 883 cm^{-1} .

Even after 75 minutes of voltage application with a large amount of powder produced and about 40 kJ of energy injected, no new peaks or peak shifts were observed. In this case, the FTIR measurement is not quantitative, in fact it is difficult to strictly control the number of moles introduced in the measurement cell. Additional RAMAN measurements and gas phase chromatography (not available during this work) could provide more information.

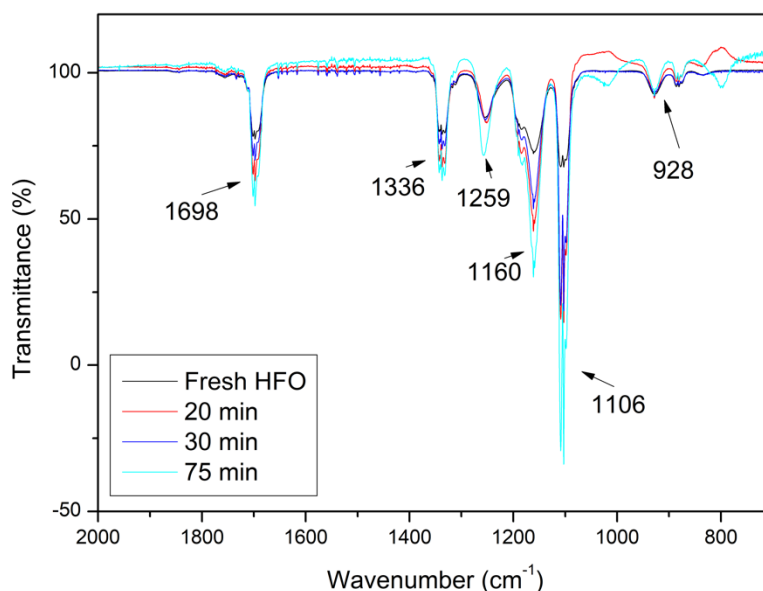


Figure 4. 30 : FTIR of HFO gas after 20, 30 and 75 minutes

Table 4. 6 : Experimental and calculated vibrational frequencies (cm^{-1}) for HFO [101]

IR (gas)		Assignment	Experimental
1698	Very strong	$\nu(\text{C}=\text{C})$	1698
1336	Very strong	$\nu_s(\text{CF}_3)$	1336
1160	Very strong	$\nu(\text{C}-\text{F})$	1160
1106	Very strong	$\nu_{as}(\text{CF}_3)$	1106
883	Weak	$\nu(\text{C}-\text{C})$	885

Infrared measurements were also carried out on the powder formed by the HFO (Figure 4. 31). In this case, the C-F bonds (1215 and 1143 cm^{-1}) are visible. The C=C double bond (1600 cm^{-1}) is not visible in the powder deposits.

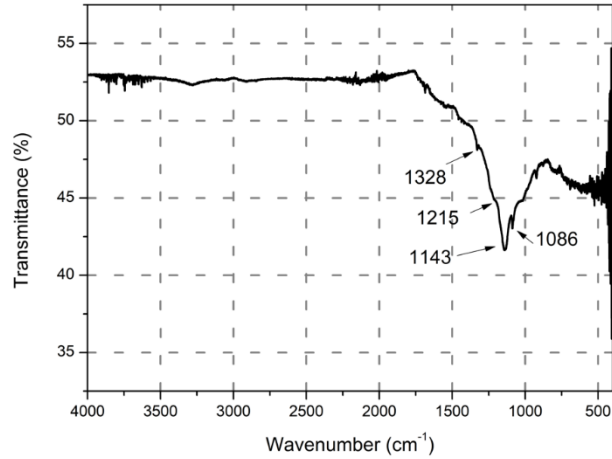


Figure 4. 31 : FTIR on HFO powder by-product

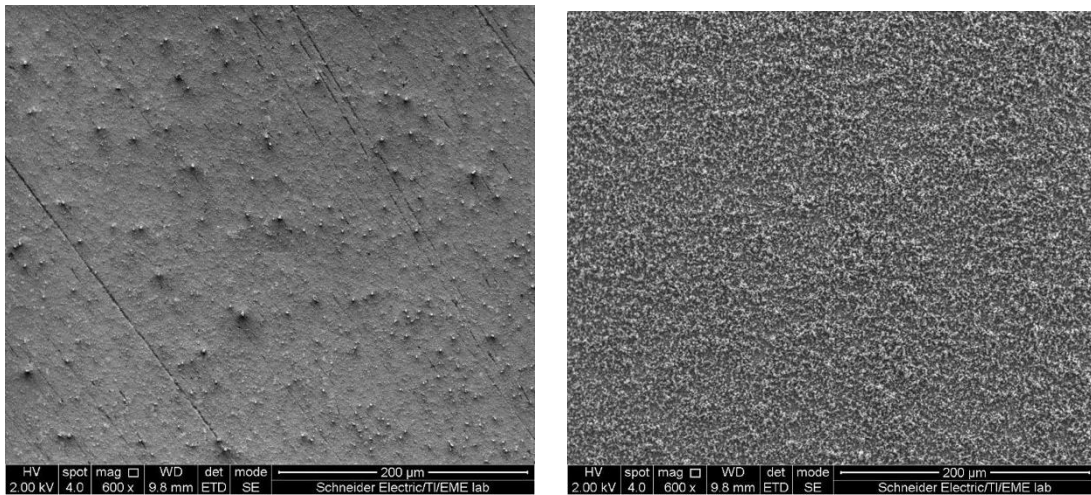


Figure 4. 32 : Images of clean and polluted electrode surface obtained by SEM [102]

Figure 4. 32 shows the surface condition of the electrodes before and after the series of breakdowns. Thanks to an EDX analysis, spectral analysis shows a main presence of carbon (Figure 4. 33): in fact, the presence of the double bond C=C in the backbone of HFO molecule makes it easier to dissociate. Fluorine and oxygen are also present. Aluminium is the electrode metal and some copper impurities were originally present on the electrode raw material. Carbon and fluorine came from the gas molecule, whereas oxygen could be formed by the reaction of the gas with the residual humidity while arcing occurs, or from a possible presence of Al_2O_2 layer that result usually from the reaction of aluminium with the ambient oxygen. Unfortunately, the EDX analysis can only identify the nature of atoms, but cannot give information about the nature of molecules present [102].

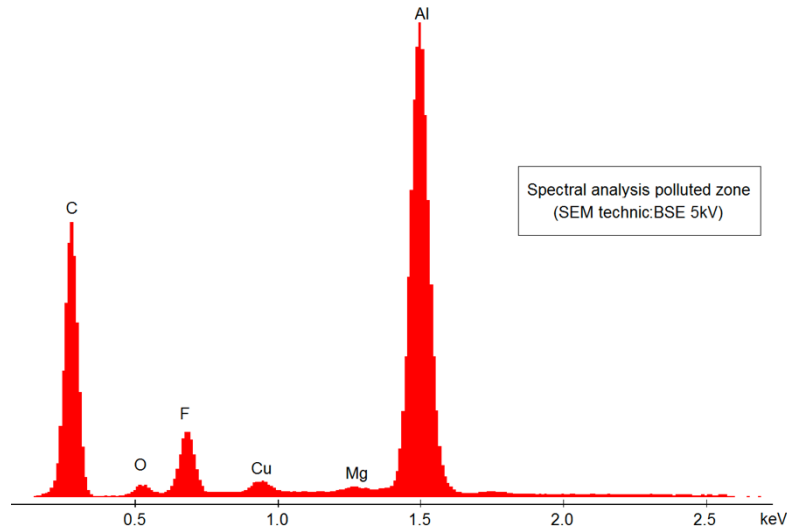


Figure 4. 33 : EDX-Spectral analysis of the dusty layer on electrodes after breakdown tests in HFO-1234ze(E) [102]

The decomposition of HFO and the formation of carbon powder are very complex phenomena. It would be necessary to make more detailed studies on the decomposition mode of this molecule. In [45], the main gases formed by decomposition of HFO-1234ze(E) are HF, C₂H₂, C₂HF, and CHF₃. The presence of HF was ascertained by the important etching of the test cell windows made of quartz: after degradation experiments, these windows became opaque. In addition to the drop of breakdown strength, the presence of aggressive by-products constitutes another drawback of HFO. In SF₆, production of HF is also observed, but in the presence of water.

These measurements did not allow to fully characterize the HFO decomposition pattern but confirmed the formation of carbon deposits with traces of fluorine.

4.VI. *Conclusions: design rules of insulation with HFO*

In addition to conclusions already obtained from divergent field experiments (chapter 3), several other practical consequences can be derived from measurements in homogeneous field in this chapter.

The main result obtained here is the large deleterious influence of HFO degradation on its practical insulating properties when the field is moderately divergent, i.e. a situation relevant of applications. New HFO in a clean environment provides breakdown properties higher than SF₆ in positive polarity (Figure 4. 4), and lower after degradation. In addition, the influence of degradation appears quite complex since it varies with electrode geometry (Figure 4. 6) and discharge energy (Figure 4. 27). The largest degradation occurs when numerous discharges of low energy are present.

In a practical medium voltage system, discharges should not occur in normal service, but it is impossible to ascertain that a system will never experience discharges, that may occur in particular occasions:

- during tests (e.g. with lightning impulse) with large overvoltage compared to the nominal AC level;
- in the presence of partial discharges, that sometimes exist for long durations during service in aged switchgear.

Partial discharges refer to a case where a large number of discharges of low intensity occur, which unfortunately corresponds to the worst situation for HFO: the accumulated energy for long periods of time can lead to a 10 times more severe HFO degradation (Figure 4. 28) compared to a single high energy discharge. A 50 pC partial discharge (PD) in a 20 kV system dissipates about 1 μ J per PD. With the pessimistic hypothesis that 1 PD occurs at each AC period, 4.3×10^6 PDs occurs every day, corresponding to 4.3 Joules dissipation. After 1 year, the accumulated energy will exceed 1 kJ, i.e. an energy producing large HFO degradation (Figure 4. 29). Of course, this rough estimation should be corrected regarding the actual parameters in a real system (HFO volume, PD amplitudes, etc.).

Nevertheless, the influence of HFO degradation must be considered if this gas is used in a practical system, to ensure its reliability over long durations.

In the following part, we try to establish basic principles for the design of insulation with HFO. This is a complicated task since the basic properties allowing calculating the classical “streamer criterion” are not known in HFO. These considerations will mainly consider the case of degraded HFO since scarce data corresponding to “new HFO” could be obtained.

4.VI.A. Initiation field in HFO in the investigated geometries

In addition to initiation fields already obtained in non-uniform field, the results obtained with more uniform field allows a more complete description. Based on Figure 3. 44 and Figure 3. 45, the initiation field as a function of distance for $R_c = 5$ and 10 mm can be added. Whatever the radius of curvature or the pressure, the initiation field of degraded HFO are slightly lower that of SF₆ (Figure 4. 34). In addition, the pressure increases the initiation voltage of the pre-discharges regardless of the radius of curvature in the degraded HFO (Figure 4. 35).

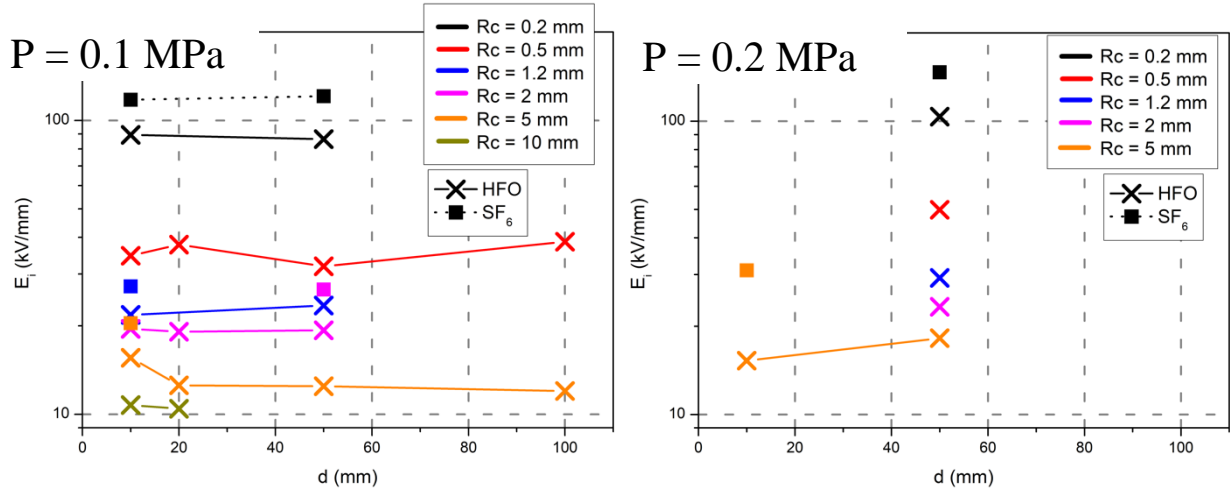


Figure 4. 34 : Value of the maximum field E_i as a function of the distance ($P = 0.1$ and 0.2 MPa) for degraded HFO

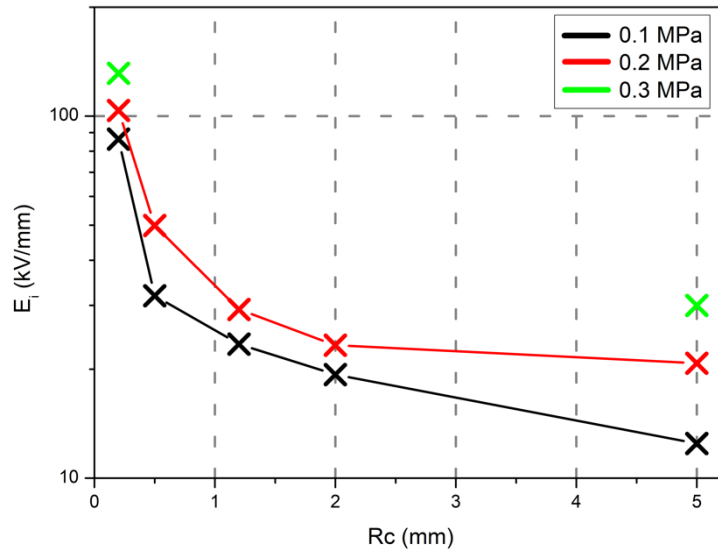


Figure 4. 35 : Value of initiation field E_i as a function of R_c for degraded HFO ($d = 50$ mm)

Figure 4. 36 represents the initiation field depending on the radius of curvature, calculated with:

- the initiation voltage (E_i at U_i) in degraded HFO;
- the 1st breakdown voltage (EI at U_{BD1}) in the fresh HFO.

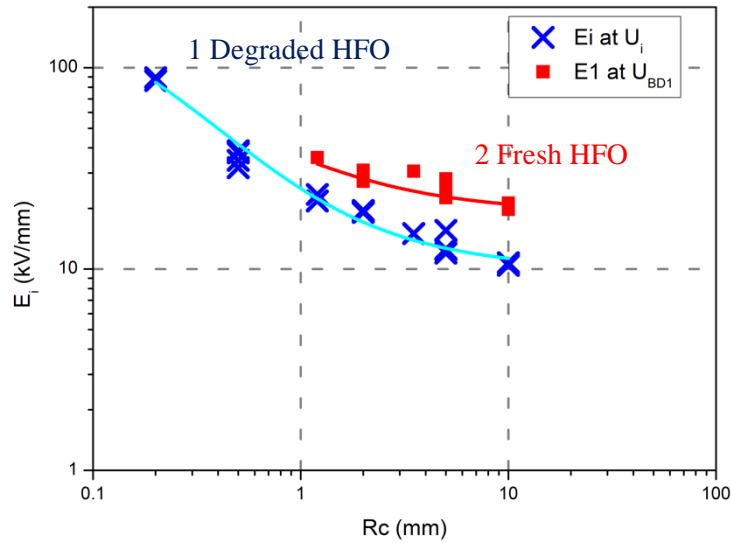


Figure 4. 36 : Initiation field as a function of the radius of curvature

The difference of initiation fields between new and degraded HFO is maximum when the breakdown field is low, which occurs in quasi uniform field with large R_c . The difference decreases when calculated initiation fields on the electrode increase, i.e. in more divergent field with low R_c .

The 2 curves in Figure 4. 36 can be fitted as: $E_{max} = \exp(a + \frac{b}{R_c+c})$ with R_c the radius of curvature of electrode in mm, E_{max} the maximum electric field in kV/mm, a, b, c : fitting parameters

Table 4. 7 : Parameter of equation $E_{max} = \exp(a + \frac{b}{R_c+c})$ for the curves showing in Figure 4. 36

Equation number	Parameters	a	b	c
1 (blue curve)	Initiation in degraded HFO	2.30	1.30	0.41
2 (red curve)	Initiation in fresh HFO	2.95	1.00	0.60

This equation represents an interesting first design criterion: depending on the radius of curvature, the initiation field is calculated. If the field is lower than equation 1 (Table 4. 7), no discharge or pre-discharge should occur. If the applied field strength is greater than equation 2, the probability of breakdown in the degraded HFO is greater than 20 % (probability obtained with up and down method). Unfortunately, this criterion valid for sphere-plane geometry cannot be generalized to any practical geometry.

4.VI.B. Use of the streamer criterion

4.VI.B.i. Uniform field under DC voltage

The criterion mainly used in the electrical industry for design of insulation is the streamer criterion. Electrical discharges in gases often start from a local electron impact–ionization avalanche, which becomes sufficiently large for self-propagation due to its own space charge. The associated condition of this so-called avalanche-to-streamer transition (or streamer inception) is often modelled by the integral equation: $\int_0^{x_{cr}} \alpha_{eff} dx = K$. The length x_{cr} is the distance at which the electric field falls to the critical field E_{cr} . This concept was initially developed for discharges in homogeneous fields. Unfortunately, α_{eff} is not known today in HFO. It is however possible to compare it with measurements and streamer criteria calculated in air and SF₆.

From the measurements obtained in DC in plane-plane geometry, Figure 4. 37 represents the streamer criterion for air and SF₆, in comparison with the breakdown voltage measurements. In a uniform field, the streamer criterion corresponds quite well to the breakdown voltage (Figure 4. 37). When a streamer is initiated, it leads directly to breakdown.

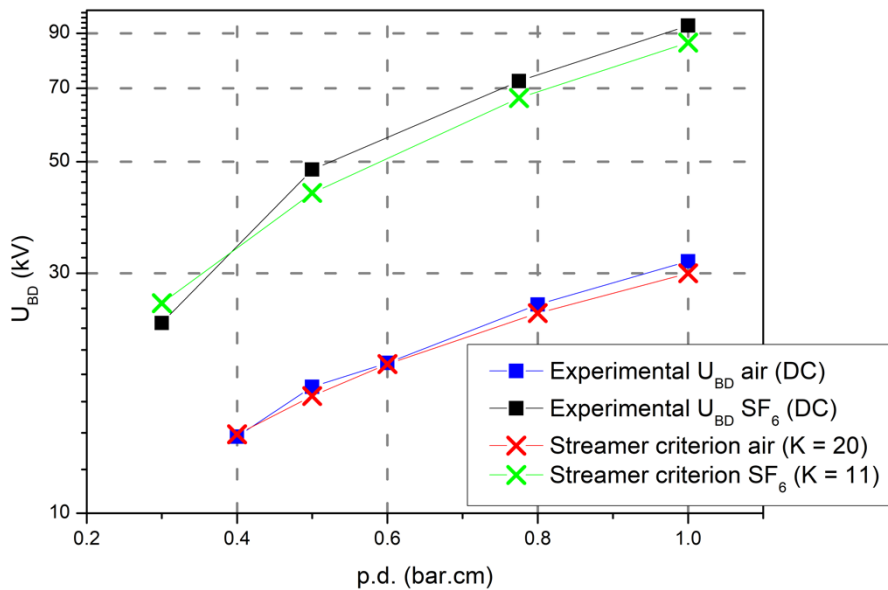


Figure 4. 37 : Streamer criteria for air and SF₆ in plane-plane geometry for $d = 50$ mm

4.VI.B.ii. Moderately divergent field ($\eta = 2.5$) under DC and impulse voltage

Similar investigations were carried out with a moderately divergent field ($R_c = 5$ mm, $d = 10$ mm, and $\eta = 2.5$). Figure 4. 38 compares the streamer criterion with the breakdown voltage of air and SF₆ under impulse STI and DC. On the plot, the color represents the measurement conditions, and the symbol shape the gas. In SF₆ and HFO, DC breakdown measurements at 0.3 MPa were not possible due to the 100 kV limitation of the power supply.

In air and SF₆, the streamer criterion corresponds to the breakdown voltage in DC, as in uniform field. On the other hand, a large difference exists between DC and STI breakdown voltage. Table 4. 8 lists the measured “impulse factor” (STI voltage/DC voltage) for the different pressures in the 3 gases.

Such correction coefficients can be used to adapt the calculated streamer criteria valid under DC to STI measurements. At fixed pressure (e.g. 0.1 MPa), air shows the highest impulse factor (2.1), followed by SF₆ (1.6), and HFO (1.3). At 0.2 MPa, the ranking of gases is identical, but the differences are lower (resp. 1.7, 1.4, 1.3). These correction coefficients are deduced from experiments and cannot be calculated from the streamer theory. They are related to the availability of seed electrons on a short time scale, i.e. a hardly predictable parameter.

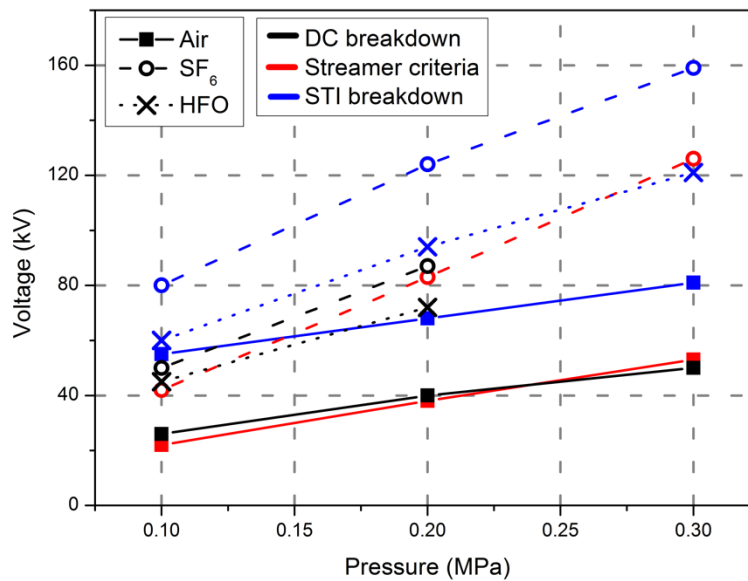


Figure 4. 38 : Criterion of streamer in air and SF₆ and comparison with measurements in DC and STI ($R_c = 5$ mm, $d = 10$ mm, $K = 20$ for air and $K = 11$ for SF₆)

Table 4. 8 : Breakdown voltage in DC and STI, and streamer criteria in air, HFO degraded and SF₆ ($R_c = 5$ mm, $d = 10$ mm)

Gas	P (MPa)	U_{BD} STI (kV)	U_{BD} DC (kV)	$U_{streamer}$ criteria	STI/ $U_{streamer}$	STI/DC
Air	0.1	55	26	22	2.5	2.1
	0.2	68	40	38	1.8	1.7
	0.3	81	50	53	1.5	1.6
HFO (degraded)	0.1	60	45	-	-	1.3
	0.2	94	72	-	-	1.3
	0.3	121	Too high	-	-	-
SF ₆	0.1	80	50	42	1.9	1.6
	0.2	124	87	83	1.5	1.4
	0.3	159	Too high	126	1.3	-

Table 4. 9 : STI breakdown voltage comparison for HFO and SF₆ (R_c = 5 mm, d = 10 mm)

P (MPa)	U _{BD} STI SF ₆ (kV)	U _{BD} STI HFO (kV)	%UBD
0.1	80	60	0.75
0.2	124	94	0.76
0.3	159	121	0.76

In HFO the streamer criterion cannot be calculated. On Figure 4. 38, it is obvious that the evolution with pressure of breakdown voltage (under DC and STI) as well as streamer criteria in air is different from electronegative gases SF₆ and HFO. From 0.1 to 0.3 MPa, the breakdown voltage in air increases only by 47%, whereas it is doubled in SF₆ and degraded HFO.

It is interesting to observe that the ratio of STI breakdown voltage (degraded HFO/SF₆) remains remarkably constant (0.76) whatever the pressure, provided breakdown is controlled by initiation (Table 4. 9). This conclusion is based on the limited conditions (R_c, d) used to investigate SF₆ in this study. It would be very interesting to extend this to other conditions, in order to check the validity of a fixed ratio.

With the assumption that degraded HFO withstands 76% of SF₆ in all conditions, a simple design method can be suggested:

- calculate the breakdown voltage in SF₆ using the “standard” method already used (streamer criterion and suitable correction coefficient);
- apply a de-rating factor of 0.76.

4.VI.B.iii. Divergent field

In a divergent field, pre-discharges occur at much lower voltages than breakdown. The breakdown voltage represents the voltage required for complete leader propagation in electronegative gases, or the voltage required for a streamer/arc transition in air. It is therefore difficult to justify using the streamer criterion to predict breakdown voltages. As shown in Figure 4. 39 and Figure 4. 40, the streamer criterion considerably underestimates the breakdown voltage. It is logically closer to the initiation voltage of discharges. From these calculations, it is clear that the streamer criteria is of little help to predict breakdown voltage in very divergent fields. The empirical formula derived from experiments (Figure 3. 43) provides a much better estimation of breakdown voltage in divergent fields ($\eta < 10$), only dependent on the gap distance.

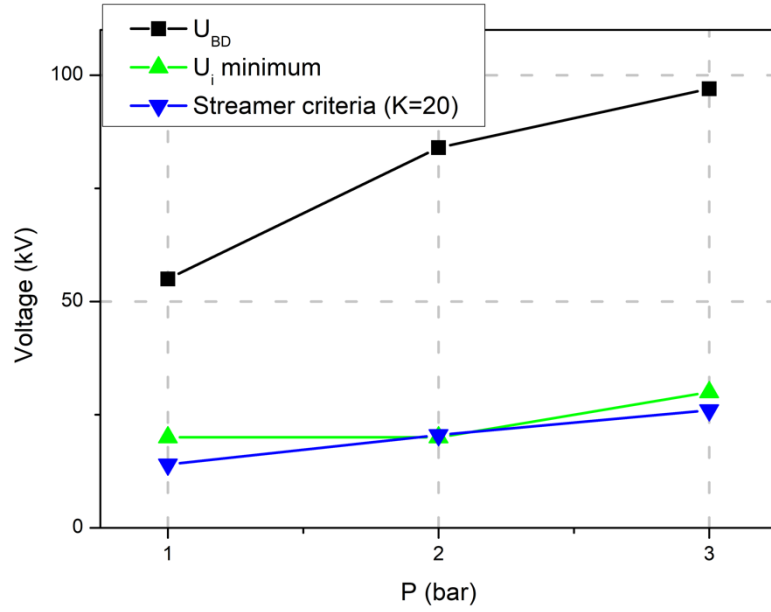


Figure 4.39 : Streamer criteria for air ($R_c = 0.2$ mm, $d = 50$ mm, $\eta = 86$, $K = 20$)

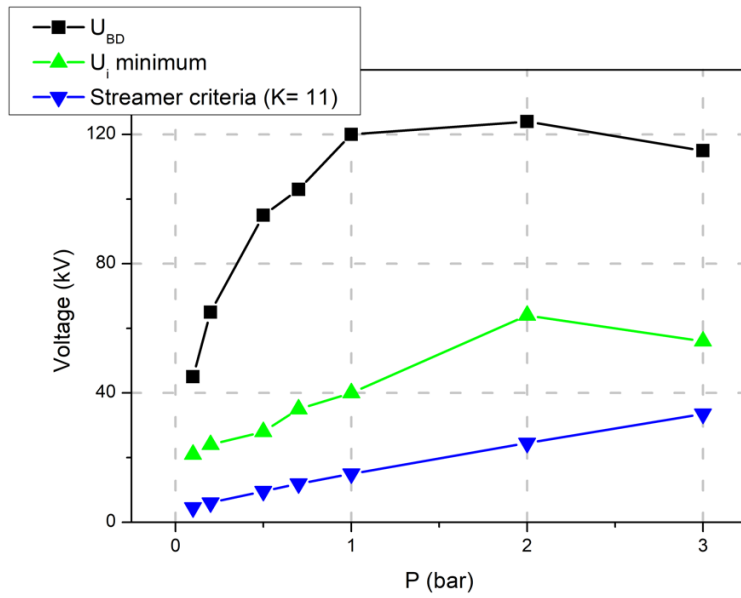


Figure 4.40 : Streamer criteria for SF_6 ($R_c = 0.2$ mm, $d = 50$ mm, $\eta = 86$, $K = 11$)

General conclusion

The work carried out during this PhD project aims to study the dielectric properties of HFO-1234ze(E) in order to replace SF₆ in medium voltage GIS.

In this context, experimental and theoretical investigations were carried out with several objectives:

1. Provide a good knowledge of the discharge process in HFO, by comparing it to air and SF₆, two reference gases used in the electrical industry;
2. Study and characterize the dielectric behavior of the HFO in a wide variety of electrode configurations, from very divergent to quasi-uniform field;
3. Derive design rules for MV applications.

Several candidates are presently studied for the replacement of SF₆ in electrical systems. Our choice was focused on HFO presenting good assets: non-toxic, non-carcinogenic, good compatibility with materials, and availability. Preliminary work had shown the potential of HFO, mainly in very divergent fields. A more precise study, carried out in this study, was necessary in order to further characterize the behavior of HFO subjected to different types of electrical stress. The main results obtained can be summarized as follows.

I. Pre-disruptive phenomena

In the degraded HFO, the characteristics of pre-breakdown phenomena generated by a point electrode are very similar to those previously reported in the literature with other electronegative gases such as SF₆.

- Streamers are created at $pd < 2.5$ MPa/mm and leaders for $pd > 2.5$ MPa/mm;
- Leaders' appearance voltages are higher in negative polarity than in positive polarity;
- Their initiation field increases with increasing pressure;
- The propagation of leaders is almost independent on pressure. It mainly depends on the applied voltage and gap distance;
- The velocity of leaders, from 10^4 to 10^5 m/s mainly depends on the applied voltage.

The major differences between leaders in SF₆ and HFO is illustrated by the stopping length measurements:

1. leaders in HFO are initiated at lower voltage;
2. once initiated, their propagation up to the opposite electrode occurs at lower voltage.

These differences explain the lower breakdown voltage recorded in HFO, both in divergent fields (where propagation is a key factor), and quasi uniform fields (where initiation induces breakdown).

II. Breakdown voltage

A wide range of field enhancement factor (η from 1 to 100) and of pressure (0.1 to 0.3 MPa) has been investigated in order to evaluate the breakdown properties of HFO. As a main result, two distinct breakdown modes were identified in the HFO.

- In quasi-homogeneous field ($\eta < 10$) the breakdown is controlled by the initiation of leaders. When a leader is initiated, it systematically leads to breakdown. When the HFO is new and electrodes clean, the impulse breakdown voltage of HFO is significantly higher than that of SF₆ (up to 160 %). After a single breakdown, the degradation of HFO produces fine dust that deposits on electrodes. As a consequence of dust on electrodes, the positive leader initiation voltage, and hence the breakdown voltage, suddenly drops, and becomes lower than in SF₆ (76 % that of SF₆). In degraded HFO, increasing the pressure has a positive impact on breakdown, that is doubled between 0.1 and 0.3 MPa. Measurements suggest that the design of insulation in degraded HFO could be simply done by calculating the breakdown voltage in SF₆ using the streamer criterion, and applying a de-rating factor of 0.76.
- In strongly divergent field ($\eta > 10$), the breakdown is controlled by the propagation of leaders. Leaders lead to breakdown as soon as they reach the opposite electrode. Under these conditions, the breakdown voltage is of the order of 80 % that of SF₆. The degradation of HFO does not affect these dielectric properties. Increasing the pressure has a very limited impact on breakdown, since leader propagation is rather insensitive to pressure. To improve the breakdown voltage, only the inter-electrode distance has a significant influence.

For MV GIS, HFO could be used as an insulating gas, and not as a cutoff gas since it gets degraded by arcs. Experiments show that the degradation is enhanced with numerous breakdown of low energy, as compared to a single discharge of equivalent energy.

Taking advantage of the very good properties of HFO in clean conditions would require to design insulation with zero breakdown probability (during service and tests), and very low level of partial discharges to prevent HFO degradation on the long term. The long breakdown time of the new HFO ($> 10 \mu\text{s}$), also suggests that with a normalized LI wave (1.2/50 μs), the breakdown voltage should

be even higher than with the long duration wave used here. Testing conditions should be also carefully studied, since breakdown in negative polarity becomes lower than positive in new HFO.

Another more conservative strategy would be to design insulation with parameters relevant for degraded HFO (i.e. corresponding to 75% of SF₆ withstand at the same pressure), with the possibility to enhance pressure to reach the same insulation level as SF₆. In quasi-uniform field, degraded HFO @ 0.25 MPa shows the same breakdown voltage as SF₆ @ 0.15 MPa

Perspectives

The dielectric properties of HFO have been studied over a wide range of conditions. Certain aspects remain however to be developed, both to better understand the discharge mechanisms and the degradation of HFO due to discharges, and to better assess its properties in industrial systems.

The physical characterization of discharges in HFO could be supplemented by more detailed measurements by emission spectroscopy. In this study, the excited species temperatures are studied throughout the discharge created with a pulse wave. The temperature of the gas could be determined and the evolution of the presence of excited species along the discharge could be considered. This will give information about the degradation process of HFO.

The identification of the by-products of HFO-1234ze(E) and their properties (toxicity, GWP, etc.) is very important, it could be carried out by RAMAN or by infrared spectroscopy techniques. The reaction of these products with other materials inside a switchgear should also be studied to predict any potential hazards associated with the use of this gas.

Concerning the characterization of HFO gas with the view to use it in medium voltage applications, and predict its breakdown strength, several additional investigations could be done:

1. change the electrode material. The present study was carried out with stainless steel as the material of the electrode. It would be interesting to carry out similar studies with different electrode materials (aluminium, copper, brass) to evaluate the effect of this material on the drop of discharge initiation field after gas degradation;
2. take measurements with a standardized lightning wave, to better fit with the actual testing conditions of devices;
3. carry out statistical study of breakdown oriented to very low breakdown probabilities. One way to avoid the problems related to HFO degradation could be to design systems with a “zero” breakdown probability, taking advantage of the very good breakdown properties of new HFO, higher than SF₆. A special attention should be paid to breakdown in negative polarity, that becomes the weak point in such conditions, contrary to most gases. The problem would be that characterization of new HFO is very time-consuming;
4. measure swarm parameters would allow calculating the streamer criteria and enhance breakdown prediction;
5. extend the comparison with SF₆ to other geometries, as suggested in the previous section, in order to further validate the ratio SF₆/degraded HFO;

6. investigate gas mixtures (see p.146). Tatarinov et al [44] have shown that the addition of nitrogen in HFO strongly decreases the conversion rate of HFO by discharges;
7. further investigate the influence of solids. In medium voltage devices, insulating solids are in contact with the gas. It would be necessary to study the behavior of HFO discharges along an insulating surface in order to validate its potential use (see p.147).

References

- [1] P. Forster and V. Ramaswamy, *Changes in atmospheric constituents and in radiative forcing*, vol. 15, no. 3. New York, 2007.
- [2] European Union, “RÈGLEMENT (CE) N°842/2006 DU PARLEMENT EUROPÉEN ET DU CONSEIL du 17 mai 2006 relatif à certains gaz à effet de serre fluorés,” 2014.
- [3] European Union, “RÈGLEMENT (UE) N°517/2014 DU PARLEMENT EUROPÉEN ET DU CONSEIL du 16 avril 2014 relatif aux gaz à effet de serre fluorés.,” 2014.
- [4] CIGRÉ Working Group D1.28, “Optimized Gas-Insulated Systems by Advanced Insulation Techniques,” *Cigré Tech. Brochure571.*, 2014.
- [5] Honeywell, “Honeywell Sells Novel Low-Global-Warming Blowing Agent To European Customers.” .
- [6] Cigre Technical Brochure, “Electric performance of new non-SF6 gases and gas mixtures for gas-insulated systems”, Working Group D1.67,” 2021.
- [7] O. Lesaint, N. Bonifaci, H. Merini, R. Maladen, and F. Gentils, “A Study of Breakdown Properties of HFO Gas under DC and Impulse Voltage,” in *2018 IEEE Conference on Electrical Insulation and Dielectric Phenomena (CEIDP)*, 2018, pp. 606–609.
- [8] L. G. Christophorou, J. K. Olthoff, and D. S. Green, *Gases for Electrical Insulation and Arc Interruption: Possible Present and Future Alternatives to Pure SF6*. 1997.
- [9] R. K. Rajput, *Power System Engineering*, Laxmi publ. New Delhi, 2006.
- [10] S. A. Montzka, E. J. Dlugokencky, and J. H. Butler, “Non-CO₂ greenhouse gases and climate change,” *Nature*, vol. 476, no. 7358, pp. 43–50, 2011.
- [11] T. F. Stocker, D. Qin, G.-K. Plattner, A. Nauels, M. M. B. Tignor, Y. Xia, S. K. Allen, V. Bex, J. Boschung, and P. M. Midgley, *Climate Change 2013: The physical science basis*. Cambridge United Kingdom and New York, USA: Cambridge University Press, 2013.
- [12] T. Europe, “Technical Guide to validate alternative gas for SF6 in electrical equipment,” pp. 1–25, 2016.
- [13] I. Levin, T. Naegler, R. Heinz, D. Osusko, E. Cuevas, A. Engel, J. Ilmberger, R. L. Langenfelds, B. Neining, C. V. Rohden, L. P. Steele, R. Weller, D. E. Worthy, and S. A. Zimov, “The global SF6 source inferred from long-term high precision atmospheric measurements and its

- comparison with emission inventories,” *Atmos. Chem. Phys.*, vol. 10, no. 6, pp. 2655–2662, 2010.
- [14] C. Sweeney, A. Karion, S. Wolter, T. Newberger, D. Guenther, J. A. Higgs, A. E. Andrews, P. M. Lang, D. Neff, E. Dlugokencky, J. B. Miller, S. A. Montzka, B. R. Miller, K. A. Masarie, S. C. Biraud, P. C. Novelli, M. Crotnell, A. M. Crotnell, K. Thoning, *et al.*, “Seasonal climatology of CO₂ across north america from aircraft measurements in the NOAA/ESRL global greenhouse gas reference network,” *J. Geophys. Res.*, vol. 120, no. 10, pp. 5155–5190, 2015.
- [15] G. Dutton, “Chromatograph for Atmospheric Trace Species (CATS) in situ Halocarbons Program.” [Online]. Available: <https://www.esrl.noaa.gov/gmd/hats/insitu/cats/index.html>. [Accessed: 28-May-2019].
- [16] J. officiel de l’Union Européenne, “RÈGLEMENT (UE) N o 517/2014 DU PARLEMENT EUROPÉEN ET DU CONSEIL du 16 avril 2014 relatif aux gaz à effet de serre fluorés et abrogeant le règlement (CE) n o 842/2006,” 2014.
- [17] “Iec 62271-1.” 2017.
- [18] “IEC60376: Specification of technical grade sulfur hexafluoride (SF₆) for use in electrical equipment,” 2005.
- [19] G. Mauthe, B. M. Pryor, L. Niemeyer, R. Probst, J. Poblitzki, H. D. Morrison, P. Bolin, P. O’Connell, and J. Henriot, “Sf₆ recycling guide,” Cigre, 1997.
- [20] Y. Qiu and E. Kuffel, “Comparison of SF₆/N₂ and SF₆/CO₂ Gas Mixtures as Alternatives to SF₆ Gas,” *IEEE Trans. Dielectr. Electr. Insulation*, vol. 6, no. 6, pp. 892–895, 1999.
- [21] A. Buttka, J. Pfeiffer, and B. Sojka, “Siemens SF₆/N₂ Circuit-Breaker for Service at Low Temperatures,” *Siemens Power Eng. Spec. Issue “HV Technol.*, vol. 6, pp. 28–37, 1984.
- [22] T. Hillers and H. Koch, “Second-generation gas-insulated line,” *Power Engineering Journal*, vol. 16, no. 3, pp. 111–116, 2002.
- [23] F. Renaud, “220 kV Gas-Insulated Transmission Line,” 2003.
- [24] T. Rokunohe, Y. Yagihashi, F. Endo, and T. Oomori, “Fundamental insulation characteristics of air, N₂, CO₂, N₂/O₂, and SF₆/N₂ mixed gases,” *Electr. Eng. Japan (English Transl. Denki Gakkai Ronbunshi)*, vol. 155, no. 3, pp. 9–17, 2006.
- [25] Y. Hoshina, M. Sato, M. Shiiki, M. Hanai, and E. Kaneko, “Lightning impulse breakdown characteristics of SF₆ alternative gases for gas-insulated switchgear,” *IEE Proc.-Sci. Meas.*

- Technol*, vol. 151, no. 4, pp. 298–304, 2006.
- [26] H. Hama, S. Okabe, R. Buhler, D. Gautschi, A. Girodet, M. Hering, D. Imamovic, K. Juhre, Y. Kieffel, J. Kindersberger, W. Koltunowicz, J. Lopez-roldan, S. Neuhold, C. Neumann, R. Pietsch, U. Riechert, T. Rokunohe, U. Schichlerler, and T. Yasuoka, “Dry Air, N₂, CO₂ and N₂/SF₆ mixtures for gas-insulated systems,” *Cigre Tech. Broch. n°730*, 2018.
- [27] S. Solomon, J. B. Burkholder, A. R. Ravishankara, and R. R. Garcia, “Ozone depletion and global warming potentials of CF₃I,” *J. Geophys. Res.*, vol. 99, no. 94, 1994.
- [28] H. Katagiri, H. Kasuya, H. Mizoguchi, and S. Yanabu, “Investigation of the performance of CF₃I gas as a potential substitute for SF₆,” *IEEE Trans. Dielectr. Electr. Insul.*, vol. 15, no. 5, pp. 1424–1429, 2008.
- [29] Physical and Chemical Properties and efficacy, *National Research Council (US) Subcommittee on Iodotrifluoromethane - Iodotrifluoromethane: Toxicity Review*. Washington, DC, USA, 2004.
- [30] A. D. Mitchell, “Genetic toxicity evaluation of iodotrifluoromethane (CF₃I),” *Genesys Study Number 94035*, 1995.
- [31] J. D. Mantilla, N. Gariboldi, S. Grob, and M. Claessens, “Investigation of the insulation performance of a new gas mixture with extremely low GWP,” in *EIC 2014 - Proceedings of the 32nd Electrical Insulation Conference*, 2014, no. June, pp. 469–473.
- [32] M. Hyrenbach, T. Hintzen, P. Müller, and J. Owens, “Alternative gas insulation in medium-voltage switchgear,” in *Proceedings of the 23rd International Conference on Electricity Distribution, Lyon, France*.
- [33] H. E. Nechml, A. Beroual, A. Girodet, and P. Vinson, “Effective ionization coefficients and limiting field strength of fluoronitriles-CO₂ mixtures,” *IEEE Trans. Dielectr. Electr. Insul.*, vol. 24, no. 2, pp. 886–892, 2017.
- [34] Y. Long, L. Guo, Z. Shen, C. Chen, Y. Chen, F. Li, and W. Zhou, “Ionization and attachment coefficients in C₄F₇N/N₂ gas mixtures for use as a replacement to SF₆,” *IEEE Trans. Dielectr. Electr. Insul.*, vol. 26, no. 4, pp. 1358–1362, 2019.
- [35] Honeywell, “The Environmental Alternative to Traditional Refrigerants,” 2015.
- [36] J. M. Calm and G. C. Hourahan, “Physical, safety and environmental data for current and alternative refrigerants,” in *Refrigeration for Sustainable Development (proceedings of the 23rd International Congress of Refrigeration (ICR 2011))*, 2011, pp. 21–26.

- [37] Y. Wang, D. Huang, J. Liu, Y. Zhang, and L. Zeng, "Alternative Environmentally Friendly Insulating Gases for SF₆," *Processes*, vol. 7, no. 216, pp. 1–14, 2019.
- [38] M. Antiñolo, I. Bravo, E. Jiménez, B. Ballesteros, and J. Albaladejo, "Atmospheric Chemistry of E- and Z-CF₃CH=CHF (HFO-1234ze): OH Reaction Kinetics as a Function of Temperature and UV and IR Absorption Cross Sections," *J. Phys. Chem. A*, vol. 121, no. 43, pp. 8322–8331, 2017.
- [39] C. Preve, R. Maladen, and D. Piccoz, "Method for Validation of New Eco - Friendly Insulating Gases for Medium Voltage Equipment," *Reaserchgate*, vol. 50, no. July, 2016.
- [40] M. Jarahnejad, "New Low Global Warming Potential(GWP) Synthetic Refrigerants," 2012.
- [41] C. Preve, G. Lahaye, M. Richaud, R. Maladen, T. Penelon, and S. Galas, "Hazard study of medium-voltage switchgear with SF₆ alternative gas in electrical room," *CIREN - Open Access Proc. J.*, vol. 2017, no. 1, pp. 198–201, 2017.
- [42] G. M. Rusch, A. Tveit, H. Muijser, M.-M. Tegelenbosch-Schouten, and G. M. Hoffman, "The acute, genetic, developmental and inhalation toxicology of trans-1,3,3,3-tetrafluoropropene (HFO-1234ze)," *Drug Chem. Toxicol.*, vol. 36, no. 2, pp. 170–180, 2013.
- [43] C. Preve, D. Piccoz, and R. Maladen, "Application of HFO1234ZEE in MV switchgear as SF₆ alternative gas," in *24th International Conference & Exhibition on Electricity Distribution (CIREN)*, 2017, pp. 42–45.
- [44] A. V. Tatarinov, I. V. Bilera, S. V. Avtaeva, V. A. Shakhmatov, P. V. Solomakhin, R. Maladen, C. Prévé, D. Piccoz, A. V. Tatarinov, D. Piccoz, I. V. Bilera, R. Maladen, V. A. Shakhmatov, C. Prévé, and P. V. Solomakhin, "Dielectric Barrier Discharge Processing of trans-CF₃CH=CHF and CF₃C(O)CF(CF₃)₂, Their Mixtures with Air, N₂, CO₂ and Analysis of Their Decomposition Products," *Plasma Chem. Plasma Process.*, vol. 35, no. 5, pp. 845–862, 2015.
- [45] R. Zhai, Z. Yang, Y. Chen, B. Feng, Z. Lv, and W. Zhao, "Theoretical and experimental studies on the combustion mechanism of Trans-1, 3, 3, 3-tetrafluoroprop-1-ene," *Energy*, vol. 189, p. 116087, 2019.
- [46] L. G. Christophorou and L. A. Pinnaduwege, "Basic physics of gaseous dielectrics," *IEEE Trans. Electr. Insul.*, vol. 25, no. 1, pp. 55–74, 1990.
- [47] Y. P. Raizer, *Gas discharge physics*, Springer. 1991.
- [48] M. J. Druyvesteyn and F. M. Penning, "The mechanism of electrical discharges in gases of low pressure," *Rev. Mod. Phys.*, vol. 12, no. 2, pp. 87–174, 1940.

- [49] N. Wiegart, L. Niemeyer, F. Pinnekamp, W. Boeck, J. Kindesberger, R. Morrow, W. Zaengl, M. Zwicky, I. Gallimberti, and S. Boggs, “Inhomogeneous field breakdown in GIS—the prediction of breakdown probabilities and voltages. Part I: Overview of a Theory for Inhomogeneous Field Breakdown in SF₆,” *IEEE Trans. Power Deliv.*, vol. 3, no. 3, pp. 931–938, 1988.
- [50] I. W. McAllister, “On the Concept of Electrode Surface Roughness with Reference to Discharge Phenomena in Strongly Electronegative Gases,” *IEEE Trans. Electr. Insul.*, vol. EI-21, no. 4, pp. 659–662, 1986.
- [51] A. Pedersen, “On the Electrical Breakdown of Gaseous Dielectrics: An Engineering Approach,” *IEEE Trans. Electr. Insul.*, vol. 24, no. 5, pp. 721–739, 1989.
- [52] A. Pedersen, “On the Assessment of New Gaseous Dielectrics for GIS,” *IEEE Power Eng. Rev.*, vol. PER-5, no. 8, p. 54, 1985.
- [53] L. B. Loeb and J. M. Meek, “The mechanism of spark discharge in air at atmospheric pressure. I,” *J. Appl. Phys.*, vol. 11, no. 6, pp. 438–447, 1940.
- [54] J. M. Meek and J. D. Craggs, *Electrical breakdown of gases*, Oxford. Great Britain, 1953.
- [55] T. M. P. Briels, J. Kos, G. J. J. Winands, E. M. Van Veldhuizen, and U. Ebert, “Positive and negative streamers in ambient air: Measuring diameter, velocity and dissipated energy,” *J. Phys. D. Appl. Phys.*, vol. 41, no. 23, 2008.
- [56] A. Luque, V. Ratushnaya, and U. Ebert, “Positive and negative streamers in ambient air: Modelling evolution and velocities,” *J. Phys. D. Appl. Phys.*, vol. 41, no. 23, pp. 1–18, 2008.
- [57] O. Eichwald, O. Ducasse, D. Dubois, A. Abahazem, N. Merbahi, M. Benhenni, and M. Yousfi, “Experimental analysis and modelling of positive streamer in air: Towards an estimation of O and N radical production,” *J. Phys. D. Appl. Phys.*, vol. 41, no. 23, 2008.
- [58] L. TREMAS, Phd thesis “Pre-breakdown and breakdown phenomena in air along insulating solids,” Université de Grenoble, 2016.
- [59] H. Kojima, K. Hotta, T. Kitamura, N. Hayakawa, A. Otake, K. Kobayashi, T. Kato, T. Rokunohe, and H. Okubo, “Classification of impulse breakdown mechanisms under non-uniform electric field in air,” *IEEE Trans. Dielectr. Electr. Insul.*, vol. 23, no. 1, pp. 194–201, 2016.
- [60] E. Marode, “The mechanism of spark breakdown in air at atmospheric pressure between a positive point and a plane. I. Experimental: Nature of the streamer track,” *J. Appl. Phys.*, vol. 46, no. 5, pp. 2005–2015, 1975.

- [61] M. Akyuz, A. Larsson, V. Cooray, and G. Strandberg, "3D simulations of streamer branching in air," *J. Electrostat.*, vol. 59, no. 2, pp. 115–141, 2003.
- [62] C. Li, U. Ebert, and W. Hundsdorfer, "Spatially hybrid computations for streamer discharges : II. Fully 3D simulations," *J. Comput. Phys.*, vol. 231, no. 3, pp. 1020–1050, 2012.
- [63] S. Singh, Y. V Serdyuk, and R. Summer, "Streamer Branching in Air: Physical Model and Simulations in Fully 3D Spatial Domain," in *2015 IEEE 11th International Conference on the Properties and Applications of Dielectric Materials (ICPADM)*, 2015, pp. 220–223.
- [64] L. Niemeyer and F. Pinnekamp, "Leader discharges in SF₆," *J. Phys. D. Appl. Phys.*, vol. 16, no. 6, pp. 1031–1045, 1983.
- [65] I. D. Chalmers, I. Gallimberti, A. Gibert, and O. Farish, "The development of electrical leader discharges in a point-plane gap in SF₆," *Proc. R. Soc. A Math. Phys. Eng. Sci.*, vol. 412, pp. 285–308, 1987.
- [66] I. Gallimberti and N. Wiegart, "Streamer and leader formation in SF₆ and SF₆ mixtures under positive impulse conditions. I. Corona development," *J. Phys. D Appl. Phys.*, vol. 2363, no. 19, pp. 1–14, 1986.
- [67] M. Seeger, L. Niemeyer, and M. Bujotzek, "Leader propagation in uniform background fields in SF₆," *J. Phys. D. Appl. Phys.*, vol. 42, no. 18, 2009.
- [68] H. Rodrigo and P. A. Chatteron, "A study of the critical pressure in SF₆/N₂ mixtures for positive point plane systems with impulse voltages," *IEEE Trans. Electr. Insul.*, no. 1, pp. 53–62, 1984.
- [69] T. Hinterholzer and W. Boeck, "Breakdown in SF₆ influenced by Corona-Stabilization," *Electr. Insul. Dielectr. Phenomena, 2000 Annu. Rep. Conf.*, vol. 1, pp. 413–416, 2000.
- [70] O. C. Feet, F. Mauseth, and K. Niayesh, "Influence of Surface Roughness on Breakdown in Air Gaps at Atmospheric Pressure Under Lightning Impulse," *IEEE*, no. 1, pp. 1–4, 2018.
- [71] A. Pedersen, "The effect of surface roughness on breakdown in SF₆," *IEEE Trans. power Appartus ans Syst.*, vol. PAS-94, no. 5, pp. 1749–1754, 1975.
- [72] A. Beroual, U. Khaled, and M.-L. Coulibaly, "Experimental investigation of the breakdown voltage of CO₂, N₂, and SF₆ Gases, and CO₂–SF₆ and N₂–SF₆ mixtures under different voltage waveforms," *Energies*, vol. 11, no. 902, pp. 1–12, 2018.
- [73] J. Ma, Q. Zhang, Z. Wu, C. Guo, T. Wen, G. Wang, and C. Gao, "Breakdown characteristics of particle-contaminated HVDC GIL under superimposed voltage of DC and impulse," *IEEE*

- Trans. Dielectr. Electr. Insul.*, vol. 25, no. 4, pp. 1439–1447, 2018.
- [74] J. Seong, W. Shin, J. Hwang, J.-G. Lee, B.-W. Lee, K.-B. Seo, and D.-H. Jeong, “Effect of humidity and electrode roughness on the AC and impulse breakdown characteristics of dry-air,” in *2012 IEEE International Conference on Condition Monitoring and Diagnosis*, 2012, pp. 770–773.
- [75] G. Berger, E. Marode, O. Belabed, B. Senouci, I. Gallimberti, and A. Osgualdo, “Effect of water vapour on the discharge regimes and the deviations from similarity law in compressed SF₆ for positive polarity,” *J. Phys. D. Appl. Phys.*, vol. 24, pp. 1551–1556, 1991.
- [76] P. Dular and C. Geuzaine, “GetDP.” [Online]. Available: <https://getdp.info/>. [Accessed: 23-Jun-2021].
- [77] P. Dular, C. Geuzaine, F. Henrotte, and W. Legros, “A general environment for the treatment of discrete problems and its application to the finite element method,” *IEEE Trans. Magn.*, vol. 34, no. 5, pp. 3395–3398, 1998.
- [78] I. Gallimberti, “The mechanism of the long spark formation,” *J. Phys. Colloq.*, pp. 1–59, 1979.
- [79] I. D. Chalmers, O. Farish, A. Gilbert, and J. Dupuy, “Leader development in short point-plane gaps in compressed SF₆,” *Science (80-.)*, vol. 131, no. 3, pp. 159–163, 1984.
- [80] T. M. P. Briels, E. M. Van Veldhuizen, and U. Ebert, “Positive streamers in air and nitrogen of varying density: Experiments on similarity laws,” *J. Phys. D. Appl. Phys.*, vol. 41, no. 23, 2008.
- [81] P. Tardiveau, N. Moreau, S. Bentaleb, C. Postel, and S. Pasquiers, “Diffuse mode and diffuse-to-filamentary transition in a high pressure nanosecond scale corona discharge under high voltage,” *J. Phys. D. Appl. Phys.*, vol. 42, no. 17, 2009.
- [82] L. Niemeyer, L. Ullrich, and N. Wiegart, “The Mechanism of Leader Breakdown in Electronegative Gases,” *IEEE Trans. Electr. Insul.*, vol. 24, no. 2, pp. 309–324, 1989.
- [83] Y. Qiu, W. Gu, Q. Zhang, and E. Kuffel, “The pressure dependence of the leader stepping time for a positive point–plane gap in SF₆ gas,” *J. Phys. D Appl. Phys.*, vol. 31, pp. 3252–3254, 1998.
- [84] E. Stoffels, A. J. Flikweert, W. W. Stoffels, and G. M. W. Kroesen, “Plasma needle: A non-destructive atmospheric plasma source for fine surface treatment of (bio)materials,” *Plasma Sources Sci. Technol.*, vol. 11, no. 4, pp. 383–388, 2002.
- [85] N. L. Allen and P. N. Mikropoulos, “Surface Profile Effect on Streamer Propagation and Breakdown in Air,” *IEEE Trans. Dielectr. Electr. Insul.*, vol. 8, no. 5, pp. 812–817, 2001.

- [86] P. N. Mikropoulos, C. A. Stassinopoulos, and B. C. Sarigiannidou, "Positive streamer propagation and breakdown in air: The influence of humidity," *IEEE Trans. Dielectr. Electr. Insul.*, vol. 15, no. 2, pp. 416–424, 2008.
- [87] F. Pinnekamp and L. Niemeyer, "Qualitative model of breakdown in SF₆ in inhomogeneous gaps," *J. Phys. D. Appl. Phys.*, vol. 16, no. 7, pp. 1293–1302, 1983.
- [88] A. N. Lagarkov and I. M. Rutkevich, *Ionization waves in electrical breakdown of gases*, Springer-V. New-York, 1994.
- [89] O. Eichwald, M. Yousfi, and O. Ducasse, "Breakdown criteria in air: An overview supported by predictive simulations," in *11ème Conférence de la Société Française d'Electrostatique Grenoble France*, 2018, pp. 1–6.
- [90] B. Bagheri, J. Teunissen, U. Ebert, M. M. Becker, S. Chen, O. Ducasse, O. Eichwald, D. Loffhagen, A. Luque, D. Mihailova, J. M. Plewa, J. Van Dijk, and M. Yousfi, "Comparison of six simulation codes for positive streamers in air," *Plasma Sources Sci. Technol.*, vol. 27, no. 9, 2018.
- [91] J. J. Lowke and F. D'Alessandro, "Onset corona fields and electrical breakdown criteria," *J. Phys. D. Appl. Phys.*, vol. 36, no. 21, pp. 2673–2682, 2003.
- [92] P. Haefliger and C. M. Franck, "Detailed precision and accuracy analysis of swarm parameters from a pulsed Townsend experiment," *Rev. Sci. Instrum.*, vol. 89, no. 2, 2018.
- [93] M. Koch, Phd thesis "Prediction of Breakdown Voltages in Novel Gases for High Voltage Insulation," Université de Zurich, 2015.
- [94] H. Itoh, M. Shimosuma, H. Tagashira, and S. Sakamoto, "Measurement of the effective ionisation coefficient and the static breakdown voltage in SF₆ and nitrogen mixtures," *J. Phys. D. Appl. Phys.*, vol. 12, no. 12, pp. 2167–2172, 1979.
- [95] J. L. Hernández-Ávila and J. De Urquijo, "Pulsed townsend measurement of electron transport and ionization in SF₆-N₂ mixtures," *J. Phys. D. Appl. Phys.*, vol. 36, no. 12, pp. 2–6, 2003.
- [96] L. G. Christophorou and J. K. Olthoff, "Electron interactions with SF₆," *J. Phys. Chem. Ref. Data*, vol. 29, no. 3, pp. 267–330, 2000.
- [97] K. Satoh, H. Itoh, Y. Nakao, and H. Takjashira, "Electron swarm development in SF₆. II. Monte Carlo simulation," *J. Phys. D. Appl. Phys.*, vol. 21, no. 6, pp. 931–936, 1988.
- [98] T. Liu, I. V. Timoshkin, S. J. Macgregor, M. P. Wilson, M. J. Given, N. Bonifaci, and R. Hanna,

- “Field-Time Breakdown Characteristics of Air, N₂, CO₂, and SF₆,” *IEEE Trans. Plasma Sci.*, vol. 48, no. 10, pp. 3321–3331, 2020.
- [99] H. Itoh, Y. Miura, N. Ikuta, Y. Nakao, and H. Tagashira, “Electron swarm development in SF₆. I. Boltzmann equation analysis,” *J. Phys. D. Appl. Phys.*, vol. 21, no. 6, pp. 922–930, 1988.
- [100] W. Wang, X. Tu, D. Mei, and M. Rong, “Dielectric breakdown properties of hot SF₆/He mixtures predicted from basic data,” *Phys. Plasmas*, vol. 20, no. 11, 2013.
- [101] J. Schwabedissen, T. Glodde, Y. V. Vishnevskiy, H. Stammeler, L. Flierl, A. J. Kornath, and N. W. Mitzel, “Structures and Properties of trans -1,3,3,3-Tetrafluoro- propene (HFO-1234ze) and 2,3,3,3-Tetrafluoropropene (HFO-1234yf) Refrigerants ,” *ChemistryOpen*, vol. 9, no. 9, pp. 921–928, 2020.
- [102] S. MERINI, “Dielectric Study of HFO1234ze(E) as an alternative gas for SF₆ in Medium Voltage Switchgear,” 2017.
- [103] “NIST Atomic Spectra Database Levels Form.” [Online]. Available: https://physics.nist.gov/PhysRefData/ASD/levels_form.html. [Accessed: 13-Jul-2021].
- [104] L. Smith, C. Heise, J. R. Esmond, and R. L. Kurucz, “Atomic spectral line database,” 1995. [Online]. Available: <https://lweb.cfa.harvard.edu/amp/ampdata/kurucz23/sekur.html>. [Accessed: 13-Jul-2021].
- [105] H. R. Griem, *Principles of plasma spectroscopy*. New York, 1964.
- [106] M. A. Gigosos and V. Cardeñoso, “New plasma diagnosis tables of hydrogen Stark broadening including ion dynamics,” *J. Phys. B At. Mol. Opt. Phys.*, vol. 29, pp. 4795–4838, 1996.
- [107] F. Roux and F. Michaud, “High-resolution Fourier spectrometry of 14N₂ infrared emission spectrum: Extensive analysis of the w1Δu → a1Πg system,” *Journal of Molecular Spectroscopy*, vol. 158, pp. 270–277, 1993.
- [108] K. P. Huber and G. Herzberg, *Molecular spectra and molecular structure, IV. Constants of diatomic molecules*, Van Nostra. New-York, 1979.
- [109] G. Herzberg, *Molecular spectra and molecular structure I. Spectra of diatomic molecules*, D. Van Nos. 1950.
- [110] B. Rosen, *Spectroscopic data relative to diatomic molecules*. Paris, 1970.
- [111] A. Lofthus and P. H. Krupenie, “The spectrum of molecular nitrogen,” *J. Phys. Chem. Ref. Data*, vol. 6, no. 1, pp. 113–307, 1977.

- [112] C. O. Laux and C. H. Kruger, "Arrays of radiative transition probabilities for the N₂ first and second positive, no beta and gamma, N₂⁺ first negative, and O₂ Schumann-Runge band systems," *J. Quant. Spectrosc. Radiat. Transf.*, vol. 48, no. 1, pp. 9–24, 1992.
- [113] P. Fauchais, *First report on measurement of temperature and concentration of excited species in optically thin plasma*, Internatio. Limoges, 1979.
- [114] A. Chachereau and C. Franck, "Characterization of HFO1234ze mixtures with N₂ and CO₂ for use as gaseous electrical insulation media," in *19th International Symposium on High Voltage Engineering, Buenos Aires, Argentina, August 28 - September 1, 2017*, 2017.
- [115] A. Hösl, J. Pachin, E. Egüz, A. Chachereau, and C. M. Franck, "Positive synergy of SF₆ and HFO1234ze(E)," *ETH - High Volt. Lab.*, pp. 6–9, 2019.
- [116] S. Théoleyre, "Techniques de coupure en moyenne tension," 2002.
- [117] Laboratory Earth system research, "Sulfur hexafluoride (SF₆) — Combined Data Set," 2019. [Online]. Available: <https://www.esrl.noaa.gov/gmd/hats/combined/SF6.html>. [Accessed: 01-Mar-2019].
- [118] D. Fulchiron, "Surtensions et coordination de l'isolement," *Cah. Tech. Merlan Gernin*, vol. 151, 1992.
- [119] N. Naudé, "Applications des DBDs," pp. 1–27.
- [120] T. W. Dakin, G. Luxa, G. Oppermann, J. Vigreux, G. Wind, and H. Winkelkemper, "Breakdown of gases in uniform fields paschen curves for nitrogen, air and sulfur hexafluoride," *Electra*, vol. 32, pp. 61–82, 1982.
- [121] L. Zhang, J. Wu, S. Wang, L. Sun, and Q. Zhang, "Critical radius phenomenon and mechanism for SF₆ gaps under very fast transient and lightning impulse voltages," *IEEJ Trans. Electr. Electron. Eng.*, vol. 13, no. 3, pp. 367–372, 2018.
- [122] G. L. Christophorou, K. J. Olthoff, and D. S. Green, "Gases for electrical insulation and arc interruption: Possible present and future alternatives to pure SF₆," *Natl. Institute Stand. Technol. (NIST), U.S. Dep. Commer. Washington, USA*, no. November, 1997.

Annexe 1: Spectroscopy of emitted light

For atomic species

The spectroscopic parameters of selected spectral lines in this work have been derived from the available atomic spectra database [103], [104].

Determination of T_{exc}

The excitation temperature, T_{exc} , is determined by fitting a thermal distribution to the appropriately weighted intensities of a set of atomic transitions for a specific atomic species in the plasma. In our experiments, the atomic species used is iron, fluor...

A key assumption in this analysis of T_{exc} is that atomic line and the electrons are each in thermal equilibrium. If the plasma is shown to be in or near local thermodynamic equilibrium (LTE), then this assumption is valid. The condition of LTE specifies that all temperatures in the plasma are equal except the blackbody radiation temperature. LTE requires that the collisional processes dominate the radiative processes in the plasma. Griem [105] has established a criterion for the determination of a plasma's proximity to LTE. This formulation places a lower limit on the electron density. The Griem criterion states

$$N_e \geq 9 \times 10^{11} \left(\frac{\Delta E}{E_H} \right)^3 \sqrt{\frac{T_e}{E_H}}$$

Where N_e is the electron density in cm^{-3} , ΔE is the energy level difference between the ground-state and the first ionization state, E_H is the ionization potential for hydrogen (13.6 eV), and T_e is the electron temperature. Evaluating the equation for an electron temperature of approximately 1 eV and for a ΔE corresponding to the ionization potential for the N_2 molecule (15.6 eV) results in an electron density threshold of $\sim 3 \times 10^{17} \text{ m}^{-3}$ for LTE. This value is well below the electron densities for the breakdown phase. Therefore, based on the Griem criteria the assumption of LTE is believed to be valid for the breakdown phase.

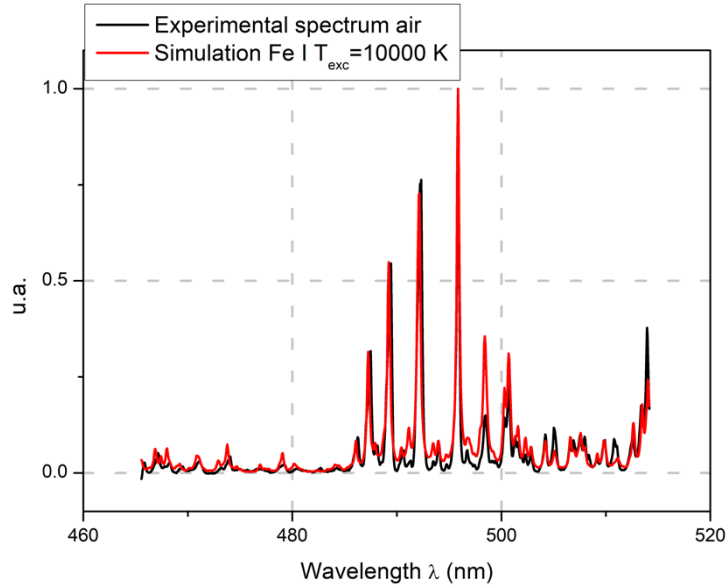


Figure 1 : Spectrum of a breakdown in the air ($R_c = 0.2$ mm, $d = 50$ mm, $P = 0.1$ MPa) corrected spectrum

The specific case of hydrogen lines

A set of tables of the Stark width of the Balmer series of hydrogen, was provided by Gigoso and Cardeñoso in 1996 [106]. These tables are available for N_e between 10^{20} m $^{-3}$ and $\sim 10^{25}$ m $^{-3}$ and T_e between 2,245 K and 224,856 K for different reduced masses of the emitter-perturbed pair μ in the range 0.5-2.0 amu. Their utilization is straightforward and convenient.

Table 1 : Hydrogen transition

	λ (nm)	Transition
H α	656.3	3d \rightarrow 2p
H β	486.1	4d \rightarrow 2p

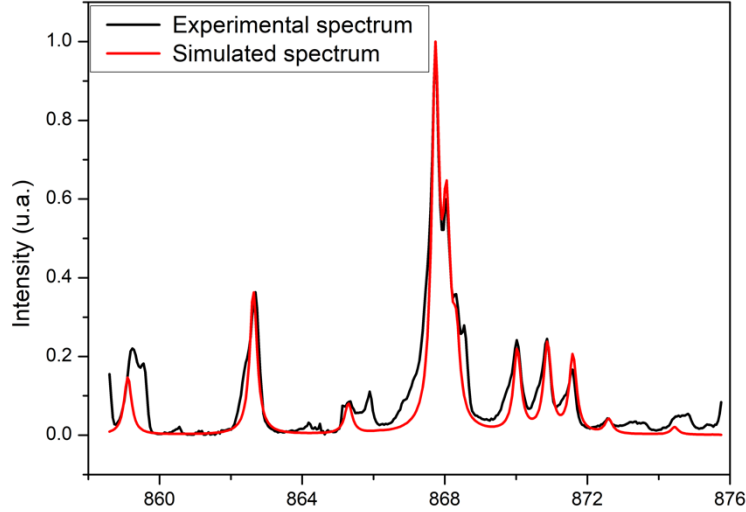


Figure 2 : Experimental spectrum and simulated spectrum of NI for breakdown in air ($R_c = 0.2$ mm, $d = 50$ mm, $P = 0.1$ MPa) corrected spectrum

For molecular species

The energy of the levels for a diatomic molecule, in Born-Oppenheimer approximation may written by

$$E = hc[T_e + G(u) + F_u(J)]$$

T_e , $G(u)$ and $F_u(J)$ are the electric, vibrational and rotational term energies respectively; h is the Planck's constant, and c is the velocity of light in vacuum. The vibrational levels can be described by an anharmonic oscillator:

$$G(u) = w_e \left(u + \frac{1}{2}\right) - w_e x_e \left(u + \frac{1}{2}\right)^2$$

Concerning the distribution of the rotational levels for given vibrational level and electronic state, one has:

$$F_u(J) = B_u J(J + 1) - D_u J^2(J + 1)^2 \dots$$

which $B_u = B_e - a_e \left(u + \frac{1}{2}\right) + g_e \left(u + \frac{1}{2}\right)^2 + \dots$ and $D_u = D_e - b_e \left(u + \frac{1}{2}\right) + \dots$ where B_0 and D_0 are rotational and centrifugal distortion rotational constants ω_e , $\omega_e x_e$ and $\omega_e \gamma_e$ the vibrational constant and B_e , a_e , γ_e , D_e , β_e the spectroscopic constants.

The intensity of line of vibrational-rotational transition can be expressed as:

$$I_{u'J'u''}^{J'J''} = C \frac{S^{J'J''} q_{u'u''}}{l^4} \exp\left(-\frac{E_u}{kT_u}\right) \exp\left(-\frac{E_r}{kT_r}\right)$$

Where $S^{J'J''}$ are Hönl-London factors for rotational transition, $q_{u'u''}$ is the Franck-Codon factor for vibrational transition, E and T are energy and temperatures; 'v' and 'r' refer to the vibrational and rotational transition correspondingly, the C parameter includes constants and concentration of particles inconsequential to our relative method for defining temperatures. Hönl-London were taken from [], Franck-Codon factors from [107].

If the rotational states are in equilibrium, they are distributed according to a Boltzmann law:

$$N_u = \frac{N_0 g_u}{Q(T_r)} e^{-E_u/kT_r}$$

N and N_0 are the numbers of molecules in level u and in the ground state respectively, Q is the partition function, which depends on the rotational temperature, g_u is the statistical weight of level u , E_u the energy of this level and k the Boltzmann constant.

The second positive band system of N_2 ($C-B$) corresponds to the radiation transitions between the electronic states of $C^3\Pi_u$ and $B^3\Pi_g$, with electronic energies at 11.03 eV and 7.35 eV, respectively. Due to the strong interaction of the spin and the orbital angular momenta, three rotational terms F_1 , F_2 and F_3 are obtained [Budo]:

$$F_1(J) = Bv \left[J(J+1) - \sqrt{y_1 + 4J(J+1)} - \frac{2y_2 - 2J(J+1)}{3y_1 + 4J(J+1)} \right] - Dv \left(J - \frac{3}{2} \right)^4$$

$$F_2(J) = Bv \left[J(J+1) - \frac{4y_2 - 2J(J+1)}{3y_1 + 4J(J+1)} \right] - Dv \left(J - \frac{1}{2} \right)^4$$

$$F_3(J) = Bv \left[J(J+1) - \sqrt{y_1 + 4J(J+1)} - \frac{2y_2 - 2J(J+1)}{3y_1 + 4J(J+1)} \right] - Dv \left(J - \frac{3}{2} \right)^4$$

$$y_1 = \Lambda^2 Y(Y-4) + \frac{4}{3}$$

$$y_2 = \Lambda^2 Y(Y-1) + \frac{4}{9}$$

$$Y = \frac{A_v}{B_v}$$

Y measures the coupling strength between the spin and the orbital angular momentum.

Table 2 shows the Franck–Condon factors for $C-B$ transition. The molecular constants of the $C^3\Pi_u$ state and $B^3\Pi_g$ state of N_2 molecule are listed in Table 3 and Table 4.

Table 2 : Franck-Condon factors of the ${}^3\Pi_u \rightarrow B^3\Pi_g$ system N_2 [107]

ν''	$\nu' = 0$	$\nu' = 1$	$\nu' = 2$	$\nu' = 3$	$\nu' = 4$
0	0.45100	0.39430	0.13340	0.02036	0.00096
1	0.32760	0.02145	0.34120	0.25380	0.05392
2	0.14680	0.20310	0.02415	0.21010	0.33270
3	0.05211	0.19810	0.06313	0.08854	0.12300
4	0.01617	0.11040	0.16060	0.00451	0.10850
5	0.00461	0.04712	0.13880	0.09324	0.00458
6	0.00124	0.01726	0.07948	0.12980	0.04084

Table 3 : Spectroscopic constants of electronic state $C^3\Pi_u$ of N_2

	[108]	[109]	[110]	[111]	[112]
Te (cm^{-1})	89136.88	89147	88977.9	88977.84	89136.88
w_e (cm^{-1})	2047.178	2035.1	2047.178	2047.178	2047.7800
$\omega_e x_e$ (cm^{-1})	28.4450	17.08	28.4450	28.4450	28.9788
$\omega_e y_e$ (cm^{-1})	2.08833	-2.15	2.08833	2.05533	2.24731
$\omega_e z_e$ (cm^{-1})	-0.5350		0.5350	-0.5350	-0.55145
B_e (cm^{-1})	1.82473	1.8259	1.82473	1.82173	1.82677
α_e (cm^{-1})	0.01868	0.0197	0.018683	0.018683	0.024
r_e (\AA)	1.1486	1.1482	1.1487	1.148688	
$D_e \times 10^{-6}$ (cm^{-1})			5.80		

Table 4 : Spectroscopic constants of electronic state $B^2\Sigma_u^+$ of N_2

	[108]	[109]	[110]	[111]	[112]	[113]
Te (cm^{-1})	25461.46	25461.5	25566.1	151233.5	25461.11	25461.5
w_e (cm^{-1})	2419.84	2419.84	2419.84	2419.84	2424.14	2419.84
$\omega_e x_e$ (cm^{-1})	23.18	23.19	23.19	23.19	24.07	23.19
$\omega_e y_e$ (cm^{-1})	-0.537	-0.5375	-0.5375		-0.30	-0.5375
$\omega_e z_e$ (cm^{-1})	-0.0495				-0.0667	
B_e (cm^{-1})	2.07456	2.083	2.085	2.073	2.08507	2.083
α_e (cm^{-1})	0.024	0.0195		0.020	0.0212	0.0195
r_e (\AA)	1.0742	1.075	1.075	1.07772		1.075
$D_e \times 10^{-6}$ (cm^{-1})	6.17		6.2			

Annexe 2: Streamer criteria

For air, $\frac{a_{eff}}{N} = 4.10^{-20} \exp\left(-\frac{985}{\frac{E}{N}+43}\right) - 30.10^{-24} (m^2) \rightarrow 94 < E/N < 1500 (Td)$

For SF₆, $\frac{a_{eff}}{N} = -9.10^{-20} \exp\left(-\frac{E/N}{2875}\right) + 8.10^{-20} (m^2) \rightarrow 360 < E/N < 5000 (Td)$

In plan-plan, $\int_0^{x_{cr}} a_{eff} dx = K$ simplified in $a_{eff} d = K$

Annexe 3: Observations during post-breakdown in HFO

Measurements and observations are still inexplicable regarding current and light recorded during the post-breakdown arc in HFO. These measurements were carried out with the STI wave, in HFO degraded in a quasi-homogeneous field ($R_c = 5$ mm, $d = 50$ mm, $P = 0.1$ MPa).

The Figure 3 shows the voltage during a breakdown in HFO and air and the corresponding current. For an equivalent voltage (90 kV), the duration during which the current circulates during the post-breakdown arc is 30 μ s for the 2 gases.

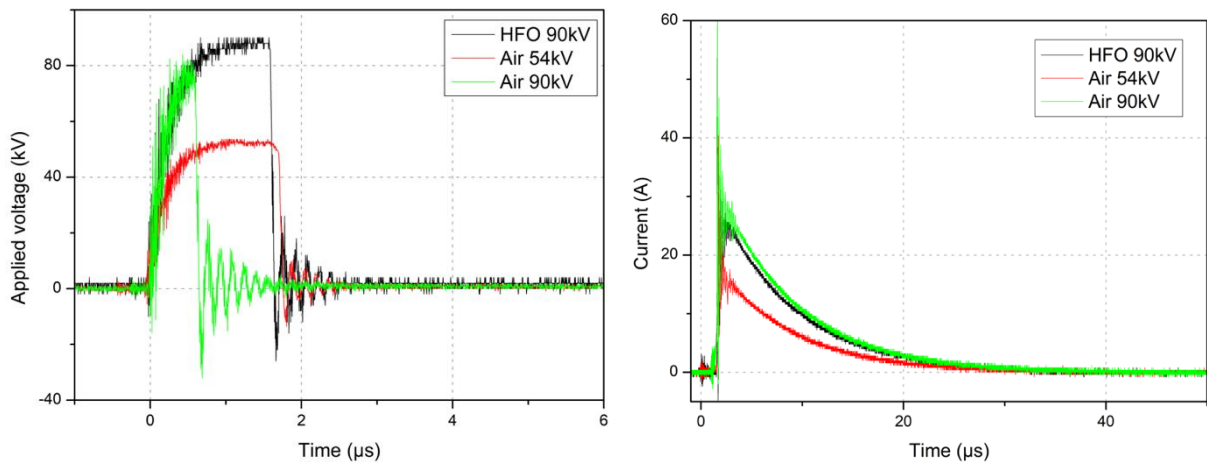


Figure 3 : Current of arc and applied voltage in air and HFO (STI, $R_c = 5$ mm, $d = 50$ mm, $P = 0.1$ MPa)

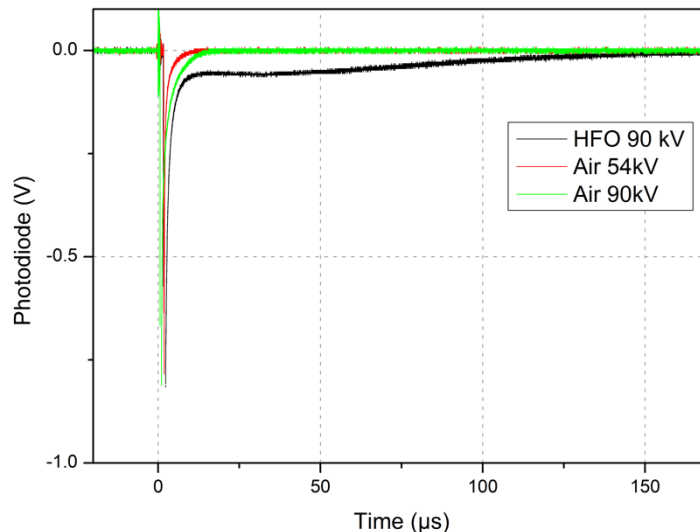


Figure 4 : Light emission recorded by a photodiode during a breakdown in the air and the HFO (STI, $R_c = 5$ mm, $d = 50$ mm, $P = 0.1$ MPa)

Figure 4 shows the corresponding light emission recorded by a photodiode. It is observed that in air, the arc emits light for less than 10 μ s. In the HFO, at an equivalent voltage, the duration of light emission during the post-breakdown arc is greater than 100 μ s.

Figure 5 is obtained with a high speed camera. As in Figure 4, light is visible in the HFO after 100 μ s, after breakdown. One can observe luminous "packets" in the inter-electrode space which gradually extinguish. These light emissions could be associated to particles in suspension, which will later be deposited on the walls of the cell and on the electrodes.



*Figure 5 : Image of emitted light 100 μ s after breakdown in HFO
($R_c = 5$ mm, $d = 50$ mm, $P = 0.1$ MPa, $U_a = 90$ kV)*

Assuming that the dust particles are charged, measurements were performed by applying a DC voltage between 2 impulses to sweep them. Figure 6 and Figure 7 do not show any gain in the breakdown voltage with DC voltage, whatever the gas used.

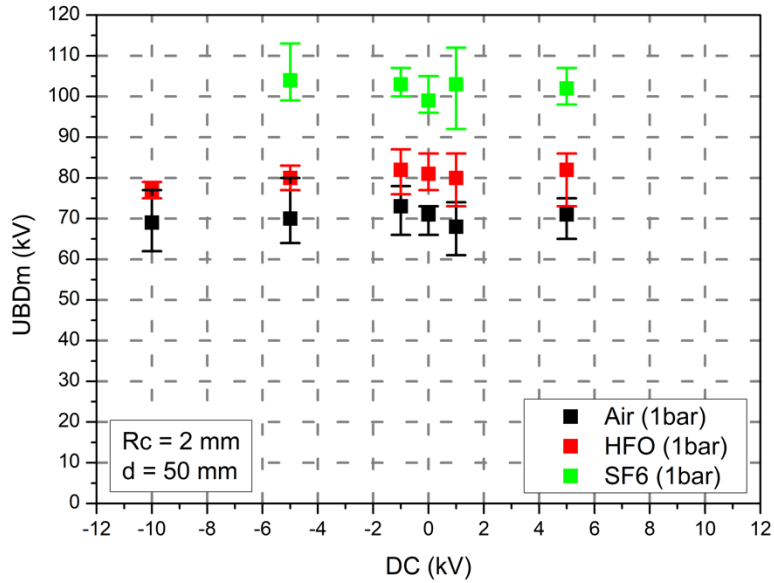


Figure 6 : ($R_c = 2 \text{ mm}$, $d = 50 \text{ mm}$, $P = 0.1 \text{ MPa}$)

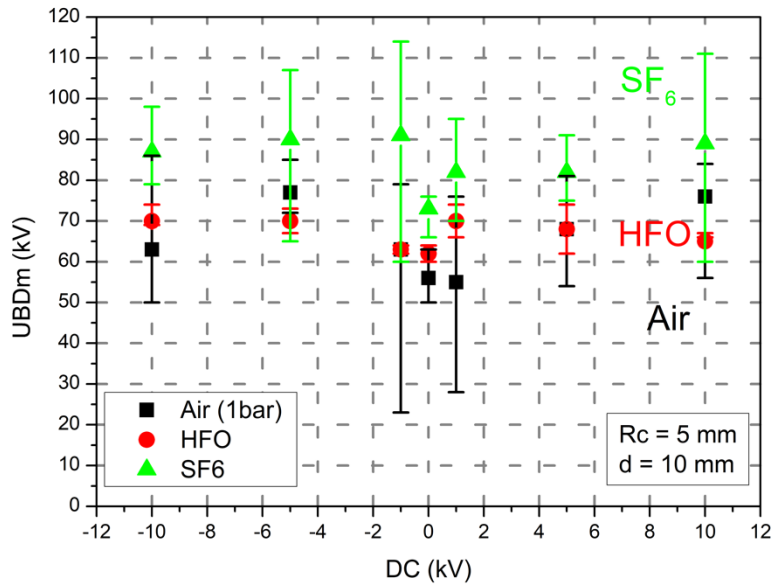


Figure 7 : ($R_c = 5 \text{ mm}$, $d = 10 \text{ mm}$, $P = 0.1 \text{ MPa}$)

Annexe 4: Perspectives

Gas characterization, study of mixtures

Tatarinov et al [44] have shown that the addition of nitrogen in HFO strongly decreases the conversion rate of HFO by discharges. No information was however provided on the production of dust by-product. We may verify that the addition of nitrogen (25% in [44]) in the HFO also decreases the deposit formation on electrodes. Chachereau et al [114] also studied theoretically the possible synergy between HFO and nitrogen (Figure 8). According to this study, it seems that a synergy effect is not present between HFO and CO₂ or N₂ (such synergistic effect exists with SF₆ in N₂), but no breakdown measurements were provided to confirm this conclusion. Hösl et al. [115] obtained a positive synergy for a mixture of 60 % HFO with 40 % SF₆, with a reduced E/N field of 425 Td (Figure 9). However, the objective is to totally remove SF₆ in future applications.

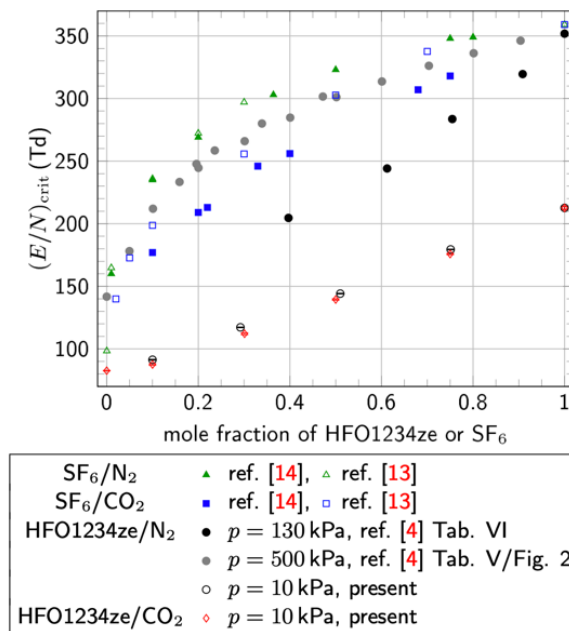


Figure 8 : Reduced critical electric field as a function of HFO1234ze or SF₆ mole fraction in N₂ or CO₂ [114]

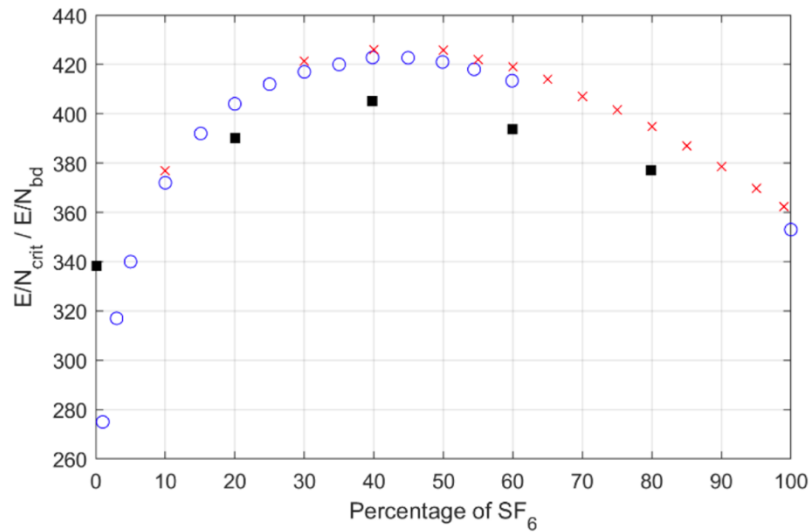


Figure 9 : Critical field strength $(E/N)_{crit}$ of mixtures of SF_6 with HFO1234ze(E). In blue circles, a measurement series at pressures of 360- 480 Pa is shown. In red crosses, we used higher, variable pressures from 4-12 kPa. In black squares, breakdown results $(E/N)_{bd}$ for the mixture of SF_6 with C_3F_6 is given at pressure of 67 kPa [115].

Effects of insulating solids on breakdown in HFO

In addition to breakdown in gas, an important aspect for MV application is the breakdown along solid insulating surfaces. This aspect has not been investigated here. Preliminary studies have shown good compatibility between HFO and various solids, despite the presence of dust deposits as shown in the Figure 10. The breakdown voltages obtained in the presence of solids are relatively close in air, SF_6 and degraded HFO for epoxy/silica and PPA in very divergent fields. However, as shown in Figure 11, a more marked degradation (channel) may occur with HFO, depending on the solid nature. This channel is probably responsible for the progressive loss of dielectric strength with HFO after numerous breakdown experiments in Figure 10. To ensure long-term reliability, such interaction between discharges and solids should be thoroughly investigated.

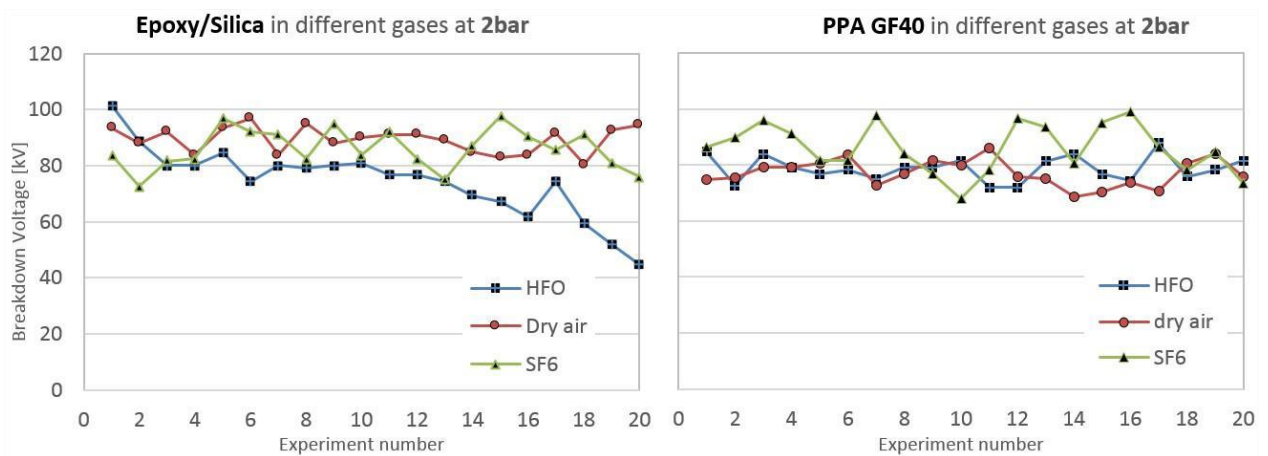


Figure 10 : Breakdown voltages solid/gas insulation with PPA and Epoxy with SF_6 , dry air and HFO1234zeE [7]

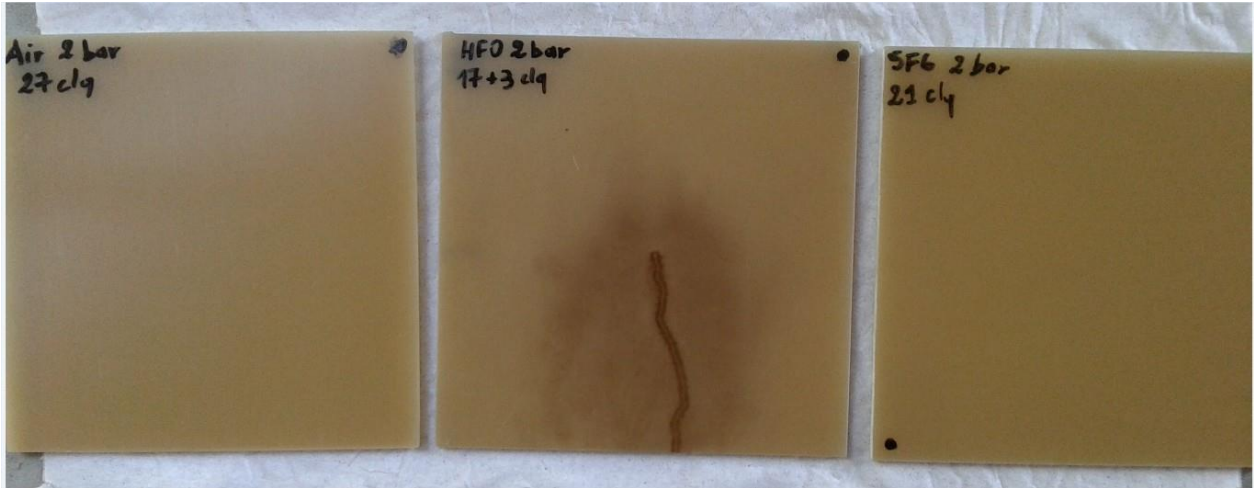


Figure 11 : Epoxy samples after 20 breakdown degradation in different gases at 0.2 MPa [7]

Résumé en français

Le remplacement du SF₆ dans les appareils électriques est au centre des préoccupations de l'industrie électrique depuis des années. En effet, le SF₆ est le gaz présentant le pouvoir de réchauffement climatique le plus élevée connu. Depuis de nombreuses années des alternatives au SF₆ sont étudiées sans succès. Les hydrofluorooléfines présentent de bonnes aptitudes pour substituer le SF₆ dans les systèmes isolés au gaz en moyenne tension.

Dans ce contexte, des études préliminaires ont révélé le potentiel du HFO-1234ze(E) en tant que gaz isolant pour de l'appareillages moyenne tension. L'objectif de ce travail est de générer des données et des connaissances pour le dimensionnement d'appareils moyenne tensions avec du HFO-1234ze(E). Les résultats expérimentaux incluent des mesures de tensions de claquage obtenues dans diverses conditions de tension (DC, choc impulsionnel), de pression (de 0.1 à 0.3 MPa), de distance inter-électrode (10 à 100 mm), et de forme d'électrodes. Cette large gamme de configurations a permis de mettre en évidence deux modes de claquage bien distincts et comparable à ceux présents dans le SF₆. Quand le champ est fortement inhomogène, géométrie la plus critique pour les appareils électriques, le claquage est « contrôlé par la propagation » de leaders. Les leaders se propagent dans l'espace inter-électrodes par sauts à des vitesses de l'ordre de 10⁶ m/s sans nécessairement conduire au claquage. Quand le champ devient plus homogène, le claquage devient « contrôlé par l'initiation ». Quand une pré-décharge s'initie, elle conduit systématiquement au claquage. La pression joue un rôle important sur la tension d'initiation. En fin, l'un des résultats importants de ces travaux est la mise en évidence de l'influence complexe entre la dégradation du HFO, la présence de particules solides à la surface de l'électrode et la perte de tenue diélectrique en champ quasi-homogène après un seul claquage.

Mots-clés : Appareillage moyenne tension, rigidité diélectrique, hydrofluorooléfine (HFO-1234ze(E)), caractérisation électrique, visualisations